

Understanding of lambda-orthogonal photo-induced reaction systems

Zur Erlangung des akademischen Grades eines

DOKTORS DER NATURWISSENSCHAFTEN

(Dr. rer. nat.)

von der KIT-Fakultät für Chemie und Biowissenschaften

des Karlsruher Instituts für Technologie (KIT)

genehmigte

DISSERTATION

von

M. Sc. Philipp Willi Kamm

1. Referent:	Prof. Dr. Andreas-Neil Unterreiner
2. Referent:	Prof. Dr. Hans-Achim Wagenknecht
Cotutelle-Referent:	Prof. Dr. Christopher Barner-Kowollik
Tag der mündlichen Prüfung:	14. Dezember 2021

Die vorliegende Arbeit wurde im Zeitraum von April 2018 bis November 2021 im Rahmen einer Cotutelle-Vereinbarung unter Anleitung von Prof. Dr. Christopher Barner-Kowollik und Prof. Dr. Andreas-Neil Unterreiner an der Queensland University of Technology (QUT) und dem Karlsruher Institut für Technologie (KIT) angefertigt.

Statement of Original Authorship

The work contained in this joint doctoral thesis undertaken between Queensland University of Technology (QUT) and Karlsruhe Institute of Technology (KIT) has not been previously submitted to meet requirements for an award at these or any other higher education institutions. To the best of my knowledge and belief, the thesis contains no material previously published by another person except where due reference is made.

Philipp W. Kamm

Date

Erklärung

Ich erkläre hiermit, dass ich die vorliegende Arbeit im Rahmen der Betreuung durch Prof. Dr. Christopher Barner-Kowollik und Prof. Dr. Andreas-Neil Unterreiner selbstständig verfasst und keine anderen als die angegebenen Quellen und Hilfsmittel verwendet habe. Wörtlich oder inhaltlich übernommene Stellen sind als solche kenntlich gemacht und die Satzung des Karlsruher Instituts für Technologie (KIT) zur *Sicherung guter wissenschaftlicher Praxis* wurde beachtet.

Des Weiteren erkläre ich, dass ich mich derzeit in keinem weiteren laufenden Promotionsverfahren befinde und auch keine vorausgegangenen Promotionsversuche unternommen habe.

Philipp W. Kamm

Datum

*"Happiness can be found even in the darkest of times
if one only remembers to turn on the light."*

~ Albus Dumbledore

ABSTRACT

Light as a carrier of energy to activate chemical reactions has often been praised for its advantageous features such as innocuousness and spatio-temporal control, especially in the form of visible light. A light beam can be aimed precisely where it is needed and be switched on and off within an instant. Through modulation of wavelength and intensity, different reaction channels can be addressed. The ability to activate two photoactive moieties individually at distinct wavelengths alongside each other is called λ -orthogonality. λ -orthogonal systems are highly sought after since they allow to exert even more control over complex reactions. Generally, orthogonality is achieved through separation of absorption bands, combining a red-shifted chromophore and a blue-shifted chromophore, and traditionally both compounds are activated at wavelengths within their respective absorption maximum. Commonly employed chromophores include tetrazoles, *ortho*-methyl benzaldehyde (*o*MBA) derivatives or styrylpyrene. Recently, it has come to attention that the most suitable wavelength for activation of photoreactions is often significantly red-shifted compared to the absorption profile. Meticulous evaluation of the wavelength-dependent reactivity (so-called action plots) is therefore imperative for harnessing the full potential of photoactive systems.

In the present thesis, a new red-shifted tetrazole, *N,N*-dimethylamino pyrene aryl tetrazole (APAT), is presented, whose reactivity reaches far into the visible light regime. Using a wavelength-tuneable *ns*-pulsed laser system, the reactivity is mapped in a small-molecule model reaction. The nitrile imine-mediated tetrazole-ene cycloaddition (NITEC) with diethylfumarate is investigated at wavelengths between 320 nm and 525 nm, and it is found that the most efficient wavelengths to trigger the photoreaction are 430-450 nm, while reactivity up to 510 nm is reported. APAT is subsequently utilised as an end-group modification functionality for polymers, using a simple LED setup at wavelengths between 452 nm and 515 nm, and full end-group conversion is observed at wavelengths up to 500 nm.

Next, APAT is combined with an *o*MBA derivative in a binary reaction mixture, with *N*-(2-hydroxy)ethyl maleimide (NHEM) as a common reaction partner. The efficiency of the NITEC reaction, as well as the *o*-quinodimethane-mediated [4+2] cycloaddition of *o*MBA, is quantified with help of kinetic studies at four different wavelengths, and it is found that full selectivity towards *o*MBA is achieved at 320 nm, while full selectivity towards APAT is

observed at 450 nm. This is attributed to large differences in quantum yields of both chromophores, in combination with differences in absorptivity. The sequence-independence and full orthogonality of the system are then demonstrated using a simple LED setup at 325 nm and 445 nm, applying both wavelengths in a predefined sequence that contains both possible switching pathways (UV→Vis and Vis→UV).

Furthermore, the concept of action plots is carefully scrutinised at the example of the [2+2] cycloaddition of styrylpyrene. A new methodology is proposed that takes into account the absorption of the sample to calculate the number of photons required, resulting in a narrower, slightly red-shifted action plot. Subsequently, the method is applied to characterise the influence of several parameters on the shape and position of the action plot, namely concentration, solvent, and temperature. It is found that these parameters can have a profound effect on the overall yield of the photoreaction but can also modulate the position of the reactivity maximum. It is observed that the wavelength-dependent reactivity is red-shifted by 10 nm when transitioning from acetonitrile to dimethyl sulfoxide (DMSO).

The overall results underpin the importance of precise control over reaction parameters when recording action plots. The concept of wavelength-dependent kinetic measurements of multiple chromophores adds another dimension to action plots and enables the implementation of a fully sequence-independent λ -orthogonal reaction system.

Keywords

[2+2] cycloaddition, 1,3-cipolar cycloaddition, absorption, action plot, chromatic orthogonality, concentration-dependence, Diels-Alder cycloaddition, nitrile imine, *o*-methylbenzaldehyde, photochemistry, photoenol, quantum yield, solvent-dependence, styrylpyrene, temperature-dependence, tetrazole, tuneable laser, wavelength-dependence, wavelength-selectivity, λ -orthogonality

ZUSAMMENFASSUNG

Licht als Energieträger zur Aktivierung chemischer Reaktionen wurde oft für vorteilhafte Eigenschaften wie Unschädlichkeit sowie räumliche und zeitliche Kontrolle gepriesen, insbesondere in Form von sichtbarem Licht. Ein Lichtstrahl kann exakt dorthin gelenkt werden, wo er benötigt wird, und kann instantan ein- oder ausgeschaltet werden. Durch Veränderung von Wellenlänge und Intensität können verschiedene Reaktionskanäle angesteuert werden. Die Möglichkeit, zwei unterschiedliche lichtaktive Komponenten bei unterschiedlichen Wellenlängen nebeneinander individuell zu aktivieren, wird als λ -Orthogonalität bezeichnet. λ -orthogonale Systeme sind begehrt, da sie eine verbesserte Kontrolle über komplexe Reaktionen ermöglichen. Meist wird die Orthogonalität durch eine Trennung der Absorptionsbanden erreicht, indem ein rotverschobenes Chromophor und ein blauverschobenes Chromophor kombiniert werden, wobei traditionell beide Komponenten bei Wellenlängen nahe ihres jeweiligen Absorptionsmaximums aktiviert werden. Zu den gängigen Chromophoren gehören Tetrazole, *ortho*-Methylbenzaldehydderivate (*o*MBA) oder Styrylpyren. In jüngerer Zeit wurde erkannt, dass die zur Aktivierung von Photoreaktionen am besten geeignete Wellenlänge im Vergleich zum Absorptionsprofil häufig deutlich rotverschoben ist. Eine gründliche Untersuchung der wellenlängenabhängigen Reaktivität (sog. Action Plots) ist daher unerlässlich, um das volle Potential lichtaktivierter Systeme auszuschöpfen.

In der vorliegenden Arbeit wird ein neues rotverschobenes Tetrazol, *N,N*-(dimethylamino)pyren aryl tetrazol (APAT), vorgestellt, dessen Reaktivität weit in den Bereich des sichtbaren Lichts hineinreicht. Unter Verwendung eines wellenlängenabstimmbaren *ns*-gepulsten Lasersystems wird die Reaktivität in einer Modellreaktion erfasst. Die Nitrilimin-vermittelte Tetrazol-En Cycloaddition (NITEC) mit Diethylfumarat wird bei Wellenlängen zwischen 320 nm und 525 nm untersucht, und es zeigt sich, dass die am besten geeigneten Wellenlängen zur Aktivierung der Photoreaktion bei 430-450 nm liegen, wobei Reaktivität bis 510 nm beobachtet wird. Anschließend wird APAT als Endgruppenmodifizierungsfunktionalität für Polymere eingesetzt, wobei ein einfacher LED-Aufbau bei Wellenlängen zwischen 452 nm und 515 nm verwendet wird und vollständiger Endgruppenumsatz bei Wellenlängen bis 500 nm beobachtet wird.

Im Anschluss wird APAT mit einem *o*MBA-Derivat in einer binären Photoreaktionsmischung kombiniert, wobei *N*-(2-hydroxy)ethylmaleimid (NHEM) als gemeinsamer Reaktionspartner

dient. Die Effizienz der NITEC-Reaktion sowie der *ortho*-Quinodimethan-vermittelten [2+4]-Cycloaddition von *o*MBA wird mit Hilfe von kinetischen Untersuchungen bei vier verschiedenen Wellenlängen quantifiziert, und es wird festgestellt, dass volle λ -Selektivität bezüglich *o*MBA bei 320 nm erreicht wird, wohingegen volle λ -Selektivität bezüglich APAT bei 450 nm beobachtet wird. Dies wird auf große Unterschiede in den Reaktionsquantenausbeuten der beiden Chromophore, in Kombination mit deutlich getrennten Absorptionsbanden, zurückgeführt. Die Sequenzunabhängigkeit und vollständige Orthogonalität des Systems wird dann anhand eines einfachen LED-Aufbaus bei 325 nm und 445 nm demonstriert, wobei beiden Wellenlängen in einer vordefinierten Sequenz angewendet werden, die beide möglichen Übergänge (UV \rightarrow Vis und Vis \rightarrow UV) enthält.

Darüber hinaus wird das Konzept der Action Plots am Beispiel der [2+2]-Cyclodimerisierung von Styrylpyren sorgfältig untersucht. Es wird eine neuartige Methode vorgestellt, welche die Absorption der Probe berücksichtigt, um die Anzahl der benötigten Photonen zu berechnen. Dies führt zu einem schmaleren, leicht rotverschobenen Action Plot. Diese Methode wird anschließend angewandt, um den Einfluss mehrerer Parameter (Konzentration, Lösungsmittel, Temperatur) auf Form und Position des Action Plots zu charakterisieren. Es zeigt sich, dass diese Parameter nicht nur die Gesamtausbeute der Photoreaktion stark beeinflussen, sondern auch die Wellenlänge des Reaktivitätsmaximums verschieben können. So wird beispielsweise die wellenlängenabhängige Reaktivität im 10 m, rotverschoben, wenn Dimethylsulfoxid (DMSO) statt Acetonitril verwendet wird.

Die Ergebnisse unterstreichen die Bedeutung der strikten Kontrolle der Reaktionsparameter bei der Messung von Action Plots. Das Konzept von wellenlängenabhängigen kinetischen Messungen in Mehrkomponentenreaktionssystemen fügt den Action Plots eine weitere Dimension hinzu und ermöglicht die Einrichtung eines vollständig sequenzunabhängigen λ -orthogonalen Reaktionssystems.

Stichworte

[2+2]-Cycloaddition, 1,3-dipolare Cycloaddition, Absorption, Action Plot, chromatische Orthogonalität, Diels-Alder Cycloaddition, Konzentrationsabhängigkeit, Lösungsmittelabhängigkeit, Nitrilimine, *ortho*-Methylbenzaldehyd, Photochemie, Photoenol, Quantenausbeuten, Styrylpyren, Temperaturabhängigkeit, Tetrazol, wellenlängenabstimmbare Laser, Wellenlängenabhängigkeit, Wellenlängenselektivität, λ -Orthogonalität

CONTENTS

ABSTRACT.....	I
ZUSAMMENFASSUNG.....	III
LIST OF FIGURES.....	IX
LIST OF SCHEMES.....	XX
LIST OF TABLES.....	XXII
LIST OF EQUATIONS.....	XXIV
ABBREVIATIONS.....	XXV
1 INTRODUCTION.....	1
2 THEORETICAL BACKGROUND.....	3
2.1 PHOTOPHYSICAL FUNDAMENTALS.....	3
2.2 CYCLOADDITIONS.....	8
2.2.1 FUNDAMENTALS.....	8
2.2.2 TETRAZOLE CHEMISTRY.....	10
2.2.3 PHOTOENOL CHEMISTRY.....	19
2.2.4 [2+2] CYCLOADDITIONS.....	20
2.3 RED-SHIFTED PHOTOCHEMISTRY.....	25
2.4 Δ-ORTHOGONALITY.....	28
2.5 LASER SYSTEMS.....	34
2.5.1 FUNDAMENTALS.....	34
2.5.2 WAVELENGTH-TUNEABLE LASER SYSTEMS.....	37
3 GREEN-LIGHT ACTIVATED CYCLOADDITIONS.....	41
3.1 OBJECTIVE.....	41
3.2 SYNTHESIS OF A RED-SHIFTED TETRAZOLE.....	44
3.2.1 SMALL MOLECULE.....	44
3.2.2 POLYMERS BEARING A MALEIMIDE END-GROUP.....	47
3.3 STEADY-STATE SPECTROSCOPY.....	50
3.4 WAVELENGTH-DEPENDENT SMALL-MOLECULE LIGATION.....	54

3.5	GREEN-LIGHT INDUCED FUNCTIONALISATION OF POLYMER END-GROUPS	62
3.6	CONCLUSION	66
4	EXPLOITING DIFFERENT REACTION QUANTUM YIELDS TO ESTABLISH SEQUENCE-INDEPENDENT Λ-ORTHOGONALITY	68
4.1	OBJECTIVE	68
4.2	PROOF OF PRINCIPLE	72
4.3	WAVELENGTH-DEPENDENT REACTION QUANTUM YIELDS	76
4.4	SEQUENCE-INDEPENDENT Λ-ORTHOGONALITY	82
4.5	CONCLUSION	86
5	CYCLOADDITIONS IN DISPARATE ENVIRONMENTS	88
5.1	OBJECTIVE	88
5.2	ACCOUNTING FOR LIGHT-ABSORPTION IN ACTION PLOTS	91
5.3	CONCENTRATION-DEPENDENCE	93
5.4	SOLVENT-DEPENDENCE	95
5.5	TEMPERATURE-DEPENDENCE	97
5.6	CONCLUSION	98
6	CONCLUDING REMARKS	100
7	OUTLOOK	102
8	EXPERIMENTAL PART	105
8.1	MATERIALS	105
8.2	ANALYSIS AND INSTRUMENTATION	106
8.2.1	NUCLEAR MAGNETIC RESONANCE (NMR) SPECTROSCOPY	106
8.2.2	DIFFUSION ORDERED SPECTROSCOPY (DOSY)	106
8.2.3	LIQUID CHROMATOGRAPHY COUPLED MASS SPECTROMETRY (LC-MS)	107
8.2.4	DMAC-SIZE EXCLUSION CHROMATOGRAPHY (SEC)	107
8.2.5	CHROMATOGRAPHY	108
8.2.6	UV/VIS SPECTROSCOPY	108
8.2.7	FLUORESCENCE SPECTROSCOPY	108

8.3	IRRADIATION SETUPS	109
8.3.1	20 HZ TUNEABLE LASER SYSTEM (QUT)	109
8.3.2	LED SETUP.....	113
8.3.3	100 HZ TUNEABLE LASER SYSTEM (KIT)	114
8.4	APAT AND DIETHYLFUMARATE PHOTOREACTION	117
8.4.1	SAMPLE PREPARATION FOR ACTION PLOT MEASUREMENTS.....	117
8.4.2	POWER SETTINGS OF THE <i>ns</i> -TUNEABLE LASER FOR ACTION PLOT EXPERIMENTS.....	117
8.4.3	ISOLATION OF CYCLOADDUCTS.....	118
8.4.4	HIGH-CONVERSION CYCLOADDITION OF APAT AND DEF	119
8.5	<i>α</i>-ORTHOGONAL PHOTOREACTIONS OF APAT AND OMBA WITH NHEM.....	120
8.5.1	SAMPLE PREPARATION FOR KINETIC MEASUREMENTS.....	120
8.5.2	POWER SETTINGS OF THE <i>ns</i> -TUNEABLE LASER FOR KINETIC MEASUREMENTS	120
8.5.3	ISOLATION OF CA _{OMBA}	121
8.5.4	DETERMINATION OF QUANTUM YIELDS.....	121
8.5.5	SAMPLE PREPARATION FOR SEQUENTIAL LED EXPERIMENT	122
8.6	[2+2] CYCLOADDITION OF STYRYLPYRENE IN DISPARATE ENVIRONMENTS	123
8.6.1	SAMPLE PREPARATION OF THE ACTION PLOT EXPERIMENTS	123
8.6.2	TEMPERATURE-DEPENDENCE STUDY.....	124
8.7	SYNTHETIC PROCEDURES	125
8.7.1	<i>N,N</i> -(DIMETHYL)AMINO PYRENE ARYL TETRAZOLE.....	125
8.7.2	MALEIMIDE END-CAPPED PMMA CHAIN.....	133
8.7.3	2-METHOXY-6-METHYLBENZALDEHYDE	136
8.7.4	HYDROXY-STYRYLPYRENE.....	137
9	REFERENCES	138
10	APPENDIX	153
10.1	NMR-SPECTRA	153
10.2	STEADY STATE SPECTROSCOPY	166
10.2.1	ABSORPTION SPECTRA.....	166
10.2.2	FLUORESCENCE SPECTRA	169

10.3	RESULTS OF APAT AND DIETHYLFUMARATE PHOTOREACTION	170
10.3.1	LC-MS RESULTS OF THE ACTION PLOT EXPERIMENTS	170
10.3.2	PROLONGED IRRADIATION TIME EXPERIMENTS	172
10.4	Λ-ORTHOGONAL PHOTOREACTIONS OF APAT AND OMBA WITH NHEM.....	173
10.4.1	RESULTS OF KINETIC MEASUREMENTS	173
10.4.2	RESULTS OF SEQUENTIAL LED-EXPERIMENT	176
10.4.3	TEMPERATURE-STABILITY OF APAT.....	177
10.5	RESULTS OF THE [2+2] CYCLODIMERIZATION OF STYRYLPYRENE.....	178
10.5.1	RESULTS OF ACTION PLOT EXPERIMENTS WITH ADJUSTED PHOTON NUMBER.....	178
10.5.2	RESULTS OF ACTION PLOT EXPERIMENT AT 5 mM CONCENTRATION	179
10.5.3	RESULTS OF ACTION PLOT EXPERIMENTS IN DMSO- D_6	179
10.5.4	RESULTS OF ACTION PLOT EXPERIMENTS AT 37 °C.....	180
11	ACKNOWLEDGEMENTS	181
12	ACADEMIC OUTPUT.....	183

LIST OF FIGURES

- Figure 1:** Energy diagram showing electronic ground and excited state as well as various vibrational ground and excited states and vertical transitions between them. vi'' and vj' are vibrational excited states of the electronic ground state and excited state, respectively. Adapted from Ref.⁵..... 5
- Figure 2:** *Jabłoński* diagram, showing possible relaxation pathways upon excitation between different electronic and vibrational states. Vertical excitation (absorption, A), intramolecular vibrational energy redistribution (IVR), vibrational relaxation (VR), radiative transitions (fluorescence, F, and phosphorescence, P), non-radiative transitions (internal conversion, IC, and intersystem crossing, ISC)..... 6
- Figure 3:** Pathways for thermally and photochemically driven [2+2] and [2+4] cycloadditions with different orbital orientations. Where orbital flaps are of the same colour, the overlap is bonding, and where they are of different colour, it is anti-bonding. The nomenclature $\pi 2s$ indicates how many π -electrons the respective reaction partner provides, and whether the involved orbital flaps are located on the same side (suprafacial, s) or opposite sides (antarafacial, a) of the molecule. Adapted from Ref.²⁰ 9
- Figure 4:** Photoexcitation of a ground state molecule leads to population of an excited singlet state. The number of nodes in the HOMO increases by +1 (from 0 to 1 in this case) and the orbital symmetry changes, allowing for stable transition states that were previously forbidden. 10
- Figure 5:** HOMO energy plotted *versus* the logarithmic reaction rate of the 1,3-cycloaddition of differently substituted tetrazoles and pent-4-en-1-ol upon UV irradiation. Copyright (2021) Wiley. Reproduced from Wang *et al.*, *Angew. Chem. Int. Ed.* **2009**, *48*, 5330-5333. Wiley-VCH Verlag GmbH & Co. KGaA, Weinheim. 15
- Figure 6:** 1,3-dipolar cycloaddition between an EGFP bearing a tetrazole moiety, and a methacrylamide, forming a fluorescent adduct. Copyright (2021) Wiley. Reproduced with permission from Song *et al.*, *Angew. Chem. Int. Ed.* **2008**, *47*, 2832-2835. Wiley-VCH Verlag GmbH & Co. KGaA, Weinheim. 16
- Figure 7:** Variety of tetrazole applications. Figures were reproduced with permission from the references indicated. Top right: Site-selective crosslinking of proteins.⁸⁴ Left: Spatially

	resolved surface modification. ⁹⁴ Bottom right: Development of functional fluorescent single-chain nanoparticles (SCNPs). ¹⁰⁷	18
Figure 8:	Applications of the Diels-Alder reaction of dienophiles and <i>o</i> -quinodimethanes, generated from <i>o</i> -methyl benzaldehydes upon UV-irradiation. Figures were reproduced with permission from the references indicated. Top left: Fabrication and functionalisation of 3D-microstructures <i>via</i> multiphoton-induced photoreaction. ¹¹⁸ Right: Formation of SCNPs. ¹²¹ Bottom left: Spatially resolved photochemical grafting on biosurfaces. ¹²⁰	20
Figure 9:	Applications of the [2+2] cyclodimerization of styrylpyrene. Figures were reproduced with permission from the references indicated. Top right: Reversible folding of single-chain nanoparticles (SCNPs). ¹³⁸ Left: Photopolymerisation of telechelic building blocks bearing styrylpyrene end-groups. ¹³⁹ Bottom right: Photocrosslinking of DNA-duplexes. ¹³⁵	23
Figure 10:	Red-shifting of tetrazoles by tethering extended conjugated systems or auxochromes. The given wavelength refers to λ_{max} of the respective absorption spectrum. ^{61, 65, 66, 73, 174, 176}	26
Figure 11:	Examples from literature, demonstrating a red-shift of the reactivity maximum compared to the absorption spectrum of a photoreactive moiety. Figures were reproduced with permission from the references indicated. a) Photoenolization of <i>o</i> MBA and subsequent cycloaddition with maleimide. ¹¹³ b) Initiation efficiency of an oxime ester in a free radical polymerization of methyl methacrylate (MMA). ¹⁸⁷ c) Photo-induced cyclodimerization of styrylpyrene. ¹³⁷	28
Figure 12:	a) Left graph: Generic absorption spectra of two photoactive compounds and the respective wavelength-dependent conversion maps (action plot, refer to section 2.3). Right graph: Conversion over time. At lower wavelengths, both units are converted simultaneously. b) Left graph: Idealized, distinct absorption spectra of two photoactive compounds. Right graph: Ideal conversion plots in a fully λ -orthogonal reaction system.	29
Figure 13:	a) Orthogonal photolysis of a coumarin-linker upon 405 nm irradiation, followed by photocleavage of an <i>o</i> -nitrobenzyl photocage after 365 nm irradiation. Reproduced with permission from <i>Wu et al., ACS Appl. Mater. Interfaces</i> 2018, 10 , 19416-19427. Copyright 2021 American Chemical Society. b) Orthogonal cleavage of carbamate derivatives, releasing carboxylic acids upon irradiation at 350 nm or 254 nm, in a sequence-independent fashion. Reproduced from <i>Tetrahedron Letters</i> , 41, Bochet, C. G.,	

Wavelength-selective cleavage of photolabile protecting groups, 6341-6346 Copyright (2021), with permission from Elsevier.	30
Figure 14: Orthogonal activation of a methoxyphenyl tetrazole at 285 nm in a mixture of acetonitrile and water. The water prevents the photoenol form being formed. In pure MeCN, the <i>o</i> MBA could be activated at 382 nm, forming the photoenol. Copyright (2021) Wiley. Reproduced with permission from <i>Menzel et al.</i> , <i>Angew. Chem. Int. Ed.</i> 2019 , <i>58</i> , 7470–7474.....	31
Figure 15: Pathway-independent synthesis of star polymers through photo-induced ligation <i>via</i> NITEC or Diels-Alder reaction of photoenols. Reversible deactivation of the photoenol precursor (<i>o</i> MBA) allows for activation of the tetrazole prior to the photoenolization step, for which the deactivated <i>o</i> MBA is hydrolysed. Reproduced from <i>Hiltebrandt et al.</i> , <i>Chem. Commun.</i> , 2016, 52 , 9426–9429 with permission from the Royal Society of Chemistry. ¹²²	32
Figure 16: Schematic diagrams of two-, three-, and four-level laser media. Arrows in red indicate the pump process. Yellow and green arrows indicate ultrafast radiationless relaxation. Blue arrows indicate stimulated emission.	35
Figure 17: Schematic illustration of the interaction of the three main components of a laser: pump source, active laser medium and resonator. Amplified photons are exiting the cavity through a semi-transparent mirror as a spatially and temporally coherent, polarised light beam.	36
Figure 18: Schematic energy-level diagrams of the most common frequency mixing processes: a) Second-harmonic generation (SHG), b) Sum-frequency generation (SFG), c) Difference-frequency generation (DFG).	38
Figure 19: Geometries of the interactions of nonlinear processes: a) Second harmonic generation. b) Sum-frequency generation. c) Difference-frequency generation.	39
Figure 20: Simplified schematic setup of the wavelength tunable laser system. A Q-switched Nd:YAG laser is pumped by a flashlamp, emitting quasi-monochromatic pulses at 1064 nm. Through a series of nonlinear optics, output wavelengths between 210 nm and 2400 nm can be achieved.	39
Figure 21: Combining the bathochromic effects of pyrene and a dimethylamino group, a stronger red-shift is induced in the final molecule.	42
Figure 22: Schematic overview over the methodology applied in the current chapter. After synthesising and carefully characterising a red-shifted tetrazole, wavelength-dependent reactivity was assessed <i>via ns</i> -pulsed laser experiments and quantified by	

LC-MS, producing a so-called action plot. Furthermore, suitable LEDs were employed for polymer ligation reactions, and the results analysed by $^1\text{H-NMR}$ spectroscopy. .43

Figure 23: Magnified signals of the $-\text{NMe}_2$ protons in the $^1\text{H-NMR}$ spectrum of the isomer mixture. For the full spectrum refer to **Figure S 12**. 45

Figure 24: $^1\text{H-NMR}$ spectrum of APAT in CDCl_3 46

Figure 25: Structures of three synthesised APAT derivatives: APAT without linker, APAT-OH, carrying an undecan-1-ol chain in *para*-position of the C^5 -phenyl ring, and APAT-COOH, carrying a carboxylic acid in the *para*-position of the C^5 -phenyl ring. 47

Figure 26: a) Tracking of the end-group fidelity through three steps of ω -hydroxy-PMMA-maleimide, showing clean removal of the benzodithio benzoyl group, followed by complete cleavage of the furan protection group. b) Structure and SEC trace in dimethylacetamide (DMAc) of the final polymer. $M_n = 4.7 \text{ kDa}$, $D = 1.15$ 49

Figure 27: Full absorption spectrum of APAT in MeCN, measured at $c = 13.8 \mu\text{M}$ in a 1 cm cuvette at ambient temperature. 50

Figure 28: Normalised absorption spectra in dimethylsulfoxide (DMSO), dichloromethane (DCM), acetonitrile (MeCN), chloroform and cyclohexane. The spectra were normalised to the absorption peak at 375 nm. All spectra were recorded at ambient temperature in 1 cm cuvettes. 51

Figure 29: Absorption and emission spectra of APAT in cyclohexane, DCM and MeCN. Spectra were recorded in 1 cm quartz cuvettes and 1 cm fluorescence cuvettes at ambient temperature. $\lambda_{\text{ex.}} = 390 \text{ nm}$. Φ_{F} = fluorescence quantum yield in MeCN (blue) and DCM (red). 52

Figure 30: LC-MS analysis of NITEC and NICAL (nitrile imine-carboxylic acid ligation) reactions of APAT with various electron deficient double bonds, as well as acetic acid. The schemes show the dipolarophile and the respective product after cycloaddition with APAT. Where head-to-head and head-to-tail conformations occur, only one is depicted in the scheme for reasons of clarity. The measured mass spectra are the integrated total ion count (TIC) over the cycloadduct peak. a) Diethylfumarate. b) N-ethylmaleimide. c) N-(2-hydroxy ethyl) maleimide. d) 2-(2-(2-methoxyethoxy)ethoxy)ethyl acrylate. e) 2-hydroxyethyl acrylate. f) Acetic acid. 55

Figure 31: Analysis of two isolated cycloadducts after NITEC reaction of APAT, CA_{DEF} and CA_{NHEM} . Left side, from top to bottom: $^1\text{H-NMR}$ spectrum of CA_{DEF} in CDCl_3 (pyrazoline signals are shown in the box), absorption spectrum ($c = 26.2 \mu\text{mol}$ in MeCN), and PDA signal from the LC-MS. Right side, from top to bottom: $^1\text{H-NMR}$

spectrum of CA _{NHEM} in toluene- <i>d</i> ₈ , absorption spectrum (<i>c</i> = 12.3 μmol in MeCN), and PDA signal of the LC-MS.....	57
Figure 32: Overlay of the absorption spectra of APAT (460 μM in MeCN) and CA _{DEF} (40 μM in MeCN) (left <i>y</i> -axis) and the wavelength-dependent reactivity profile (action plot) of the photoinduced NITEC reaction between APAT and DEF (right <i>y</i> -axis). All experiments were conducted in MeCN and repeated two or three times to obtain error bars. For a detailed description of the laser setup, data processing and conditions of all action plot experiments, refer to 8.3.1.	59
Figure 33: a) Fluorescence spectra before and after 30 min irradiation with a 450 nm LED. Spectra were recorded in MeCN and show a drop in fluorescence intensity by a factor of ~100. b) Photograph of samples before and after irradiation under UV light.....	61
Figure 34: Overlaid APAT absorption spectrum and emission spectra of the LEDs employed for polymer-end-group modification.....	62
Figure 35: Analysis of products after irradiation at 500 nm for 48 h and preparative SEC. a) ¹ H-NMR spectrum with zoomed inlet into the aromatic region. Absence of the vinylic signal at δ = 6.75 ppm indicates full conversion of the PMMA-maleimide. b) COSY measurement, confirming that the two signals at δ = 5.06 ppm and δ = 5.59 ppm correspond to the two adjacent pyrazoline protons. c) DOSY measurement, confirming that all relevant signals are attributed to protons attached to a polymer chain. d) SEC traces before and after irradiation. Left graph: RI trace displays a slight shift to lower retention times, corresponding to higher molecular weight (before : M _n = 4.7 kDa, Đ = 1.16, after : M _n = 4.8 kDa, Đ = 1.09). Right graph: UV-Vis scan at 420 nm shows no signal before the reaction. After ligation and formation of CA _{PMMA-Mal} the shape of the UV-Vis trace follows the RI trace, confirming successful tethering of the chromophore..	63
Figure 36: Polymer end-group modification and ¹ H-NMR analysis. (a) Reaction scheme of the NITEC between a maleimide end-capped PMMA chain and APAT, forming the pyrazoline cycloadduct. (b) Zoom into the aromatic region of ¹ H-NMR spectra of CA _{PMMA-Mal} after polymer end-group modification. Reaction conversion was determined by comparing the resonance integrals of the aromatic protons (a = 13 H) and remaining vinylic protons of the maleimide end-group (b = 2 H). For reference, the spectrum of PMMA-Mal is depicted in blue.	64
Figure 37: Two photo-active moieties can display overlapping absorption profiles. Yet, due to strongly deviating reactivity in different wavelength-regimes, they can individually	

be addressed, forming cycloadducts in a fully orthogonal and pathway-independent fashion.	69
Figure 38: Schematic methodology followed in the current chapter. Employing a wavelength-tuneable <i>ns</i> -pulsed laser system, the reaction kinetics of two small-molecule ligation reactions are evaluated. After establishing the optimum wavelengths, an LED-sequence is applied to demonstrate the orthogonal addressability of both units alongside each other.	70
Figure 39: Left <i>y</i> -axis: Absorption spectra of <i>o</i> MBA and APAT in MeCN. Right <i>y</i> -axis: Wavelength-dependent reactivity profiles (action plots) of NITEC between APAT and diethylfumarate (DEF), as well as cycloaddition of <i>o</i> MBA and <i>N</i> -ethyl maleimide (NEM). APAT action plot was adapted from <i>Kamm et al., Chem. Commun.</i> 2021 , 57, 3991 (refer to chapter 3). <i>o</i> MBA action plot was adapted from <i>Menzel et al., J. Am. Chem. Soc.</i> , 2017, 139 , 15812-15820.	72
Figure 40: Top graphs: Exemplary chromatograms after photoreactions between <i>o</i> MBA and NHEM, as well as APAT and NHEM, showing the peak separation on the column. The scan wavelength of the UV detector was 214 nm. Bottom graphs: Absorption spectra of <i>o</i> MBA, CA _{<i>o</i>MBA} , APAT and CA _{APAT} . The molar absorption coefficient of each species $\epsilon_{214\text{ nm}}$ was used to calculate the photo-adduct yield from the peak integral ratio of the chromatograms.	74
Figure 41: Overlaying absorption spectra of the starting materials, APAT, <i>o</i> MBA and NHEM, as well as the cycloadducts formed during the photoreaction, CA _{APAT} and CA _{<i>o</i>MBA} . The vertical lines represent the wavelengths of laser light employed for the kinetic studies.	76
Figure 42: Time-dependent formation of CA _{APAT} and CA _{<i>o</i>MBA} upon cycloaddition during irradiation with a) 500 μ J pulses of 320 nm. b) 500 μ J pulses of 360 nm. c) 364 μ J pulses of 390 nm. d) 2000 μ J pulses of 450 nm. All experiments were carried out at ambient temperature, using a 20 Hz pulsed laser system. The bottom <i>x</i> -axis shows the irradiation time in s or min. The top <i>x</i> -axis shows the incident photon equivalents, relative to the amount of APAT and <i>o</i> MBA, which is calculated from the irradiation time and the pulse energy of the laser.	77
Figure 43: a) Structures of CAAPATH, CAAPAT = and APAT. b) Exemplary chromatogram after 30 min irradiation at 450 nm. b) Zoomed mass spectra of all species: CAAPATH: <i>m/z</i> [M+H] ⁺ = 503.2078; found: 503.2074. CAAPAT =: <i>m/z</i> [M+H] ⁺ = 501.1921; found: 501.1920. APAT: <i>m/z</i> [M+H] ⁺ = 390.1713; found: 390.1714. c) Extracted PDA signals of	

the LC-MS, showing similarities between the aromatic species CAAPAT = and APAT, whereas the absorption profile of CAAPATH differs significantly.	80
Figure 44: Overlay of the absorption spectra of both photoactive chromophores (<i>o</i> MBA and APAT) and the normalised emission spectra of the employed LEDs (325 nm 0.67 W and 445 nm 10 W).....	82
Figure 45: Photo-cycloadduct yield of CA _{<i>o</i>MBA} and CA _{APAT} after sequential irradiation with LEDs at two disparate wavelengths (325 nm, 0.67 W and 445 nm, 10 W). Due to faster reaction kinetics of the <i>o</i> MBA cycloaddition, samples were taken in 15 min intervals in the UV regime, and in 40 min intervals in the visible light regime. A dark period of 120 min was added between the two possible switching pathways (UV→Vis and Vis→UV). <i>o</i> MBA is converted exclusively through 325 nm irradiation, while APAT only reacts to 445 nm light.	83
Figure 46: LC-MS chromatograms after irradiation with a 445 nm 10 W LED. CAAPATH and CAAPAT = increase over time, while APAT decreases. Similarly, the amount of SP2 slowly increases over time, reaching a relative peak integral of 10 %.	84
Figure 47: Exploiting differences in reaction quantum yields, it is possible to orthogonally activate <i>o</i> MBA (with UV light) and APAT (with visible light) in any order.	86
Figure 48: How efficiently a reaction proceeds at different wavelengths depends on a number of variables, i.e., the fraction of photons that lead to an excitation event, the concentration, the solvent, or the temperature.	89
Figure 49: Methodology applied to investigate the effect of the different parameters: Wavelength-dependent conversion measurements were carried out using a 100 Hz <i>ns</i> -pulsed laser system, varying either the number of incident photons, the styrylpyrene concentration, or the solvent. ¹ H-NMR spectroscopy was used to analyse and quantify the reaction outcome.	90
Figure 50: a) Structures of styrylpyrene and the dimer after [2+2] photodimerization. b) Absorption spectrum of styrylpyrene (measured at 69 μM in MeCN at ambient temperature, 1 cm cuvette).	91
Figure 51: a) Overlay of the absorption spectrum of styrylpyrene and the applied photon counts. A logarithmic scale was chosen for the latter, to better visualise the shape of the profile. b) Action plots of the dimerization of styrylpyrene upon constant photon irradiation (adapted from Marschner <i>et al.</i> , <i>Macromolecules</i> 2018, 51, 3802-3807) and upon irradiation with the photon number adjusted to the absorption spectrum. Error	

bars were obtained through 3x repetition of each experiment. For comparison, the absorption spectrum of styrylpyrene is overlaid.	92
Figure 52: Overlay of the action plots of the dimerization of styrylpyrene at concentrations 5 mM and 10 mM in MeCN, with a constant number of absorbed photons. Inset: Normalised action plots. To make the slight blue-shift more visible, the error bars are enveloped.	94
Figure 53: Overlay of absorption spectra of styrylpyrene in MeCN and DMSO, as well as solvent-dependent action plots (at 10 mM concentration in the respective solvent)..	96
Figure 54: Overlay of absorption spectra of styrylpyrene at 20 °C and 37 °C, as well as temperature-dependent action plots (at 10 mM concentration).....	98
Figure S 1: Experimental setup for the tuneable laser experiments at QUT. Energy output is adjusted using an attenuator and read out with an energy meter before the sample is inserted into the sample holder.	110
Figure S 2: Calibration of the glass vial transmittance.	111
Figure S 3: Setup of the LED irradiation experiments.....	113
Figure S 4: Experimental setup for the tunable laser experiments at KIT. The energy output is regulated with the attenuator and controlled with the energy meter. Measurement of energy and irradiation of samples cannot be carried out simultaneously. An individual setting of the attenuator is necessary before each irradiation experiment. The shutter was opened and closed manually <i>via</i> the connected computer.	114
Figure S 5: Calibration of the glass vial transmittance.....	115
Figure S 6: Based on 1D and 2D NMR spectra the isomeric structure of <i>N,N</i> -dimethyl pyrene-1,8-diamine could be confirmed. All spectra were measured at ambient temperature in CDCl ₃ . For clarity, only the relevant regions are shown and the rest of the spectra is omitted. a) Possible isomeric structures (1,6- and 1,8-isomer) of the product. b) ¹ H-NMR spectrum. c) COSY, showing ³ J couplings between protons. d) ¹³ C-NMR spectrum. e) HMBC, showing multiple-bond correlations between ¹ H and ¹³ C nuclei. f) DEPTQ-135-NMR spectrum, showing only primary and tertiary carbons. (-CH and -CH ₃).	128
Figure S 7: ¹ H-NMR spectrum in CDCl ₃ of the isolated polymeric fraction after polymer end-group ligation of APAT and maleimide end-capped PMMA at 452 nm for 2.5 h.....	153

Figure S 8: ¹ H-NMR spectrum in CDCl ₃ of the isolated polymeric fraction after polymer end-group ligation of APAT and maleimide end-capped PMMA at 500 nm for 3.7 h.....	154
Figure S 9: ¹ H-NMR spectrum in CDCl ₃ of the isolated polymeric fraction after polymer end-group ligation of APAT and maleimide end-capped PMMA at 515 nm for 4.7 h.....	154
Figure S 10: ¹ H-NMR spectrum of CA _{oMBA} in MeCN-d ₃	155
Figure S 11: ¹ H-NMR spectrum of <i>N,N</i> -dimethyl pyrene-1-amine in CDCl ₃	155
Figure S 12: ¹ H-NMR spectrum of <i>N,N</i> -dimethyl nitropyrene-1-amine. Relative amounts of the three isomers can be estimated by integrating the -NMe ₂ signals at $\delta = 3.10$ - 3.14 . <i>N,N</i> -dimethyl-3-nitropyrene-1-amine is the only isomer displaying a singlet, stemming from the H-atom in the C ² -position of the pyrene.....	156
Figure S 13: ¹ H-NMR spectrum of <i>N,N</i> -dimethyl pyrene-1,8-diamine in CDCl ₃	156
Figure S 14: COSY measurement of <i>N,N</i> -dimethyl pyrene-1,8-diamine in CDCl ₃	157
Figure S 15: ¹³ C-NMR spectrum of <i>N,N</i> -dimethyl pyrene-1,8-diamine in CDCl ₃	157
Figure S 16: HMBC measurement of <i>N,N</i> -dimethyl pyrene-1,8-diamine in CDCl ₃	158
Figure S 17: DEPTQ-135 measurement of <i>N,N</i> -dimethyl pyrene-1,8-diamine in CDCl ₃	158
Figure S 18: HSQC measurement of <i>N,N</i> -dimethyl pyrene-1,8-diamine in CDCl ₃	159
Figure S 19: ¹ H-NMR spectrum of (<i>E</i>)- <i>N'</i> -benzylidene-4-methylbenzenesulfonohydrazide in DMSO- <i>d</i> ₆	159
Figure S 20: ¹ H-NMR spectrum of APAT in CDCl ₃	160
Figure S 21: ¹³ C-NMR spectrum of APAT in CDCl ₃	160
Figure S 22: ¹ H-NMR spectrum of 11-hydroxyundecyl-4-formylbenzoate in CDCl ₃	161
Figure S 23: ¹ H-NMR spectrum of 11-hydroxyundecyl (<i>E</i>)-4-((2-tosylhydrazineylidene)methyl)benzoate in DMSO- <i>d</i> ₆	161
Figure S 24: ¹ H-NMR spectrum of 11-hydroxyundecyl 4-(2-(8-(dimethylamino)pyren-1-yl)-2H-tetrazol-5-yl)benzoate in CDCl ₃	162
Figure S 25: ¹ H-NMR spectrum of methyl (<i>E</i>)-4-((2-tosylhydrazineylidene)methyl)benzoate in DMSO- <i>d</i> ₆	162
Figure S 26: ¹ H-NMR spectrum of methyl 4-(2-(8-(dimethylamino)pyren-1-yl)-2H-tetrazol-5-yl)benzoate in CDCl ₃	163
Figure S 27: ¹ H-NMR spectrum of 4-(2-(8-(dimethylamino)pyren-1-yl)-2H-tetrazol-5-yl)benzoic acid in THF- <i>d</i> ₈	163
Figure S 28: ¹ H-NMR spectrum of 2-(2-hydroxyethyl)-3a,4,7,7a-tetrahydro-1H-4,7-methanoisindole-1,3(2H)-dione (furan-protected <i>N</i> -(2-hydroxy)ethyl maleimide) in CDCl ₃	164

Figure S 29: ¹ H-NMR spectrum of 2-((4R,7S)-1,3-dioxo-1,3,3a,4,7,7a-hexahydro-2H-4,7-epoxyisoindol-2-yl)ethyl-4-cyano-4-((phenylcarbonothioyl)thio)pentanoate (chain-transfer agent, CTA) in CDCl ₃	164
Figure S 30: ¹ H-NMR spectrum of maleimide-end-capped PMMA chain in CDCl ₃	165
Figure S 31: ¹ H-NMR spectrum of 2-methoxy-6-methyl benzaldehyde (o-methylmenzaldehyde, oMBA) in DMSO- <i>d</i> ₆	165
Figure S 32: Concentration series of the absorption spectra of APAT (left) and CA _{DEF} (right) in MeCN. All spectra were measured in 1 cm quartz cuvettes at ambient temperature.	166
Figure S 33: Linear fits of the absorbance (OD) at 392 nm (scan wavelength of the LC-MS UV detector) after recording UV/Vis spectra of APAT (concentrations 6.94 μM, 13.9 μM, 27.8 μM, 55.6 μM, 111 μM and 222 μM) and CA _{DEF} (2.67 μM, 5.34 μM, 13.4 μM, 26.7 μM, 40.1 μM) in MeCN. The linear regression lines gave the absorption coefficients $\epsilon_{392\text{ nm}APAT} = 9600\text{ L mol}^{-1}\text{ cm}^{-1}$ and $\epsilon_{392\text{ nm}CADEF} = 20500\text{ L mol}^{-1}\text{ cm}^{-1}$	166
Figure S 34: Linear fit of the absorbance (OD) at 402 nm after recording UV/Vis spectra of APAT in MeCN at concentrations 6.94 μM, 13.9 μM, 27.8 μM, 55.6 μM, 111 μM and 222 μM. Slope of the linear regression line gave the absorption coefficient $\epsilon_{402\text{ nm}} = 10080\text{ L mol}^{-1}\text{ cm}^{-1}$	167
Figure S 35: Switching APAT absorption through pH changes. Adding tosylsulfonic acid induces a hypsochromic shift into the UV region. Adding an equal amount of triethylamine restores the original absorption spectrum. Spectra were recorded at <i>c</i> = 0.32 mM in a 2 mm cuvette, at ambient temperature.	167
Figure S 36: Concentration series of the absorption spectra of CA _{APAT} (left), oMBA (centre) and CA _{oMBA} (right). CA _{APAT} and oMBA were measured in MeCN. CA _{oMBA} was measured in MeCN/H ₂ O (92:8), as per the LC-MS gradient. All spectra were measured in 1 cm quartz cuvettes at ambient temperature.	168
Figure S 37: Linear fits of the absorbance (OD) at 214 nm (scan wavelength of the LC-MS UV detector) after recording UV/Vis spectra of oMBA (concentrations 3.0 μM, 8.9 μM, 26.7 μM, 59.3 μM and 88.9 μM), CA _{oMBA} (concentrations 16.2 μM, 48.7 μM, 97.3 μM and 146 μM) APAT (concentrations 6.94 μM, 13.9 μM, 27.8 μM, 55.6 μM, and 111 μM), and CA _{APAT} (0.37 μM, 1.2 μM, 3.6 μM, 12.0 μM, 36 μM and 108 μM) in MeCN.....	168
Figure S 38: Fluorescence spectra of styrylpyrene in MeCN and DMSO after 370 nm excitation.	169

- Figure S 39:** Action plot of NITEC between APAT and DEF, including two additional data points after 25-fold increase of incident photons at wavelengths 510 nm and 515 nm, yielding 3 % and 0.6 % of CA_{DEF} , respectively..... 172
- Figure S 40:** LC-MS chromatogram after 465 nm irradiation of APAT and diethylfumarate for 180 min. After determining the peak integral ratio and taking into account the molar absorptivity at the scan wavelength for both species, the conversion is calculated to be 89 %..... 172
- Figure S 41:** Experimental time-dependent conversions (dots) of *o*MBA cycloaddition and APAT cycloaddition with NHEM in MeCN during irradiation with a) 500 μ J pulses of 320 nm, b) 500 μ J pulses of 360 nm, c) 364 μ J pulses of 390 nm and d) 2000 μ J pulses of 450 nm. All experiments were conducted at ambient temperature, using 20 Hz laser irradiation. Best-fit theoretical simulations used to determine reaction quantum yield are shown as solid lines..... 175
- Figure S 42:** Testing of the temperature-stability of APAT. A mixture of APAT and maleimide end-capped PMMA in MeCN was heated to 60 °C for 2.5 h, then 70 °C for 1 h, and then 80 °C for another 1.5 h. Samples were withdrawn and measured in $CDCl_3$ at ambient temperature. For clarity, only the characteristic aromatic region of the 1H -NMR spectra is shown. The signal at 6.55 ppm corresponds to the vinylic protons of the maleimide. No change of signals was detected in the 1H -NMR spectra, indicating that APAT is stable at $T \leq 80$ °C, which is close to the solvent boiling point. Therefore, we rule out thermal formation of the nitrile imine. This is consistent with literature, which states that tetrazoles are temperature-stable up to ~160-220 °C. 177

LIST OF SCHEMES

- Scheme 1:** Schematic examples of some cycloadditions. For clarity, no substituents or hetero atoms are depicted here. [2+2] cycloadditions lead to a cyclobutane-type derivative (left), whereas Diels-Alder reactions lead to cyclohexene derivatives (middle). 1,3-dipolar cycloadditions (right) result in five-membered ring structures, which can be aromatic depending on the type of dipolarophile. 8
- Scheme 2:** a) Numbering scheme for tetrazoles. b) Tautomerisation between the 1*H* and the 2*H* form..... 10
- Scheme 3:** Schematic routes for tetrazole synthesis. a) Cycloaddition of benzonitrile and sodium azide forms an *H*-free 5-aryl tetrazole, which is able to undergo tautomerisation. b) Metal-catalysed *N*-arylation of *H*-free tetrazole and aryl boronic acids leads to formation of 1,5-diaryl tetrazole and 2,5-diaryl tetrazole..... 12
- Scheme 4:** Synthesis of a 2,5-disubstituted tetrazole: Starting from an arene diazonium salt (**I**) and phenyl-sulfonylhydrazone (**II**), in a first step the diazonium salt couples to the amine nitrogen of the hydrazone, displacing a hydrogen and forming intermediate (**III**). Rearrangement leads to the formazan (**IV**). In a Bamford-Stevens type reaction, after deprotonation and cleaving of the hydrosulfonyl benzene leaving group, intermediate (**V**) is formed, which can cyclise to form the tetrazole (**VI**). Scheme according to the mechanism suggested by *Ito et al.*⁵⁴ 13
- Scheme 5:** Tetrazole photolysis, formation of nitrile imine and reaction thereof with an (electron-deficient) double bond (nitrile imine-mediated tetrazole-ene cycloaddition, NITEC). For a more in-depth description refer to the main text..... 14
- Scheme 6:** Mechanism of the reaction of *o*MBA and *N*-ethyl maleimide *via* the *o*-quinodimethane intermediate. Upon photoexcitation and ISC into the triplet state, *o*MBA forms the *Z*-photoenol. After isomerisation, the *Z*-isomer undergoes efficient Diels-Alder reaction with maleimide.¹¹³ 19
- Scheme 7:** [2+2] cycloaddition of asymmetrically substituted double bonds and subsequent cleavage into different monomers. 21
- Scheme 8:** Orthogonal dimerization of *o*MBA after photoenolization in the UV, and of styrylpyrene, after irradiation in the visible light regime. Adapted from *Bialas et al., Adv. Mater.* **2019**, *31*, 1807288. 33

Scheme 9: Reaction route for a new red-shifted <i>N,N</i> -dimethylamino pyrene aryl tetrazole (APAT).....	44
Scheme 10: Reaction route for synthesis of a reversible addition-fragmentation chain transfer agent and polymerisation of methyl methacrylate, yielding a PMMA-chain equipped with a maleimide, which is able to undergo [2+3] cycloaddition with highly reactant nitrile imines.	48
Scheme 11: NITEC between APAT and DEF. DEF was added in a 4-fold excess, and reactions were carried out in degassed MeCN, and irradiated at wavelengths between 320 nm and 525 nm.....	58
Scheme 12: Reaction schemes of the photoreactions between APAT and NHEM, as well as <i>o</i> MBA and NHEM. Reactions were carried out using 450 nm and 360 nm laser light, respectively. The compounds were dissolved in MeCN and degassed with dry N ₂ ..	73

LIST OF TABLES

Table 1: Various photoactive moieties that are able to undergo reversible [2+2] photodimerization. ^{134, 135}	22
Table 2: Summarised results of polymer end-group modifications, employing different LEDs.	65
Table 3: Results of the initial experiments, evaluating the λ -orthogonality of the APAT/ <i>o</i> MBA system.	75
Table 4: Summary of the wavelength-dependent kinetic experiments and determination of reaction quantum yields. Dashes mean that no quantum yield could be determined due to negligible conversion.	81
Table 5: Summarised findings after investigating the dimerization of styrylpyrene, varying different parameters.	99
Table S 1: Transmittance of the glass vials used for the laser experiments at QUT.	112
Table S 2: Transmittance of the glass vials used for the laser experiments at KIT.	116
Table S 3: Required laser pulse energy for each wavelength, resulting in a constant number of photons after irradiation for 15 min at a pulse rate of 20 Hz. ^a Because wavelengths between 300-400 nm are generated by sum frequency generation (SFG), laser output energies in this range are significantly reduced, giving pulse energies between 165 and 690 μ J. The lower pulse energy was compensated by adjusting the irradiation time for the indicated experiments accordingly.	117
Table S 4: Detailed specifications of the laser experiments for the kinetic study.	120
Table S 5: Detailed specifications of the laser experiments for the attenuation-adjusted action plot, the concentration dependent action plot, and the solvent-dependent action plot.	123
Table S 6: Results of the laser experiments. Reaction conversion was determined via LC-MS. Error bars were obtained through 3x repetition of every experiment. Due to very long irradiation time the experiments between 320 nm and 400 nm were repeated 2x. ...	170
Table S 7: Results of the laser experiments. Reaction conversion was determined via LC-MS. Error bars were obtained through 3x repetition of every experiment.	173
Table S 8: Quantum yield simulation parameters.	174

Table S 9: Results of the sequential LED experiment. Reaction conversion was determined via LC-MS. Uncertainties of absorption coefficients were used to calculate errors.....	176
Table S 10: Results of the action plot experiments with adjusted photon number. Reaction conversion was determined via $^1\text{H-NMR}$ spectroscopy. Error bars were obtained through 3x repetition of every experiment.	178
Table S 11: Results of the action plot experiments at 5 mM concentration. Reaction conversion was determined via $^1\text{H-NMR}$ spectroscopy. Error bars were obtained through 3x repetition of every experiment.....	179
Table S 12: Results of the action plot experiments in $\text{DMSO-}d_6$. Reaction conversion was determined via $^1\text{H-NMR}$ spectroscopy. Error bars were obtained through 3x repetition of every experiment.	179

LIST OF EQUATIONS

(2-1).....	3
(2-2).....	3
(2-3).....	4
(2-4).....	4
(2-5).....	4
(2-6).....	4
(2-7).....	4
(2-8).....	4
(2-9).....	4
(2-10).....	34
(2-11).....	37
(3-1).....	54
(4-1).....	81
(8-1).....	107
(8-2).....	108
(8-3).....	109
(8-4).....	110
(8-5).....	111
(8-6).....	111
(8-7).....	122
(8-8).....	122
(8-9).....	122
(8-10).....	122
(8-11).....	122

ABBREVIATIONS

2PA	Two-photon absorption
A	Absorption
AIBN	Azo(bisisobutyronitrile)
APAT	(<i>N,N</i> -dimethyl)amino pyrene aryl tetrazole
API	Active pharmaceutical ingredient
BBO	β -barium borate
CA	Cycloadduct
CH	Cyclohexane
COSY	Correlation spectroscopy
CTA	Chain transfer agent
DABCO	1,4-Diazabicyclo[2.2.2]octan
DAE	diarylethene
DASA	Donor-acceptor Stenhouse-adduct
DCM	Dichloromethane
DEF	Diethylfumarate
DEPTQ	Distortionless Enhancement by Polarization Transfer with retention of Quaternaries
DFG	Difference-frequency generation
DFT	Density functional theory
DLW	Direct laser writing
DMAc	Dimethyl acetamide
DMAP	<i>N,N</i> -dimethylaminopyridine
DMF	Dimethylformamide
DMSO	Dimethyl sulfoxide
DNA	Desoxyribonucleic acid
DOSY	Diffusion-ordered spectroscopy
DOX	Doxorubicin
DP	Degree of polymerisation
EA	Ethyl acetate
EDC·HCl	1-Ethyl-3-(3-dimethylaminopropyl) carbodiimide-hydrochloride
EGFP	Enhanced green-fluorescent protein
ESI-MS	Electrospray ionisation-mass spectrometry
F	Fluorescence
FMO	Frontier molecular orbital
HEA	2-Hydroxy acrylate
HMBC	Heteronuclear Multiple Bond Correlation
HOMO	Highest occupied molecular orbital
HSQC	Heteronuclear Single Quantum Coherence
IC	Internal conversion
ICT	Intramolecular charge-transfer
ISC	Intersystem crossing
IVR	Intramolecular vibrational energy redistribution
LBO	Lithium triborate

LC-MS	Liquid chromatography-mass spectrometry
LE	Locally excited state
LED	Light emitting diode
LUMO	Lowest occupied molecular orbital
MMA	methylmethacrylate
M_n	Number average molecular weight
mTEGA	(2-(2-(2-methoxyethoxy)ethoxy)ethyl acrylate
Nd:YAG	Yttrium aluminium garnet with neodymium dopant
NEM	<i>N</i> -ethyl maleimide
NHEM	<i>N</i> (2-hydroxy)ethyl maleimide
NI	Nitrile imine
NICAL	Nitrile imine-carboxylic acid ligation
NIR	Near infrared
NITEC	Nitrile imine-mediated tetrazole-ene cycloaddition
NMR	Nuclear magnetic resonance
OD	Optical density
<i>o</i> MBA	<i>Ortho</i> -methyl benzaldehyde
OPO	Optical parametric oscillation
P	Phosphorescence
PAH	Polycyclic aromatic hydrocarbon
PAT	Pyrene aryl tetrazole
PBS	Phosphate buffered saline
PDA	Photodiode array
PDMAEMA	Poly[2-(<i>N,N</i> -dimethylaminoethyl)methylacrylate]
PMMA	Poly(methylmethacrylate)
RAFT	Reversible activation-fragmentation chain transfer
R_f	Retention factor
RI	Refractive index
SCNP	Single-chain nanoparticle
SE	Stimulated emission
SEC	Size exclusion chromatography
SFG	Sum-frequency generation
SHG	Second harmonic generation
shRNA	Short-hairpin ribonucleic acid
THF	Tetrahydrofuran
THG	Third harmonic generation
TIC	Total ion count
TLC	Thin-layer chromatography
TMEDA	Tetramethylethylenediamine
UV	ultraviolet
Vis	Visible
VR	Vibrational relaxation

1 INTRODUCTION

Traditionally, most synthetic chemical reactions are initiated thermally, with control and selectivity exerted through well designed functional groups. However, heat as a source of energy displays an inherent lack of spatial and temporal control, as well as low selectivity towards specific reactants. In contrast, light can be aimed precisely where it is needed and can be switched on and off in an instant. Furthermore, specific reaction channels can be addressed by altering the wavelength or intensity of the incident light, thereby enabling selective formation or cleavage of covalent bonds. By introducing a multicomponent system of photoactive compounds, each susceptible to a different wavelength regime, it is possible to activate both units individually through appropriate selection of the irradiation wavelength. For instance, only compound A is converted when applying long wavelength light, while compound B remains intact. Conversely, when switching to shorter wavelengths, conversion of A ceases, and B commences reaction instead. Ideally, both reactions can be addressed entirely independently, with no mutual cross talk between both photochemical processes, termed λ -orthogonality. In principle, it offers advanced control even over complex reaction systems, combining the modularity of conventional protection-group chemistry with the simplicity of one-pot reactions and the non-invasiveness of photochemistry. To date, however, most λ -orthogonal systems suffer from disadvantages, requiring either additional reactants, or irradiation in a predefined sequence of wavelengths, since short-wavelength light tends to activate both compounds. While separation of the absorption bands of both compounds is necessary to overcome the obstacle of simultaneous photoactivation, it is often not sufficient; It has been demonstrated that the wavelength-dependent reactivity can significantly differ from the absorption profiles. Thus, the latter do not necessarily allow for determination the most suitable activation wavelength of a chromophore. To understand and subsequently design λ -orthogonal photo-induced reaction systems, it is therefore critical to map their reactivity as a function of wavelength, a concept which has been captured in so-called action plots, where a molecule is irradiated at specific wavelengths, with the number of incident photons kept constant at each wavelength.

The aim of the present thesis is to demonstrate how a synthetic rationale can be used to design red-shifted photoactive chromophores, and how targeted assessment and manipulation of their wavelength-dependent reactivity can help establishing a truly sequence-independent λ -orthogonal reaction system.

Chapter 2 gives an overview over the fundamentals of general photochemistry, and of the specific chromophores used in the present thesis, focussing on mechanistic aspects and applications in literature, as well as synthesis where applicable. An introduction is given into the principles of red-shifted chemistry and λ -orthogonality. The chapter closes with an explanation of the wavelength-tuneable laser systems used for conducting wavelength-dependent irradiation experiments, given the crucial role they play in the present thesis.

Chapter 3 introduces a newly developed red-shifted tetrazole as a visible light-activated moiety. The wavelength-dependent reactivity is explored in a small-molecule model reaction, using a wavelength-tuneable *ns*-pulsed laser system, and steps are taken towards utilizing the molecule for polymer functionalisation in a simple LED-setup.

Chapter 4 demonstrates how action plots can assist in selecting suitable wavelengths for orthogonal stimulation of a multicomponent system, using the previously introduced tetrazole and a literature-known *ortho*-methyl benzaldehyde. The kinetics of both photoactive motifs alongside each other are recorded at different wavelengths, allowing for the design of an LED-driven fully sequence-independent λ -orthogonal batch reaction, where both compounds are converted independently at two different wavelengths.

Chapter 5 proposes a new type of action plot, supplying a chromophore with a photon count adjusted to the absorption profile. This technique is then used to explore how varying critical reaction parameters during a photoreaction can significantly alter the outcome with regard to the wavelength-dependent reactivity. Using a literature-known styrylpyrene system, the influence of parameters such as concentration, solvent and temperature are evaluated in the [2+2] cyclodimerization reaction.

Chapter 6 summarises the findings of the present thesis.

Chapter 7 gives an outlook into possible future applications of the concepts and discoveries found in the present thesis.

2 THEORETICAL BACKGROUND

2.1 Photophysical Fundamentals

Photochemistry is the science that seeks to understand how interaction of matter with electromagnetic radiation leads to chemical reactions. Absorption of an electromagnetic field quantum (photon) of a given wavelength λ (or frequency ν) by a molecule leads to transition into an excited state, from where the molecule may either relax through one of several pathways, or reactions may occur.¹ The absorption probability depends on the electronic properties of the molecule as well as the wavelength of the incident photon. By measuring the attenuation of a light beam passing through a sample (more precisely: the ratio of intensities of the incident light beam I_0 and the transmitted light beam I) an absorption spectrum can be obtained by plotting the absorbance A versus the wavelength λ . For dilute solutions, A (also called optical density OD) follows the *Beer-Lambert* law:²

$$A = OD = \log \frac{I_0}{I} = \varepsilon(\nu)cl \quad (2-1)$$

Herein, I_0 is the reference intensity of an incident light beam, I is the intensity after passing through the sample, $\varepsilon(\nu)$ is the wavelength-dependent decadic molar absorption coefficient, c is the concentration of the absorbing molecule and l is the path length. The sum of all $\varepsilon(\nu)$ over the frequency band is called the integrated absorption coefficient \mathcal{A} :³

$$\mathcal{A} = \int \varepsilon(\nu) d\nu = \frac{\pi \nu_{fi} N_A}{3 \varepsilon_0 \hbar c} |\mu_{fi}|^2 \quad (2-2)$$

Here, ν_{fi} is the resonance frequency of the transition $f \leftarrow i$ between an initial state i and a final state f , N_A is the Avogadro constant, ε_0 is the vacuum permittivity, \hbar the reduced Planck constant, c is the speed of light and μ_{fi} is the transition dipole moment of $f \leftarrow i$. Conveniently, this is a direct link between a measurable quantity $\varepsilon(\nu)$ and a calculated quantity μ_{fi} , which allows for correlation of the absorption spectrum and the transition rate: Absorption of photons and subsequent transitions between the electronic ground state and excited states result from perturbation of the electric dipole moment of a molecule with the electric field component E of a photon, the rate of transition between two states ψ^i and ψ^f being proportionate to the square of the transition dipole moment:³

$$|\mu_{fi}|^2 = \langle \psi^f | \hat{\mu} | \psi^i \rangle^2 \quad (2-3)$$

Here, ψ^i and ψ^f are the wavefunctions of the initial and the final state, respectively, and $\hat{\mu}$ is the dipole operator. Due to the substantial difference in mass of nuclei and electrons, it is justified to assume that the latter change their positions quasi-instantaneously to any change in nuclear positions. Hence, it is possible to split the wavefunction into an electronic part and a vibrational part $\psi^{f,i} = \psi_e^{f,i} \psi_v^{f,i}$. Furthermore, the dipole operator can be split into an electronic contribution and a nucleic contribution $\hat{\mu} = \hat{\mu}_e + \hat{\mu}_N$. This separation of electronic and nuclear motion is known as *Born-Oppenheimer* approximation, and leads to the dipole moment assuming the following form:³

$$\mu_{fi} = \langle \psi_e^f \psi_v^f | \hat{\mu}_e + \hat{\mu}_N | \psi_e^i \psi_v^i \rangle \quad (2-4)$$

$$\approx \langle \psi_e^f \psi_v^f | \hat{\mu}_e | \psi_e^i \psi_v^i \rangle + \langle \psi_e^f \psi_v^f | \hat{\mu}_N | \psi_e^i \psi_v^i \rangle \quad (2-5)$$

$$= \langle \psi_v^f | \psi_v^i \rangle \langle \psi_e^f | \hat{\mu}_e | \psi_e^i \rangle + \langle \psi_e^f | \psi_e^i \rangle \langle \psi_v^f | \hat{\mu}_N | \psi_v^i \rangle \quad (2-6)$$

Due to the orthogonality of electronic wavefunctions of different states, the first integral of the second term in (2-6) is zero. The vibrational overlap integral of the wavefunctions of the initial and the final state, $\langle \psi_v^f | \psi_v^i \rangle$, is shortened as S and the formula now reads:

$$\mu_{fi} = S \langle \psi_e^f | \hat{\mu}_e | \psi_e^i \rangle \quad (2-7)$$

S is the overlap integral and the second integral is the electronic dipole moment. The transition probability is proportionate to the *Franck-Condon* factor $|\mu_{fi}|^2 \propto |S|^2$.⁴ The intensity of a transition between two states is then given by the dimensionless oscillator strength f :³

$$f = \frac{4\pi m_e \nu_{fi}}{N_A e^2} |\mu_{fi}|^2 \propto |S|^2 \quad (2-8)$$

Here, m_e is the electron mass, ν_{fi} is the resonance frequency of the transition $f \leftarrow i$, N_A the Avogadro constant and e the elementary charge. Whether a transition is allowed or forbidden is reflected in f : $f \approx 1$ for allowed transitions and $f \ll 1$ for forbidden transitions. f is linked to the integrated absorption coefficient \mathcal{A} :³

$$f = \frac{4m_e c \epsilon_0}{N_A e^2} \mathcal{A} \quad (2-9)$$

(2-9) is obtained through combination of (2-8) and (2-2), hence allowing for correlation of ϵ and $|S|^2$. Consequently, higher molar absorption coefficients are found for transitions with a higher *Franck-Condon* factor. In a simplified graph where only a slice of the potential surfaces of two states is considered, the potential energy *versus* the relative positions of the nuclei looks as depicted in **Figure 1**.

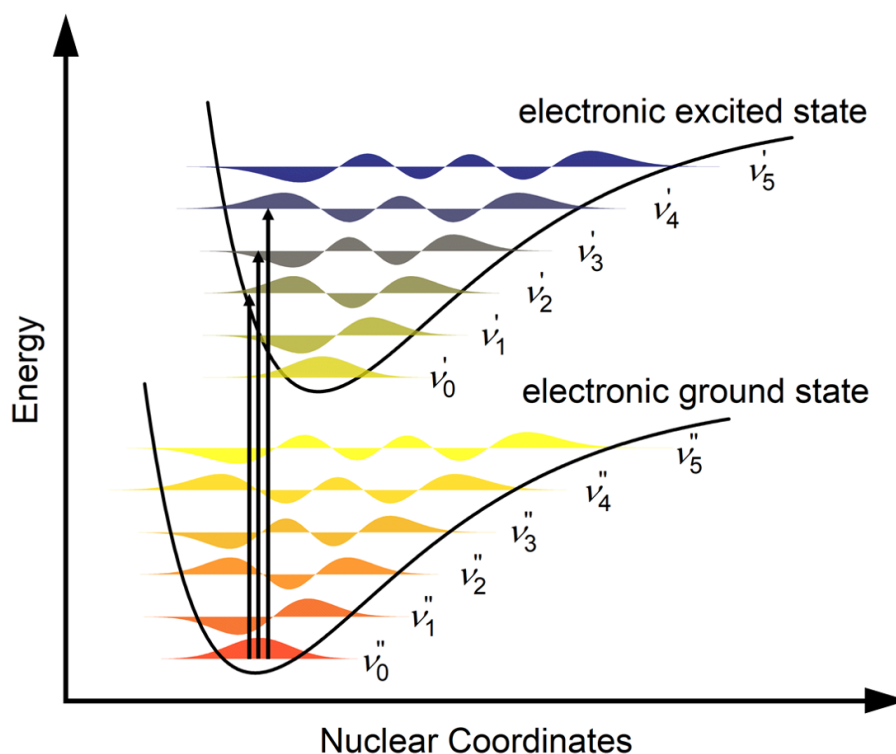


Figure 1: Energy diagram showing electronic ground and excited state as well as various vibrational ground and excited states and vertical transitions between them. v_i'' and v_i' are vibrational excited states of the electronic ground state and excited state, respectively. Adapted from Ref.⁵

According to the *Born-Oppenheimer* approximation, on the timescale of electronic transitions, the positions of the nuclei are unchanged and hence the transition occurs vertically in **Figure 1**. This has two consequences: For a given electronic state, a manifold of vibrational excited states is accessible. For this reason, absorption spectra do not consist of narrow peaks but are rather broad instead, showing overlapping peaks of the vibrational transitions. The distribution of peak intensities follows the *Franck-Condon* principle, that is, transitions are more probable for higher vibrational overlap.⁶ Furthermore, since the nuclei are assumed to be static in position during the transition, the excited molecule retains approximately ground-state geometry. Thus, immediately after excitation the molecule relaxes to vibrational ground state through population of adjacent vibrational modes within 10^{-11} - 10^{-13} s. This is called intramolecular vibrational energy redistribution (IVR).⁷

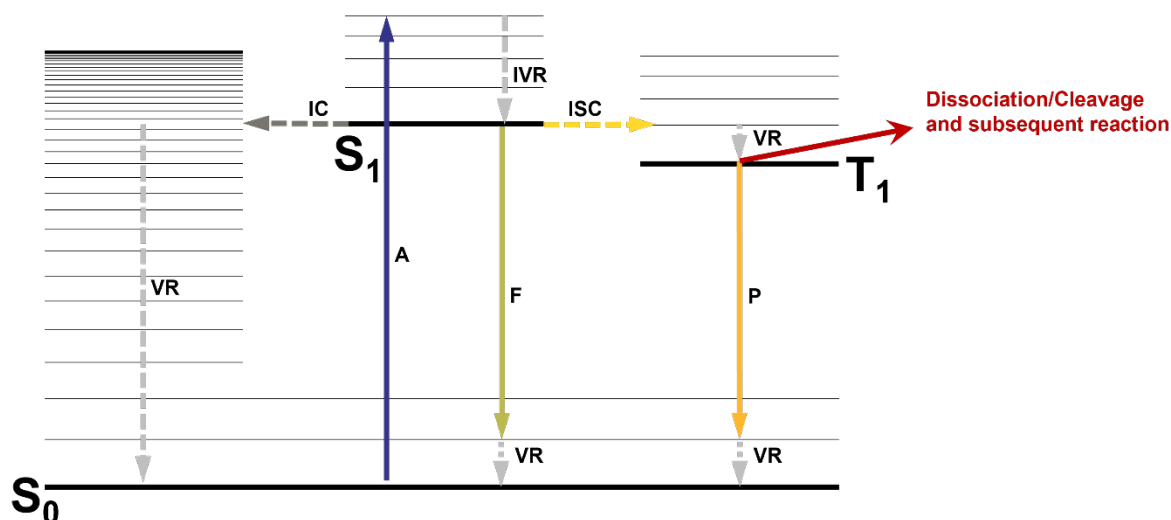


Figure 2: Jablonski diagram, showing possible relaxation pathways upon excitation between different electronic and vibrational states. Vertical excitation (absorption, A), intramolecular vibrational energy redistribution (IVR), vibrational relaxation (VR), radiative transitions (fluorescence, F, and phosphorescence, P), non-radiative transitions (internal conversion, IC, and intersystem crossing, ISC).

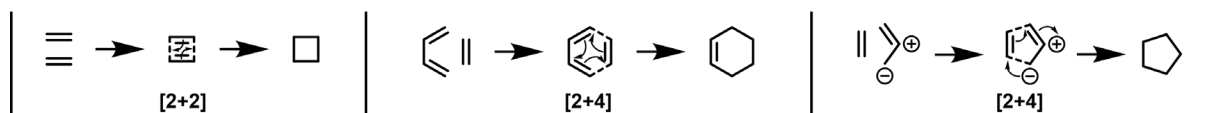
Excited states of molecules usually have a finite lifetime. Upon entering the excited state and reaching vibrational ground state through IVR, a molecule has several ways to undergo relaxation, which are summarised in the Jablonski inspired diagram in **Figure 2**.⁸ In most cases, molecules relax into the lowest excited electronic state through a combination of energy dissipation (IVR or vibrational relaxation, VR) and spin-allowed non-radiative transitions between potential energy surfaces of the same spin-multiplicity (internal conversion, IC), i.e., between singlet states ($S_2 \rightarrow S_1$) or triplet states ($T_2 \rightarrow T_1$). This usually occurs within 10^{-12} s or less.⁹ The equivalent spin-forbidden non-radiative process occurs between states of different multiplicity typically on a much slower timescale (i.e., $S_1 \rightarrow T_2$) and is called intersystem crossing (ISC). Radiative transitions involve emission of a photon of sufficient energy to relax into a higher excited vibrational state of the electronic ground state. The spin-allowed process is called fluorescence (F) and generally takes place on a timescale of 10^{-10} - 10^{-7} s,¹⁰ which is why VR and IC are usually complete prior to radiation and, thus, transition occurs from the vibrational ground state of S_1 (*Kasha's rule*).¹¹ Hence, in an absorption-emission spectrum, the emission maximum is positioned at lower energies compared to the absorption maximum (*Stokes shift*). Accordingly, the spin-forbidden process called phosphorescence (P) occurs from the vibrational ground state of T_1 on a much slower timescale of milliseconds to seconds.¹² Because T_1 is often lower lying than S_1 , phosphorescence is generally red-shifted compared to fluorescence.⁹ Importantly, many photo-induced reactions have been shown to occur from

triplet states, such as cleavage of photo-initiators,^{13, 14} photoenolization of *o*-alkyl-substituted aromatic ketones,^{15, 16} [2+2] cycloadditions^{17, 18} or formation of 1,3-dipoles.¹⁹ Given the crucial role of the latter three in the current thesis, they are described in detail in the following chapter.

2.2 Cycloadditions

2.2.1 Fundamentals

Cycloadditions are bimolecular reactions where two reaction partners form a concerted transition state that involves reorganisation of π -electrons and formation of two new σ -bonds.²⁰ The result is a ring-type structure whose number of members depends on the initial reaction partners. Such reactions are usually classified by the number of π -electrons involved in the transition state. Each integer indicates the number of π -electrons of one of the two reaction partners, respectively (i.e. [2+2], [2+4] or [4+4]).²⁰ Common examples for [2+2] cycloadditions are ketene-olefine cycloadditions or the Paternò-Büchi reaction, which occur between two distinct reaction partners,^{21, 22} but reactions between two identical molecules (cyclodimerization) may also occur.²³ Diels-Alder reactions, an example of a [2+4] cycloaddition, are considered one of the most versatile synthetic tools to form carbon-carbon bonds, and their discovery by *Otto Diels* and *Kurt Alder* was awarded the *Nobel Prize in Chemistry* in 1950.²⁴



Scheme 1: Schematic examples of some cycloadditions. For clarity, no substituents or hetero atoms are depicted here. [2+2] cycloadditions lead to a cyclobutane-type derivative (left), whereas Diels-Alder reactions lead to cyclohexene derivatives (middle). 1,3-dipolar cycloadditions (right) result in five-membered ring structures, which can be aromatic depending on the type of dipolarophile.

Another important class of [2+4] cycloadditions are 1,3-dipolar cycloadditions. Here, a heteroatomic charged species containing four delocalised π -electrons in a three-atom system reacts with a so-called dipolarophile, typically a substituted alkene or alkyne.²⁰

Pathway and outcome of concerted pericyclic reactions such as cycloadditions were first rationalised by *Woodward* and *Hoffman* in 1965, for which the *Nobelprize in Chemistry* in 1981 was awarded.^{25, 26} The principles developed are called *Woodward-Hoffmann* rules and state that orbital symmetry needs to be conserved during a pericyclic reaction.²⁷ The frontier molecular orbitals of the participating molecules must be oriented in a way that allows for an accessible transition state to form. The term frontier molecular orbitals (FMOs) refers to the orbitals

involved in the reaction, that is, typically, the highest-occupied molecular orbital (HOMO) of one reaction partner, and the lowest-unoccupied molecular orbital (LUMO) of the other. **Figure 3** demonstrates how overlap of FMOs can be achieved in systems of various numbers of π -electrons.²⁰

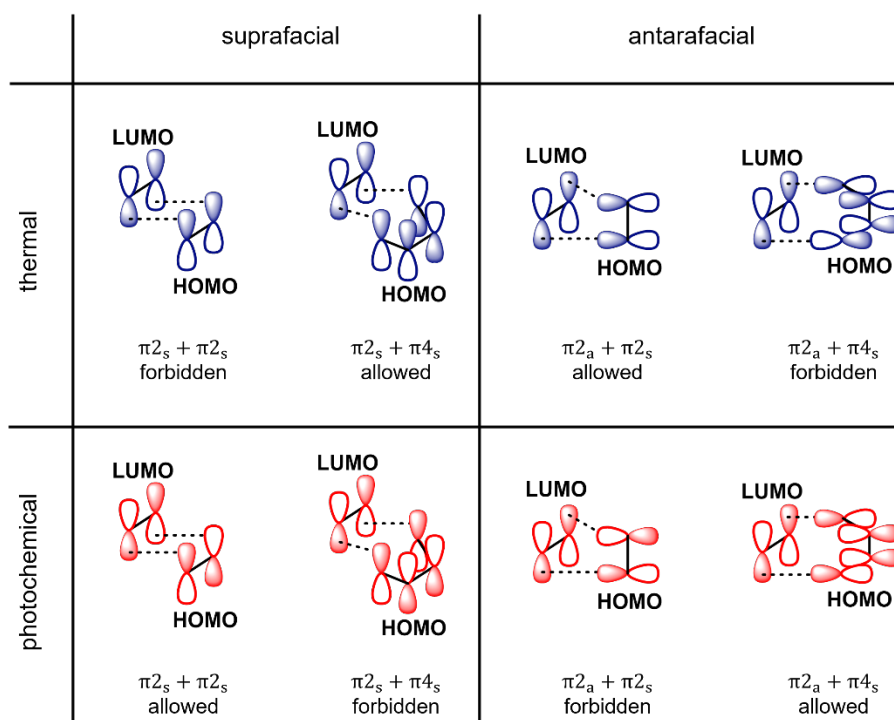


Figure 3: Pathways for thermally and photochemically driven [2+2] and [2+4] cycloadditions with different orbital orientations. Where orbital flaps are of the same colour, the overlap is bonding, and where they are of different colour, it is anti-bonding. The nomenclature $\pi 2_s$ indicates how many π -electrons the respective reaction partner provides, and whether the involved orbital flaps are located on the same side (suprafacial, s) or opposite sides (antarafacial, a) of the molecule. Adapted from Ref.²⁰

In case of a thermal reaction, if two reaction partners are arranged face-to-face (suprafacial) an energetically favoured transition state can only be formed for systems containing $4n + 2$ π -electrons (i.e., a [2+4] system), where the orbital overlap is bonding. For systems containing $4n$ π -electrons (i.e., a [2+2] system), however, this results in one bonding and one antibonding overlap, preventing the new σ -bonds from being formed. An alternative way to achieve bonding orbital overlap is through arrangement of opposite faces (antarafacial) of the π -systems in a *Mobius*-type topology. Since this orientation comes with a lot of ring-strain, it is unlikely to occur for small π -systems.²⁰

However, if a single electron of one of the reaction partners enters an excited state upon absorption of a photon, the orbital symmetry of the FMO changes (refer to **Figure 4**). Hence, it is now possible for a $4n$ π -electron system (i.e., [2+2] or [4+4]) to approach in a suprafacial

arrangement and enter a stable transition state according to the *Woodward-Hoffmann* rules.²⁰ This demonstrates the critical role that light can play in cycloaddition chemistry. An indirect, yet common way to employ light in cycloaddition chemistry is by photochemical generation of reactive intermediates that subsequently can undergo thermal cycloaddition. Examples include the generation of nitrile imines from tetrazoles,²⁸ inverse electron-demand Diels-Alder cycloaddition of tetrazines,²⁹ or photoenolization of *ortho*-methyl phenyl ketones and aldehydes.³⁰

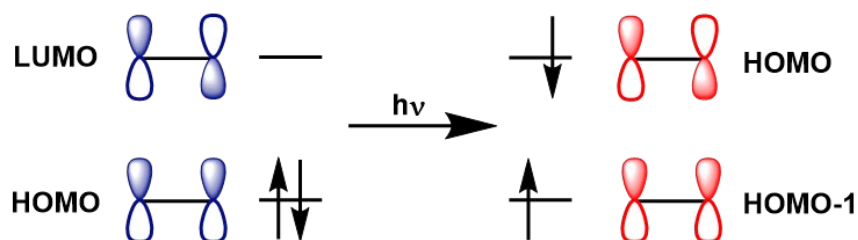
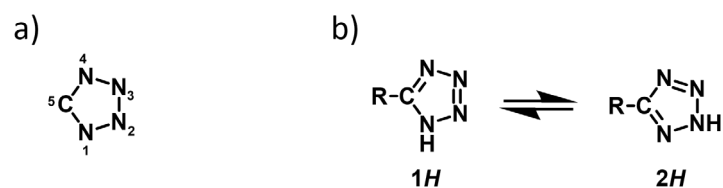


Figure 4: Photoexcitation of a ground state molecule leads to population of an excited singlet state. The number of nodes in the HOMO increases by +1 (from 0 to 1 in this case) and the orbital symmetry changes, allowing for stable transition states that were previously forbidden.

2.2.2 Tetrazole Chemistry

Tetrazoles are a class of heterocyclic compounds, containing four nitrogen atoms and a carbon atom. As such, tetrazoles are surprisingly stable and found widespread use in drug design thanks to their bioisosterism to carboxylic acids.^{31, 32} Initially synthesized through reaction of dicyanophenylhydrazine with nitric acid in 1885 by *Bladin*, tetrazoles constitute a very old class of heterocycles,³³ but have since undergone a remarkable renaissance with regard to both synthesis and applications (refer to chapters 2.2.2.1 and 2.2.2.3). Especially in the last decade, increasingly sophisticated synthetic routes have been established, and great effort has been put into investigation of the electronic structure, geometry, reactivity, and other crucial properties of tetrazoles.³⁴

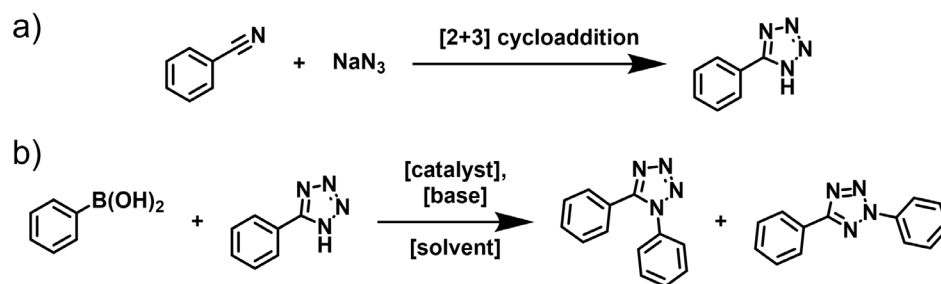


Scheme 2: a) Numbering scheme for tetrazoles. b) Tautomerisation between the 1H and the 2H form.

The simplest numbering scheme of tetrazoles is depicted in **Scheme 2a**. In general, tetrazoles can take two tautomeric forms. Monosubstituted tetrazoles (1*H*- and 2*H*-tetrazole, **Scheme 2b**) are known to undergo tautomerisation in solution. The equilibrium depends on the solvent and the nature of the substituents,³⁵ but the 2*H* tautomer is predominant in the gas-phase.³⁶ For many applications, doubly substituted (1,5- and 2,5-disubstituted) tetrazoles are relevant, where the *H*¹ or *H*² atom is replaced by an alkyl or phenyl group. An important characteristic of both tautomeric forms is their aromaticity, which constitutes their relatively high chemical and thermal stability. The aromatic character is expressed by delocalisation of six π -electrons over five ring-atoms, forming a planar conjugated system.³⁵ In both forms, three pyridine-type N-atoms are present, as well as one pyrrole-type N-atom. The lone electron pair of the latter participates in the conjugated system. The bond-lengths reflect the aromaticity and range between 1.26 Å and 1.36 Å.³⁷ The extent of aromaticity generally depends on the position and nature of the substituents, but it is higher for the 2*H* tautomer due to more uniform bond lengths and π -electron distribution.³⁸ A third tautomer, 5*H* tetrazole, exists, but is nonaromatic due to sp^3 hybridization of the C⁵ atom.³⁹ Studies suggest that the tetrazole ring is a strong electron-acceptor.³⁷

2.2.2.1 Synthesis

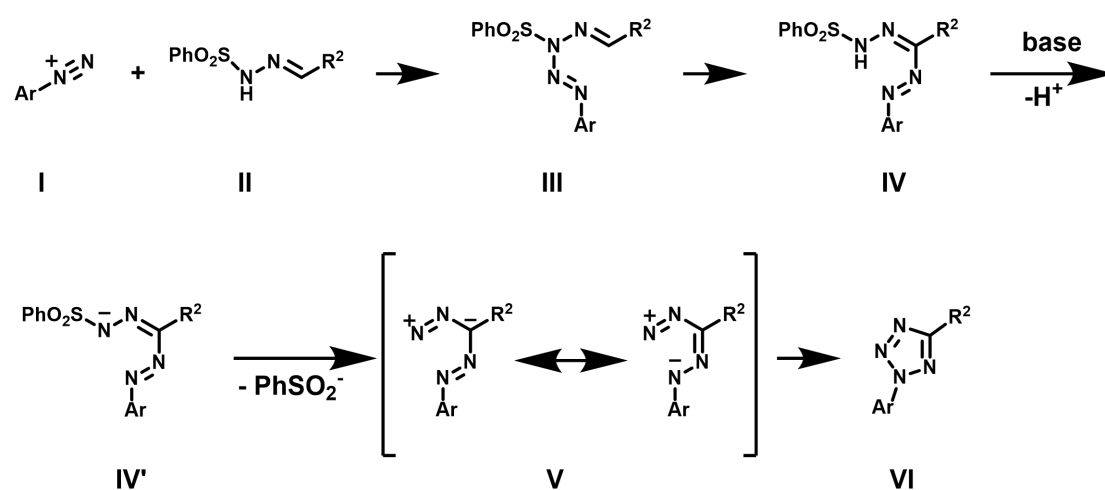
Constant increase in potential applications of tetrazoles and growing demand for complex structures and substitution patterns in recent years gave rise to a plethora of synthetic routes. For 1,5- and 2,5 disubstituted tetrazoles, these protocols can be divided into two classes: Ring-forming approaches and N-arylation of 5-substituted 1*H* or 2*H* tetrazoles. Naturally, synthetic chemists encounter the problem of forming both tautomeric species, which stresses the importance of developing regioselective synthetic methods. Following the first tetrazole synthesis by *Bladin* in 1885 in Uppsala,³³ *Hantzsch* and *Vagt* reported [2+3] cycloaddition of azides and nitriles, resulting in 5-substituted 1*H* tetrazole (refer to **Scheme 3a**).⁴⁰ To this day, variations of this route are of critical importance in tetrazole synthesis, and have been modified to fulfil requirements such as efficiency, eco-friendliness, operational simplicity and extended substrate scope.⁴¹⁻⁴⁵ *H*-free tetrazoles can subsequently be functionalised *via* metal-catalysed N-arylation (**Scheme 3b**). Numerous protocols have been established and the number of related publications is constantly rising. These methods vary in transition metal, co-catalyst, or solvents employed. Examples include *Chan-Lam* type coupling of aryl boronic acids with *H*-free tetrazoles, using Cu₂O and O₂ in DMSO,⁴⁶ [Cu(OH)(TMEDA)]₂Cl₂, K₂CO₃ and O₂ in dichloromethane,⁴⁷ or Cu(OAc)₂ and base in dichloromethane.⁴⁸



Scheme 3: Schematic routes for tetrazole synthesis. a) Cycloaddition of benzonitrile and sodium azide forms an *H*-free 5-aryl tetrazole, which is able to undergo tautomerisation. b) Metal-catalysed *N*-arylation of *H*-free tetrazole and aryl boronic acids leads to formation of 1,5-diaryl tetrazole and 2,5-diaryl tetrazole.

Recently, *Livingstone et al.* introduced a modular approach, utilising tandem *Suzuki*-hydrogenolysis. Using both Cu and Pd catalysts for the C- and N-arylation of a 1-benzyl-5-bromotetrazole core, they synthesised a variety of 2,5-disubstituted tetrazoles.⁴⁹ Due to the tautomerisation equilibrium between the 1*H* and 2*H* form of *H*-free tetrazoles, *N*-arylations can result in product mixtures, containing 1,5- and 2,5-disubstituted tetrazoles in varying amounts. *Aridoss* and *Laali* synthesised a library of tetrazoles through non-catalysed coupling of 5-aryl tetrazole with benzyl or butyl bromide. They found that the 2,5-regioisomer is the major product, but also obtained the 1,5-regioisomer in relative amounts of 8-40 %.⁵⁰ While the tautomerisation equilibrium depends on multiple factors such as solvent and C⁵-substitution, steric effects probably also play a role in determining which regioisomer is formed predominantly. Furthermore, studies suggest that in metal catalysed reactions the catalysis mechanism has an influence on the formation of regioisomers.⁵¹

Since photo-active tetrazoles were the focus of this thesis, synthetic strategies for the synthesis of 2,5-substituted tetrazoles are of particular interest (refer to chapter 2.2.2.2 for the mechanism of tetrazole photoreactions). Ring-closing reactions that often start from arene diazonium salts rather than from pre-formed tetrazole structures can overcome the issue of regioisomer formation but can have other limitations instead. Pioneering work was undertaken by *Lippman et al.*, who synthesised 2-phenyl-5-carboxy tetrazole through coupling of a 2-(2-phenylhydrazono)acetic acid and 1-azido-2,3,6-tribromobenzene.^{52, 53} The most commonly used synthetic route in literature was published by *Ito et al.*, who suggested condensation of phenylsulfonylhydrazones and arene diazonium salts *via* a formazan intermediate in basic ethanol or pyridine (**Scheme 4**). The reaction has demonstrated good substance scope, but requires handling of heat-sensitive, potentially explosive diazonium salts, and suffers from laborious purification steps.⁵⁴



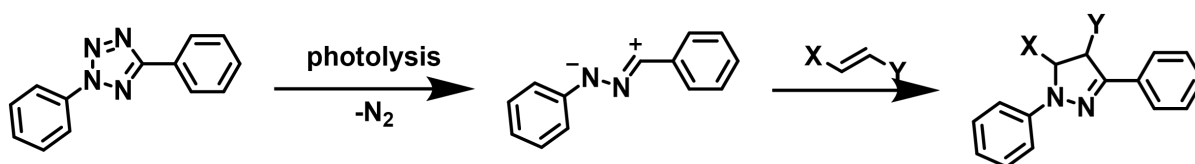
Scheme 4: Synthesis of a 2,5-disubstituted tetrazole: Starting from an arene diazonium salt (**I**) and phenylsulfonylhydrazone (**II**), in a first step the diazonium salt couples to the amine nitrogen of the hydrazone, displacing a hydrogen and forming intermediate (**III**). Rearrangement leads to the formazan (**IV**). In a Bamford-Stevens type reaction, after deprotonation and cleaving of the hydrosulfonyl benzene leaving group, intermediate (**V**) is formed, which can cyclise to form the tetrazole (**VI**). Scheme according to the mechanism suggested by *Ito et al.*⁵⁴

More recent advances in this field include reaction between arene diazonium salts and formamidine, with addition of iodine,⁵⁵ or reaction of aromatic aldehydes with methyl- or benzylhydrazine, followed by treatment with di-*tert*-butyl azodicarboxylate and [bis(trifluoroacetoxy)iodo]-benzene.⁵⁶ The latter, however, only accessed N-methyl or N-benzyl tetrazoles, as opposed to N-aryl derivatives, which are widely used for tetrazole photoreactions. A library of 2-aryl-5-acyl tetrazoles was available through [2+3] cycloaddition of arene diazonium salts with an array of α -diazocarbonyl derivatives in the presence of silver nitrate and DABCO.⁵⁷

It is apparent that literature in recent years accounted for the rapidly developing field of applications where tetrazoles are needed. Scientists nowadays can pick from a growing palette of synthetic methods fulfilling highly specialised demands such as regioselectivity, efficiency, functional group tolerance, substrate scope and more. This allows for selection of synthetic routes that meet the specific requirements of different applications. However, most publications address the synthesis of 1,5-disubstituted tetrazoles, and break-through methods to access 2,5-diaryl tetrazoles remain relatively scarce.

2.2.2.2 1,3-Dipolar Cycloaddition of Nitrile Imines

2,5-Disubstituted tetrazoles have undergone a remarkable resurgence in photochemical applications, ever since the first report on their photolysis.⁵⁸ Huisgen and Sustmann found that the photoreaction between crotonic acid and 2,5-diaryl tetrazole had similar kinetic constants and regioisomeric reaction products as the 1,3-dipolar cycloaddition of hydrazonyl chloride upon thermolysis, which led them to the conclusion that both reactions must have a common intermediate.⁵⁸ They reasoned that irradiation of tetrazoles hence results in ejection of molecular nitrogen and formation of a 1,3-dipolar nitrile imine (NI) intermediate (**Scheme 5**, left arrow). These findings could later be confirmed through direct spectroscopic methods.⁵⁹ ⁶⁰ The versatility of the nitrile imine-mediated tetrazole-ene cycloaddition particularly for photo-induced heterocycle synthesis was recognised by Wang *et al.* in 2007, who screened differently substituted 2,5-tetrazoles and the reaction of the respective nitrile imines with a range of 1,3-dipolarophiles, using 300 nm UV light.⁶¹ After that, researchers made efforts to increase the versatility of the reaction (refer to **2.2.2.3**), and explored avenues to trigger the reaction with lower energy wavelengths (refer to **chapter 2.3**). Thermal formation of nitrile imines from tetrazoles is possible as well, but requires temperatures of 160 °C to 220 °C.⁶² Mild photolysis therefore is the preferred way to generate nitrile imines.



Scheme 5: Tetrazole photolysis, formation of nitrile imine and reaction thereof with an (electron-deficient) double bond (nitrile imine-mediated tetrazole-ene cycloaddition, NITEC). For a more in-depth description refer to the main text.

The right arrow in **Scheme 5** depicts the simplified 1,3-dipolar cycloaddition of a NI with a generic double bond. In case of an olefine reaction partner, the resulting cycloadduct is a pyrazoline derivative, which can be further oxidized either through addition of oxidants,^{63, 64} or spontaneously.^{65, 66} The degree to which spontaneous rearomatization occurs seems to depend on substrates and solvents, but can vary and is difficult to predict. Several effects complicate the reaction outcome even more, since NIs can react with a range of substrates, and the nature of the substrate will determine the regioselectivity and the reaction rate of the cycloaddition. Among the suitable dipolarophiles are olefines, alkynes, carbon-heteroatom double or triple bonds, and various nucleophiles. In many cases, these dipolarophiles are

asymmetric, possibly yielding a mix of 4-substituted or 5-substituted cycloadducts. The ratio of regioisomers is mostly guided by steric effects, but these may coincide with electronic substitution effects as well.^{67, 68} However, while frontier molecular orbital (FMO) theory or density functional theory (DFT) are used to rationalise these effects, there still are many exceptions to this, and quantitative prediction is arduous.⁶⁹⁻⁷¹ Similarly, steric effects and FMO theory can be utilised to illuminate reaction rates of 1,3-dipolar cycloadditions—as was indicated in chapter 2.2.1.

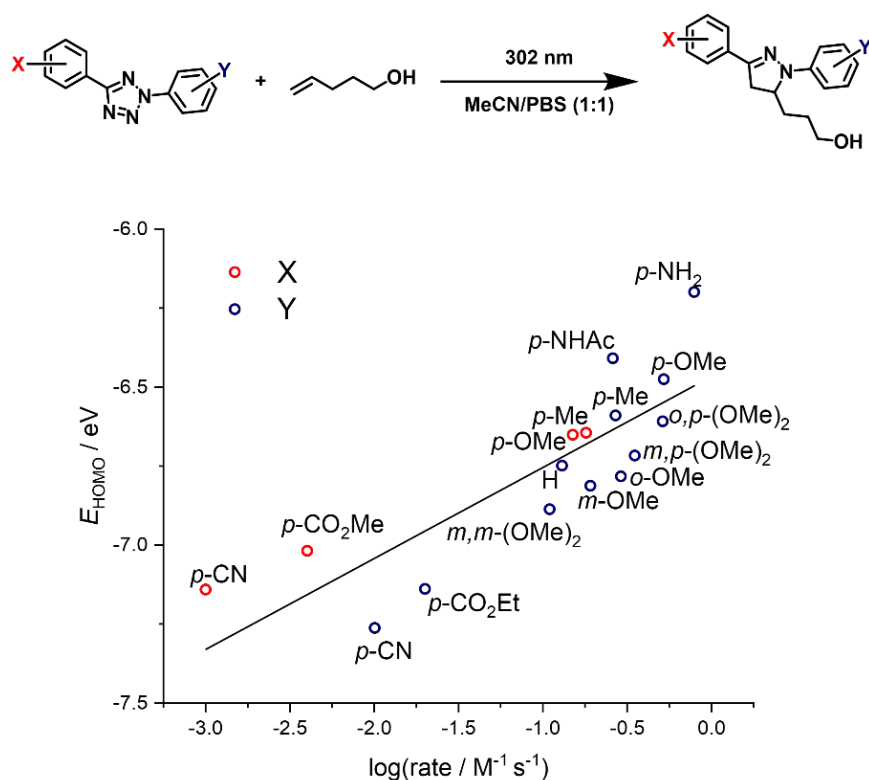


Figure 5: HOMO energy plotted *versus* the logarithmic reaction rate of the 1,3-cycloaddition of differently substituted tetrazoles and pent-4-en-1-ol upon UV irradiation. Copyright (2021) Wiley. Reproduced from Wang *et al.*, *Angew. Chem. Int. Ed.* **2009**, *48*, 5330-5333. Wiley-VCH Verlag GmbH & Co. KGaA, Weinheim.

In a pioneering study from 2007, Wang *et al.* calculated HOMO energies of a library of differently substituted tetrazoles and correlated it to the reaction rate of the respective NITEC reaction (refer to **Figure 5**).⁷² With this comprehensive screening, groundwork was laid for the rational design of efficient tetrazoles. However, a decade later Blasco *et al.* found that singlet-triplet splitting is critical for enabling tetrazoles to enter the triplet state through ISC.⁷³ They used DFT calculations of three tetrazoles to determine the singlet and triplet state energies and correlated them to experimental data. Indeed, it was found that an energetic proximity of the vertical S_1 state to a triplet state was prerequisite for an efficient NITEC reaction. This was

confirmed by quenching experiments, using oxygen as a triplet quencher, which completely inhibited the NITEC reaction, proving that ISC is necessary for the formation of the nitrile imine intermediate.⁷³

2.2.2.3 Applications of Nitrile-Imine Mediated Tetrazole-Ene Cycloaddition (NITEC) Reactions

Ever since their resurrection by *Wang et al.* in 2007,⁶¹ the photochemistry of tetrazoles has garnered increasing interest in many applications due to the wide range of substrates they can interact with, as well as their “click”-like features.⁷⁴ Consequently, their use as efficient functionalisation tools especially in the context of biochemistry has been given the moniker “photoclick chemistry”.⁷⁵ The fields they have successfully been utilised in span from general synthetic chemistry over bio-orthogonal ligation and functionalisation to advanced materials chemistry and polymer science.⁷⁶ Importantly, the fluorescent nature of many cycloadducts gave rise to a plethora of self-reporting ligation procedures. For instance, tetrazoles have been used in the development of a series of photoactive amino acids, which can be incorporated into proteins and allow for self-reporting post-translational modifications.^{28, 77} Another example of their use in synthesis was demonstrated by *Pla et al.*, who exploited 5-(methylthio)tetrazoles as photoactive synthons in the synthesis of polycyclic pyrazolines.⁷⁸ Moreover, tetrazoles have been used as precursors for the synthesis of active pharmaceutical ingredients (APIs),⁷⁹ or even as biologically active components, although their use therein does not necessarily stem from photoactivity, but rather their bioisosterism to carboxy groups.⁸⁰

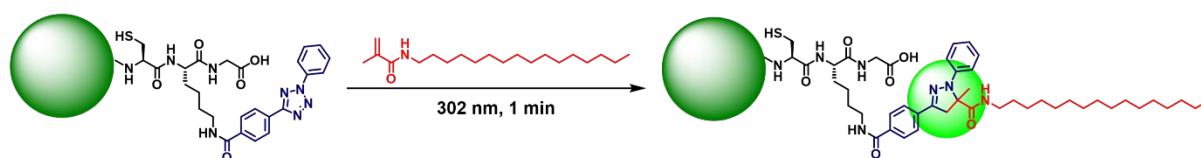


Figure 6: 1,3-dipolar cycloaddition between an EGFP bearing a tetrazole moiety, and a methacrylamide, forming a fluorescent adduct. Copyright (2021) Wiley. Reproduced with permission from Song *et al.*, *Angew. Chem. Int. Ed.* **2008**, *47*, 2832-2835. Wiley-VCH Verlag GmbH & Co. KGaA, Weinheim.

One of the most important tetrazole application in biochemical contexts is ligation or labelling of biomolecules. *Song et al.* equipped enhanced green-fluorescent protein (EGFP) with a diaryltetrazol motif, and subsequently triggered the 1,3-cycloaddition at 302 nm, coupling the

modified protein with a nonpolar methacrylamide (refer to **Figure 6**).⁸¹ They reported very fast reaction (< 1 min) and high tolerance towards proteinaceous groups. The same group later reported the inverse process, decorating the protein with a dienophile and employing the tetrazole as the ligating unit.⁷⁵

In recent years, more studies emerged, reporting the reactivity of nitrile imines towards substrates other than dipolarophiles. While this arguably raises the question of the true bio-orthogonal “click” nature of the tetrazole photoreaction,⁸² it has led to many different applications, like protein labelling through reaction of tetrazoles and carboxylic acids.⁸³ Other examples of applications in the field of biochemistry include protein crosslinking (**Figure 7**),⁸⁴ ⁸⁵ potential agents for integrated phenotypic screening and target identification for applications in cancer-related diagnoses and therapy,⁸⁶ or as highly fluorescent chemosensors.^{87, 88}

Outside of biomedical applications, tetrazoles have been widely employed in material science and polymer chemistry. While the first study on a step-growth polymerization through 1,3-dipolar cycloaddition of bistetrazole monomers in 1968 used pyrolysis for the generation of the nitrile imines,⁸⁹ the corresponding light-driven process was not reported until much later.^{90, 91} Due to the spatial and temporal control provided by light-driven chemistry, applications flourished where selective NI formation is required, i.e., in spatially resolved surface patterning.^{92, 93} The photochemical nature of the reactions allows for simple use of shadow masks to trigger the reaction at defined positions. A study by *Rodriguez-Emmenegger et al.* from 2013 demonstrated functionalisation of polydopamine films with antifouling polymer-brushes through NITEC coupling (**Figure 7**).⁹⁴ Further applications of tetrazoles in surface chemistry are manifold, including ligation protocols for generation of light-responsive surfaces,⁹⁵ DNA-functionalisation to gold nanorods,⁹⁶ and others.⁹⁷⁻¹⁰¹

Likewise, tetrazoles have found common use in polymer ligation and crosslinking. The alteration of polymer properties through 1,3-cycloaddition of tetrazoles with various dipolarophiles was reported as early as 1994 by *Darkow et al.*^{102, 103} Since then, increasingly complex crosslinking routines have been established, spanning from intermolecular ligation by end-group ligation,¹⁰⁴ or side-chain crosslinking with bifunctional crosslinkers,^{105, 106} to intramolecular formation of single chain nanoparticles (SCNPs, refer to **Figure 7**).¹⁰⁷

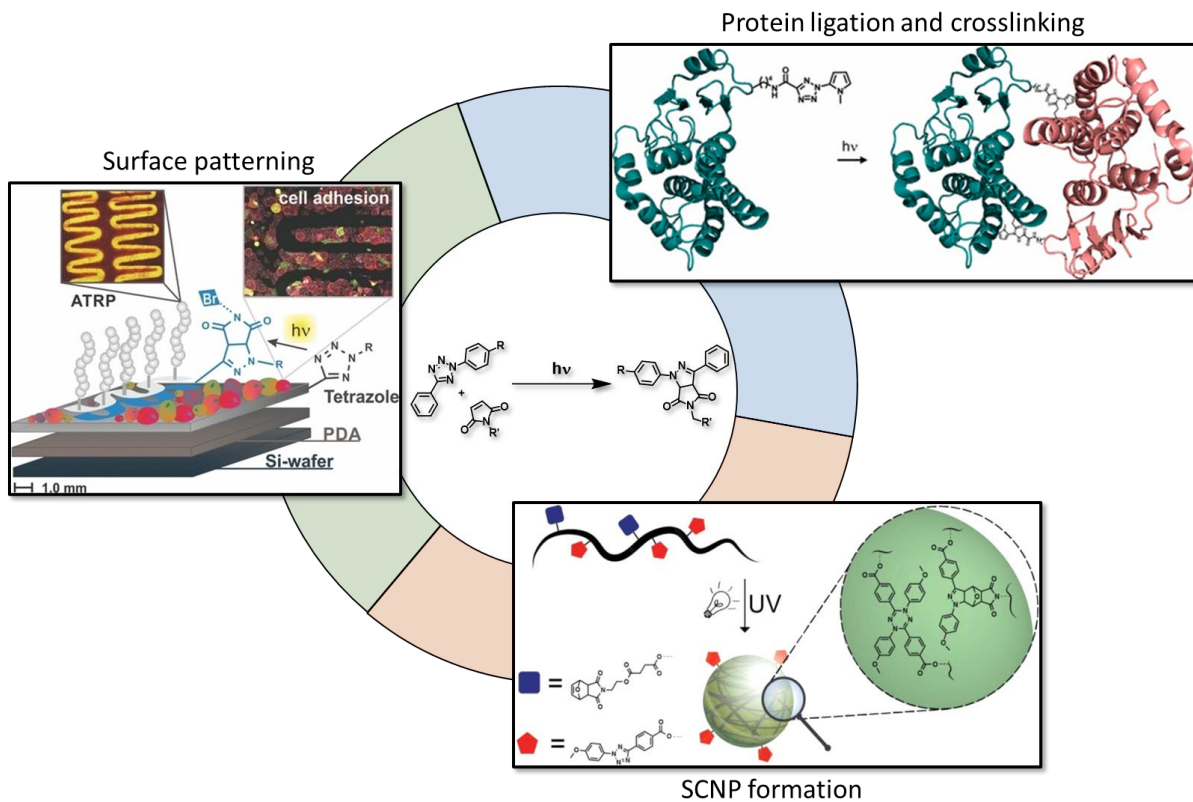
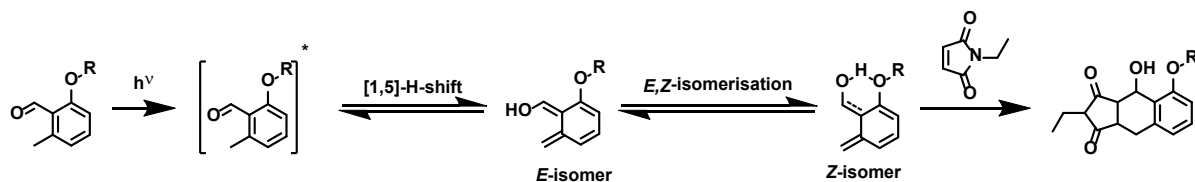


Figure 7: Variety of tetrazole applications. Figures were reproduced with permission from the references indicated. Top right: Site-selective crosslinking of proteins.⁸⁴ Left: Spatially resolved surface modification.⁹⁴ Bottom right: Development of functional fluorescent single-chain nanoparticles (SCNPs).¹⁰⁷

2.2.3 Photoenol Chemistry

The photochemical enolization (or photoenolization) of *ortho*-alkyl benzophenones was first described in 1961 by Yang *et al.*¹⁰⁸ They reported that benzophenones bearing an *o*-alkyl group with an α -hydrogen, upon irradiation with UV light, would undergo intramolecular hydrogen transfer to form the enol. The photo-generated enol (photoenol) would react efficiently with dimethyl acetylenedicarboxylate, forming the respective cycloadduct. Mechanistic studies later concluded that the enolization occurs from a triplet state.^{109, 110} This seminal work was rediscovered much later by Gruending *et al.*, who utilized the photoenolization for highly efficient polymer-polymer ligation.¹¹¹

A modified version of the reactant, *ortho*-methyl benzaldehyde (*o*MBA), was utilized for surface modification shortly after by Pauloehrl *et al.*¹¹² Studies show that upon entering the triplet state, the enol is generated from the *o*MBA through [1,5]-H-shift and subsequent *E,Z*-isomerisation *via* a conical intersection.¹¹³ The *Z*-isomer is stabilised due to intramolecular hydrogen bonding, extending the lifetime of the isomer, which is highly reactive towards dienophiles (refer to **Scheme 6**).¹¹⁴⁻¹¹⁶ Furthermore, it was recently reported that the photoenol, in the absence of a suitable dienophile, can also undergo [4+4] dimerization.¹¹⁷



Scheme 6: Mechanism of the reaction of *o*MBA and *N*-ethyl maleimide *via* the *o*-quinodimethane intermediate. Upon photoexcitation and ISC into the triplet state, *o*MBA forms the *Z*-photoenol. After isomerisation, the *Z*-isomer undergoes efficient Diels-Alder reaction with maleimide.¹¹³

Because the photocycloaddition of *o*-quinodimethane and maleimide satisfies many conditions of so-called *click* chemistry,⁷⁴ it has found widespread applications, *i.e.*, in macromolecular chemistry. Examples include fabrication of 3D microstructures,¹¹⁸ DNA functionalisation,¹¹⁹ surface modification,¹²⁰ formation of single-chain nanoparticles (SCNPs),¹²¹ and polymer ligation of complex macromolecular structures.¹²²

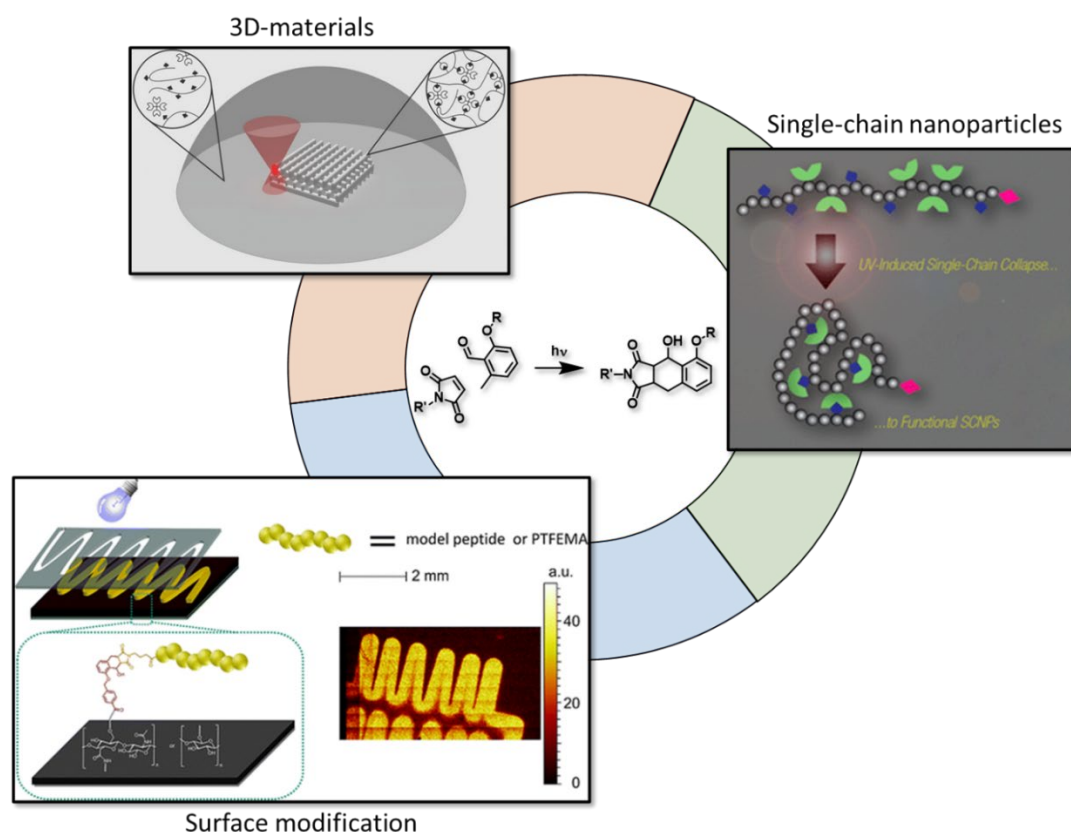
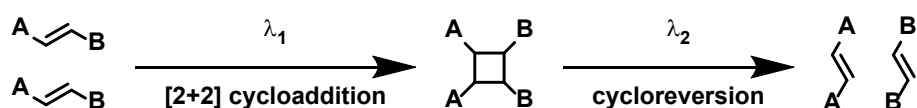


Figure 8: Applications of the Diels-Alder reaction of dienophiles and *o*-quinodimethanes, generated from *o*-methyl benzaldehydes upon UV-irradiation. Figures were reproduced with permission from the references indicated. Top left: Fabrication and functionalisation of 3D-microstructures *via* multiphoton-induced photoreaction.¹¹⁸ Right: Formation of SCNPs.¹²¹ Bottom left: Spatially resolved photochemical grafting on biosurfaces.¹²⁰

2.2.4 [2+2] Cycloadditions

As indicated in the previous sections, [2+2] cycloadditions can occur photochemically between chemically distinct or identical π -systems. In the current thesis, focus is placed on the dimerization reaction of styrylpyrene, this chapter mainly covers [2+2] cycloadditions between identical molecules (cyclodimerization). As described in the paragraph on mechanistic aspects of cycloadditions (refer to **section 2.2.1**), and as indicated by the orbital symmetries in **Figure 3** and **Figure 4** therein, photodimerization of double bonds requires the encounter of a photochemically excited molecule and a ground state molecule. This prerequisite in combination with the limited lifetime of excited states and competing relaxation pathways (refer to the *Jabłoński* diagram in **Figure 2**, **section 2.1**) is a limiting factor for this type of reaction. In many vinylic systems, *cis/trans* isomerisation is another possible deactivation pathway, further narrowing the reaction manifold. In a [2+2] cycloaddition two

double bonds are combined, forming a non-aromatic cyclobutane structure. This decrease in conjugation causes a blue-shifted absorption spectrum of the formed cycloadduct. Conversely, employing short wavelength light can trigger the cycloreversion reaction, restoring the initial monomers. However, cycloreversion reactions do not necessarily lead to recovery of the initial monomers, but can instead yield new compounds, depending on the symmetry of the starting materials. In the case of asymmetrically substituted double bonds, the product composition after cycloreversion will differ from the initial composition, as is displayed in **Scheme 7**.

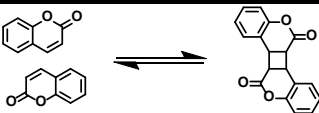
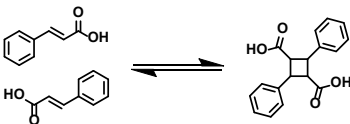
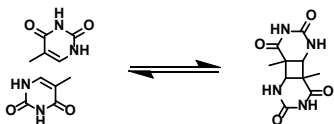
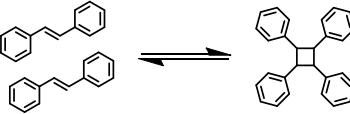
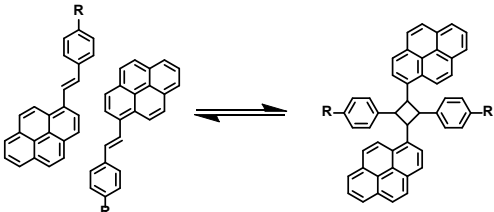


Scheme 7: [2+2] cycloaddition of asymmetrically substituted double bonds and subsequent cleavage into different monomers.

[2+2] Photocycloadditions have found widespread use in synthetic chemistry, biochemistry, or material science, and the reversibility of the reaction gave rise to a plethora of applications, particularly in ligation chemistry. Examples for [2+2] cycloaddition moieties that have been used for ligation reactions include coumarin,¹²³⁻¹²⁵ cinnamic acid,¹²⁶ thymine¹²⁷ or stilbene.¹²⁸ **Table 1** shows a series of photoactive moieties that have been employed for reversible [2+2] cycloaddition.

The mechanism of these reactions has been extensively studied; however, some aspects remain unexplored. While it was suggested that the reaction environment plays a role in determining whether formation of the *syn*-dimer or the *anti*-dimer is preferred through controlling the multiplicity of the reactive species,^{129, 130} more recent studies dispute this claim and propose a mechanism *via* an excited triplet state.¹⁸ Therefore, the limited lifetime of the excited states requires sufficient proximity of the reaction partners. Several strategies have been employed to overcome this hindrance. By adding triplet sensitizers or Lewis acids, the excited state dynamics can be manipulated, either facilitating ISC into the triplet state, or by exacerbating radiationless decay of the involved excited states.^{131, 132} Alternatively, reaction partners can be prearranged or brought to close proximity, i.e., by supramolecular catalysis.¹³³

Table 1: Various photoactive moieties that are able to undergo reversible [2+2] photodimerization.^{134, 135}

Reaction Scheme	Monomer	$\lambda_{\text{dimerization}}$	$\lambda_{\text{cycloreversion}}$
	Coumarin ¹³⁴	> 350 nm	< 260 nm
	Cinnamic acid ¹³⁴	> 300 nm	< 260 nm
	Thymine ¹³⁴	< 300 nm	< 260 nm
	Stilbene ¹³⁴	> 300 nm	< 260 nm
	Styrylpyrene ¹³⁵	> 450 nm	< 350 nm

While evidently much focus has been laid on the illumination of [2+2] cycloadditions, much less attention was paid to the reverse reaction. The understanding thereof is critical, however, since several concomitant effects complicate the system: Cycloreversion of dimers is triggered at shorter wavelengths due to the inherent blue-shift that occurs during dimerization. Usually, the absorption spectra of the monomer and the dimer are not fully separated, yet overlap at least partially, implying that certain wavelengths may trigger both the cyclisation and the cycloreversion simultaneously, until a photostationary state is developed, leading to an equilibrium between both forms. The reversibility of the system is therefore constrained, severely limiting its usefulness in applications. The degree of the reversibility depends on the overlapping absorption spectra as well as the wavelength of incident light.¹³⁶ It is therefore crucial to monitor the wavelength-dependent behaviour of a reaction. Provided that detailed reactivity maps are available, reversible [2+2] cycloadditions are a powerful tool for implementation of λ -orthogonal systems (also refer to **section 2.4**). Cyclisation of a chromophore A can be triggered at lower-energy wavelengths, forming the dimer A-A. On the other hand, high-energy wavelengths can activate a suitable second chromophore B, while

simultaneously supporting the cycloreversion of dimer A-A and therefore actively suppressing the formation to begin with.¹³⁷

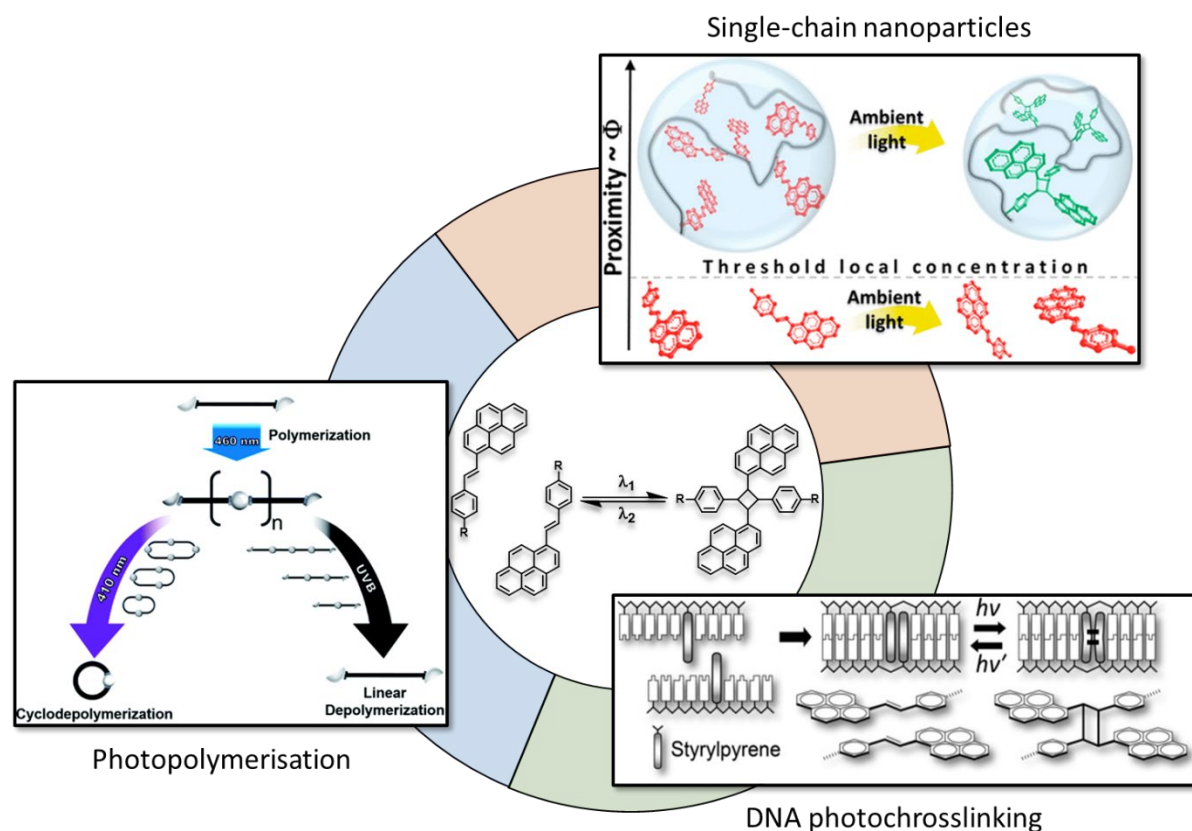


Figure 9: Applications of the [2+2] cycloaddition of styrylpyrene. Figures were reproduced with permission from the references indicated. Top right: Reversible folding of single-chain nanoparticles (SCNPs).¹³⁸ Left: Photopolymerisation of telechelic building blocks bearing styrylpyrene end-groups.¹³⁹ Bottom right: Photocrosslinking of DNA-duplexes.¹³⁵

To date, most reversible [2+2] cycloadditions are activated using UV light, which has a high proclivity to cause unsolicited side reactions, especially in multicomponent or biological systems.¹⁴⁰ Furthermore, UV light suffers from lower penetration depth.¹⁴¹ Therefore, it is beneficial to identify photoactive moieties that can be activated using visible light. In 1980, *Kovalenko et al.* reported red-shifted dimerization of diarylethylenes, bearing a pyrene chromophore.^{142, 143} Recently, this photoreaction was rediscovered and utilized for reversible photocrosslinking of DNA-strands.¹³⁵ Not much later *Marschner et al.*, and, in parallel, *Truong et al.*, reported reversible polymer-polymer ligation under visible light.^{137, 144}

This convenient reaction has since been employed for a multitude of applications such as formation of hydrogels¹⁴⁵, photopolymerisation,¹³⁹ or single-chain folding.^{138, 146} Modification of the pyrene moiety allowed for even more red-shifted activation.¹⁴⁷ Furthermore, several

recent publications combined styrylpyrene with other photo-reactive moieties to demonstrate wavelength-selective ligation, i.e., with photoenolization and subsequent Diels-Alder reaction of *ortho*-methyl benzaldehyde (*o*MBA),^{148, 149} or photoinduced [4+4] cyclodimerization of anthracene.¹⁵⁰

2.3 Red-Shifted Photochemistry

Traditionally, most photoreactions are triggered with light in the UV range.¹⁵¹⁻¹⁵³ However, this comes with several drawbacks: High energy irradiation often causes irreversible side-reactions and are harmful to biological systems.¹⁵⁴⁻¹⁵⁶ Moreover, virtually every organic compound displays absorption in this wavelength region, leading to competing absorption and limiting the amount of radiation available for the desired photoreaction.^{157, 158} This is particularly detrimental in multi-component systems and biological tissue, where many different chromophores are present, severely limiting the penetration depth of UV light.¹⁵⁹ Furthermore, greater variety of absorbing compounds in a given mixture increases the chances of photodamage and unwanted side reactions. Consequently, great potential for biocompatible reaction systems lies in red-shifted photo-sensitive compounds. Photons in the visible or even infrared wavelength regime carry less energy and are therefore less harmful to tissue, while also displaying enhanced penetration depth. Significant progress in this discipline has been made over the last years, and several approaches to achieve photo-activation in the visible or NIR regime have been implemented.^{66, 160, 161}

A common way to activate photoreactions using red-shifted light is two-photon absorption (2PA), where two photons are absorbed simultaneously and therefore only half the energy (corresponding to double the wavelength) is needed to reach excited states.^{162, 163} Since this is a non-linear effect (refer to **2.5.2.1**), it is related to higher-order terms of Beer-Lambert's law, hence being observed only at high intensities. In practice, this is realised by focussing a laser beam. Only within the laser focus (voxel), intensities are high enough to induce 2PA, therefore offering advanced spatial resolution as well as the ability to penetrate deeper into the sample. Applications include microfabrication¹⁶⁴, multiphoton microscopy,¹⁶⁵ direct laser writing (DLW),¹⁶⁶ or photodynamic therapy.¹⁶⁷ However, the prerequisite high two-photon absorption coefficients are not easily achieved in many molecules, and the need for a sophisticated femtosecond laser system is limiting the pervasiveness of the technology in synthetic laboratories.

A readily available technique are photocatalysts, which absorb light in a wide range of wavelengths from visible to infrared and can be utilised as photosensitisers or catalysts, i.e. for synthesis of polymers.¹⁶⁸⁻¹⁷¹ Including additives in a reaction mixture can lead to yet more adverse side reactions, or complications with removing the catalyst from the mixture.¹²²

The most common method to achieve red-shifted reactivity is to introduce a bathochromic shift to the absorption spectrum of a photo-reactive compound, mostly achieved through introduction of an extended π -system, resulting in a lower HOMO-LUMO gap and thus facilitating excitation at longer wavelengths.⁵ Such was realized i.e. for diarylethenes¹⁵⁷ (DAEs) or azobenzenes.¹⁷² The former were recently utilized by *Feringa* and coworkers as photoswitches to reversibly activate and deactivate the trigger-wavelength of molecular motors. That is, DAEs undergo cyclization upon irradiation with appropriate wavelengths, while an attached molecular motor's ability to rotate (also photo-driven) depends on whether the DAE is closed or opened.¹⁷³ Common ways to introduce extended conjugated systems are polycyclic aromatic hydrocarbons (PAHs), i.e. naphthalene,¹⁷⁴ anthracene,¹⁷⁵ or pyrene.¹⁷⁶⁻¹⁷⁸ Similarly, coumarin derivatives or conjugated oligothiophenes have been employed to induce bathochromic shift of the absorbance.^{66, 174} Because PAHs and extended conjugated systems inherently show a red-shifted absorption spectrum, they offer a straight-forward route to lower the activation energy. However, they can also suffer from disadvantages such as health concerns,¹⁷⁹ limited solubility,¹⁸⁰ or synthetic obstacles.

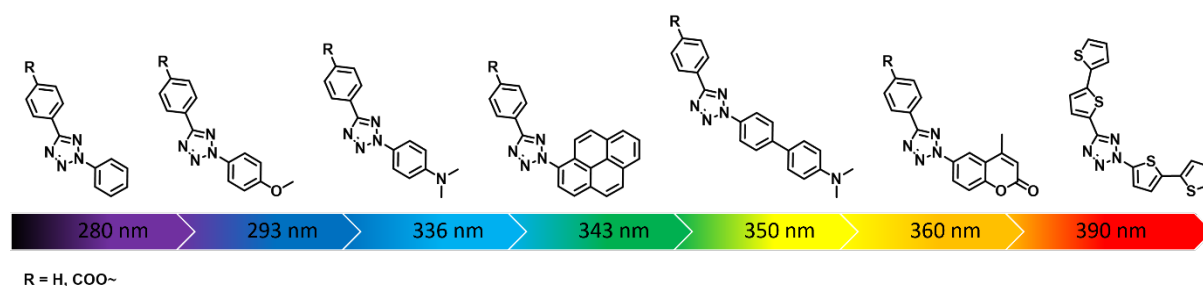


Figure 10: Red-shifting of tetrazoles by tethering extended conjugated systems or auxochromes. The given wavelength refers to λ_{\max} of the respective absorption spectrum.^{61, 65, 66, 73, 174, 176}

Instead of fusing more rings together, in order to increase the activation wavelength, chromophores can also be decorated with smaller groups that – on their own – do not display any significant absorbance, yet have a bathochromic effect once attached to a chromophore. Such groups are called auxochromes. They usually require free ion pairs that can contribute to the conjugated system, hence increasing the electron density and inducing bathochromic shift.¹⁸¹ Examples include -OH, -OR, -NH₂ or -NR₂ groups. The electron-donating ability of substituents is often quantified empirically by the *Hammett* parameter,¹⁸² or by the global electrophilicity index, in an attempt to rationalise the red-shifting potency of substituents.¹⁸³ This way, even slight modifications to complex systems can introduce significant changes in absorbance, and be employed to tune the absorption spectrum of a given compound over the whole visible spectrum, i.e., of donor-acceptor Stenhouse-adducts (DASAs),¹⁸⁴ or

polymethines.¹⁸⁵ An early study, *Lin* and coworkers utilised electron-donating groups to introduce a series of red-shifted tetrazoles.⁶¹ They employed substituents such as methoxy group, a tertiary amino group, or a styryl group, positioned on the *N*-phenyl ring.^{61, 65} Recently, *Heo* et al. demonstrated a very intriguing proof-of-concept work, adjusting the electron density of benzoic acid ester units immobilised on a gold surface by applying different voltages, tuning the reactivity of the saponification reaction.¹⁸⁶ However, they did not investigate any absorption properties, or photochemical features.

When attempting to tune the absorption profile (and hence the activation wavelength of photoreactions), it has to be noted that attaching red-shifting chromophores does not necessarily come with enhanced photo-reactivity in the low energy regime, as was demonstrated by our group.⁷³ We evaluated experimental and theoretical data of various tetrazole derivatives and stated that a dialkylamino-biphenyl-functionalized tetrazole, despite showing red-shifted absorption, does not undergo NITEC reaction. This discrepancy between absorptivity and reactivity was attributed to the inefficiency of the ISC, preventing the tetrazole from entering a triplet state.⁷³ Likewise, *Lin* and coworkers reported a lack of photoreactivity for red-shifted tetrazoles carrying a diarylacetylene moiety, or a diaryl-1,3-butadiene moiety.¹⁷⁴ It appears that absorption profiles alone fall short of predicting the reactivity of a given chromophore. This observation is in line with a series of studies, reporting a non-congruence of the absorption spectra and wavelength-dependent reactivity profiles of a number of photoactive molecules.^{113, 137, 145, 187, 188} *Menzel* et al. published an in-depth analysis of the wavelength-dependent reactivity of the photoenolization of *ortho*-methyl benzaldehyde (*o*MBA), stating that both the excited-state dynamics as well as complex light attenuation within the reaction mixture play a role.^{113, 158} Consequently, the most effective wavelength to activate the *o*MBA (330 nm) was red-shifted compared to the absorption maximum (316 nm) (refer to **Figure 11a**).¹¹³ This effect is even more pronounced in the initiation efficiency of oxime ester photoinitiators, where the most suitable activation wavelength (405 nm) is red-shifted by 78 nm compared to the absorption maximum (327 nm) (refer to **Figure 11b**).¹⁸⁷ The wavelength-dependent [2+2] cyclodimerization of styrylpyrene displayed a 59 nm red-shift between the absorption maximum (376 nm) and the dimerization maximum (435 nm) (refer to **Figure 11c**).¹³⁷ Probing a photo-induced reaction system with a range of disparate, monochromatic wavelengths is therefore paramount when pursuing a complete picture of the photochemical potential of a reaction system. Ideally, the overall number of incident photons at each wavelength is kept constant, to be able to draw meaningful conclusions from the

wavelength-dependent experiments. Knowing the most efficient wavelength can assist in determining the mildest-possible reaction conditions. Moreover, detailed understanding of a chromophore's wavelength-dependent behaviour is prerequisite for multi-component systems, where several photoactive moieties are to be addressed independently alongside each other.

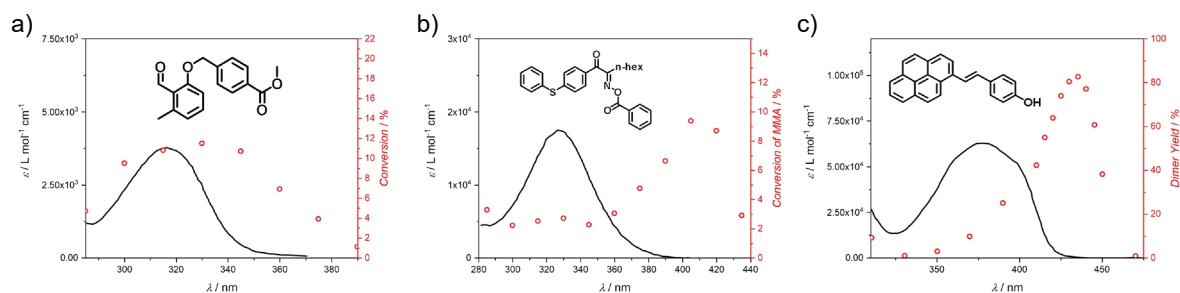


Figure 11: Examples from literature, demonstrating a red-shift of the reactivity maximum compared to the absorption spectrum of a photoreactive moiety. Figures were reproduced with permission from the references indicated. a) Photoenolization of *o*MBA and subsequent cycloaddition with maleimide.¹¹³ b) Initiation efficiency of an oxime ester in a free radical polymerization of methyl methacrylate (MMA).¹⁸⁷ c) Photo-induced cyclodimerization of styrylpyrene.¹³⁷

2.4 λ -Orthogonality

Since the development of new light sources such as lasers and LEDs, photochemistry has gained popularity in many modern applications such as photocuring of materials, tuning material properties, or advanced synthetic protocols.¹⁸⁹⁻¹⁹² Yet, more sophisticated systems require exceptional control over all involved components. This can be achieved by targeting multiple species alongside each other, in an independent fashion. Light as a trigger offers a superior level of control, in that the incident wavelength and intensity can be adjusted. Independently addressing multiple photoactive compounds in a single reaction mixture is called chromatic orthogonality,¹⁹³ wavelength-selectivity,¹⁴⁴ or λ -orthogonality.¹⁹⁴ This concept has been implemented in a range of applications such as wavelength-selective protection groups,¹⁹⁵ molecular switches,¹⁹⁶ altering material properties,¹⁹⁷ or ligation and post-functionalization of polymers.^{198, 199} Furthermore, λ -orthogonal ligation can provide critical improvements for direct laser writing (DLW), as it allows to manipulate two properties of a photoresist independently.¹⁶⁶ For this purpose, it is crucial to identify photo-sensitive systems that display distinct absorption bands or, more specifically, distinct wavelength-

dependent reactivity. This is a challenging task, however, since usually absorption bands overlap, even when one of the components is red-shifted. As shown in **Figure 12a**, this leads to simultaneous conversion of both species, if activated in the short-wavelength region. In many cases, it is therefore necessary to apply different wavelengths in a defined sequence: First, the compound mix is irradiated with long-wavelength light, converting exclusively the red-shifted species. Once full conversion is reached, the blue-shifted moiety can be addressed. This sequence-dependent orthogonality has been demonstrated several times in literature.²⁰⁰⁻

203

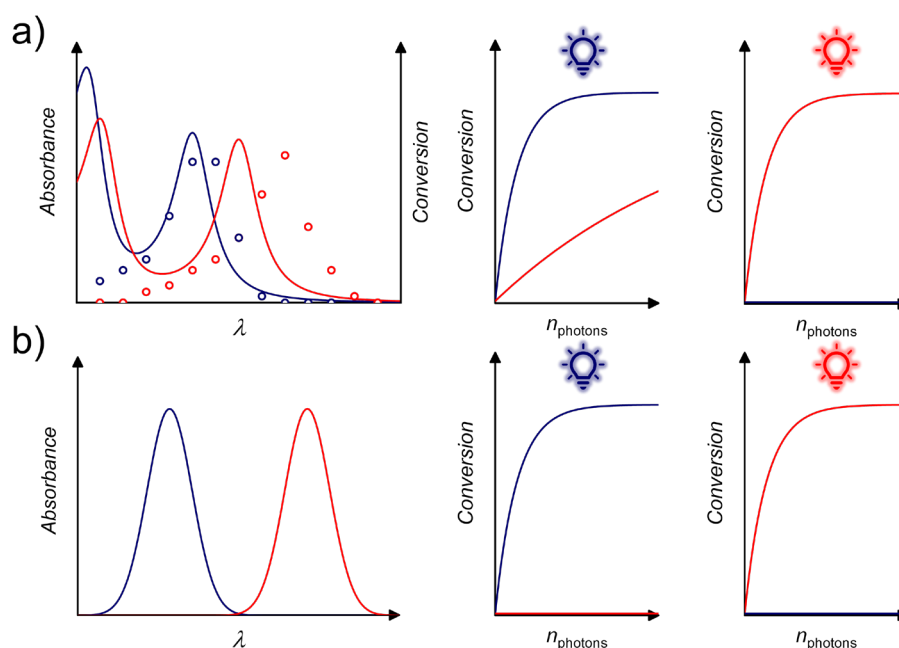


Figure 12: a) Left graph: Generic absorption spectra of two photoactive compounds and the respective wavelength-dependent conversion maps (action plot, refer to **section 2.3**). Right graph: Conversion over time. At lower wavelengths, both units are converted simultaneously. b) Left graph: Idealized, distinct absorption spectra of two photoactive compounds. Right graph: Ideal conversion plots in a fully λ -orthogonal reaction system.

Wu et al. demonstrated orthogonal and sequential release of short-hairpin ribonucleic acid (shRNA) and photocaged doxorubicin (DOX) from photoresponsive mesoporous silica nanoparticles (PMSNs) (**Figure 13a**). The shRNA was attached to the nanoparticle surface *via* coumarin-linked polycationic poly[2-(*N,N*-dimethylaminoethyl)methacrylate] (PDMAEMA) chain. Upon 405 nm irradiation, photolysis of the coumarin linker led to detachment of the polycation, releasing the shRNA. At 365 nm, DOX was released through photo-induced decarboxylation of a *o*-nitrobenzyl derivative linker. However, the authors stress that the longer wavelength light must be used prior to the shorter wavelength, and even then, 405 nm irradiation led to partial release of the DOX drug.²⁰⁴

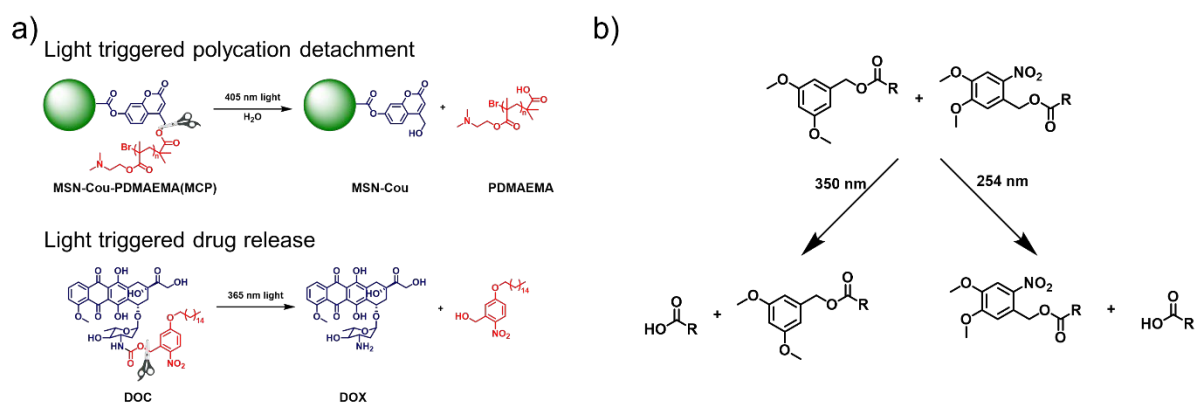


Figure 13: a) Orthogonal photolysis of a coumarin-linker upon 405 nm irradiation, followed by photocleavage of an *o*-nitrobenzyl photocage after 365 nm irradiation. Reproduced with permission from Wu *et al.*, *ACS Appl. Mater. Interfaces* 2018, **10**, 19416-19427. Copyright 2021 American Chemical Society. b) Orthogonal cleavage of carbamate derivatives, releasing carboxylic acids upon irradiation at 350 nm or 254 nm, in a sequence-independent fashion. Reproduced from *Tetrahedron Letters*, 41, Bochet, C. G., Wavelength-selective cleavage of photolabile protecting groups, 6341-6346 Copyright (2021), with permission from Elsevier.

While the previously mentioned report is rather recent, indeed, there are much earlier advances in the field of sequence independent λ -orthogonality. As early as 2000, Bochet demonstrated the cleavage of photo-caged protection groups, achieving a promising degree of sequence-independent λ -orthogonality. Employing a set of photolabile carbamate derivatives, which released carboxylic acid upon photo-induced cleavage, they were able to address the different photo-labile units at specific wavelengths (**Figure 13b**). Critically, both units displayed strongly disparate photolysis kinetics at each wavelength, allowing – to a certain degree – for a sequence-independent addressability. However, the degrees of selectivity were overall still modest, and each wavelength partly led to unsolicited activation of the opposite moiety.²⁰⁵ Interestingly, the same publication also reported that his approach is not generally applicable. In a second investigated system, the shorter wavelength-activated compound acted as a photosensitizer, leading to simultaneous conversion of the long wavelength-activated species. Like the two previously mentioned systems, the majority of literature reports concerning sequence-independent photo-activation revolves around photo-caged protection groups.²⁰⁶⁻²⁰⁸ Likewise, effectively sequence-independent orthogonal activation has been demonstrated for photoswitches.^{209, 210} However, examples for λ -orthogonal – let alone sequence-independent – bond-formation are scarce.

The concept of photo-active moieties that are kinetically preferred at certain wavelengths was further explored recently by our team.²¹¹ We observed that the reaction quantum yield of a red-shifted *ortho*-methyl benzaldehyde (*o*MBA) thioether significantly decreased when we

attempted to carry out the reaction in a mixture of water and acetonitrile, while the reaction proceeded normally and with high efficiency in absence of water (pure acetonitrile).²¹¹ This allowed for the photo-activation of a UV-responsive tetrazole at 285 nm, performing NITEC with *N*-ethyl maleimide (NEM), while the *o*MBA remained unaffected. After removing the water, *o*MBA could be activated with 382 nm light, forming an *o*-quinodimethane (photoenol), undergoing cycloaddition with NEM (Figure 14). The requirement to remove the water, however, might be a limiting factor for applications of the system. Moreover, the use of highly energetic UV light can cause side-reactions, limits the penetration depth of incident lights, and can be harmful for biological tissue.^{140, 141, 156}

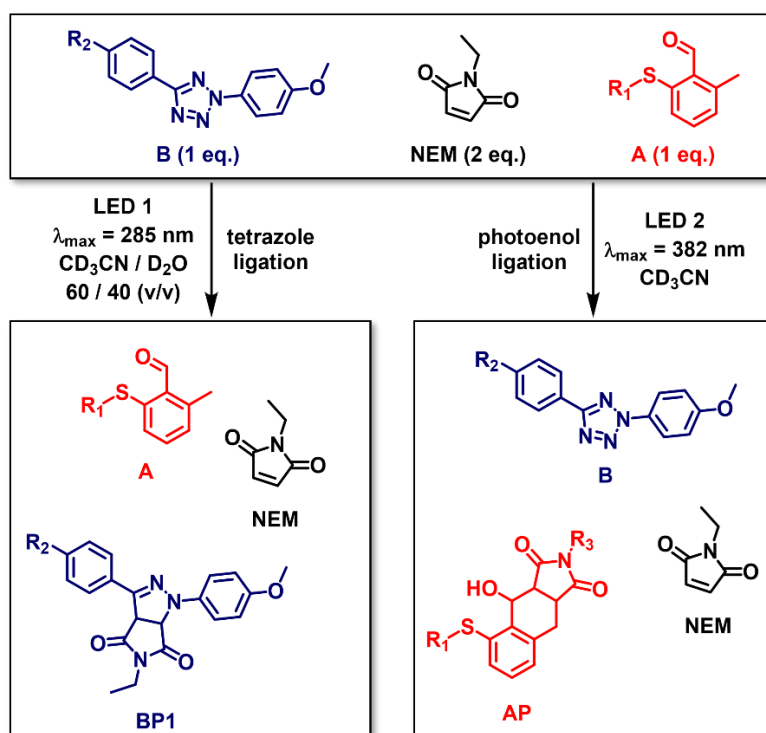


Figure 14: Orthogonal activation of a methoxyphenyl tetrazole at 285 nm in a mixture of acetonitrile and water. The water prevents the photoenol form being formed. In pure MeCN, the *o*MBA could be activated at 382 nm, forming the photoenol. Copyright (2021) Wiley. Reproduced with permission from Menzel *et al.*, *Angew. Chem. Int. Ed.* **2019**, *58*, 7470–7474.

Earlier, we employed a system of two functional polymers, bearing a tetrazole and an *o*MBA end-group, respectively.¹⁹⁴ Upon activation with 310–350 nm light, the *o*MBA underwent photoenolization, enabling thermal [2+4] cycloaddition with maleimide. Following full conversion thereof, the tetrazole end-capped polymer could be activated with 270–310 nm light. The generated nitrile imine reacted with maleimide in a 1,3-dipolar cycloaddition.¹⁹⁴ In a later publication, the obstacle of sequence-dependence could be overcome by reversibly

deactivating the long-wavelength activatable unit.¹²² Through condensation with hexylamine, photoenolization of the *o*MBA was prevented, allowing the more blue-shifted tetrazole to be activated first.¹²² However, the system still suffered from the need for additives, as well as activation in the UV regime (**Figure 15**).

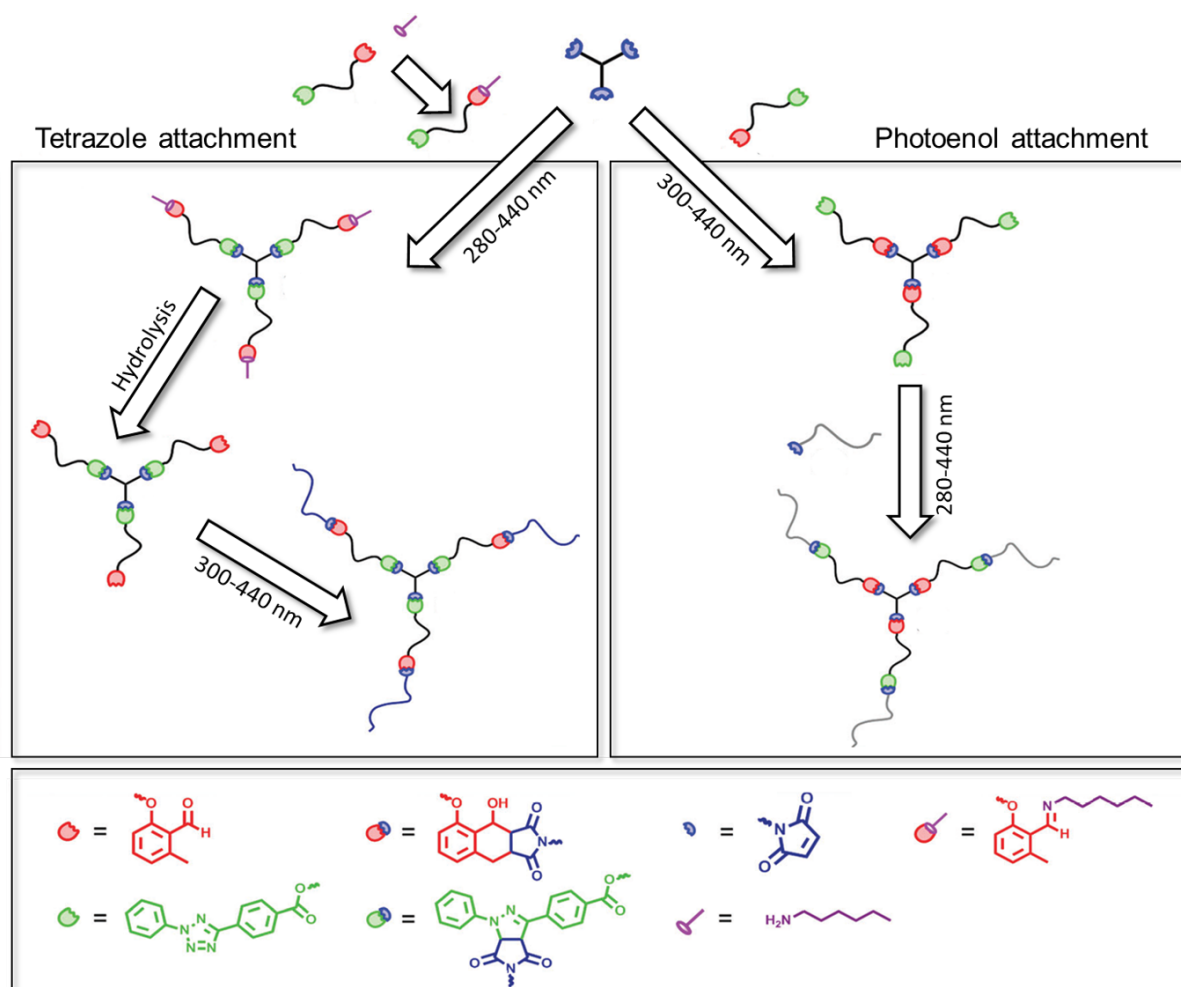
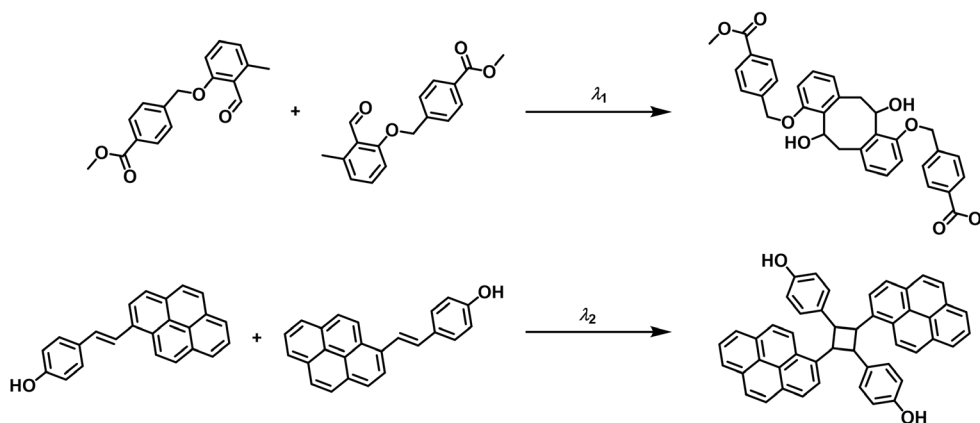


Figure 15: Pathway-independent synthesis of star polymers through photo-induced ligation *via* NITEC or Diels-Alder reaction of photoenols. Reversible deactivation of the photoenol precursor (*o*MBA) allows for activation of the tetrazole prior to the photoenolization step, for which the deactivated *o*MBA is hydrolysed. Reproduced from Hillebrandt *et al.*, *Chem. Commun.*, 2016, **52**, 9426–9429 with permission from the Royal Society of Chemistry.¹²²

A potent tool for λ -orthogonal systems is the photo-induced dimerization of styryl pyrene (refer to introductory **chapter 2.2.4**). Upon irradiation in the visible light, the system undergoes [2+2] cycloaddition, forming a strongly blue-shifted dimer. Conversely, cycloreversion of the dimer can be activated in the UV regime.¹³⁷ Consequently, in a binary mixture with a UV-activated moiety present alongside styrylpyrene, not only can UV light be used to activate the UV-responsive unit, but also actively suppress dimerization of styrylpyrene by triggering the cycloreversion. This feature was exploited by our group in 2019, introducing

a system of styrylpyrene and *o*MBA for orthogonal curing of resins.¹⁹⁹ While styrylpyrene could be dynamically dimerized and cleaved with visible and UV light, respectively, *o*MBA – upon photoenolization in the UV – underwent [4+4] photocycloaddition to form dimers as well (**Scheme 8**).



Scheme 8: Orthogonal dimerization of *o*MBA after photoenolization in the UV, and of styrylpyrene, after irradiation in the visible light regime. Adapted from *Bialas et al.*, *Adv. Mater.* **2019**, *31*, 1807288.

It must be noted that the absorption spectra of the starting monomer and the dimer can overlap. Correspondingly, the wavelength-dependent reactivity profiles can overlap, as well. At certain wavelengths, it is therefore possible to trigger the cyclization and the cycloreversion simultaneously, leading to the formation of a photostationary state, preventing the reaction from reaching high conversion. This is, indeed, a limiting factor of reversible cycloaddition reactions for λ -orthogonal chemistry, once again underlining the relevance of highly resolved wavelength-dependent reactivity mapping.^{137, 212} The effect can be compensated in solution, where molecules can freely diffuse after photo-scission and thus avoid recyclization, as was shown for coumarin derivatives.¹³⁶ When confined to a surface, though, the molecules dimerize again. Since the monomers are in too close proximity, they are fully exposed to back-and-forth reaction, leading to a wavelength-dependent equilibrium. This is especially detrimental in surface chemistry, where molecules are usually immobilised on a surface, or polymeric applications since polymers – due to their size – have a limited mobility as well.

Conclusively, significant advances in the development of sequence-independent λ -orthogonal reaction systems have been made, especially in recent years. However, the number of reports on bond-forming reaction systems is still limited. Current systems still either lack the wavelength-selectivity to be called truly λ -orthogonal, or they rely on additives or alternation of the reaction conditions, adding more steps in the reaction processes. There is still much room for exploration of photo-induced systems that can overcome these obstacles.

2.5 Laser Systems

Light amplification by stimulated emission of radiation (laser) has become a powerful and widely used technique, be it in every-day and industrial applications such as laser pointers, rangefinders, laser cutting, laser beam welding, optical storage reading and laser surgery, or as an advanced research tool for analytical chemistry, physics, biology, and astronomy. After being first described theoretically by *Albert Einstein*,^{213, 214} stimulated emission (SE) was adopted for amplification of microwave radiation (hence called *maser*) by *Gordon, Zeiger* and *Townes*.²¹⁵ Shifting wavelengths into the visible light was first achieved by *Theodore Maiman* in 1960.²¹⁶ Lasers come with a number of advantages that set them apart from common light sources and led to ubiquitous applications in research and industry. The light is spatially and temporally coherent, which means the beam has a very narrow frequency width and does not broaden even over long distances. Furthermore, the light is polarised, and laser pulses can be very short (femtoseconds, 10^{-15} s;²¹⁷ and even attoseconds, 10^{-18} s, have been achieved²¹⁸) and reach extremely high intensities.²¹⁹

2.5.1 Fundamentals

In principle, three fundamental components are needed to construct a laser:²²⁰

- Pump source
- Active laser medium
- Resonator

The pump source is the primary source of energy, which excites the active laser medium (or gain medium) into an excited state. Generally, the population of states in thermal equilibrium follows the *Boltzmann* distribution, that is, most species (molecules, atoms, ions) are in the ground state and only few are in the excited state, and the difference in population follows the equation:

$$\Delta N = N_1 - N_2 \quad (2 - 10)$$

Here, N_1 and N_2 are the number of ions in the ground and excited state, respectively. In thermal equilibrium, it is $\Delta N > 0$. Since stimulated emission is the reverse process of absorption, between two given states both can be induced by the same wavelength. In thermal

equilibrium, however, absorption $E_2 \leftarrow E_1$ and spontaneous emission are more likely than stimulated emission $E_2 \rightarrow E_1$, due to the higher number of molecules in the ground state. For SE to be the dominating process, population inversion $\Delta N < 0$ must be reached, for which the active laser medium needs to fulfil certain requirements. In a two-level system like the one illustrated in **Figure 16**, population inversion can never be reached. Even if competing processes like spontaneous emission are neglected, after equal population $\Delta N = 1$ is reached, absorption and SE have equal probabilities to be induced by the pump process.

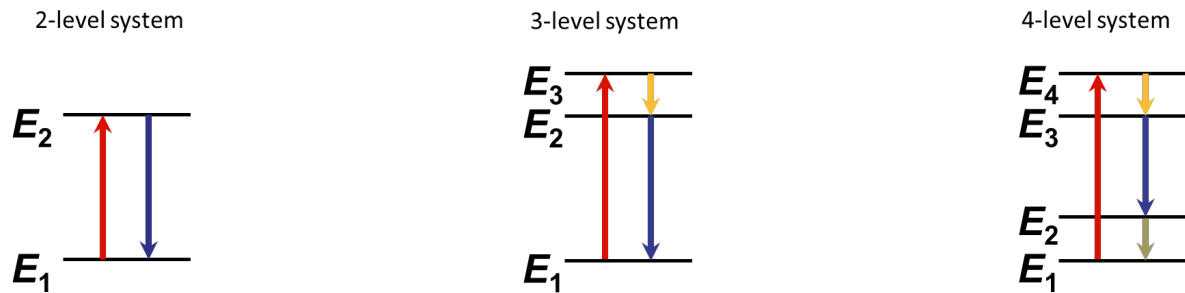


Figure 16: Schematic diagrams of two-, three-, and four-level laser media. Arrows in red indicate the pump process. Yellow and green arrows indicate ultrafast radiationless relaxation. Blue arrows indicate stimulated emission.

In a three-level system, such as the one in **Figure 16**, E_3 has a much shorter lifetime than E_2 . After excitation, the gain medium undergoes ultrafast radiationless relaxation into the upper laser level E_2 . Thus, SE caused by the pump wave is circumvented. SE (and therefore net laser gain) can occur if more ions are in the upper laser level than in the lower laser level. Since the lower laser level is the ground state, strong pump powers are required to achieve population inversion. An example of a three level medium is ruby ($\text{Cr}^{3+}:\text{Al}_2\text{O}_3$).²²¹ Population inversion can be reached more efficiently in a four-level system, where E_4 and E_2 are short-living states, and E_3 is long-living. Through rapid depopulation of E_2 , reabsorption into the upper laser level is avoided. Hence, in an excited four-level system – given sufficiently low rate of spontaneous emission – there is always population inversion $\Delta N = N_2 - N_3 < 0$ and the gain rises linearly with the pump power. A prominent example for a four level laser medium is yttrium aluminium garnet with neodymium dopant (Nd:YAG). Here, the lifetimes τ_3 and τ_2 of the upper and lower laser levels E_3 and E_2 are $230 \mu\text{s}$ and 30 ns , respectively.²¹⁹

In a basic laser setup, the active laser medium is placed in a resonator, consisting of two opposing mirrors of defined distance (**Figure 17**). A photon that can form stationary waves within the resonator is self-amplified as it passes through the inversely populated active laser medium, where it generates a second photon through SE. Newly generated photons match

the incident ones in phase, polarisation, and direction, and, for their part, can generate new photons. If the amplification is higher than the cavity loss (due to absorption, scattering, or ejection) laser action begins.

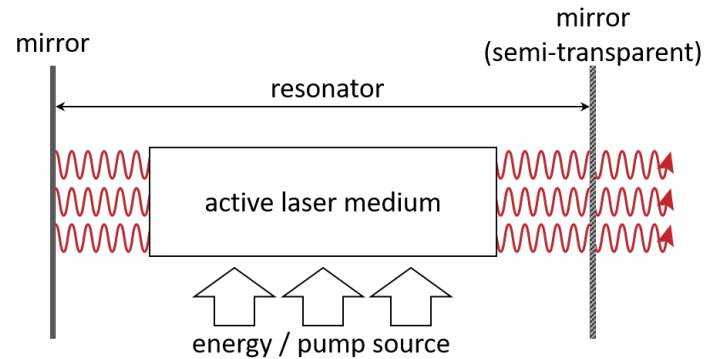


Figure 17: Schematic illustration of the interaction of the three main components of a laser: pump source, active laser medium and resonator. Amplified photons are exiting the cavity through a semi-transparent mirror as a spatially and temporally coherent, polarised light beam.

The temporal profile of the laser operation depends on the pump frequency, the amplification per pump cycle, and the lifetimes of the laser levels involved.²²² If the relaxation times are short compared to the pump-process, after a short time a quasi-stationary population of states will be reached, providing for a continuous laser mode (continuous wave, CW). In the opposite case, where the lifetime of the upper laser level is high compared to the rise time of the pump pulse, large population inversion is reached before emission can be induced, leading to high gain and therefore high laser power. Consequently, the upper laser level will be depleted faster than the pump pulse can refill it.²²² The technique of Q-switching was developed to avoid irregular sequences of “spikes” in favour of a single, high-powered pulse. That is, the cavity loss during the pump process is kept high for a certain period (corresponding to a low Q-value of the cavity). This way, depletion of the upper laser level is prevented, and population inversion is built up. Once the Q-value is “switched”, the quality of the resonator promptly increases, resulting in a very high energy laser pulse. The repetition rate of a pulsed laser is determined by the switching cycles of the Q-value. Typical pulse durations for Q-switched lasers are in the order of 10 ns, and the powers reach up to 10^9 W.²²²

2.5.2 Wavelength-Tuneable Laser Systems

As per the fundamental laser principles introduced in the previous chapter, laser devices generally emit only one wavelength. Since the ability to tune the output wavelength of a laser is of great relevance in many spectroscopic applications, several techniques have been developed to achieve tuneable laser systems. Since such systems play a critical role in the current thesis, the fundamental principles are hereby described in more detail.

2.5.2.1 Nonlinear Optics

Both laser systems employed in this thesis work under the same principle of operation: To convert the output wavelength of the Nd:YAG laser (1064 nm) into a wide range of wavelengths in the UV, visible and infrared, nonlinear optical processes are used. The term “nonlinear” refers to higher order terms in the response of a system to an applied electromagnetic field.²²³ These terms become relevant only at high light intensities, where the displacement of the electrons relative to the equilibrium cannot be described by a harmonic motion model. When high-intensity laser light is applied to a material, the time-dependent polarization $\vec{P}(t)$ of the medium can be described by the following formula:²²³

$$\begin{aligned}\vec{P}(t) &= \varepsilon_0\chi^1\vec{E}(t) + \varepsilon_0\chi^2\vec{E}^2(t) + \varepsilon_0\chi^3\vec{E}^3(t) + \dots \\ &= \vec{P}^{(1)}(t) + \vec{P}^{(2)}(t) + \vec{P}^{(3)}(t) + \dots\end{aligned}\tag{2 – 11}$$

Here, ε_0 is the vacuum permittivity, χ^i is a rank $i + 1$ tensor describing the i th-order nonlinear optical susceptibility and $\vec{E}(t)$ is the electric field. This simplification assumes that the medium is lossless and dispersionless. The higher-order susceptibilities are in the order of 10^{-12} m/V (χ^2) and 10^{-24} m/V (χ^3) and correlated processes are therefore very unlikely, but can be observed given that a sufficiently high intensity optical field is applied.²²⁴ Another prerequisite for second-order nonlinear processes is that they can only occur in anisotropic, noncentrosymmetric crystals such as β -BaB₂O₄ (β -barium borate, BBO) or LiB₃O₅ (lithium triborate, LBO), since otherwise the polarization function (2 – 12) is odd and, hence, does not contain even terms.²²⁵

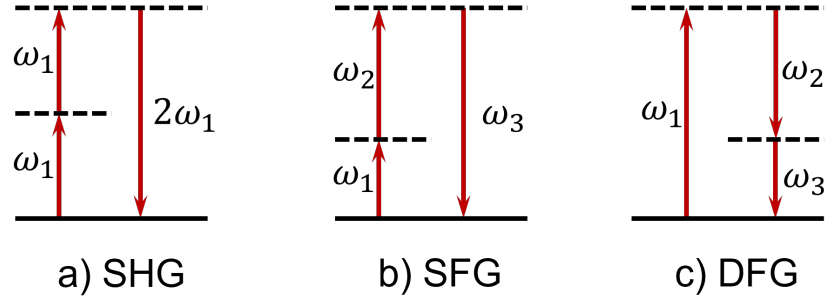


Figure 18: Schematic energy-level diagrams of the most common frequency mixing processes: a) Second-harmonic generation (SHG), b) Sum-frequency generation (SFG), c) Difference-frequency generation (DFG).

Second-harmonic generation: When a laser beam enters a material for which the second-order susceptibility is non-zero, it can lead to second-harmonic generation (SHG). For instance, input light at a wavelength of 1064 nm is frequency-doubled to an output wavelength of 532 nm. This can be envisioned as simultaneous conversion of two photons of frequency ω_1 and creation of one photon of frequency $2\omega_1$ (refer to **Figure 18a** and **Figure 19a**).²²³

Sum-frequency generation: If two laser beams of different wavelengths are incident upon a nonlinear material, sum-frequency generation (SFG) can occur, of which SHG is only one specific case. Again, this process can be visualized by simultaneous conversion of two photons of frequencies ω_1 and ω_2 and creation of a photon of frequency ω_3 so that $\omega_3 = \omega_1 + \omega_2$ (refer to **Figure 18b** and **Figure 19b**).²²³

Optical parametric amplification and optical parametric oscillation: In an analogue process, two photons of different frequencies ω_1 and ω_2 entering a nonlinear material can lead to difference-frequency generation, also called optical parametric amplification (OPA).²²³ Here, the incident and emitted frequencies follow the equation $\omega_3 = \omega_1 - \omega_2$ (refer to **Figure 18c** and **Figure 19c**).²²³ Energy conservation demands that in this process, a photon of frequency ω_1 is converted and two photons of ω_2 and ω_3 are formed. Because the lower input frequency is already present, this amounts to a stimulated two-photon emission (hence the term amplification). If this setup is positioned in a resonator cavity, the setup is called optical parametric oscillator (OPO) and the output wavelengths can reach considerable intensities. Since the above stated condition can be fulfilled for any $\omega_2 < \omega_1$, various ω_3 outputs are possible. The output frequency can be controlled by adjusting the phase-matching condition and using wavelength-selective optics. Thus, a tuneable laser setup can be achieved. In this model, ω_2 is called *signal* frequency and ω_3 is called *idler* frequency.²²³

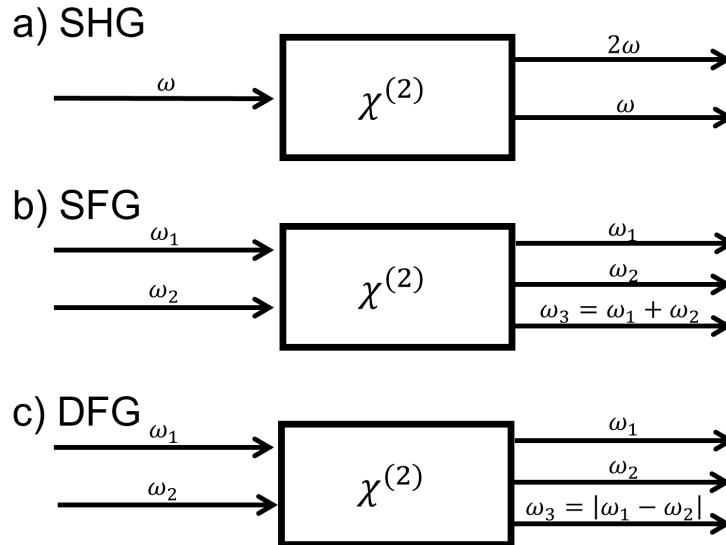


Figure 19: Geometries of the interactions of nonlinear processes: a) Second harmonic generation. b) Sum-frequency generation. c) Difference-frequency generation.

Third-harmonic generation: Unlike the previously described effects, third-order nonlinear processes can occur in materials with or without an inversion symmetry. Third-order polarization $P^{(3)}$ is proportional to the third power of the electric field as per (2 – 12). In a process called third-harmonic generation (THG), three photons of incident frequency ω_1 are converted and one photon of frequency $3\omega_1$ is formed.²²³ Since, comparatively speaking, THG is a highly inefficient process, for practical applications, the third harmonic is usually not generated through THG of the fundamental wave directly. Instead, the second harmonic is generated through SHG, followed by SFG with the fundamental, as is the case in the tuneable laser system described in the following chapter.

2.5.2.2 Setup of the Tuneable Laser System

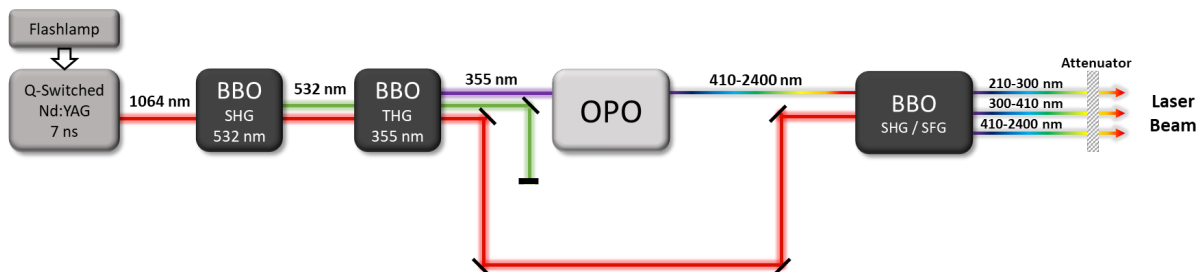


Figure 20: Simplified schematic setup of the wavelength tuneable laser system. A Q-switched Nd:YAG laser is pumped by a flashlamp, emitting quasi-monochromatic pulses at 1064 nm. Through a series of nonlinear optics, output wavelengths between 210 nm and 2400 nm can be achieved.

In the current thesis, two different tuneable *ns*-pulsed laser systems were used. The general setup is described in the following. For the exact specifications of the setups, refer to **chapter 8.3.1**. Coherent pumping of a neodymium-doped yttrium aluminium garnet crystal ($\text{Nd}^{3+}:\text{Y}_3\text{Al}_5\text{O}_{12}$, Nd:YAG) is achieved by flashlamps or diodes. Q-switched 1064 nm pulses are released at a repetition rate of 20 Hz (or 100 Hz). The beam is passed through a series of two BBO crystals, generating 532 nm light (through SHG), followed by SFG of the second harmonic and the fundamental wave, generating 355 nm light (refer to **Figure 20**). The third-harmonic is directed into an OPO, which generates a signal wavelength between 410 nm and 2400 nm. To achieve wavelengths in the UV regime, this signal output can be subjected to SFG with the fundamental wavelength, yielding wavelengths between 300 nm and 410 nm. Furthermore, even lower wavelengths are generated through second-harmonic generation of the OPO output beam, resulting in wavelengths between 210 nm and 300 nm. The energy of the output beam is then adjusted by an attenuator or a neutral density filter.

3 GREEN-LIGHT ACTIVATED CYCLOADDITIONS

3.1 Objective

Photochemistry offers several advantages over conventional thermal chemistry: Spatio-temporal control, innocuousness and non-invasiveness are considered trademarks of light-driven reactions.²²⁶ With light becoming an ever more important tool in fields like medicine,²²⁷ material science,^{191, 228} or biochemistry,²²⁹ scientists strive to overcome obstacles such as harmfulness of UV radiation,¹⁴⁰ tissue penetration depth¹⁴¹ and unsolicited side reactions. Photoactive groups that can react upon visible light stimuli are highly sought-after, since they fulfil these requirements.^{155, 230} By combining multiple photoactive units and activating them independently alongside each other, λ -orthogonal reaction systems can be established that offer more rigorous control over complex reaction routes.^{144, 184, 208, 209, 212, 231}

However, to implement truly λ -orthogonal photo-induced reaction systems, detailed knowledge of the wavelength-dependent reactivity of all involved reactants is critical. Whereas intuition may suggest that λ_{max} is the most suitable wavelength to trigger photoreactions, the wavelength-dependent reactivity can differ from the absorption profile.^{137, 187} Consequently, determining the most effective wavelengths for activation of a given photoreactive moiety is imperative. Pulsed laser systems are a powerful tool to activate photoreactions with monochromatic light, exerting control over wavelength, pulse number, and pulse energy. By probing a photoactive system at various wavelengths, with the number of incident photons kept constant at all wavelengths, a detailed reactivity map for a given chromophore is obtained.¹⁸⁷ Once this data has been compiled for all relevant chromophores, λ -orthogonal reaction systems can be achieved by more commonly available, spectrally broad - yet controlled - LED setups.

Tetrazoles are a common photoactive compound due to their efficiency, biorthogonality and versatility.²³⁰ Upon stimulation with appropriate wavelengths, tetrazoles can eliminate molecular nitrogen, N₂, forming a reactive nitrile imine, which can then act efficiently in a 1,3-dipolar cycloaddition with electron-deficient double bonds.⁶² Since its rediscovery in 2007,⁶¹ the photo-induced nitrile imine-mediated tetrazole-ene cycloaddition (NITEC) has undergone

remarkable development: modification of nucleic acids,²²⁹ protein labelling,⁸¹ hydrogel assembly,²³² polymer ligation,¹⁷⁶ or nano- and microparticle modification are among its many applications.^{233, 234} Yet, in most studies, UV-A or UV-B light was employed to activate the reactions. Efforts have been made to shift the activation wavelength of tetrazoles from the UV into the visible light regime, i.e., through tethering the tetrazole moiety to extended conjugated systems such as pyrene or oligothiophenes,^{66, 176} or through decorating the *N*-substituted phenyl ring with an electron-donating auxochrome such as a methoxy group or an amino group.^{65, 72} However, no NITEC has been reported to be activated at wavelengths beyond 420 nm,¹⁷⁶ and so far, the photochemistry of tetrazoles has only just started to harness the full spectrum of visible light. It was hypothesised that further red-shift could be achieved by using a combination of the above mentioned strategies: The extended aromatic system of pyrene has already been established as a red-shifting chromophore on the tetrazole, but can possibly be further modified with an electron-donating group such as an amino group, which – in multiple reports – has had a similar effect on the absorption spectrum and activation wavelength compared to the non-substituted tetrazole.

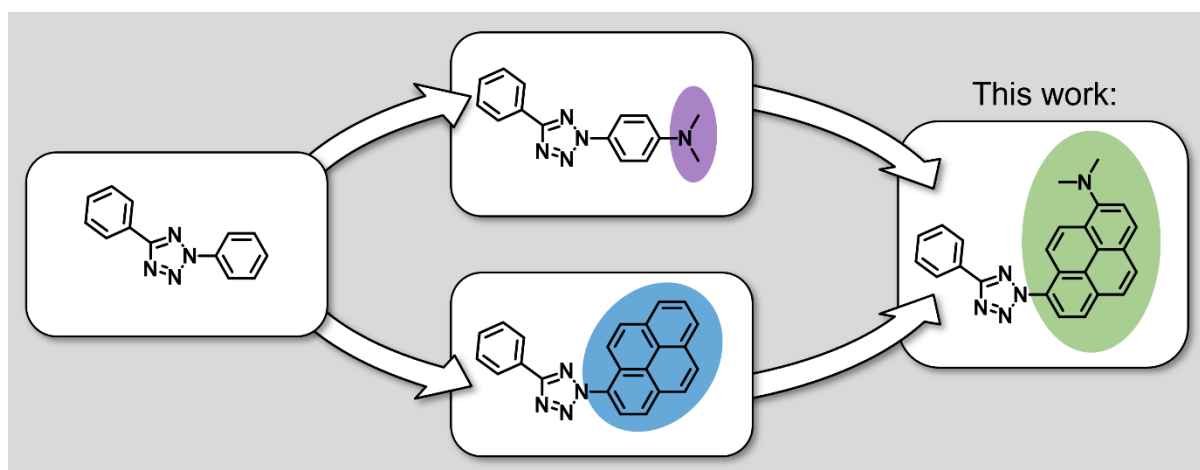


Figure 21: Combining the bathochromic effects of pyrene and a dimethylamino group, a stronger red-shift is induced in the final molecule.

In the present chapter, advances are made to expand the toolset of visible light-activated tetrazoles beyond the blue light regime. It demonstrates how synthetic rationale can be used to tune the absorbance of a tetrazole to extend well into the visible light region, allowing for photoactivation at up to 515 nm. Employing a wavelength-tuneable *ns*-pulsed laser system, the wavelength-dependent reactivity is probed over a wide range of wavelengths for an exemplary small-molecule ligation reaction. To analyse and quantify the reaction products, liquid chromatography coupled with high-resolution mass spectrometry is used. As a proof

of concept, the tetrazole is also utilised for end-group functionalisation of a poly(methyl) methacrylate based polymer.

Initially, synthesis and detailed spectroscopic characterisation of the new tetrazole are described. Subsequently, the wavelength-dependent laser experiments are specified, and the results discussed and compared with literature. Following the compilation of wavelength-dependent reactivity data, polymer end-group modification experiments with LEDs are described and discussed in detail.

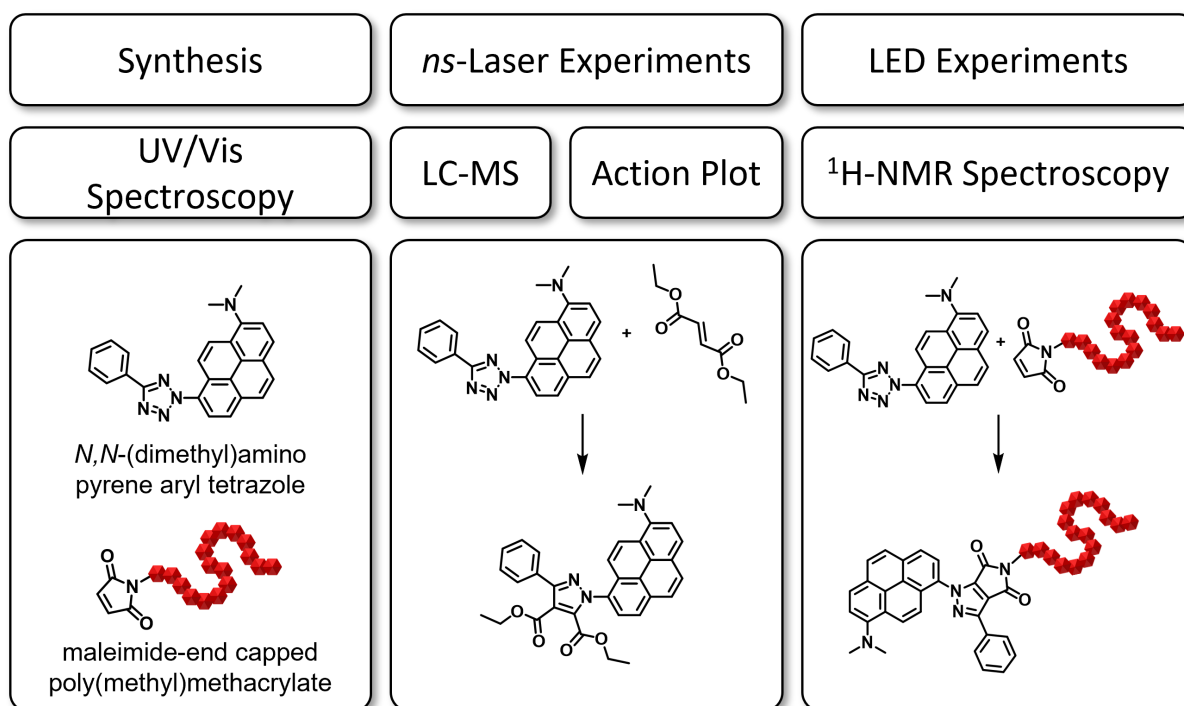


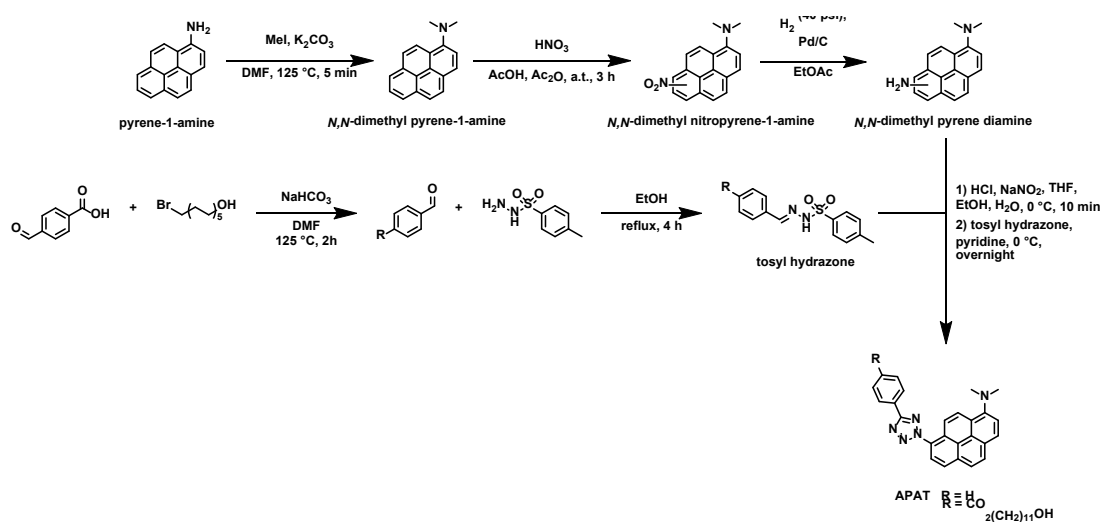
Figure 22: Schematic overview over the methodology applied in the current chapter. After synthesising and carefully characterising a red-shifted tetrazole, wavelength-dependent reactivity was assessed *via ns*-pulsed laser experiments and quantified by LC-MS, producing a so-called action plot. Furthermore, suitable LEDs were employed for polymer ligation reactions, and the results analysed by ¹H-NMR spectroscopy.

Parts of this chapter were reproduced with permission from P. W. Kamm, J. P. Blinco, A.-N. Unterreiner, C. Barner-Kowollik, *Chem. Commun.* **2021**, 57, 3991.

3.2 Synthesis of a Red-Shifted Tetrazole

3.2.1 Small Molecule

Traditionally, literature-known pyrene aryl tetrazole (PAT) is synthesised according to a procedure from *Ito et al.*, starting from pyrene-1-amine, diazotation and, finally, coupling with a formazan intermediate (refer to chapter 2.2.2.1).⁵⁴ Following this, the starting material for synthesis of a modified *N,N*-(dimethyl)amino pyrene aryl tetrazole (APAT) must be a disubstituted *N,N*-(dimethyl) pyrene diamine. There are few procedures reported for synthesis of disubstituted pyrenes. While not all of them indicate issues with isomer formation, it is likely that the possibility of this was simply left unmentioned.²³⁵ Introducing a second substituent naturally leads to a mixture of either (1,3)-, (1,6)-, or (1,8)-disubstituted pyrene.²³⁶ For the most part, either halogen groups (-Br) or nitro groups are introduced, which allow for simple post-modification. Given that an amino group is required for diazotation in the final tetrazole formation step,⁵⁴ nitration and subsequent reduction to the amino group was the preferred route. Hence, in an initial step, a modified literature procedure by *Ludwanowski et al.* was followed,¹⁴⁷ rendering the amino group less prone to side reactions, as well as enhance the electron-donating properties.⁶⁵ Methylation of pyrene-1-amine was achieved in high yield and purity, and the product could be subjected to nitration without further purification (for the detailed procedure refer to 8.7.1.1, and for the ¹H-NMR spectra refer to 10.1).



Scheme 9: Reaction route for a new red-shifted *N,N*-dimethylamino pyrene aryl tetrazole (APAT).

Introducing a second substituent to pyrene-1-amine

Due to the inherent formation of different isomers once a second substituent is introduced to a pyrene core, the reaction conditions were optimized diligently, in order to maximise the product yield. Therefore, in the following paragraph a detailed description of the underlying considerations is given. Generally, the nitration reaction proved to be a balancing act, since double nitration had to be avoided, while still aiming for high conversion of the starting material. Following a modified literature procedure,²³⁶ *N,N*-dimethyl pyrene-1-amine was nitrated using concentrated nitric acid as a nitrating agent in a mixture of glacial acetic acid and acetic anhydride at ambient temperature. The reaction progress was followed carefully by thin layer chromatography (TLC), to avoid product loss due to over-nitration. Starting material, desired product as well as double-nitrated side-product were readily distinguished on the TLC plate due to changes in R_f value, colour, and fluorescence (for the exact procedure refer to 8.7.1.2). In parallel, the reaction progress was quantified by $^1\text{H-NMR}$ spectroscopy. Once the amount of double-nitrated product started to increase, the reaction was quenched. By integrating the signals of the $-\text{NMe}_2$ group, the relative amounts of the different mono-nitrated isomers could be determined to be 20 % of the 1,3-isomer and 40 % for the 1,6- and die 1,8-isomer, respectively.

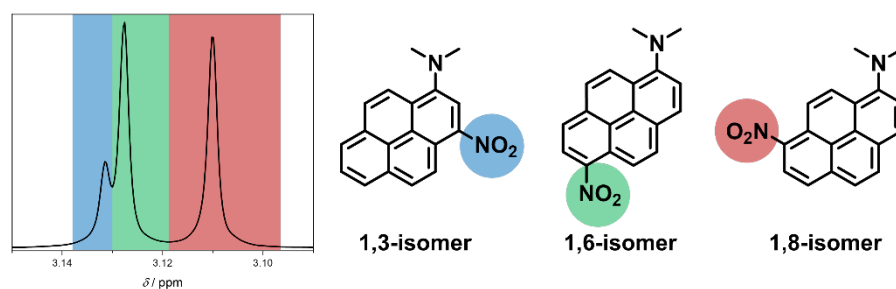


Figure 23: Magnified signals of the $-\text{NMe}_2$ protons in the $^1\text{H-NMR}$ spectrum of the isomer mixture. For the full spectrum refer to **Figure S 12**.

While the isomeric mixture could be separated from the starting material and minor amounts of double-nitrated side-product, attempts to separate the isomers were unsuccessful. A study by *Hashimoto* et al. notes that pyrene-diamine isomers are separated more effectively than their nitro analogues.²³⁷ Separation was therefore carried out after the next step, which involved catalytic hydrogenation of *N,N*-dimethyl nitropyrene-1-amine to the corresponding *N,N*-(dimethyl) pyrene diamine (for the exact procedure, NMR-spectra, as well as a detailed

description of the determination of the regio-isomeric structure, refer to section 8.7.1.3). Only *N,N*-dimethyl pyrene-1,8-diamine could be isolated in sufficient quantities. Isomerically pure *N,N*-dimethyl pyrene-1,6-diamine was isolated in minor amounts, while no pure *N,N*-dimethyl pyrene-1,3-diamine was obtained. A large fraction of the latter two isomers remained inseparable.

After successful isolation of the 1,8-isomer, the next step involved diazotation and formation of the tetrazole. A diazotation route that was reported for pyrene aryl tetrazole synthesis, using NaBF_4 and aqueous HBF_4 ,²³⁴ did not lead to precipitation of the desired diazonium salt. This may be attributed to the additional dimethylamino group, which acts as base and alters the solubility in the acidic diazotation mixture, possibly preventing the diazonium salt from precipitating. As a consequence, a different diazotation route was chosen, which is more widely reported in literature and uses NaNO_2 and HCl in a mixture of water and ethanol.⁵⁴ To increase solubility, tetrahydrofuran (THF) was added to the mixture. The diazonium salt was *in situ* added to a prepared ice-cold solution of a previously synthesised tosyl hydrazone in pyridine, and, while warming up overnight, the tetrazole was formed and could be purified *via* column chromatography (for the exact synthetic procedure of the tosyl hydrazone and the tetrazole, refer to 8.7.1.4 and 8.7.1.5, and for the NMR spectra, refer to **Figure S 19-Figure S 21**). In the following, *N,N*-dimethyl amino pyrene aryl tetrazole is abbreviated APAT.

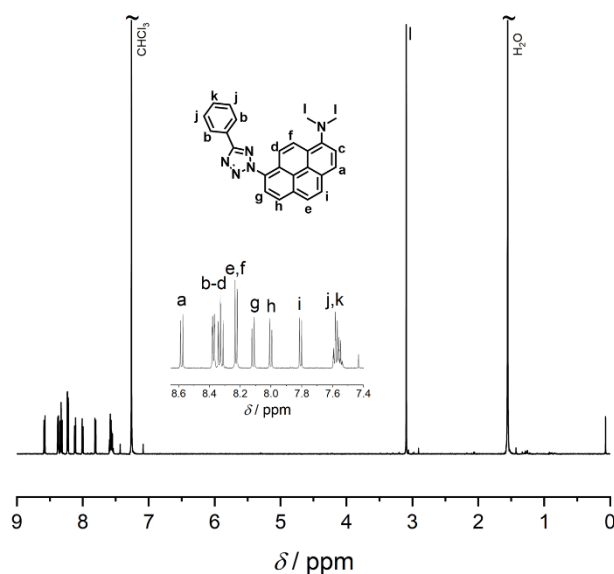


Figure 24: ¹H-NMR spectrum of APAT in CDCl₃.

The ¹H-NMR spectrum shows clean resonances, whose integrals amount to 13 aromatic signals, as well as a singlet, corresponding to six protons of the dimethylamino group. Liquid-

chromatography coupled mass spectrometry was employed to confirm purity as well as exact mass of the product. The mass spectrum shows the $[M+H]^+$ species, as well as a second species with a mass difference of 28.0063, corresponding to the nitrile imine species after loss of molecular nitrogen $[M-N_2+H]^+$. This is attributed to the electrospray ionisation process of the mass spectrometer.

Similarly, a small variety of tetrazoles were synthesised, bearing linkers on the C⁵-phenyl ring, enabling the attachment of a polymer chain. This was achieved simply by varying the tosyl hydrazone in the last reaction step: First, an undecanol linker was introduced, decorating the final tetrazole with a hydroxy functionality. Second, a tosyl hydrazone bearing a methylester group was synthesised, equipping the final tetrazole with a carboxylic acid functionality after saponification of the ester. Employing the methylester instead of the carboxylic acid was necessary, since the product could not be purified when a free carboxylic acid group was present. This was attributed to the zwitterionic nature of the molecule, severely impacting the solubility in organic solvents. Hence, synthesis and purification were carried out with a methylester group, and only afterwards the carboxylic group was restored through saponification. For the exact procedures, refer to 8.7.1.8 and 8.7.1.11, and for the NMR spectra, refer to **Figure S 24** and **Figure S 27**.

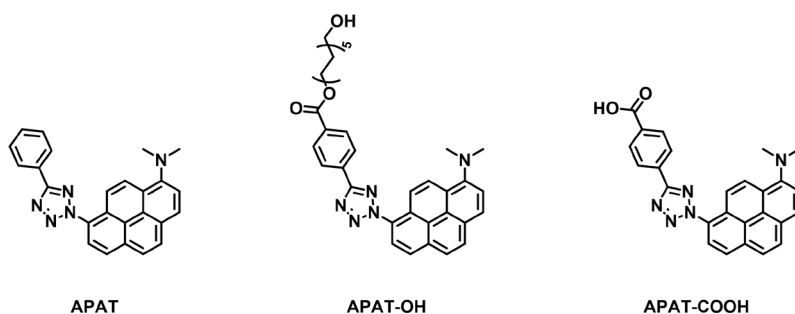
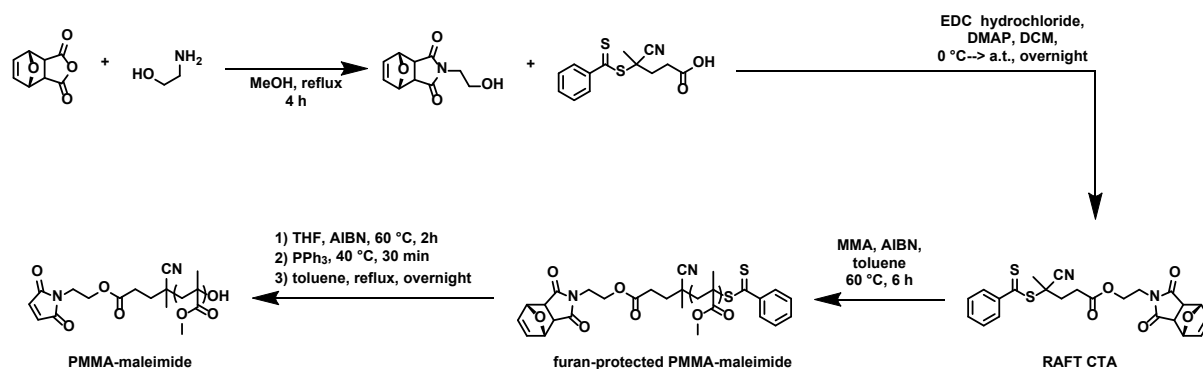


Figure 25: Structures of three synthesised APAT derivatives: APAT without linker, APAT-OH, carrying an undecan-1-ol chain in *para*-position of the C⁵-phenyl ring, and APAT-COOH, carrying a carboxylic acid in the *para*-position of the C⁵-phenyl ring.

3.2.2 Polymers Bearing a Maleimide End-Group

To explore the ability of APAT as a post-functionalisation agent for polymers, a poly(methyl)methacrylate-based polymer, bearing an electron-deficient dipolarophile as an end-group, was synthesised *via* reversible-activation-fragmentation chain transfer (RAFT)

polymerisation. RAFT polymerisation technique was selected, because it offers relatively high end-group fidelity and excellent control over the chain-length. Starting from a furan-protected maleic anhydride, the synthetic route outlined in **Scheme 10** was followed.



Scheme 10: Reaction route for synthesis of a reversible addition-fragmentation chain transfer agent and polymerisation of methyl methacrylate, yielding a PMMA-chain equipped with a maleimide, which is able to undergo [2+3] cycloaddition with highly reactant nitrile imines.

First, a condensation reaction of furan-protected maleic anhydride and 2-aminoethanol yielded the corresponding *N*-(2-hydroxy)ethyl maleimide, which was subsequently transformed into the RAFT agent (chain transfer agent, CTA) through esterification. Following purification by column chromatography, the CTA was employed for RAFT polymerisation of methyl methacrylate (MMA). Since the kinetics of end-group reactions are chain-length dependent,²³⁸ a medium molecular weight was targeted, that allowed for facilitated work-up and precipitation. Following polymerisation, a range of post-polymerisation modification reactions were conducted. The ω -terminal dithiocarbonyl group which is intrinsically integrated during the polymerisation constitutes a competing, highly coloured chromophore that is inclined to undergo side reactions. For this reason, it was transformed into a peroxide group and subsequently reduced to a hydroxy group, using triphenylphosphine.²³⁹ Finally, the maleimide was deprotected by heating and stirring in toluene. For detailed descriptions of all reaction steps, refer to chapters **8.7.2.1** to **8.7.2.5**. The final polymer, bearing a maleimide and a hydroxy end-group, was subjected to size-exclusion chromatography, to determine the molecular weight distribution and the number average of the molecular weight ($M_n = 4.7$ kDa (SEC), $M_n = 5.2$ kDa ($^1\text{H-NMR}$), $D = 1.15$). Furthermore, size-exclusion-chromatography coupled with electrospray-ionisation mass spectrometry (SEC-ESI-MS) and $^1\text{H-NMR}$ were employed to confirm end-group fidelity (refer to **Figure 26**).

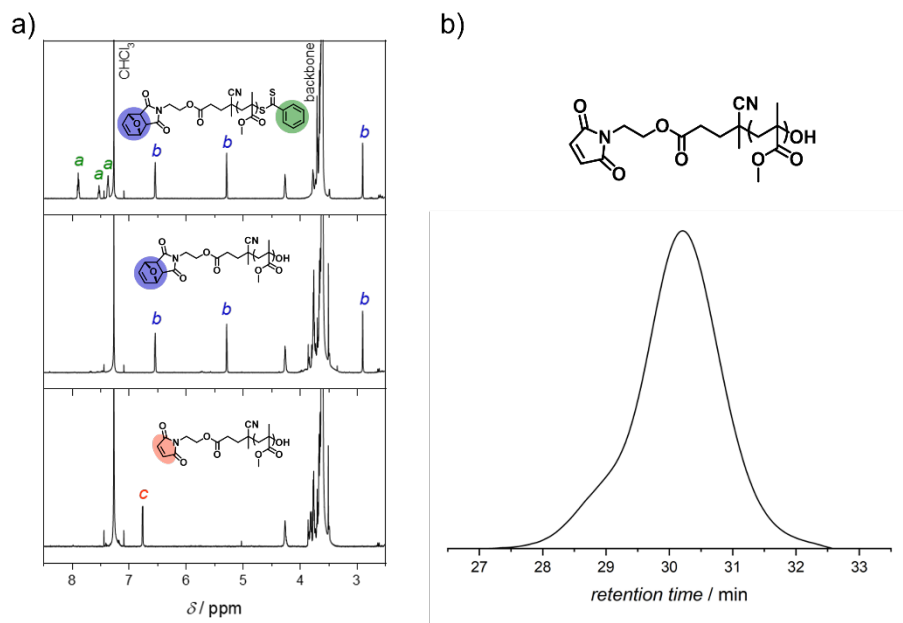


Figure 26: a) Tracking of the end-group fidelity through three steps of ω -hydroxy-PMMA-maleimide, showing clean removal of the benzodithio benzoyl group, followed by complete cleavage of the furan protection group. b) Structure and SEC trace in dimethylacetamide (DMAc) of the final polymer. $M_n = 4.7$ kDa, $D = 1.15$.

3.3 Steady-State Spectroscopy

In the following section, steady-state UV/Vis and fluorescence spectroscopy of APAT are presented and analysed. Spectra were recorded at varying substance concentrations, in various solvents and at different pH-values. Emphasis is laid on determining exact absorption coefficients, whose role in photoreactions is critical, since they determine the number of photons absorbed, as well as the penetration depth of the incident light.

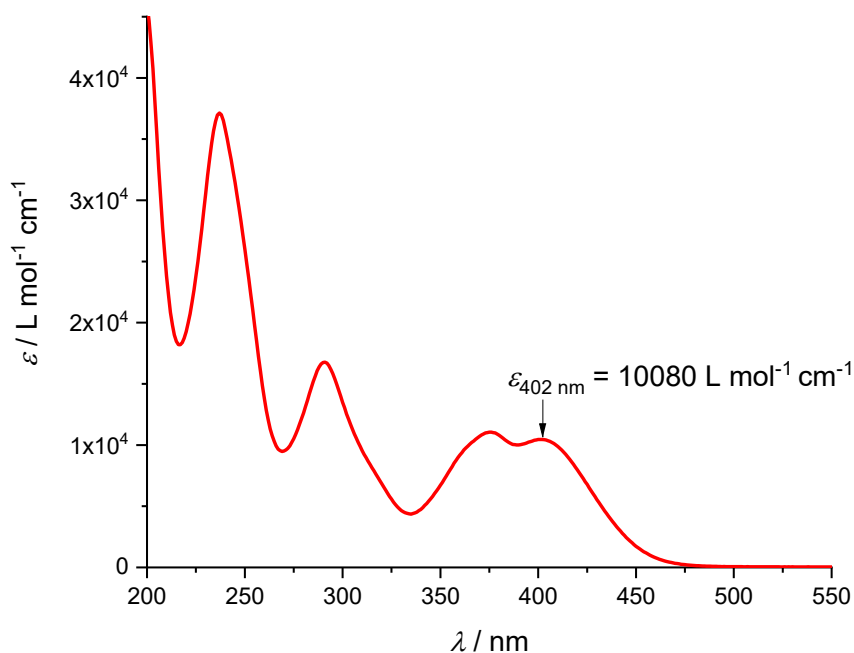


Figure 27: Full absorption spectrum of APAT in MeCN, measured at $c = 13.8 \mu\text{M}$ in a 1 cm cuvette at ambient temperature.

First, absorption was measured in acetonitrile at various concentrations, to obtain absorption coefficients through linear fitting (for full fitted data, refer to 10.2). In **Figure 27**, the full absorption spectrum is shown, displaying a distinctively shaped broad absorption band in the UV-A and visible light region, as well as a series of narrower absorption bands at shorter wavelengths. The broad, long-wavelength absorption band features two local maxima at 375 nm ($\epsilon = 10\,660 \text{ L mol}^{-1} \text{ cm}^{-1}$) and 402 nm ($\epsilon = 10\,080 \text{ L mol}^{-1} \text{ cm}^{-1}$), respectively. At wavelengths longer than 400 nm, absorbance slowly tails until $\sim 500 \text{ nm}$. On the short wavelength side of the band, a scarcely pronounced shoulder at $\sim 360 \text{ nm}$ is visible. The short-wavelength absorption bands at 237 nm and 291 nm have higher absorption coefficients ($35\,800 \text{ L mol}^{-1} \text{ cm}^{-1}$ and $16\,170 \text{ L mol}^{-1} \text{ cm}^{-1}$, respectively) and are rather featureless, the latter exhibiting only

an indistinct shoulder at ~315 nm. No quantum chemical calculations were conducted in this thesis, but in order to assign the absorption bands to electronic transitions, the spectrum can be compared to that of a literature-known pyrene aryl tetrazole (PAT, which lacks the dimethylamino group).⁷³ The results of that study indicated that the long-wavelength absorption band of PAT (at ~343 nm) can be attributed to a HOMO-LUMO transition into low-lying electronic singlet states, with $S_1 - S_2$ being the dominant transition. In non-substituted pyrene derivatives, this transition is usually accompanied by several prominent vibronic transitions. Broadening and red-shifting of these features indicate an intramolecular charge-transfer (ICT) character of the S_1 state.²⁴⁰ For APAT, a significantly red-shifted second absorption band is observed, overlapping with the shorter-wavelength band. The electron-withdrawing nature of the tetrazole functionality,³⁷ as well as the electron-pushing nature of the dimethylamino auxochrome are expected to act as a donor-acceptor system.⁶⁵

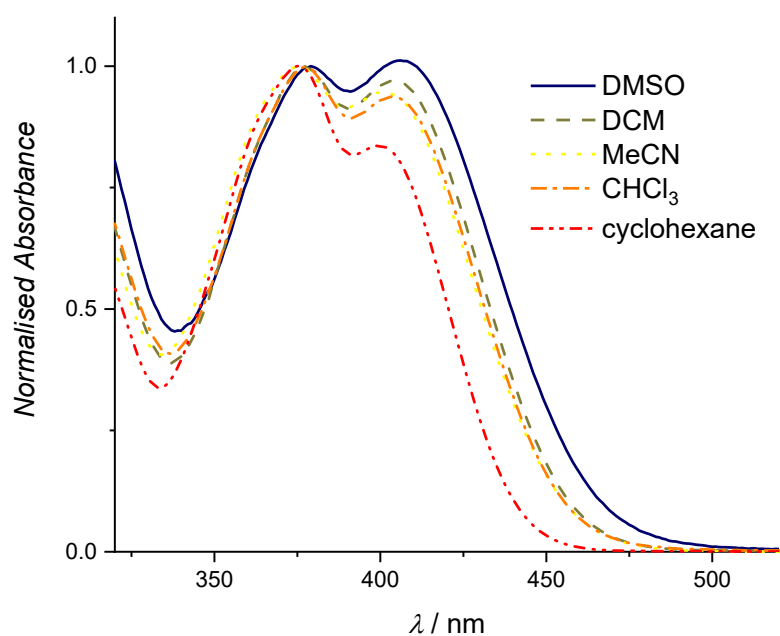


Figure 28: Normalised absorption spectra in dimethylsulfoxide (DMSO), dichloromethane (DCM), acetonitrile (MeCN), chloroform and cyclohexane. The spectra were normalised to the absorption peak at 375 nm. All spectra were recorded at ambient temperature in 1 cm cuvettes.

Hence, absorption spectra were recorded in several solvents of different polarity, revealing a significant solvent-dependence of the relative intensity of the most red-shifted band (402 nm). In **Figure 28**, the red-shifted absorption band is displayed for DMSO, DCM, MeCN, chloroform and cyclohexane. All spectra were normalised to the absorption maximum at 375 nm), emphasising the change in relative intensity of the longer-wavelength band. Clearly, the absorption band at 402 nm is most dominant in DMSO, surpassing the 375 nm absorption

band in intensity, stretching well beyond 500 nm. Following the decreasing solvent polarity, the intensity and broadness of the right band is lowered. When APAT was dissolved in cyclohexane, no absorbance could be detected beyond 475 nm. These findings strongly indicate that an ICT state is the reason for the red-shifted absorption of APAT. An excited ICT state is more polar than the ground state. In polar solvents, it is stabilised, thus decreasing the energy gap between S_0 and the ICT state, leading to red-shifted spectral properties.²⁴¹ This is especially the case in the fluorescence spectra of APAT, where a strong red-shift of emission was observed when transitioning to more polar solvents.

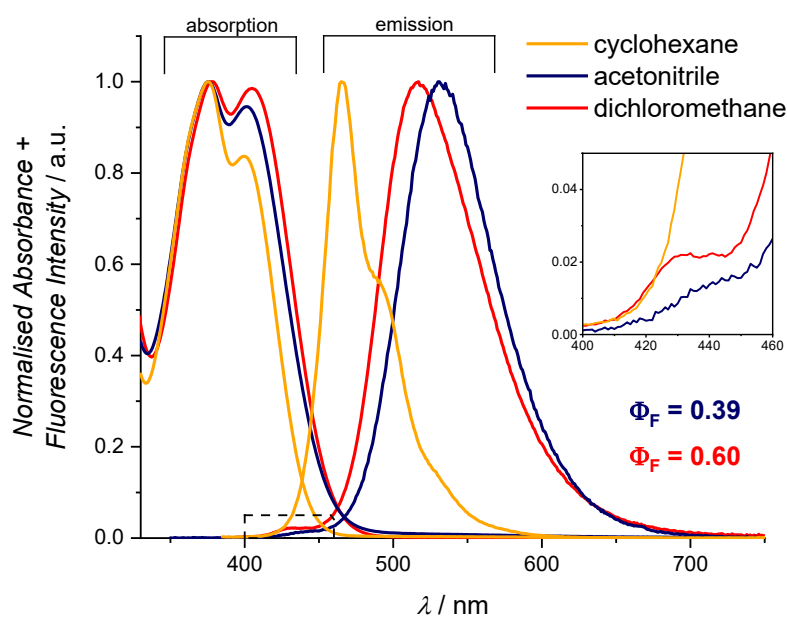


Figure 29: Absorption and emission spectra of APAT in cyclohexane, DCM and MeCN. Spectra were recorded in 1 cm quartz cuvettes and 1 cm fluorescence cuvettes at ambient temperature. $\lambda_{ex.} = 390$ nm. Φ_F = fluorescence quantum yield in MeCN (blue) and DCM (red).

In **Figure 29** the normalised absorption and emission spectra of APAT in cyclohexane, MeCN and DCM are shown. The cyclohexane emission band peaks at 465 nm, but also displays an additional emission band at ~ 490 nm, and a weak emission band at ~ 530 nm. Multimodal emission can indicate dimer or excimer formation, which is also supported by the low solubility of APAT in cyclohexane.²⁴²⁻²⁴⁴ The emission spectra in DCM and MeCN show strong bathochromic shifts, peaking at 517 nm (APAT in DCM) and 531 nm (APAT in MeCN). Both emission bands are featureless and broad. Interestingly, both spectra display a weak emission band in the shorter-wavelength region at ~ 430 nm (**Figure 29**, inset), potentially suggesting the presence of a locally excited (LE) state.²⁴⁵ To quantify the fluorescence quantum yield, emission spectra of APAT were measured in MeCN and DCM and compared to a fluorescence

standard (coumarin 307) in ethanol. The fluorescence quantum yield is 39 % in MeCN, and 60 % in DCM. These observations solidify the assumption that APAT, upon excitation, enters a highly fluorescent ICT state with high fluorescence quantum yield. Yet, a significant portion of photons may lead to other events (i.e., intersystem crossing (ISC) into a triplet state), as the excited state dynamic of APAT are not yet fully revealed.

On a side note, APAT displays an interesting feature when acid is added to a solution of APAT in MeCN. The absorbance promptly shifts towards the UV regime, rendering the solution colourless (**Figure S 35**). The recorded absorption spectrum displays remarkable resemblance with the unsubstituted PAT. The dimethylamino group can act as a base, thus being protonated by a sufficiently strong acid. While the lone electron pair under neutral conditions contributes to the electron density of the aromatic system, this is no longer the case when the amino group is protonated. The push-pull effect is therefore eliminated, and the bathochromic effect nullified. By adding a base such as triethylamine the process is fully reversed, restoring the initial absorption spectrum.

3.4 Wavelength-Dependent Small-Molecule Ligation

After successful synthesis and thorough characterisation of APAT, wavelength-dependent reactivity was investigated. The aim was to detect the most effective irradiation wavelength, that is, the wavelength that leads to highest conversion upon irradiation with a given number of photons. Plotting the conversion *versus* the wavelength is called *action* plot. This method was pioneered by our group, using a *ns*-pulsed laser system to trigger photoreaction at specific wavelengths, i.e., oxime ester photoinitiators,¹⁸⁷ *o*-methyl benzaldehydes,¹¹³ or pyreneacyl sulfides.¹⁷⁷ The energy output of the laser is adjusted so that emission of a constant number of photons is ensured in every irradiation experiment. Another goal was to determine the most red-shifted wavelength that still leads to conversion. To do so, an analysing method had to be established that allowed for reliable and precise quantification of the photoreaction products. The synthesis of APAT required multiple reaction steps, which involve separation of isomers as well as a notoriously low-yielding final step (refer to 8.7.1). ¹H-NMR spectroscopy was not a favourable option for analysing a large number of experiments, given the lack of sensitivity and high demand of sample material. Consequently, high performance-liquid chromatography coupled with a high-resolution mass spectrometer was chosen as analysing method. Liquid chromatography (LC) allows for separating the different products present in a reaction mixture and quantifying them *via* a UV detector. Moreover, it is possible to scan at different wavelengths and even obtain a qualitative absorption spectrum thanks to a photodiode array (PDA), offering valuable insight into all the reaction products. Additionally, the connected mass spectrometer is a powerful tool for identifying the relevant species. To convert the integrated chromatogram peaks into a product yield, different absorption coefficients at the scan wavelength must be taken into account. The yield C_{CA} is then calculated according to equation (3 – 1).

$$C_{CA} = \frac{\frac{I_{CA}}{\varepsilon_{CA}}}{\frac{I_{CA}}{\varepsilon_{CA}} + \frac{I_{SM}}{\varepsilon_{SM}}} \quad (3 - 1)$$

Herein, I_{CA} is the peak integral of the cycloadduct, I_{SM} is the peak integral of the starting material (APAT), and ε_{CA} and ε_{SM} are the molar decadic absorption coefficients at the scan wavelength of the UV detector. As per the sample preparation specifications of the employed LC instrument, samples had to be prepared in MeCN at a maximum concentration of 0.5 mg

mL⁻¹. To minimise the number of parameters that could influence the LC results, it was opted to prepare the sample solutions for the photoreactions according to the LC requirements, avoiding alternation or modification of the samples between photoreaction and analysis. This way, the reaction mixtures after irradiation could simply be filtered into the LC sample vials.

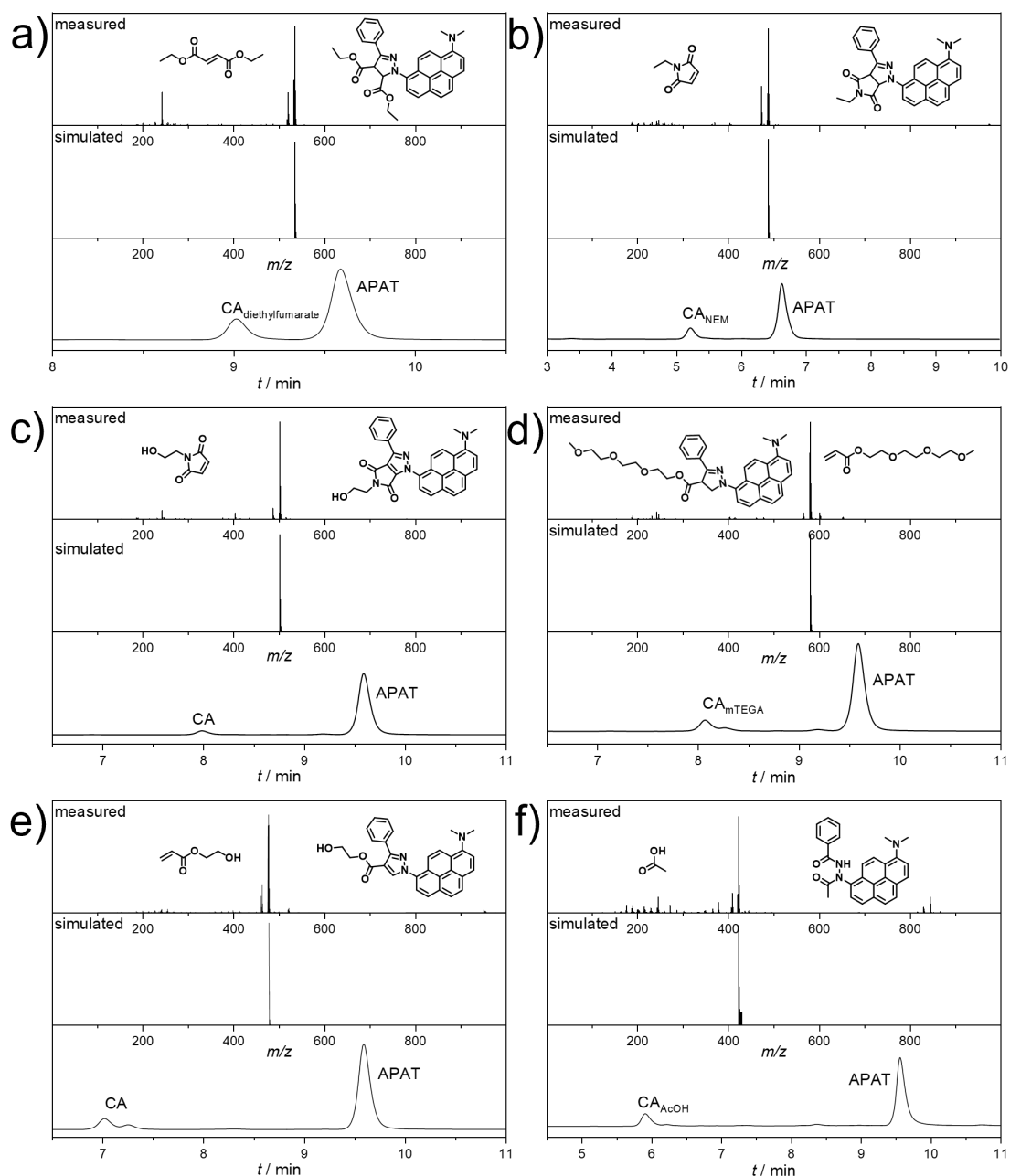


Figure 30: LC-MS analysis of NITEC and NICAL (nitrile imine-carboxylic acid ligation) reactions of APAT with various electron deficient double bonds, as well as acetic acid. The schemes show the dipolarophile and the respective product after cycloaddition with APAT. Where head-to-head and head-to-tail conformations occur, only one is depicted in the scheme for reasons of clarity. The measured mass spectra are the integrated total ion count (TIC) over the cycloadduct peak. a) Diethylfumarate. b) N-ethylmaleimide. c) N-(2-hydroxy ethyl) maleimide. d) 2-(2-(2-methoxyethoxy)ethoxy)ethyl acrylate. e) 2-hydroxyethyl acrylate. f) Acetic acid.

To explore the substrate scope of the nitrile imine-mediated tetrazole-ene cycloaddition (NITEC) photoreaction of APAT, and to determine the reaction partner best suited for the wavelength-dependent small-molecule model ligation reaction, experiments were conducted using different dipolarophiles and nucleophiles. Experiments were carried out for 15 min at 460 nm in MeCN, at an APAT concentration of 0.46 mM, with a 4-fold excess (1.84 mM) of the respective dienophile. The sample solutions after irradiation were analysed by LC-MS (scan wavelength $\lambda_{\text{scan}} = 392$ nm) and the product composition, conversion, and peak separation on the column were evaluated. In addition to a range of common electron-deficient enes such as diethylfumarate (DEF, **Figure 30a**), *N*-ethyl-maleimide (NEM, **Figure 30b**) and *N*-(2-hydroxy)ethylmaleimide (NHEM, **Figure 30c**), two acrylic acid ester derivatives were selected (2-(2-(2-methoxyethoxy)ethoxy)ethyl acrylate, mTEGA, and 2-hydroxyethyl acrylate, HEA, refer to **Figure 30d** and **Figure 30e**).²⁴⁶ Furthermore, acetic acid was tested as a reaction partner for nitrile imine-carboxylic acid ligation (NICAL, refer to **Figure 30f**).^{82, 247} Note that for these reactions, the molar absorption coefficients were not determined for all species. The measure of reaction progress is therefore the relative peak integral ratio, rather than the conversion. NITEC of APAT with DEF after 15 min of irradiation led to clean formation of the cycloadduct CA_{DEF}, with a relative peak integral ratio of 22 %. Formation of the cycloadduct is confirmed *via* mass spectrometry. Two similar isotopic patterns are observed with a mass difference of $\Delta m/z = 2.0141$, indicating loss of H₂. This is related to rearomatization of the pyrazoline cycloadduct (refer to the introductory chapter (2.2.2)). From the total ion count alone, it is hard to quantify the extent to which rearomatization occurred. However, the chromatogram indicates that one species is predominant, given the symmetry of the chromatogram peak and the uniformity of the PDA signal. When NEM and NHEM were used as dipolarophiles, good peak separation was observed in both cases. Unlike DEF, the mass spectra of both experiments show exclusively the rearomatized pyrazole adduct. However, the overall conversion was lower, with relative peak integral ratios of 17 % (NEM) and 6 % (NHEM). Cycloaddition of APAT and mTEGA, as well as APAT and HEA, was confirmed in both cases, with excellent peak separation on the column. Yet, two product peaks appear in the chromatogram, corresponding to the pyrazoline product and the pyrazole product. It is also noted that acrylates possess asymmetrically substituted double bonds, possibly leading to formation of head-to-head or head-to-tail cycloadducts. These regioisomers cannot be distinguished by mass spectrometry may display disparate retention times on the column due to different polarity. Cycloaddition with mTEGA led to a peak integral ratio of 14 %, while HEA yielded 16 %. Furthermore, successful NICAL reaction between APAT and acetic acid was also

confirmed, yielding 16 % average peak ratio. In conclusion, clean reactions of APAT with a range of substrates was demonstrated.

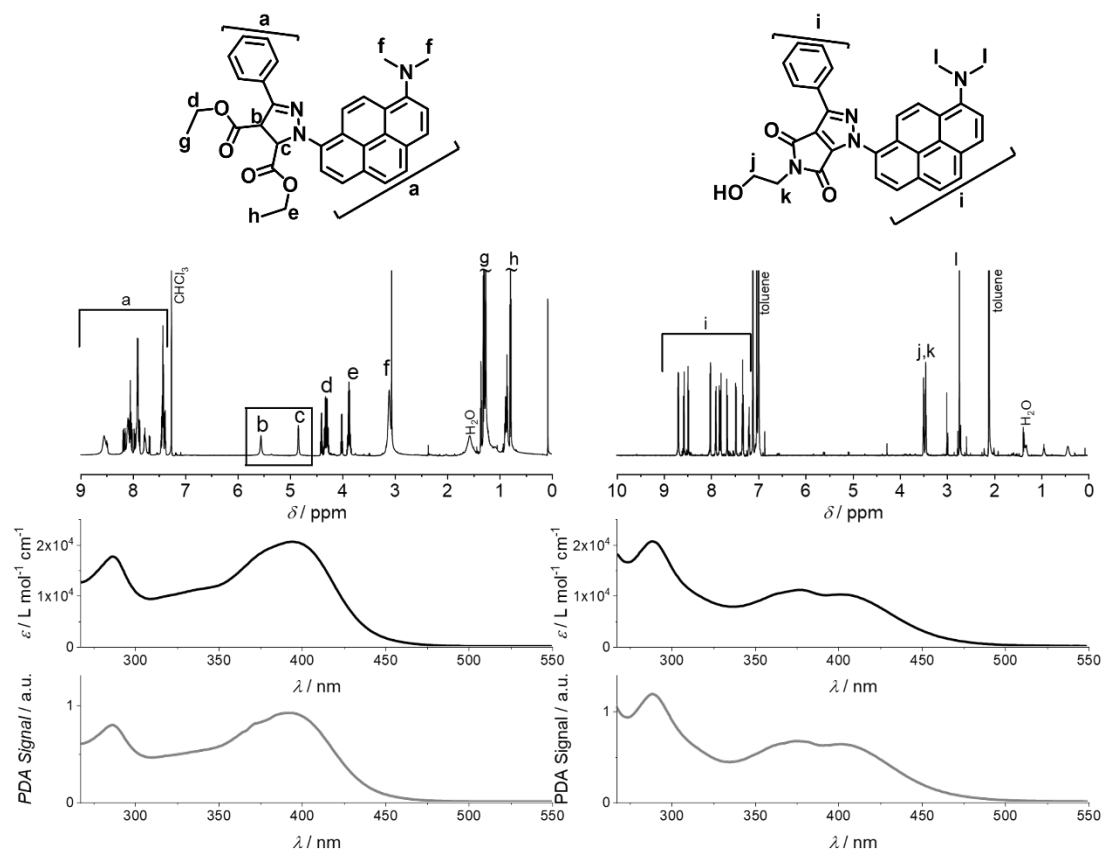
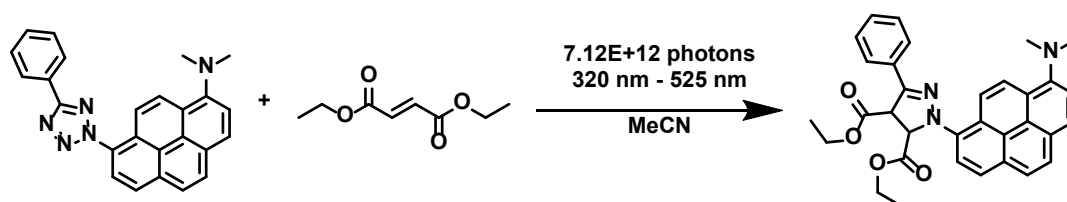


Figure 31: Analysis of two isolated cycloadducts after NITEC reaction of APAT, CA_{DEF} and CA_{NHEM} . Left side, from top to bottom: 1H -NMR spectrum of CA_{DEF} in $CDCl_3$ (pyrazoline signals are shown in the box), absorption spectrum ($c = 26.2 \mu\text{mol}$ in MeCN), and PDA signal from the LC-MS. Right side, from top to bottom: 1H -NMR spectrum of CA_{NHEM} in toluene- d_8 , absorption spectrum ($c = 12.3 \mu\text{mol}$ in MeCN), and PDA signal of the LC-MS.

To identify the nature of the cycloadducts CA_{DEF} and CA_{NHEM} (pyrazoline *vs* pyrazole), the reactions were repeated in larger batches and the reaction products isolated (for the exact procedures, refer to 8.4.3). The 1H -NMR spectrum of CA_{DEF} in **Figure 31** shows two signals related to the pyrazoline protons, and minor amounts of rearomatized cycloadduct. The low degree of rearomatization, as well as the presence of two sets of product peaks, indicate formation of two diastereomers (4*S*-5*R* and 4*R*-5*S* diastereomer), due to the *trans*-substitution of the fumarate. The corresponding absorption spectrum in MeCN largely differs from the APAT spectrum, in that the absorption band has only one maximum at 392 nm. This is in agreement with the PDA signal of the LC-MS. Hence, it was concluded that the pyrazoline species is formed during the photoreaction. On the other hand, in the 1H -NMR spectrum of CA_{NHEM} , pyrazoline signals are absent, indicating full rearomatization of the cycloadduct.

Rearomatization is probably facilitated for of the formed diastereomers (4*S*-5*S* and 4*R*-5*R*) due to the *cis*-substitution of the maleimide. Correspondingly, the absorption spectrum of CA_{NHEM} in MeCN largely resembles that of APAT. This resemblance is attributed to the aromatic pyrazole being structurally akin to the tetrazole, while the non-aromatic pyrazoline ring of CA_{DEF} significantly alters the electronic structure of the chromophore.²⁴⁸ The PDA signal of CA_{NHEM} is shaped similarly to the absorption spectrum of the isolated compound. Conclusively, photoreaction between APAT and NHEM leads to generation of the rearomatized pyrazole adduct.



Scheme 11: NITEC between APAT and DEF. DEF was added in a 4-fold excess, and reactions were carried out in degassed MeCN, and irradiated at wavelengths between 320 nm and 525 nm.

After considering the results of the series of experiments, ultimately, DEF was chosen as ligation partner for the wavelength-dependent model reaction. The main advantages are sufficient peak separation on the column, formation of a single product (pyrazoline cycloadduct), and the highest relative peak integral ratio out of all the tested substrates (i.e., ~3.5 times higher than NITEC of APAT and NHEM). With the developed analytical method at hand, photoreactions were conducted with the same setup, employing wavelengths between 320 nm and 525 nm in steps of 5 nm, 10 nm, or 20 nm. Each experiment was repeated three times, to obtain error bars. At each wavelength, the energy output of the laser was adjusted with the aid of an attenuator, ensuring a constant number of emitted photons (7.12×10^{19} photons per 15 min of irradiation). However, adjustments had to be made in the UV region at 400 nm and below. As a result of sum-frequency generation (SFG, refer to introductory chapter 2.5.2.2) the output power of the laser is significantly lower in this wavelength range. Since the required number of photons could not be provided within 15 min, irradiation time had to be adjusted accordingly. After each photoreaction, the samples were submitted to LC-MS, the reaction yield was determined using formula (3 – 1), and the average yield for every wavelength was plotted *versus* wavelength. The obtained action plot is presented in **Figure 32**.

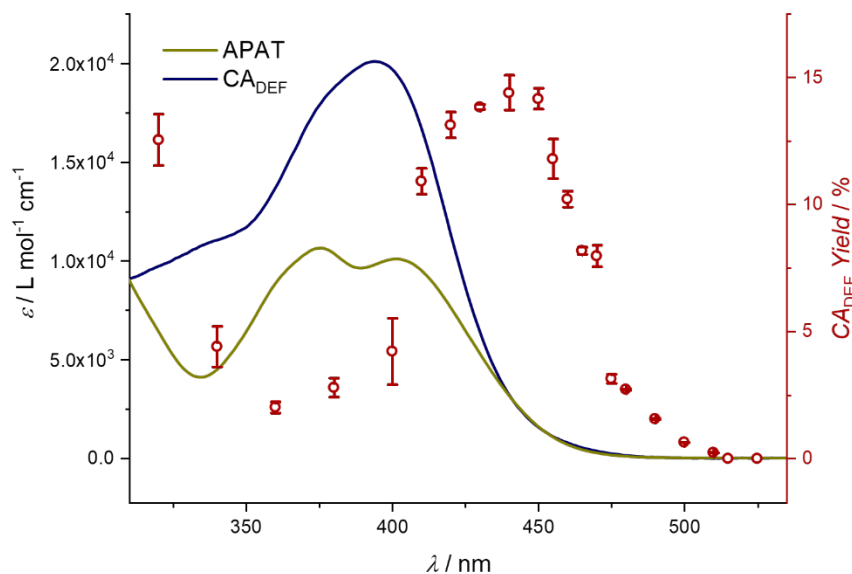


Figure 32: Overlay of the absorption spectra of APAT (460 μM in MeCN) and CA_{DEF} (40 μM in MeCN) (left y -axis) and the wavelength-dependent reactivity profile (action plot) of the photoinduced NITEC reaction between APAT and DEF (right y -axis). All experiments were conducted in MeCN and repeated two or three times to obtain error bars. For a detailed description of the laser setup, data processing and conditions of all action plot experiments, refer to 8.3.1.

It becomes obvious that the wavelength-dependent reactivity does not follow the absorption profile of APAT, but instead behaves rather counter-intuitive. The reactivity minimum at 360 nm (2 % yield) is shifted by 25 nm compared to the absorption minimum (335 nm). While the absorption spectrum shows two local maxima in the probed wavelength range (376 nm and 402 nm), only one broad reactivity curve is observed, peaking between 430 and 450 nm. Beyond 450 nm, the reactivity gradually decreases. At 500 nm, merely 0.6 % yield are recorded, dropping to 0.2 % at 510 nm (refer to **Figure S 39**). No formation of cycloadduct was observed at wavelengths 515 nm and beyond. To test the limits of the red-shifted reactivity, the experiments at 510 nm and 515 nm were repeated once, with a 25-fold increased number of photons, yielding 3 % and 0.6 % of CA_{DEF} , respectively. It is thus demonstrated that – although significantly less efficient than with blue light – green light is still sufficient to activate the tetrazole. To date, this is the most red-shifted wavelength employed to trigger photo-induced NITEC.

While the chemical behaviour in the visible light regime is of key interest, APAT demonstrates very intriguing properties in the UV as well. Whereas reactivity plummets in the region between 340 nm and 400 nm (2.0 – 4.4 %), it increases again at shorter wavelengths (320 nm),

almost reaching peak reactivity (12.5 %). This behaviour is unprecedented in the literature reporting action plots.^{113, 137, 177, 187, 249} Interestingly, the local absorption maximum $\lambda_{\text{max}} = 375$ nm falls within the reactivity dip. The reason for this non-congruence is not fully understood, but the lowered reactivity may be attributed to mainly three factors that likely contribute to different degrees:

- Lower penetration depth due to high absorbance of the photoactive compound.¹¹³ At a concentration of 0.46 mM, the absorption band of APAT ($\epsilon \approx 10^4$ L mol⁻¹ cm⁻¹) has an optical density of ~ 4.6 per centimetre of pathlength, meaning that more than 65 % of photons are absorbed within entering the first millimetre of the sample solution, as per Beer-Lambert's law. More than 99.99 % of photons are absorbed within one centimetre (total pathlength of the sample.) At more red-shifted wavelengths, APAT has a lower molar absorption coefficient, increasing the penetration depth and the number of photons available for absorption throughout the reaction volume. For instance, at 437 nm, roughly 1 % of photons is transmitted through the sample without leading to an excitation event. With longer wavelengths, this percentage gradually increases, until almost all photons pass through the sample without being absorbed. This correlates with the gradual decrease of reaction yield in the action plot, after the peak between 430 nm and 450 nm. It is plausible that a trade-off between sufficient penetration depth and a small enough fraction of transmitted photons is found in this wavelength region.
- Competing absorption of the formed cycloadduct. CA_{DEF} displays a broad absorption band that roughly coincides with the low-reactivity region between 340 and 400 nm.¹⁵⁸ This effect is more significant in later stages of the experiment, where most of APAT has already reacted and CA_{DEF} absorbs most of the photons. Consequently, the chance for excitation events that lead to photoreaction is lowered. To minimise this effect, the reactions were driven to low conversions, where competing absorption is negligible. Nevertheless, it was shown that high yield is possible by running an experiment with prolonged irradiation time at 465 nm (refer to section **8.4.4**). A CA_{DEF} yield of 89 % could be reached after a substantially increased number of photons (**Figure S 40**)
- Differences in the excited state dynamics of the populated excited states. Generally, the excited state manifold of APAT is largely unknown. The 375 nm absorption band may not lead to efficient population of the excited states necessary for photoreaction, but rather follow different relaxation pathways.⁷³

Displaying a dip in reactivity, APAT is a promising candidate for λ -orthogonal reaction systems. Red-shifted reactivity is not the only prerequisite, but also lack of reactivity in the shorter wavelength regions. However, the fact that reactivity is recovered at 320 nm underlines the importance of sufficiently resolved wavelength-dependent reactivity studies.

Besides displaying an increase of reactivity in the further UV region, the photoreaction of APAT shows another highly interesting anomaly. In literature, NITEC reactions are often praised for their fluorogenic nature, that is, the starting material is non-fluorescent, whereas the cycloadduct strongly emits in the visible light regime.^{90, 104, 250} NITEC reactions are therefore considered self-reporting, making it easy to track the reaction progress even with the naked eye. By contrast, APAT itself is a relatively strong fluorophore, with a fluorescence quantum yield of 39 % in MeCN (see chapter 3.3). On the other hand, the resulting cycloadduct is almost non-fluorescent, making this reaction the first example of a reverse self-reporting NITEC system, where fluorescence is switched off during the course of the reaction. **Figure 33** shows the visible drop in fluorescence intensity after 30 min irradiation with a 450 nm LED.

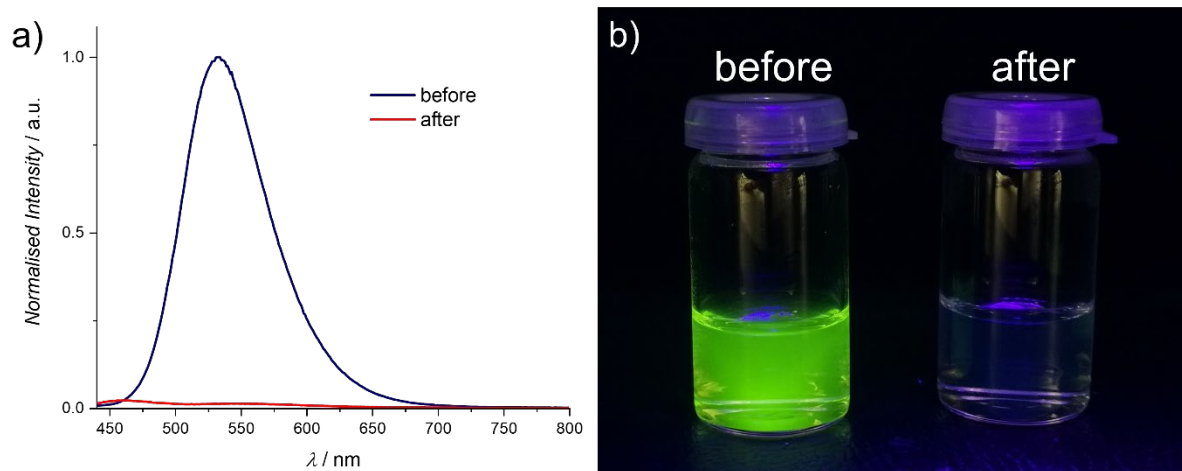


Figure 33: a) Fluorescence spectra before and after 30 min irradiation with a 450 nm LED. Spectra were recorded in MeCN and show a drop in fluorescence intensity by a factor of ~ 100 . b) Photograph of samples before and after irradiation under UV light.

3.5 Green-Light Induced Functionalisation of Polymer End-Groups

Once a detailed map of the wavelength-dependent reactivity of APAT was established, steps were taken towards a proof-of-concept experiment for polymer end-group functionalisation. Employing a poly(methyl)methacrylate-based polymer (refer to 3.2.2), bearing a maleimide moiety as an end-group, polymer end-group functionalisation was tested with three different LEDs. Polymer end-group modification and ligation reactions are important tools for building hierarchical structures or forming networks (refer to introductory chapter 2.2.2.3), and LEDs are a widely accessible and convenient irradiation source to do so.

To quantify the degree of conversion, an analysing method had, once again, to be established. Liquid chromatography-mass spectrometry cannot be applied for analysing polymers. The analogous method of size exclusion chromatography-mass spectrometry, however, is not suited to quantify the reaction progress. It was therefore reasoned that NMR-spectroscopy is the most appropriate method since introduction of several aromatic signals (stemming from the APAT chromophore) could be easily tracked. To ensure sufficient conversion of the polymer end-group, APAT was employed in a 4-fold excess. Reactions were carried out in degassed 15 mL crimp vials, with three LEDs ranging from 452 nm to 515 nm (Figure 34).

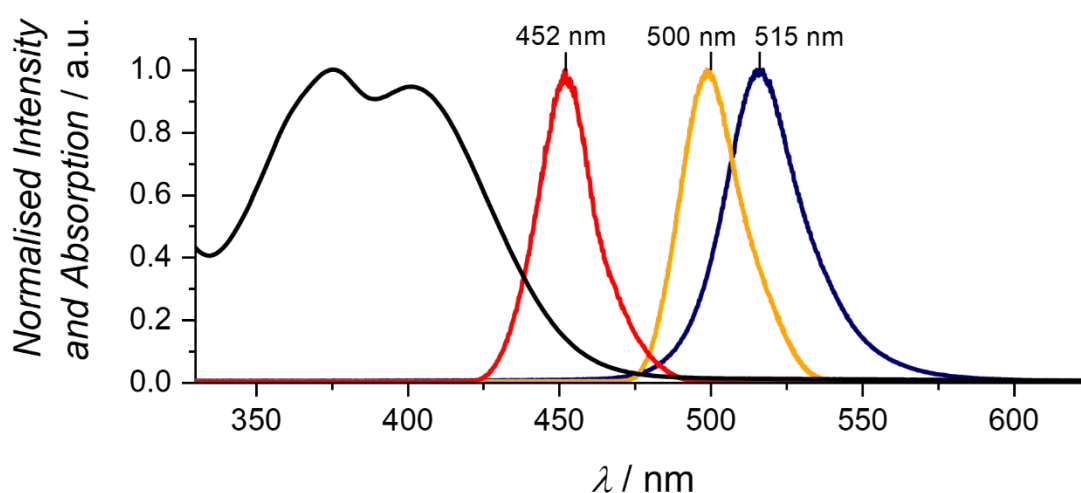


Figure 34: Overlaid APAT absorption spectrum and emission spectra of the LEDs employed for polymer-end-group modification.

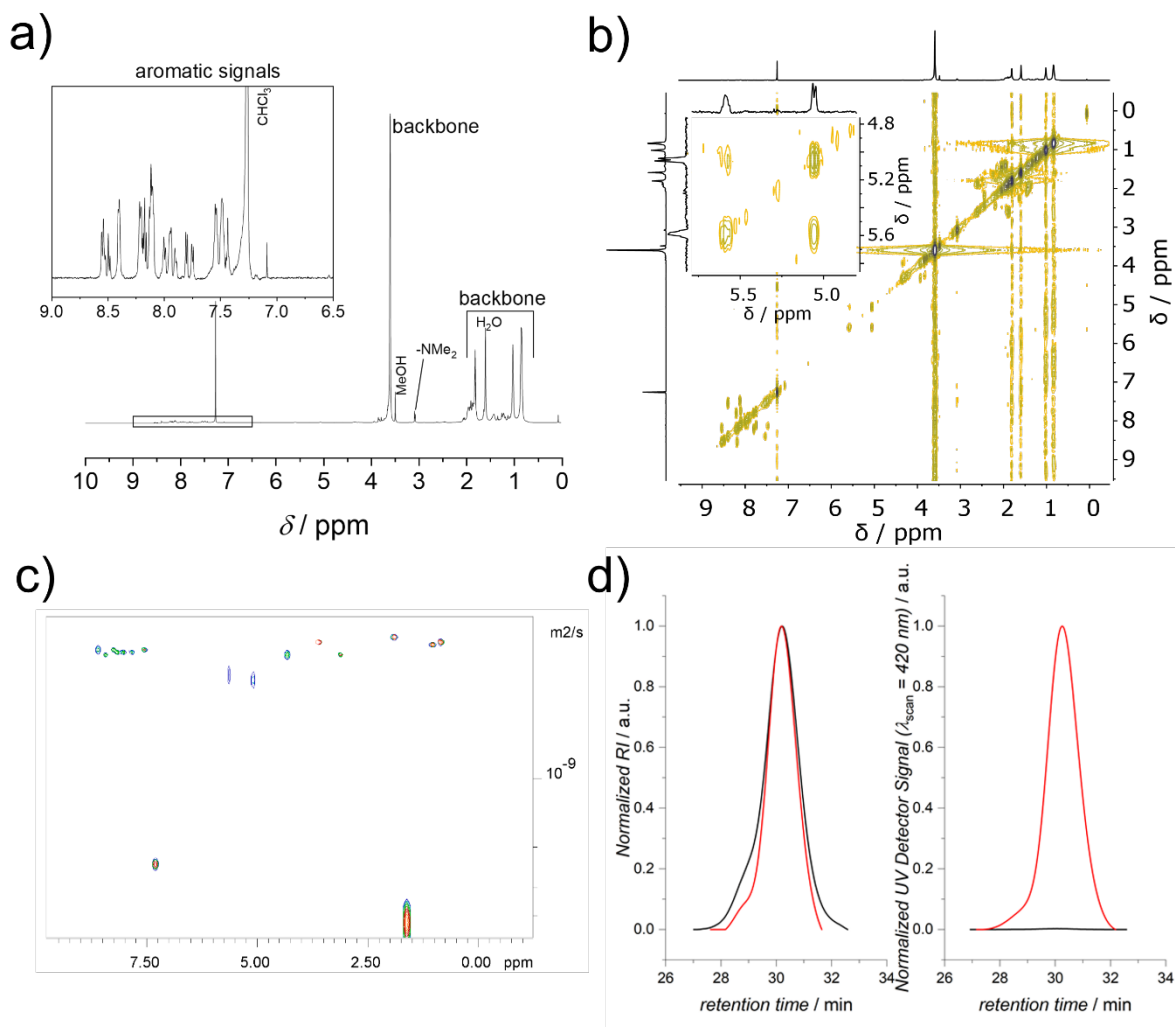


Figure 35: Analysis of products after irradiation at 500 nm for 48 h and preparative SEC. a) $^1\text{H-NMR}$ spectrum with zoomed inlet into the aromatic region. Absence of the vinylic signal at $\delta = 6.75$ ppm indicates full conversion of the PMMA-maleimide. b) COSY measurement, confirming that the two signals at $\delta = 5.06$ ppm and $\delta = 5.59$ ppm correspond to the two adjacent pyrazoline protons. c) DOSY measurement, confirming that all relevant signals are attributed to protons attached to a polymer chain. d) SEC traces **before** and **after** irradiation. Left graph: RI trace displays a slight shift to lower retention times, corresponding to higher molecular weight (**before**: $M_n = 4.7$ kDa, $\mathcal{D} = 1.16$, **after**: $M_n = 4.8$ kDa, $\mathcal{D} = 1.09$). Right graph: UV-Vis scan at 420 nm shows no signal before the reaction. After ligation and formation of $\text{CA}_{\text{PMMA-Mal}}$ the shape of the UV-Vis trace follows the RI trace, confirming successful tethering of the chromophore.

To account for different power outputs of the employed LEDs, the irradiation time was adjusted accordingly (for a detailed description of the LED setup, refer to section 8.3.2). A fourth experiment with prolonged irradiation time was carried out with the 500 nm LED, exploring the possibility to drive the reaction to full conversion with green light. Upon completion of each experiment, the reaction mixture was subjected to preparative size exclusion chromatography, separating the polymeric fraction from any possible remaining

APAT. The polymeric fraction was analysed by $^1\text{H-NMR}$ spectroscopy (**Figure 35a**), correlation spectroscopy (COSY, **Figure 35b**) and diffusion-ordered spectroscopy (DOSY, **Figure 35c**), confirming that the aromatic signals are attached to the polymer chain. Furthermore, the SEC trace before and after the reaction shows that the chromophore was attached to the polymer chain, indicated by a response of the UV/Vis detector at 420 nm (**Figure 35d**).

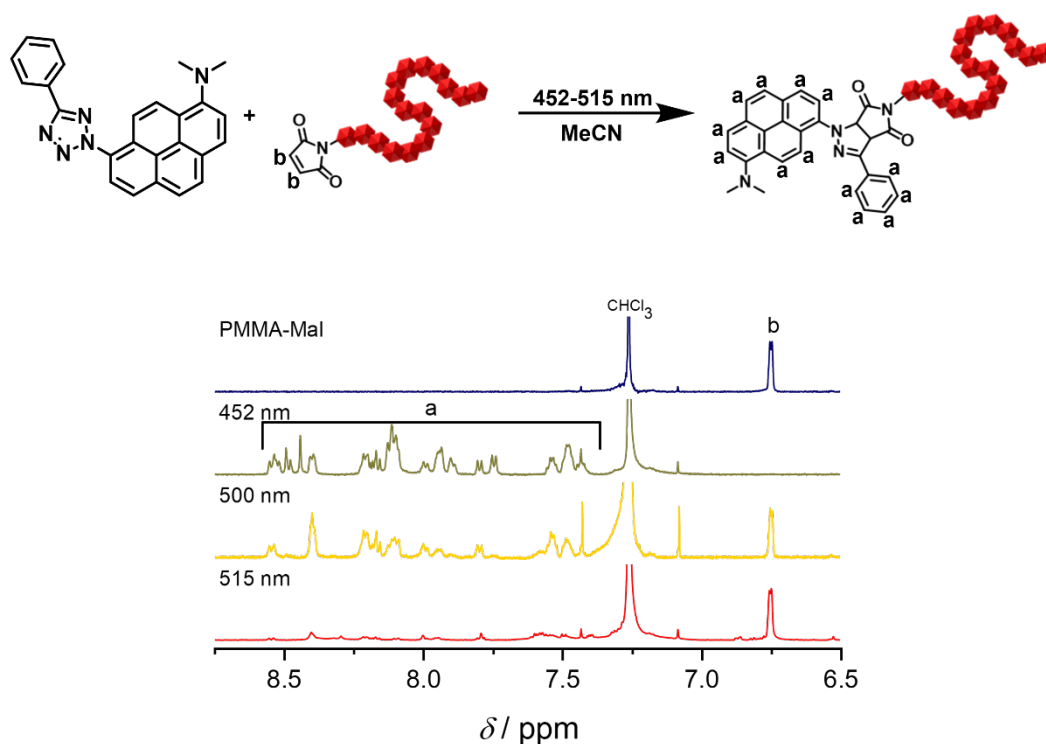


Figure 36: Polymer end-group modification and $^1\text{H-NMR}$ analysis. (a) Reaction scheme of the NITEC between a maleimide end-capped PMMA chain and APAT, forming the pyrazoline cycloadduct. (b) Zoom into the aromatic region of $^1\text{H-NMR}$ spectra of $\text{CA}_{\text{PMMA-Mal}}$ after polymer end-group modification. Reaction conversion was determined by comparing the resonance integrals of the aromatic protons ($a = 13 \text{ H}$) and remaining vinylic protons of the maleimide end-group ($b = 2 \text{ H}$). For reference, the spectrum of PMMA-Mal is depicted in blue.

Through integration of the aromatic signals, as well as the vinylic signals of the unreacted PMMA-maleimide, both species were quantified, and the reaction conversion was calculated (**Figure 36**). After 2.5 h of irradiation at 452 nm, the $^1\text{H-NMR}$ spectrum of the resulting polymer shows no remaining maleimide signals, indicating full conversion of the polymer end-group. The spectrum displays two signals at $\delta = 5.06 \text{ ppm}$ and $\delta = 5.59 \text{ ppm}$, corresponding to the pyrazoline protons (refer to **Figure S 7**). At 500 nm, irradiation was stopped after 3.7 h, to account for the different power output of the LED, as well as differences in the photon energy. The peak integral ratio in the $^1\text{H-NMR}$ spectrum indicates 50 %

conversion. Conveniently, the unreacted APAT could be recovered from the preparative SEC in high purity and can be subjected to further photoreactions if desired. Critically, repeating the same experiment with substantially longer irradiation times of 48 h yielded 100 % of modified polymer end-groups, despite only minimal overlap of the LED emission spectrum and the absorption spectrum of APAT. After irradiating at 515 nm for 4.3 h, the $^1\text{H-NMR}$ spectrum displays mere trace amounts of $\text{CA}_{\text{PMMA-Mal}}$, which could not be satisfactorily quantified, with the conversion being in the low single-digit percent range. These findings of the experiments are summarised in **Table 2**.

Table 2: Summarised results of polymer end-group modifications, employing different LEDs.

λ / nm	t / h	<i>Conversion / %</i>
452	2.5	100
500	3.7	50
	48	100
515	4.3	~1-2

The trends observed in these experiments agree with the small-molecule study presented in chapter 3.4. The reaction is most efficient around 450 nm, and lower conversion is achieved at more red-shifted wavelengths. Yet even a 500 nm LED led to full conversion of the end-group, upon irradiation for 48 h, proving that green light is sufficient to activate APAT.

3.6 Conclusion

Conclusively, in the present chapter, a new red-shifted tetrazole was synthesised and spectroscopically characterised. Employing synthetic rationale, this approach combined the red-shifting features of an extended aromatic pyrene chromophore with the electron-donating properties of a dimethylamino group (*N,N*-dimethyl aminopyrene aryl tetrazole, APAT). The resulting tetrazole shows unprecedented bathochromic absorption, accompanied by a strong solvent effect that is likely the result of an intramolecular charge-transfer state. Moreover, the molecule displays interesting halochromic characteristics. Successful NITEC was demonstrated between APAT and a range of different dipolarophiles, and successful NICAL was carried out with AcOH as a nucleophile. Importantly, during the photoreaction, fluorescence dropped significantly, demonstrating a self-reporting behaviour that diametrically opposes literature reports of other NITEC reactions.

The wavelength-dependent reactivity of APAT was evaluated in detail, by means of a small-molecule model reaction of APAT and diethylfumarate. Employing a set number of constant incident photons, the photoreaction was triggered at wavelengths between 320 nm and 525 nm, and the outcome analysed *via* LC-MS. The resulting action plot displayed features which are unprecedented in literature. After relatively high reactivity in the far UV (320 nm), the conversion plot drops significantly in the wavelength-range between 340 nm and 400 nm, and increases again in the visible range, reaching peak conversion between 430 nm and 450 nm. Beyond, the reactivity decreases again, but successful activation of APAT is confirmed up to 505 nm. To date, this is the most red-shifted tetrazole activated in a one-photon process. The existing toolset of visible light activated tetrazoles is thereby extended by a margin of almost 100 nm. The unique observation that the action plot has two maxima with a drop in reactivity in between emphasises the importance of wavelength-dependent studies when attempting to implement new chromophores.

With the detailed understanding of wavelength-dependent reactivity at hand, steps were taken towards applying APAT in polymer ligation chemistry. Employing a maleimide end-capped PMMA, NITEC reaction was triggered using spectrally broad, widely available blue and green light LEDs between 452 and 515 nm. Full conversion of the maleimide end-groups was observed up to 500 nm upon irradiation for a sufficiently long time. This is a promising

outlook for future applications of APAT, such as network formation, 3D lithography, or λ -orthogonal systems.

4 EXPLOITING DIFFERENT REACTION QUANTUM YIELDS TO ESTABLISH SEQUENCE-INDEPENDENT λ -ORTHOGONALITY

4.1 Objective

In the following chapter, a strategy for implementing sequence-independent λ -orthogonality is proposed. λ -Orthogonality is a feature of photochemical multi-component reactions, containing multiple photoreactive moieties alongside each other, each individually addressable with a different colour of light. The development of such multicomponent systems is necessary to pave the way for multicomponent resists for 3D laser lithography,²⁵¹ or complex macromolecular architectures.^{197, 198} A key advantage is the ability to not only target various chromophores individually, but to do so in a sequence-independent fashion. Applying different wavelengths of light in any order provides all the benefits of protection-group chemistry, such as orthogonality and modularity, while retaining the simplicity of a one-pot single-step reaction. Ideally, different reactions in a vessel are switched on and off merely by changing the colour of incident light.

However, establishing multicomponent systems that can be activated orthogonally poses several difficulties. Even red-shifted chromophores usually feature higher-energy absorption bands, overlapping with the bands of other components in the mixture. Thus, in most cases, simultaneous activation of multiple target species is unavoidable when irradiating in the spectral UV region. The spectral overlap therefore dictates the order in which different wavelengths are applied to a semi- λ -orthogonal system. The low-energy activated unit must be fully converted before the high-energy activated moiety is addressed – otherwise the applied shorter-wavelength light would at least partially trigger both reactions. General strategies to overcome this obstacle involve further separating the absorption bands of both species, demonstrated by a number of reports on λ -orthogonal photo-labile protection groups or photo-caged moieties.^{206, 252, 253} Still, there are few publications that deal with bond-forming photochemistry that can be utilised orthogonally and sequence-independently.^{199, 211}

Another problem is the non-congruence of the absorption profile and the wavelength-dependent reactivity of photo-active systems, which has been reported in literature multiple times.^{113, 137, 187} Likewise, (*N,N*-dimethyl)amino pyrene aryl tetrazole (APAT), which was introduced in the previous **chapter 3**, displays a significant red-shift of the reactivity maximum, compared to the absorption maximum. Doubtlessly, it is critical to rigorously assess the wavelength-dependent reactivity of all involved species, to be able to accurately select the optimal conditions for a λ -orthogonal system.

Overlapping absorption profiles, as well as overlapping reactivity profiles, are problematic when trying to address individual chromophores in a mixture. A third factor is, however, often overlooked when action plots are presented. Quantitative reaction quantum yields are rarely mentioned, making it hard to compare different action plots with regard to their potential in λ -orthogonal chemistry. Recently, *Menzel et al.* demonstrated the importance of quantum yields by introducing a binary reaction system, of which one component became inactive upon presence of water.²¹¹ The reaction quantum yield was therefore controlled by the solvent environment.

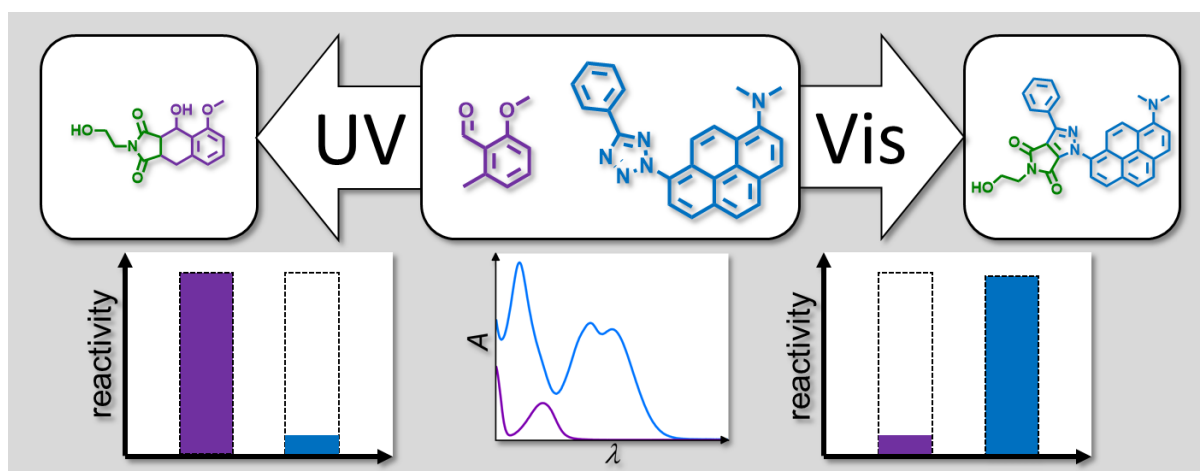


Figure 37: Two photo-active moieties can display overlapping absorption profiles. Yet, due to strongly deviating reactivity in different wavelength-regimes, they can individually be addressed, forming cycloadducts in a fully orthogonal and pathway-independent fashion.

While in the preceding **chapter 3** no reaction quantum yields were determined, the laser output energies and irradiation times indicated that the reaction quantum yield of APAT is rather low. It was therefore reasoned that by combining APAT with a UV-activated photo-active unit with a high quantum yield, a sequence-independent λ -orthogonal system could be realised (refer to **Figure 37**). The wavelength-dependent photoenolization and subsequent

[2+4] cycloaddition of *ortho*-methyl benzaldehyde (*o*MBA) has been reported to proceed with high efficiency at wavelengths between 285 and 390 nm.¹¹³

In the present chapter, steps are taken towards implementing such a system. Employing two photo-active moieties with disparate wavelength-dependent reactivity and quantum yield, a fully sequence-independent λ -orthogonal photo-induced reaction system is established: APAT and *o*MBA. Critically, the two units display inherently different reactivities and the orthogonality does not rely on any form of additive or altered reaction conditions (other than change in light colour).

Initially, kinetic studies are performed on mixtures of both compounds, using a *ns*-pulsed laser system at different wavelengths. The results are analysed by liquid chromatography-mass spectrometry. From the obtained kinetic plots, reaction quantum yields are obtained, using a *Matlab*® script and a number of input parameters. Hence, λ -orthogonality factors can be calculated at different wavelengths, and the wavelengths most suited for a λ -orthogonal

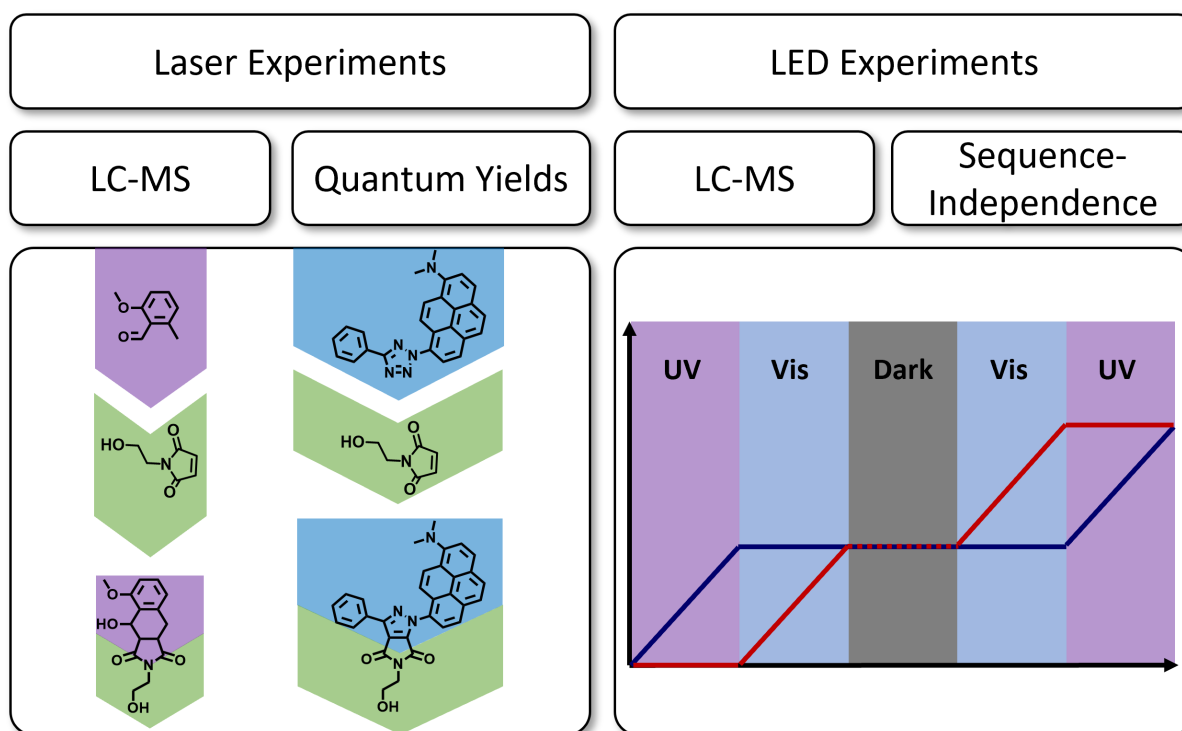


Figure 38: Schematic methodology followed in the current chapter. Employing a wavelength-tunable *ns*-pulsed laser system, the reaction kinetics of two small-molecule ligation reactions are evaluated. After establishing the optimum wavelengths, an LED-sequence is applied to demonstrate the orthogonal addressability of both units alongside each other.

experiment can be determined. Subsequently, the sequence-independence of the system is demonstrated in a sequential LED experiment. Altering nothing but the colour of the incident

light, both small molecule reactions can be triggered individually alongside each other (refer to **Figure 38**).

Parts of this chapter were reproduced with permission from P. W. Kamm, L. L. Rodrigues, S. L. Walden, J. P. Blinco, A.-N. Unterreiner, C. Barner-Kowollik, *Chem. Sci.*, **2021**, 13, 531-535.

All irradiation experiments, spectroscopic measurements, data analysis and isolation of the cycloadducts were performed by the PhD candidate. Synthesis and purification of *o*MBA was performed by Leona L. Rodrigues. Simulation of quantum yields with a *Matlab*® script, as well as the writing thereof, were performed by Sarah L. Walden. Absorption spectra of *o*MBA and *N*-(2-hydroxy)ethyl maleimide (NHEM) in 5 cm cuvettes were measured by Philipp Neidinger.

4.2 Proof of Principle

Several publications report that the wavelength-dependent reactivity of a light-responsive unit can significantly differ from its absorption profile. It is therefore not feasible to use absorption spectra for the prediction of ideal irradiation conditions. Instead, action plots show which wavelengths are most effective to trigger a photoreaction. In **Figure 39**, the action plots of APAT and an *o*MBA derivative are shown. While APAT is most reactive at 440 nm, the action plot displays a reactivity minimum at 360 nm. At 320 nm, reactivity significantly increases, almost reaching peak level again. On the other hand, *o*MBA is most efficient at 330 nm, and reactivity decreases towards shorter and longer wavelengths alike.

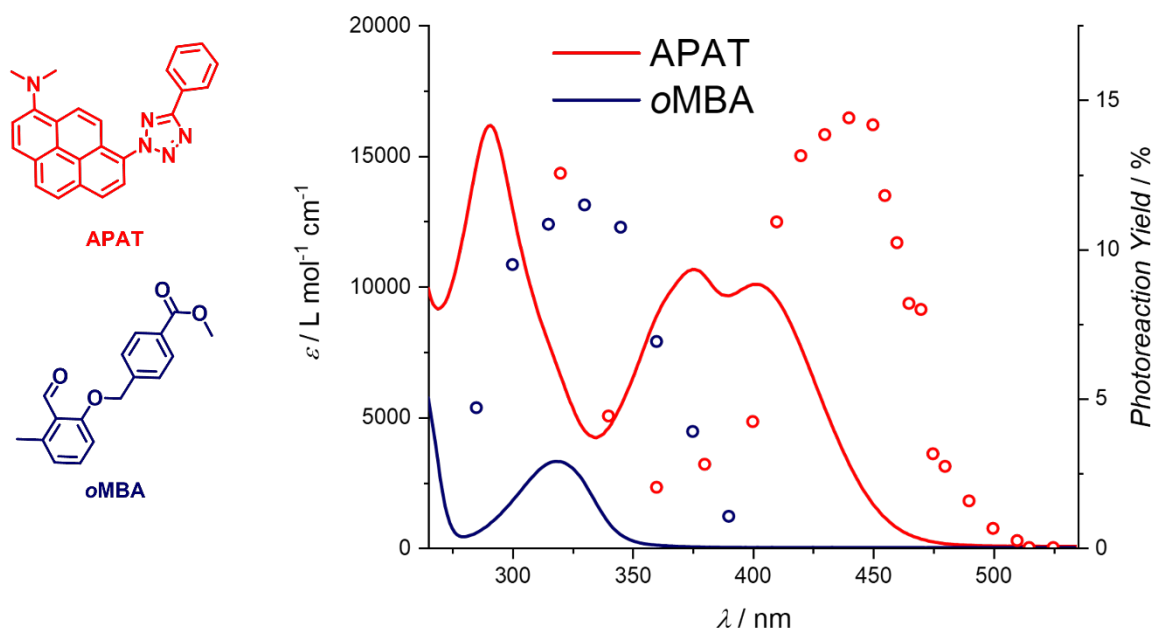
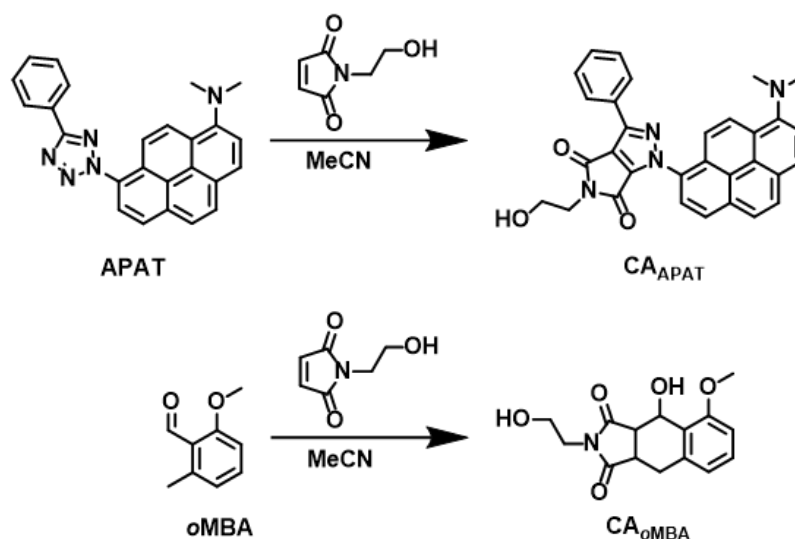


Figure 39: Left *y*-axis: Absorption spectra of *o*MBA and APAT in MeCN. Right *y*-axis: Wavelength-dependent reactivity profiles (action plots) of NITEC between APAT and diethylfumarate (DEF), as well as cycloaddition of *o*MBA and *N*-ethyl maleimide (NEM). APAT action plot was adapted from *Kamm et al., Chem. Commun.* **2021**, 57, 3991 (refer to **chapter 3**). *o*MBA action plot was adapted from *Menzel et al., J. Am. Chem. Soc.*, 2017, **139**, 15812-15820.

For a proof-of-principle experiment, 360 nm and 450 nm were therefore chosen as irradiation wavelengths to probe the degree of orthogonality. For simplicity, a slightly different *o*MBA derivative was selected for the photoreaction, bearing a methoxy group instead of the methylbenzoate derivative linker. This *o*MBA derivative was chosen because of its availability and a retention time on the column that is distinct from APAT. Changing the linker does not drastically change the absorption spectrum (as was confirmed by absorption spectroscopy),

nor the wavelength-dependent reactivity, since the benzoic acid methyl ester is not conjugated to the photo-active site.

Initially, the reaction conditions had to be optimised. Initial experiments with diethyl fumarate (DEF) as a reaction partner revealed that no sufficient separation of *o*MBA and the respective cycloadduct CA_{oMBA} on the column was achieved, preventing analysis and quantification of the cycloadducts. Therefore, *N*-(2-hydroxy)ethyl maleimide was used as a reaction partner instead. The reaction schemes of the final photoreactions are displayed in **Scheme 12**.



Scheme 12: Reaction schemes of the photoreactions between APAT and NHEM, as well as *o*MBA and NHEM. Reactions were carried out using 450 nm and 360 nm laser light, respectively. The compounds were dissolved in MeCN and degassed with dry N₂.

NHEM proved to provide a much better peak separation on the column (refer to **Figure 40**, top graphs). When analysing the mass spectrum of CA_{oMBA} , an m/z value of 274.1069 was found, corresponding to the cycloadduct after elimination of water ($[M+H]^+ = 274.1074$; $\Delta m/z = -1.8$ ppm). This is a result of the electrospray ionization process of the mass spectrometer. To confirm this, the photoreaction of *o*MBA and NHEM was conducted in a larger quantity and CA_{oMBA} was isolated (for the exact procedure, refer to **chapter 8.5.3**). The ¹H-NMR-spectrum confirms that the elimination of H₂O does not occur during the photoreaction. The isolated cycloadduct was also analysed spectroscopically, in order to obtain molar absorption coefficients. For quantification of the LC-MS chromatograms, the same method was utilised that was introduced in **chapter 3**. Due to the blue-shifted absorption of CA_{oMBA} , the scan wavelength of the UV-detector was set to 214 nm. This way, all relevant species could be recorded in one chromatogram. Isolation and spectroscopic analysis of

CA_{APAT} were already introduced in the previous chapter. Note that in **chapter 3**, CA_{APAT} was labelled CA_{NHEM} to distinguish from CA_{DEF} (different dipolarophiles). In the present chapter, the label CA_{APAT} is to distinguish from CA_{oMBA} (different photo-active moieties). All absorption spectra are shown in **Figure 40**, bottom graphs. The spectrum of CA_{oMBA} was recorded in a solvent mixture (MeCN/H₂O; 92:8), according to the eluent composition at the respective retention time. This is due to the solvent gradient employed for the chromatography (for detailed setup, refer to **section 8.2.3**)

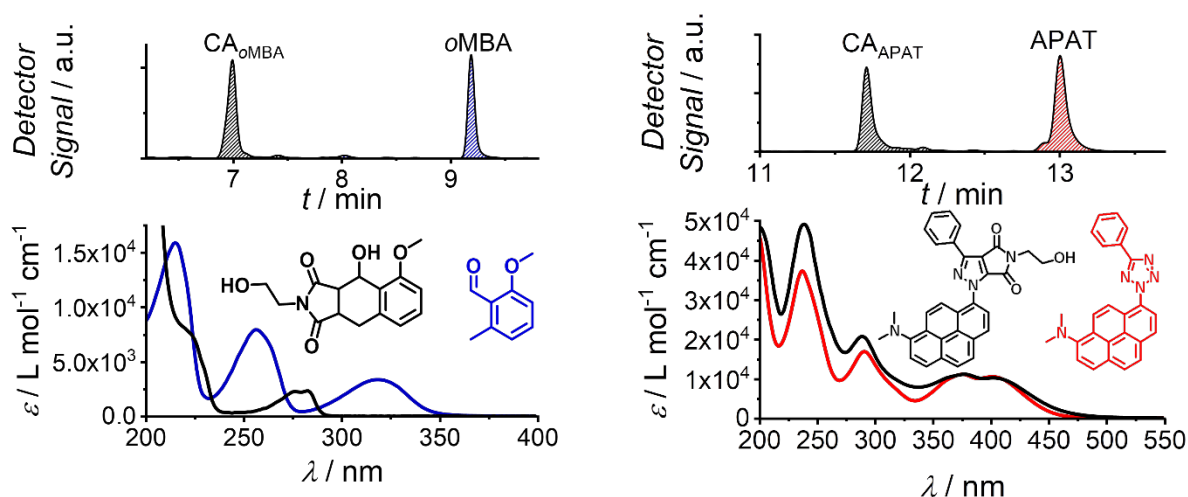


Figure 40: Top graphs: Exemplary chromatograms after photoreactions between *o*MBA and NHEM, as well as APAT and NHEM, showing the peak separation on the column. The scan wavelength of the UV detector was 214 nm. Bottom graphs: Absorption spectra of *o*MBA, CA_{oMBA}, APAT and CA_{APAT}. The molar absorption coefficient of each species $\epsilon_{214 \text{ nm}}$ was used to calculate the photo-adduct yield from the peak integral ratio of the chromatograms.

First, *o*MBA and APAT were irradiated separately with NHEM (at 360 nm and 450 nm, respectively), to evaluate their light-responsive behaviour in isolation. The resulting chromatograms were correlated with the molar coefficient at 214 nm of each species (refer to **chapter 10.2**), and photoreaction yields were calculated from the peak integrals as per the method introduced previously. After irradiation of *o*MBA (0.46 mM) and NHEM (1.84 mM) for 2 min at 360 nm, a CA_{oMBA} yield of 92 % is observed. Contrarily, when APAT (0.46 mM) and NHEM (1.84 mM) are irradiated for 15 min at 450 nm, only 9 % of CA_{APAT} are formed. Next, in a comparative experiment, tertiary mixtures of *o*MBA, APAT and NHEM were prepared and irradiated at 360 nm and 450 nm, to assess if λ -orthogonal activation is possible. In order to comply with the LC-MS sample preparation requirements, the concentrations of *o*MBA and APAT were adjusted. The overall concentrations were 0.23 mM APAT, 0.23 mM *o*MBA and 1.84 mM NHEM. After 2 min of 360 nm irradiation, 28 % of CA_{oMBA} are found, alongside a mere 0.2 % of non-rearomatized CA_{APAT}, demonstrating a remarkable selectivity

towards *o*MBA at 360 nm, with only trace amounts of APAT being converted. On the other hand, after 450 nm, no CA_{oMBA} could be detected, whereas 14 % of CA_{APAT} were found, demonstrating significant selectivity towards *o*MBA at this wavelength. The results are summarised in **Table 3**.

Table 3: Results of the initial experiments, evaluating the λ -orthogonality of the APAT/*o*MBA system.

λ / nm (t / min)	Eq. (<i>o</i> MBA:APAT:NHEM)	CA_{oMBA} Yield / %	CA_{APAT} Yield / %
360 (2)	2:0:8	92	-
450 (15)	0:2:8	-	9
360 (2)	1:1:8	28	0.2
450 (15)	1:1:8	0	14

It becomes apparent that the recorded conversions in the mixed experiment differ from those in the isolated experiments. In the case of *o*MBA, the conversion after 360 nm irradiation decreases by 70 % when APAT is present in the mixture, attributed to the competing absorption of the second chromophore. The concentration of both chromophores was halved in this experiment, while that of the reaction partner was kept constant. Consequently, penetration depth of the incident laser light, as well as the kinetics of the cycloaddition reaction, were affected. These effects will be further discussed in the following chapter. In the case of APAT, conversion is increased by a factor of 1.5 in the mixed experiment. Since competing absorption of *o*MBA does not play a role at 450 nm, this is solely attributed to the altered concentration of APAT.

Conclusively, these preliminary experiments showed that the APAT/*o*MBA system is a promising candidate for λ -orthogonal experiments. Both photoactive compounds could be individually addressed at 360 nm and 450 nm wavelengths. However, at 360 nm, minor conversion of APAT occurred, with *o*MBA reaching just 28 % conversion. Naturally, the unsolicited formation of CA_{APAT} will continue even more when higher conversion of *o*MBA is approached. Correspondingly, while no CA_{oMBA} was observed at 450 nm, this may change when APAT is to be converted more than 14 %. Thus, detailed investigations of the wavelength-dependent reactivity of both compounds were conducted and are described in the following section.

4.3 Wavelength-Dependent Reaction Quantum Yields

To quantify the differences in reactivity of both *o*MBA and APAT, reaction quantum yields of both chromophores were determined at different wavelengths. To that end, kinetic studies were conducted, monitoring the conversion of both photoreactions over time. Subsequently, the reaction quantum yield was determined by performing least square fits of the experimental data to a library of theoretical conversions simulated in *Matlab*®, based on a range of different quantum yields Φ . Starting from input parameters $c(t_0)$ and $\epsilon(\lambda)$ of each species, as well as pulse energy E_p and irradiation wavelength λ , the conversion after each pulse was calculated iteratively for the different Φ , yielding a simulated reaction conversion. For a detailed description of the iterative process, refer to 8.5.4. The *Matlab*® script was written by Dr Sarah L. Walden (QUT), who also performed the simulation of the quantum yields.

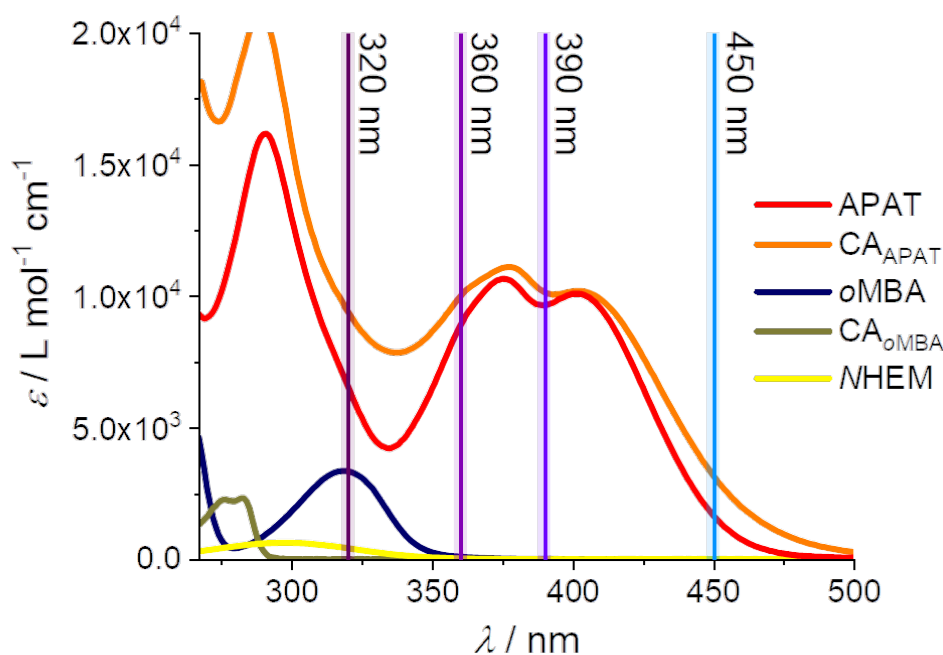


Figure 41: Overlaying absorption spectra of the starting materials, APAT, *o*MBA and NHEM, as well as the cycloadducts formed during the photoreaction, CA_{APAT} and CA_{oMBA} . The vertical lines represent the wavelengths of laser light employed for the kinetic studies.

In addition to the wavelengths employed for the proof-of-principle experiment (previous section, 360 nm and 450 nm), 390 nm was chosen as an in-between wavelength. Moreover, 320 nm is an interesting wavelength for two reasons: It is close to the absorption maximum of

*o*MBA, and a very efficient activation wavelength as per the action plot.¹¹³ Furthermore, the action plot of APAT displays a significant increase in conversion, compared to 360 nm (refer to **Figure 39**). The overlaid absorption spectra of all species, including the cycloadducts which also act as competing chromophores during the reaction, are displayed in **Figure 41**. The vertical lines represent the wavelengths of incident laser light. As is evident from the graph, at different wavelengths the different species present in the mixture contribute to

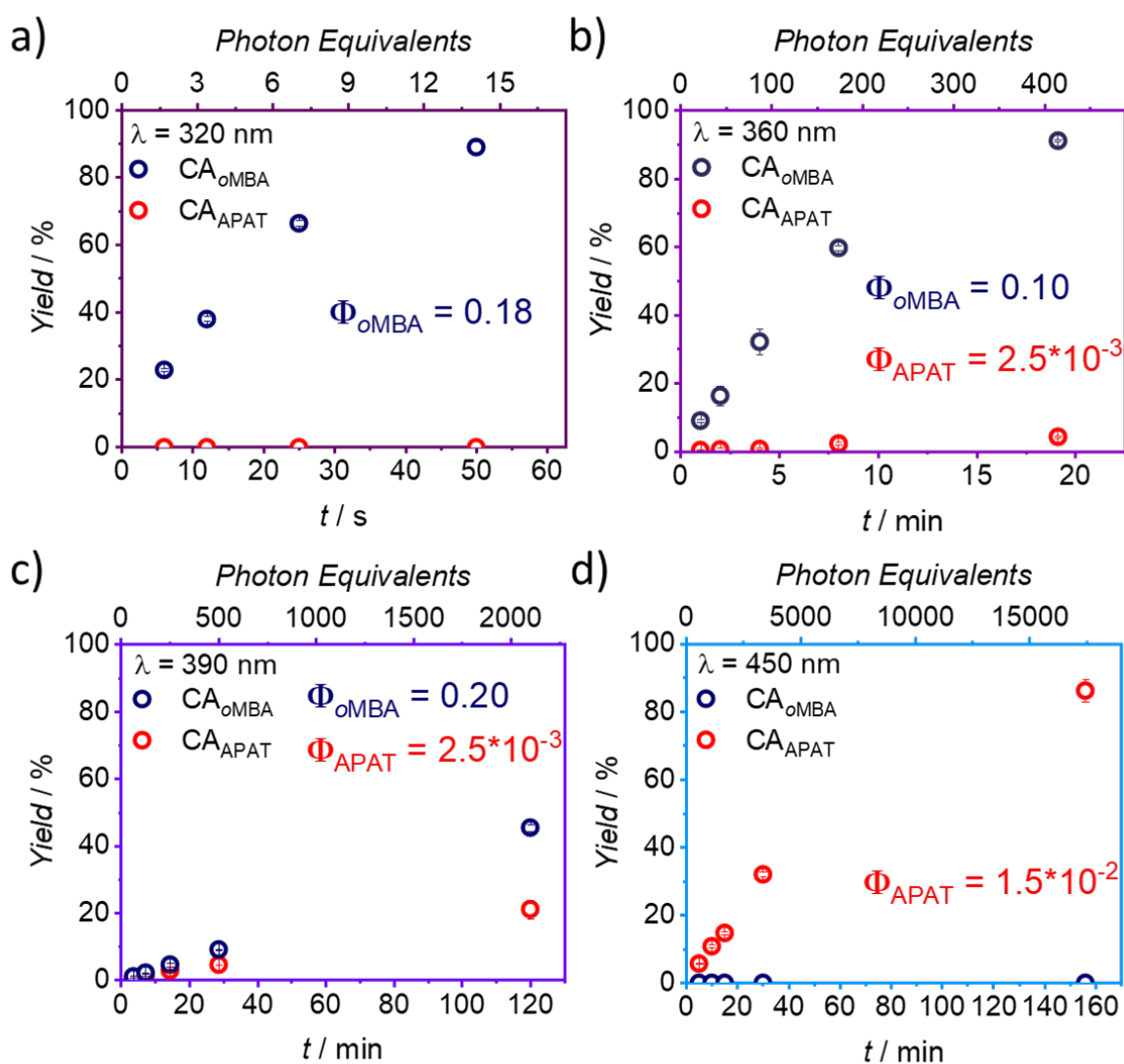


Figure 42: Time-dependent formation of CA_{APAT} and CA_{oMBA} upon cycloaddition during irradiation with a) 500 μ J pulses of 320 nm. b) 500 μ J pulses of 360 nm. c) 364 μ J pulses of 390 nm. d) 2000 μ J pulses of 450 nm. All experiments were carried out at ambient temperature, using a 20 Hz pulsed laser system. The bottom x -axis shows the irradiation time in s or min. The top x -axis shows the incident photon equivalents, relative to the amount of APAT and *o*MBA, which is calculated from the irradiation time and the pulse energy of the laser.

various degrees to the overall sample absorption. Since the concentration of all compounds is a function of the reaction time, their contribution to the overall sample absorption changes during the reaction.

In **Figure 42**, the time-dependent yield of CA_{APAT} and CA_{oMBA} is shown for irradiation wavelengths 320 nm, 360 nm, 390 nm, and 450 nm. The irradiation times were chosen to cover a wide range of conversions, the longest experiment yielding approximately 90 % conversion. The only exception is the 390 nm experiment, which was only driven to 45 % $oMBA$ conversion (as well as 21 % APAT conversion), due to the poor energy output of the laser at this wavelength. Reaching 90 % conversion of either species would have drastically increased the irradiation time, which seemed impractical.

In **Figure 42a**, $oMBA$ cleanly forms the cycloadduct with NHEM, reaching 89 % conversion after just 50 s, or ~ 15 eq. of incident photons. $\Phi_{320\text{ nm}}^{oMBA}$ was determined to be $0.18 (\pm 0.2)$. During this time, no detectable amount of CA_{APAT} was formed, thus no $\Phi_{320\text{ nm}}^{APAT}$ was determined. It is apparent that the selectivity towards $oMBA$ at 320 nm is outstanding, leading to CA_{oMBA} as the sole photo-adduct. This result is especially interesting because the molar absorption coefficient of APAT outweighs that of $oMBA$ by a factor of two ($\epsilon_{320\text{ nm}}^{oMBA} = 3\,300\text{ L mol}^{-1}\text{ cm}^{-1}$; $\epsilon_{320\text{ nm}}^{APAT} = 6\,600\text{ L mol}^{-1}\text{ cm}^{-1}$). Additionally, while NHEM only displays relatively weak absorption at 320 nm ($\epsilon_{320\text{ nm}}^{NHEM} = 420\text{ L mol}^{-1}\text{ cm}^{-1}$), its 8-fold excess means that the contribution to the overall attenuation is on par with that of $oMBA$.

At 360 nm irradiation, the selectivity of the reaction system is decreased, as is apparent in **Figure 42b**. While a CA_{oMBA} yield of 91 % is reached within 19 min (~ 400 eq. of photons), simultaneously, 4 % of CA_{APAT} are formed. The overall lower reactivity of $oMBA$ can be attributed to the drastically lowered molar absorption coefficient ($\epsilon_{360\text{ nm}}^{oMBA} = 100\text{ L mol}^{-1}\text{ cm}^{-1}$), while at the same time the absorptivity of APAT increases ($\epsilon_{360\text{ nm}}^{APAT} = 8\,900\text{ L mol}^{-1}\text{ cm}^{-1}$), meaning that a large fraction of the incident photons is not available for the photoenolization. These factors amount to $\Phi_{360\text{ nm}}^{oMBA} = 0.10 (\pm 0.2)$, dropping by 40 % compared to the value at 320 nm. This drop is in excellent agreement with literature, where $oMBA$ retained ~ 60 % of its reactivity when moving from 320 nm to 360 nm.¹¹³ On the other hand, the action plot of APAT suggests that APAT is significantly less reactive at 360 nm than at 320 nm (by a factor of ~ 6). Still, no CA_{APAT} was observed at the shorter wavelength, whereas 4 % conversion are reached at the latter, amounting to $\phi_{360\text{ nm}}^{APAT} = (2.5 \pm 0.5) 10^{-3}$. This apparent inconsistency is a result of the much shorter irradiation times of the 320 nm experiment, which did not allow for

determination of $\Phi_{320\text{ nm}}^{APAT}$. It is however expected that APAT will commence conversion if longer irradiation times were used.

A similar trend is observed in the 390 nm experiment, which is shown in **Figure 42c**. The discrepancy between the molar absorption coefficients of APAT and *o*MBA is even more drastic. APAT absorbance is approximately the same as before ($\epsilon_{390\text{ nm}}^{APAT} = 9\,600\text{ L mol}^{-1}\text{ cm}^{-1}$), but it was not possible to obtain reliable values for $\epsilon_{390\text{ nm}}^{oMBA}$ $\epsilon_{390\text{ nm}}^{NHEM}$ due to the low absorption coefficients. It was therefore assumed that $\epsilon_{390\text{ nm}}^{oMBA}$ and $\epsilon_{390\text{ nm}}^{NHEM}$ are lowered by a factor of 1000 compared to the respective absorption maximum, with a relative error of 50 %. While this allowed for determination of $\Phi_{390\text{ nm}}^{oMBA} = 0.20 (\pm 0.18)$, this result must be treated with great care. The error is obtained through error propagation from the least square fit process of the *Matlab*® script, and the uncertainty of the absorption coefficient. For APAT, the reaction quantum yield was determined to be $\Phi_{390\text{ nm}}^{APAT} = (2.5 \pm 0.5) 10^{-3}$, comparable with the value at 360 nm. While again the quantum yields of APAT and *o*MBA differ by orders of magnitude, the difference in absorbance compensates for this effect, resulting in comparable conversions after 120 min of irradiation. The final product composition contains 45 % of CA_{oMBA} and 21 % of CA_{APAT} . Obviously, 390 nm provides the least selectivity, making it the least suited wavelength for λ -orthogonal experiments.

In **Figure 42d**, exclusively CA_{APAT} is formed, reaching 86 % product yield after 156 min of irradiation. During this time, no detectable amount of CA_{oMBA} is generated. This demonstrates a remarkable selectivity towards APAT at 450 nm irradiation. $\Phi_{450\text{ nm}}^{APAT}$ was determined to be $(1.5 \pm 0.5) 10^{-2}$, resulting in a 6-fold increase in reactivity. Again, this is in good agreement with the earlier results presented in the previous chapter. Because no CA_{oMBA} was formed, no quantum yield $\Phi_{450\text{ nm}}^{oMBA}$ was determined.

Importantly, some of the irradiation experiments yielded varying amounts of non-rearomatized pyrazoline adduct (CA_{APAT}^H , refer to **Figure 43a**). The degree to which rearomatization occurred varied in the different experiments, ranging from 51 % to 100 % (with full or nearly full rearomatization in the majority of cases). As was described in section **chapter 3.4**, the absorption spectra of the pyrazole species, CA_{APAT}^- and CA_{APAT}^H diverge due to differences in the conjugation of the aromatic system (**Figure 43c**). To calculate the photoreaction yield from the chromatogram peaks, it is therefore necessary to determine the molar absorption coefficient $\epsilon_{214\text{ nm}}$ of both species. However, attempts to isolate both cycloadducts led to exclusive formation of the aromatic pyrazole species CA_{APAT}^- . As a

consequence, for the analysis of the chromatograms both species were treated as one, applying the absorption coefficient determined in the preceding **section 4.2** for both products (**Figure 43b**). This seemed like a suitable approximation: Even when experiments were repeated three times under the same conditions (to obtain error bars) the recorded relative amounts of CA_{APAT}^- and CA_{APAT}^H varied. However, when the peak integrals of both species were summed up and treated as one, CA_{APAT}^{total} , the value was consistent throughout each triplicate. It is therefore assumed that the molar absorption coefficient at the LC-MS detector scan wavelength is approximately the same for CA_{APAT}^H and CA_{APAT}^- .

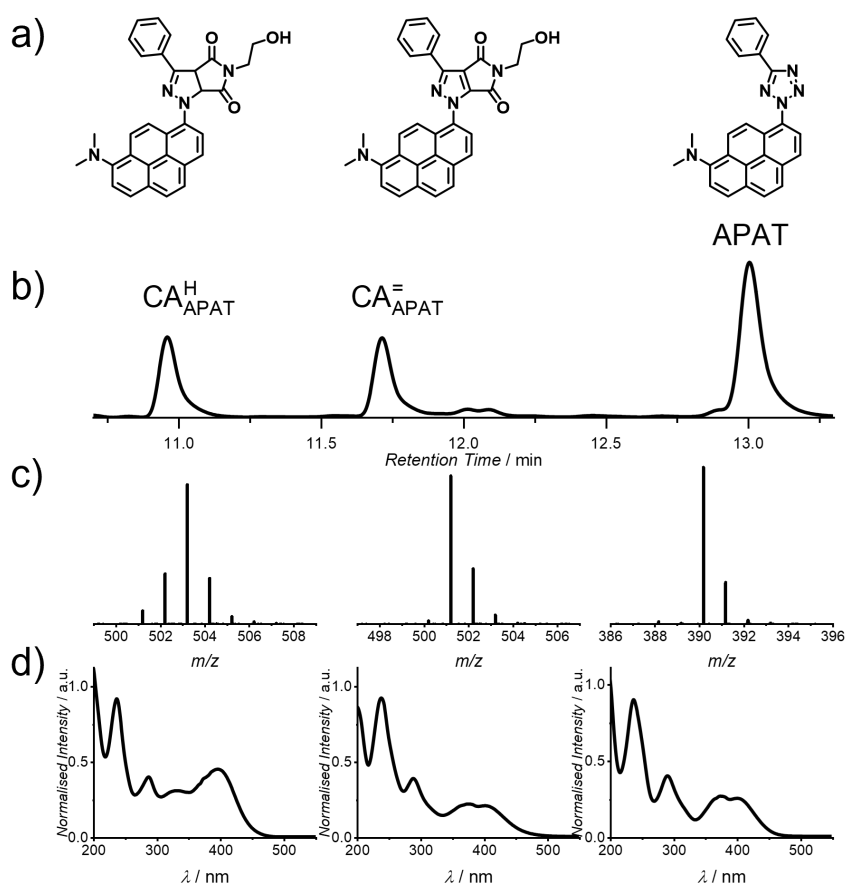


Figure 43: a) Structures of CA_{APAT}^H , CA_{APAT}^- and APAT. b) Exemplary chromatogram after 30 min irradiation at 450 nm. b) Zoomed mass spectra of all species: CA_{APAT}^H : m/z $[M+H]^+ = 503.2078$; found: 503.2074. CA_{APAT}^- : m/z $[M+H]^+ = 501.1921$; found: 501.1920. APAT: m/z $[M+H]^+ = 390.1713$; found: 390.1714. c) Extracted PDA signals of the LC-MS, showing similarities between the aromatic species CA_{APAT}^- and APAT, whereas the absorption profile of CA_{APAT}^H differs significantly.

The results of the experiments are summarised in **Table 4**. The wavelength-selectivity S_λ at a given wavelength λ was defined as the ratio of the difference and the sum of the pseudo-first order rate constants of the exponential fit of the respective kinetic plots.

$$S_{\lambda} = \frac{k_1^{\lambda} - k_2^{\lambda}}{k_1^{\lambda} + k_2^{\lambda}} \quad (4 - 1)$$

Formula (4 – 1) is an attempt to give an index for the degree of wavelength-selectivity. The rate constants k_1^{λ} and k_2^{λ} are the rate constants for the *o*MBA and the APAT photoreaction at a given wavelength, respectively. The resulting wavelength-selectivity S_{λ} ranges from 1 (full selectivity towards *o*MBA, no APAT conversion) over 0 (no selectivity; equal reaction rate of both compounds) to -1 (full selectivity towards APAT; no *o*MBA conversion). If the wavelength-selectivity at two wavelengths is -1 and 1, the system is fully λ -orthogonal. To draw meaningful conclusions from this measure, at least one of the photoreactions should reach high conversion. In the present experiments, a yield of 90 % was targeted (except for the 390 nm experiment, where reaction times were very long, hence the *o*MBA cycloaddition was only driven to 45 %). These rate constants were calculated from the temporal progress of the reaction, and they do not take into account differences in the laser energies at different wavelengths. Thus, they do not allow for comparison of rate constants across experiments at different wavelengths. However, they do allow for comparison of the reaction kinetics for *o*MBA and APAT *within* one experiment, and ultimately determine whether or not the system reaches full selectivity at a given wavelength.

Table 4: Summary of the wavelength-dependent kinetic experiments and determination of reaction quantum yields. Dashes mean that no quantum yield could be determined due to negligible conversion.

		320 nm	360 nm	390 nm	450 nm
	Yield / %	91	89	45	0
<i>o</i> MBA	Φ^{oMBA}	0.18 (0.2)	0.10 (0.2)	0.20 (0.18)	-
	k_{oMBA} / s^{-1}	$4.3 \cdot 10^{-2}$	$2.0 \cdot 10^{-3}$	$7.9 \cdot 10^{-5}$	0
	Yield / %	0	4	21	86
APAT	Φ^{APAT}	-	$(2.5 \pm 0.5) \cdot 10^{-3}$	$(2.5 \pm 0.5) \cdot 10^{-3}$	$(1.4 \pm 0.5) \cdot 10^{-2}$
	k_{APAT} / s^{-1}	0	$4.1 \cdot 10^{-5}$	$3.2 \cdot 10^{-5}$	$2.0 \cdot 10^{-4}$
	λ -Selectivity	1	0.96	0.42	1

With *o*MBA and APAT reaching full selectivity at 320 nm and 450 nm, respectively, the foundation is laid for a fully λ -orthogonal system. In the following section, this is demonstrated by a sequential LED experiment.

4.4 Sequence-Independent λ -Orthogonality

A major advantage of orthogonally addressable photoreactions is the simplicity with which control is exerted over the system; Merely by switching the colour of light, different reactions can be turned on and off within one reaction vessel, ideally achieved without the need to open the vessel, i.e., to add or remove catalysts, solvents, or co-reagents. As was outlined in the introductory **chapter 2.4**, this has so far not been achieved for irreversible ligation reactions.

In the previous section, the wavelength-selectivity of the APAT/*o*MBA system was established for wavelengths 320 nm and 450 nm. However, data points were obtained through individual laser experiments, without switching the colour of light mid-experiment. To demonstrate the applicability of the system in an easy-to-operate setup, the following section describes LED irradiation of an APAT/*o*MBA/NHEM mixture, employing widely available irradiation sources, activating different reactions solely by switching the LED.

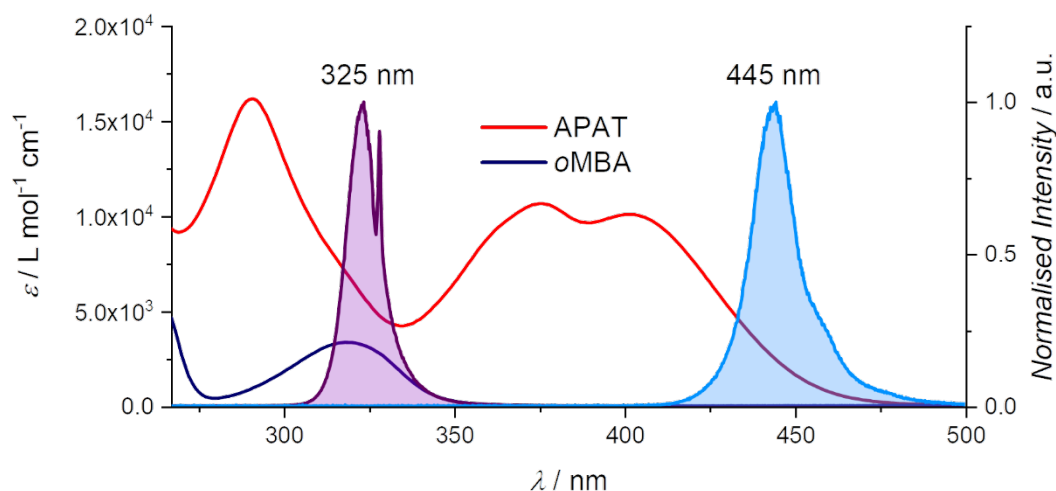


Figure 44: Overlay of the absorption spectra of both photoactive chromophores (*o*MBA and APAT) and the normalised emission spectra of the employed LEDs (325 nm 0.67 W and 445 nm 10 W).

A crimp vial was equipped with a solution of APAT, *o*MBA and NHEM in MeCN, as well as a stir bar. After sealing, the mixture was degassed and subjected to irradiation with an LED setup, employing a 325 nm 0.67 W LED for the UV-activated unit and a 445 nm 10 W LED for the visible light-activated unit (for a detailed description of the sample preparation and irradiation setup, refer to **section 8.3.2**). Since this setup uses a different light source as well as a stir bar (which was not used in the laser experiments for practical reasons), the reaction

speed may vary compared to the laser experiments. Since APAT reacts a lot slower than *o*MBA, the visible light intervals must be longer than the UV intervals. However, this effect is partly compensated for by the difference in LED output powers. **Figure 44** shows how the emission spectra of the employed LEDs overlap with the absorption spectra of *o*MBA and APAT.

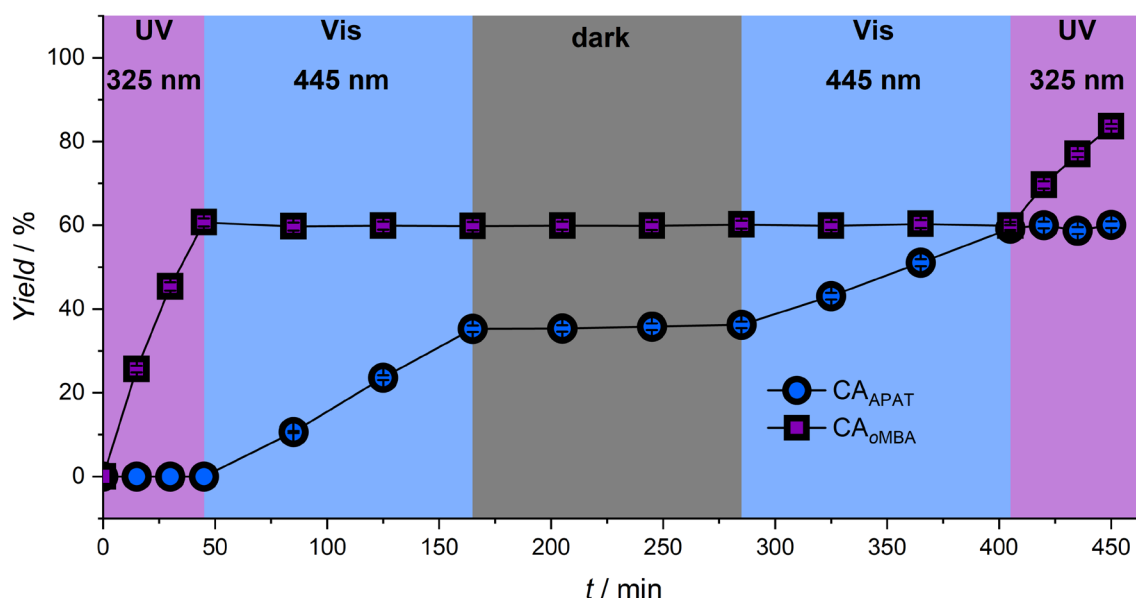


Figure 45: Photo-cycloadduct yield of CA_{oMBA} and CA_{APAT} after sequential irradiation with LEDs at two disparate wavelengths (325 nm, 0.67 W and 445 nm, 10 W). Due to faster reaction kinetics of the *o*MBA cycloaddition, samples were taken in 15 min intervals in the UV regime, and in 40 min intervals in the visible light regime. A dark period of 120 min was added between the two possible switching pathways (UV→Vis and Vis→UV). *o*MBA is converted exclusively through 325 nm irradiation, while APAT only reacts to 445 nm light.

After some initial test runs, the duration of the UV intervals was set to 45 min (with samples taken every 15 min), while the visible light intervals were set to 120 min (with samples taken every 40 min). To ensure that no thermal reaction was induced during the prolonged irradiation with a high-powered LED, a thermal test reaction was carried out, heating a solution of APAT and a suitable dipolarophile in MeCN for several hours. Yet, no change of the starting material was found after heating to 80 °C, which is close to the solvent boiling point (refer to **Figure S 42**). This is in line with literature reports, stating that tetrazoles are stable up to 160 °C - 220 °C.⁶²

To test the sequence independence of the system, both possible pathways (UV→Vis and Vis→UV) were applied, with a dark period in between. Samples were taken with a N₂-filled syringe and subjected to LC-MS. Analysis of the chromatograms was done according to the

method introduced earlier, and the resulting plot of the conversion over time is presented in **Figure 45**. During the first 45 min, the sample was irradiated with 325 nm light. From the conversion plot, it is apparent that exclusively *o*MBA is activated in this wavelength regime, with an overall yield of 60 % CA_{oMBA} after 45 min. During the same period, no CA_{APAT} could be detected. After switching to a 445 nm LED, APAT commenced conversion, reaching 35 % CA_{APAT} yield after 120 min, while the amount of CA_{oMBA} stagnated at 60 %. During the following 120 min dark period, neither photoreaction proceeded. When the 445 nm LED was switched back on, APAT conversion continued, overall yielding 60 % CA_{APAT} . Again, *o*MBA was not activated until the setup was once more switched to the 325 nm LED. Whereas APAT did not react, *o*MBA conversion proceeded, reaching a final 84 % of CA_{oMBA} yield.

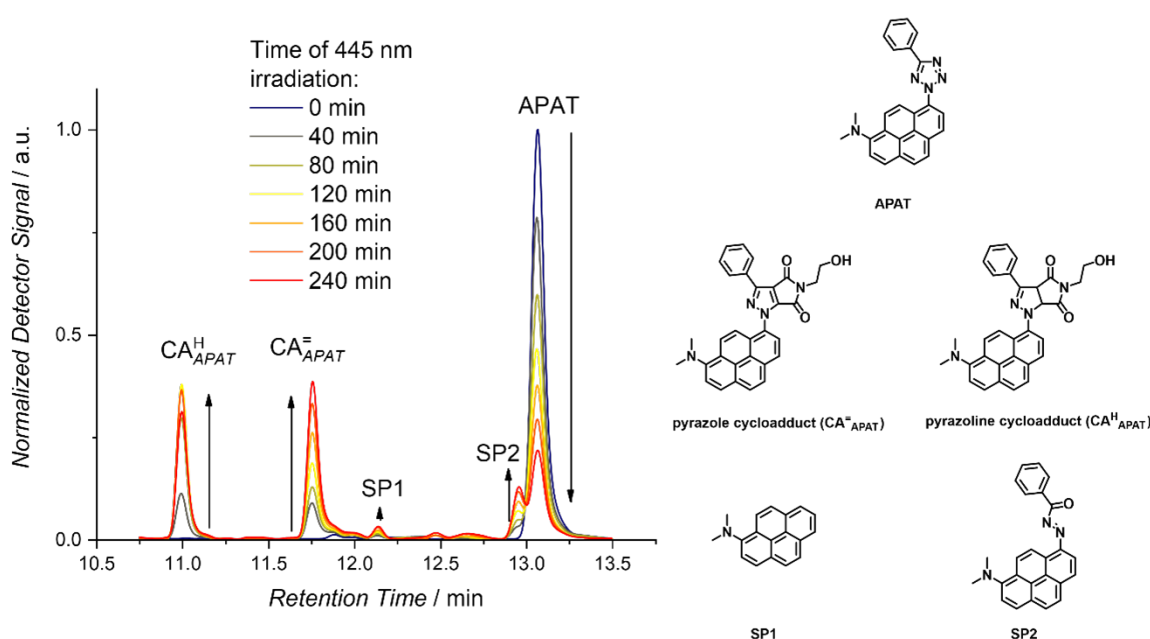


Figure 46: LC-MS chromatograms after irradiation with a 445 nm 10 W LED. CA_{APAT}^H and $CA_{APAT}^=$ increase over time, while APAT decreases. Similarly, the amount of SP2 slowly increases over time, reaching a relative peak integral of 10 %.

On a side note, some notable observations were made when analysing the reaction mixtures after irradiation. Unlike in the laser experiments described in the previous section, the degree of rearomatization of the cycloadduct was much lower. As per the recorded chromatograms at 214 nm scan wavelength (refer to **Figure 46**), the fractional prevalence of $CA_{APAT}^=$ ranged between 35 % and 58 %. It is speculated that this difference can be attributed to the presence of oxygen and moisture in the reaction vessel, which was introduced when the rubber septum was repeatedly penetrated to withdraw samples, monitoring the conversion as a function of time. This is also supported by the formation of minor amounts of side product. The

chromatograms in **Figure 46** display another peak at 13 min retention time (labelled SP2). While the product could not be isolated, the mass spectrum suggested that it corresponds to the adduct after nucleophilic reaction of water with the nitrile imine. Again, this is associated with the presence of moisture in the reaction vessel. No molar absorption coefficient could be determined for the side product, but the relative peak integral at the end of the reaction amounts to 10 %. Moreover, traces of *N,N*-dimethyl pyren-1-amine were present in the mixture, but the relative amount did not change during the course of the reaction and is likely attributed to an impurification of the starting materials.

Still, these results clearly demonstrate that *o*MBA and APAT can be addressed fully independently in a one-pot reaction, simply by switching the colour of the incident light. This was achieved in a simple benchtop setup, employing widely available LEDs as light sources. Critically, the reactions proceed to high conversions and – once sealed – require no more change of the reaction system, i.e., no catalysts, solvent changes, or protection groups.

4.5 Conclusion

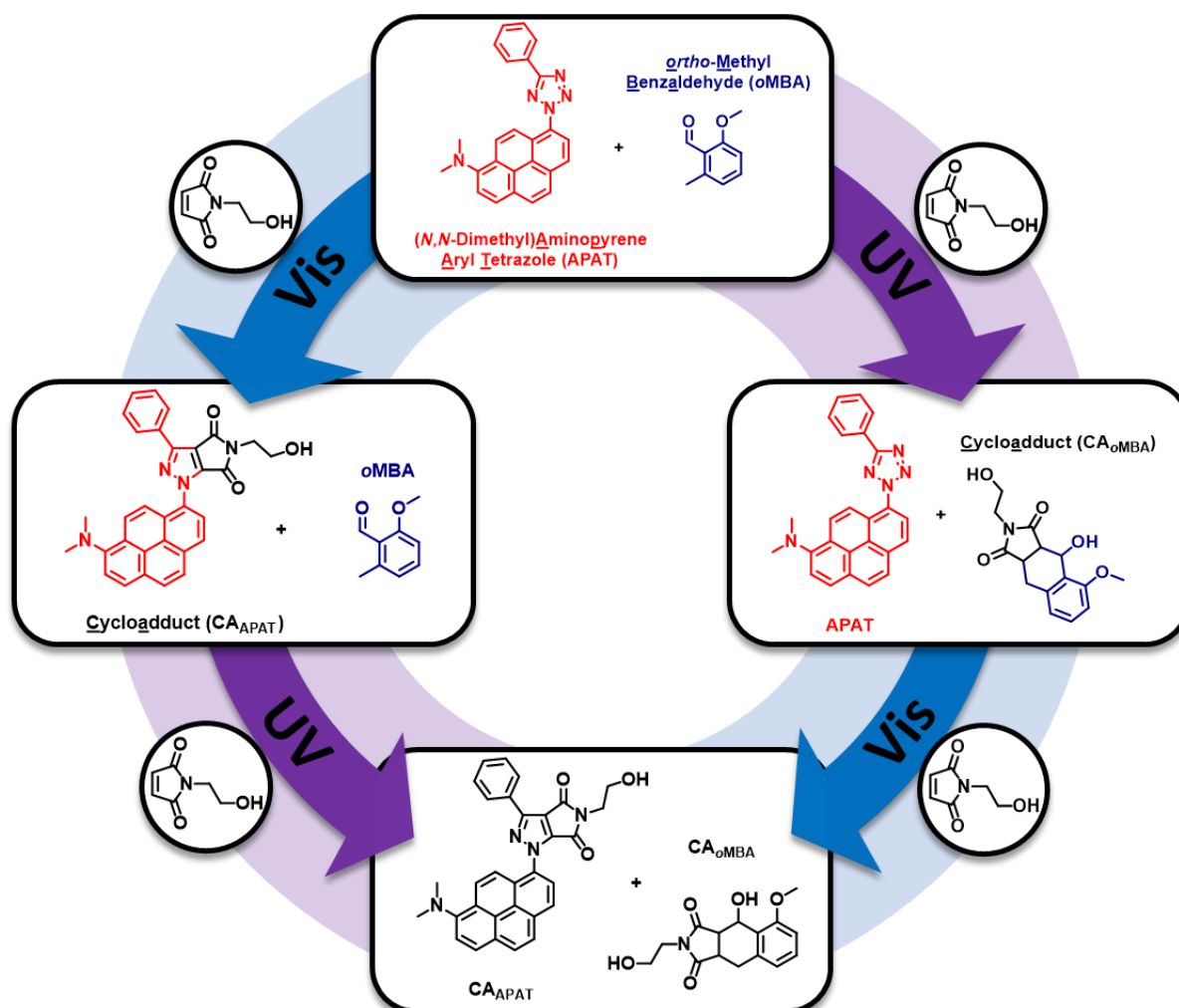


Figure 47: Exploiting differences in reaction quantum yields, it is possible to orthogonally activate *o*MBA (with UV light) and APAT (with visible light) in any order.

Conclusively, in the present chapter, a newly developed visible light-activated *N,N*-dimethyl aminopyrene aryl tetrazole (APAT) was employed alongside a methoxy-substituted *o*-methyl benzaldehyde (*o*MBA) to establish a fully sequence-independent λ -orthogonal ligation system without the need for protection groups, catalysts, or other additives. Exploiting reaction quantum yields that differ by orders of magnitude, the two reactive chromophores can be activated independently and in any order by simply switching the colour of light. Upon UV irradiation, *o*MBA quickly reacts with *N*(2-hydroxy)ethyl maleimide (NHEM) *via* a hydroxy *o*-quinodimethane intermediate, while APAT undergoes nitrile imine-mediated tetrazole-ene cycloaddition with NHEM upon visible light irradiation.

Initially, proof-of-concept experiments were carried out by selecting wavelengths based on detailed literature-known wavelength-dependent reactivity profiles (action plots). After ascertaining a high wavelength-selectivity for both compounds at 360 nm and 450 nm, respectively, detailed kinetic studies were conducted. By probing the reaction system at four different wavelengths (320 nm, 360 nm, 390 nm, 450 nm), the photoadduct yield for both cycloadducts CA_{oMBA} and CA_{APAT} was plotted as a function of incident photons. A measure for the wavelength-selectivity was introduced, unveiling 320 nm and 450 nm as the most appropriate wavelengths for orthogonal activation of *o*MBA and APAT. From the obtained kinetic data, reaction quantum yields were calculated through an iterative simulation process, using a *Matlab*® script, revealing that the reaction quantum yield of APAT is several orders of magnitude lower than that of *o*MBA. This discrepancy allows for activation of *o*MBA with UV light, without simultaneous activation of APAT.

The ability to target the two active chromophores with two colours of light independently of the applied order was then demonstrated using an LED setup. The tertiary mixture, containing two orthogonal chromophores (*o*MBA and APAT) and a dipolarophile (NHEM) was subjected to a predefined sequence of wavelengths: First, the UV→Vis pathway was tested, followed by the reverse Vis→UV pathway, with a dark period in between. Both photoreactions proceeded fully independently, without any mutual interplay of the involved chromophores.

This λ -orthogonal system opens an avenue for highly controllable applications such as multimaterial photoresists in orthogonal 3D lithography, or advances architecture of complex networks.

5 CYCLOADDITIONS IN DISPARATE ENVIRONMENTS

5.1 Objective

In the present chapter, a number of influencing variables are investigated, deepening the understanding of the wavelength-dependent reactivity of a photo-active moiety. To obtain a full view of the photochemical potential of a reaction system, it is not necessarily sufficient to simply probe the reaction conversion at different wavelengths under constant photon count (so-called action plot). I.e., in the previous chapter, in addition to the action plot, detailed assessment of reaction quantum yields at different wavelengths was prerequisite for the establishment of a truly sequence-independent λ -orthogonal system. To utilize photo-active chromophores in complex reaction systems, it is not only imperative to have precise knowledge over the wavelength-dependent reactivity. It is also helpful to understand how certain parameters may influence the action plot. Having these interrelationships at hand is critical to make photo-active systems universally applicable and overcome obstacles that may limit the usefulness of a reaction, i.e., by extending the palette of solvents to choose from, or identifying the ideal range of concentrations within to operate.

A versatile and widely used photo-active system is styrylpyrene, which can undergo [2+2] photodimerization upon excitation with UV or visible light. The reaction is particularly interesting for development of λ -orthogonal systems, where a short wavelength activated species and a long wavelength-activated species (i.e., styrylpyrene) perform photoreactions abreast to one another independently in their respective wavelength regimes. The blue-shifted [2+2] cycloadduct of styrylpyrene undergoes cycloreversion upon irradiation in the UV. If the UV-active moiety is irradiated first, the [2+2] cycloaddition of styrylpyrene is therefore actively suppressed, providing sequence-independence of the reaction system. Thanks to this advantage, styrylpyrene has been employed for a number of applications such as photocrosslinking of polymers^{138, 212} or DNA,¹³⁵ hydrogelation,¹⁴⁴ or photopolymerisation,¹³⁹ and was also exploited together with *ortho*-methyl benzaldehyde (*o*MBA) in λ -orthogonal photocuring systems.¹⁹⁹

Despite the widespread applications, however, critical parameters of this reaction remain unexplored. While wavelength-dependent reactivity has been investigated for the [2+2]

cyclodimerization and cycloreversion of styrylpyrene, certain criteria that may affect the shape of the action plot are yet to be reported.

Herein, the dimerization reaction of styrylpyrene is investigated on four unprecedented levels:

- 1) A modified procedure for obtaining action plots, taking into account the light attenuation of a chromophore mixture. This is especially important in applications that are limited by light penetration depth, i.e., batch reactions with long pathlength, or non-stirred environments.
- 2) The influence of concentration on the reactivity of the dimerization. While lower concentration allows for deeper light penetration, it also lowers the probability of an excited molecule to encounter a ground state molecule to perform dimerization. It is unclear which of these effects prevails.
- 3) The effect of solvent on the dimerization reaction. Solvents come with many critical variables, such as polarity or viscosity, and different solvents may stabilise transition states to different degrees.
- 4) The effect of elevated temperature on the dimerization reaction. While higher temperatures often accelerate reactions, they can also affect the *cis/trans* equilibrium of styrylpyrene and therefore have an influence on the course of the reaction.

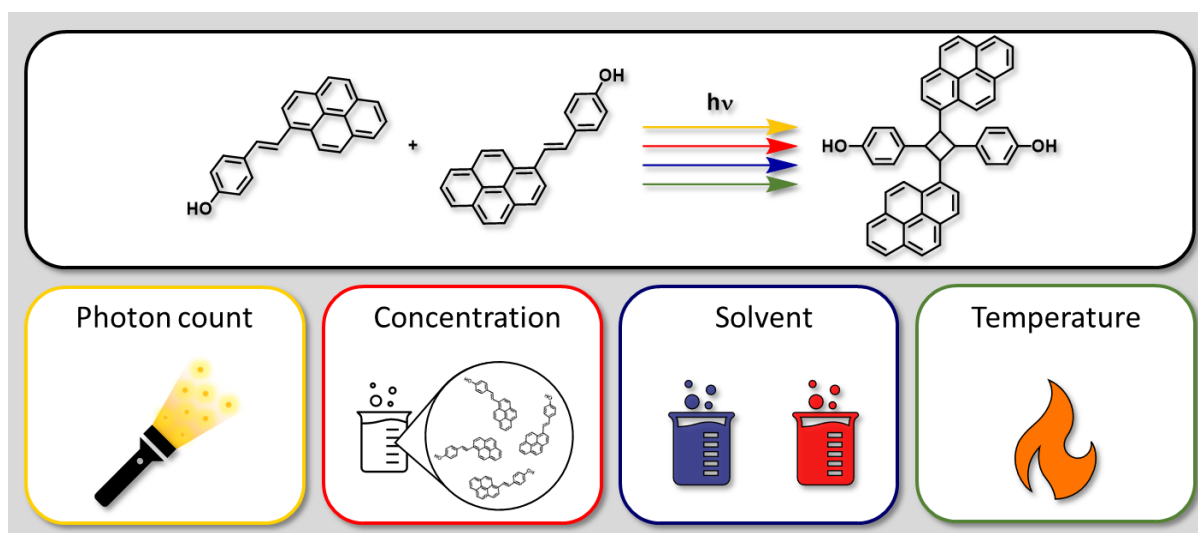


Figure 48: How efficiently a reaction proceeds at different wavelengths depends on a number of variables, i.e., the fraction of photons that lead to an excitation event, the concentration, the solvent, or the temperature.

Initially, wavelength-dependent photoreactions were conducted in $\text{MeCN-}d_3$, using a *ns*-pulsed laser system operating at a 100 Hz repetition rate, with either the incident photons kept

constant at all wavelengths, or with the photon count adjusted for the absorbance of the solution. The products of the irradiation experiments were analysed by $^1\text{H-NMR}$ spectroscopy, as was established previously.¹³⁷

Secondly, the experiments with constant photon count were repeated at a halved styrylpyrene concentration. Like before, conversion was quantified by $^1\text{H-NMR}$ spectroscopy, and plotted as a function of the irradiation wavelength to obtain the action plot.

Thirdly, the experiments with constant photon count were repeated but $\text{MeCN-}d_3$ was switched for $\text{DMSO-}d_6$ and, again, the reaction outcome analysed by $^1\text{H-NMR}$ spectroscopy.

Last, experiments were carried out at elevated temperature ($37\text{ }^\circ\text{C}$) and the results analysed *via* $^1\text{H-NMR}$ spectroscopy.

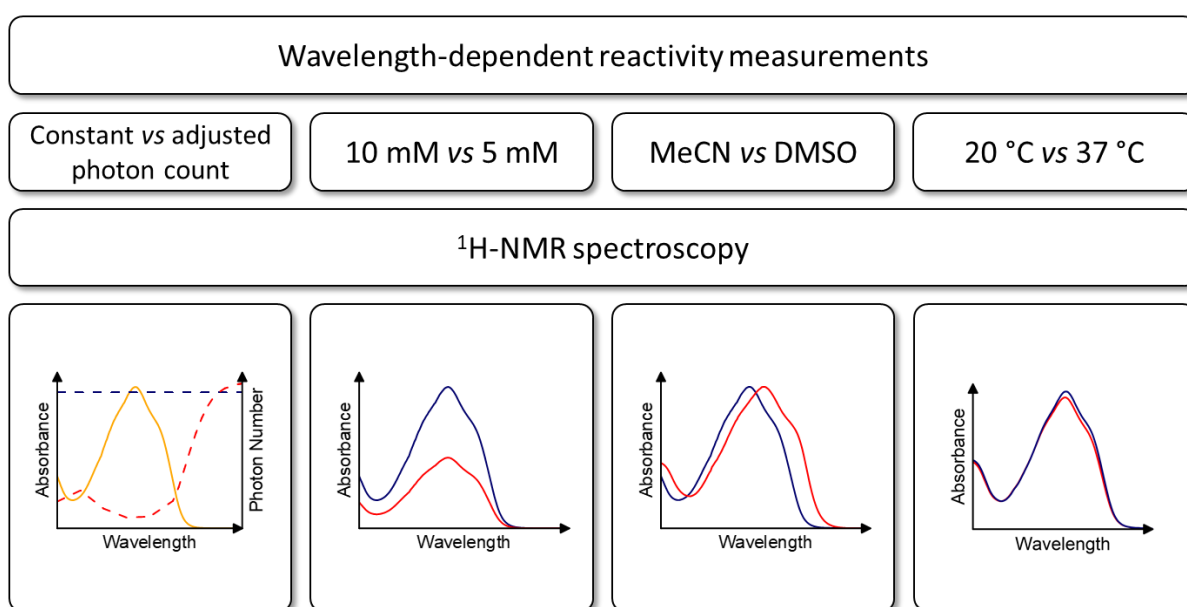


Figure 49: Methodology applied to investigate the effect of the different parameters: Wavelength-dependent conversion measurements were carried out using a 100 Hz *ns*-pulsed laser system, varying either the number of incident photons, the styrylpyrene concentration, or the solvent. $^1\text{H-NMR}$ spectroscopy was used to analyse and quantify the reaction outcome.

Parts of this chapter were reproduced with permission from D. E. Marschner, P. W. Kamm, H. Frisch, A.-N. Unterreiner and C. Barner-Kowollik, *Chem. Commun.*, 2020, **56**, 14043. Sample preparation, wavelength-dependent laser experiments, as well as absorption and $^1\text{H-NMR}$ spectroscopy, were performed by the PhD candidate. Synthesis and purification of styrylpyrene, as well as analysis of the $^1\text{H-NMR}$ spectra was performed by David Marschner. Fluorescence spectra were measured by Markus Zieger.

5.2 Accounting for Light-Absorption in Action plots

Plotting the conversion of a reaction as a function of the irradiation wavelength is helpful for characterising a given chromophore and evaluating its potential for λ -orthogonal systems. These so-called action plots have been recorded for a number of molecules (see also previous chapters).^{137, 145, 187, 211} A defining feature of action plot measurements is that they employ a constant number of photons at all wavelengths. It is found that the reactivity cannot be predicted by analysing the absorption profile alone, and that the reactivity plot can be significantly red-shifted compared to the absorption profile. This is because (steady state) absorption spectra represent the ground state of a molecule, whereas photoreactions occur after relaxation through an excited state manifold, which is inaccessible by absorption spectroscopy alone.

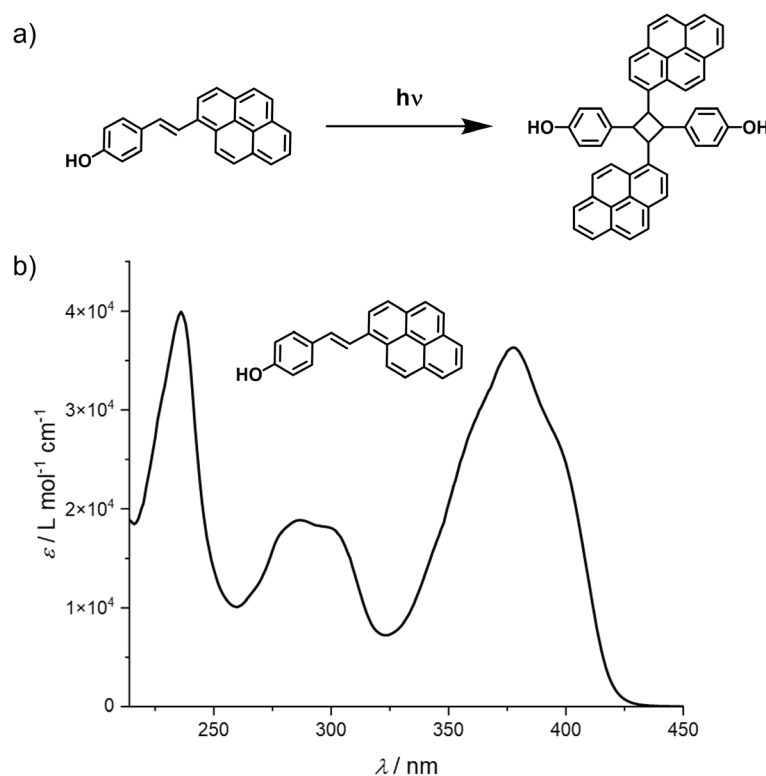


Figure 50: a) Structures of styrylpyrene and the dimer after [2+2] photodimerization. b) Absorption spectrum of styrylpyrene (measured at 69 μM in MeCN at ambient temperature, 1 cm cuvette).

By adjusting the number of photons in an action plot experiment to the absorption spectrum of the chromophore, providing less photons where absorbance is high and more photons where absorbance is low, a modified reactivity map is obtained. At wavelength regions with

low absorbance, the samples are provided with more photons, to account for the lower excitation probability. At wavelength regions with high absorbance, less photons are supplied, accounting for the higher excitation probability. Rather than a constant number of incident photons, this technique provides a sample with a constant number of *absorbed* photons, ultimately allowing to approximate a chromophore's inherent reactivity at a certain wavelength without calculation of exact quantum yields.

Figure 50 shows the absorption spectrum of styrylpyrene in MeCN, peaking at 378 nm ($\epsilon_{\text{max}} = 36\,300 \text{ L mol}^{-1} \text{ cm}^{-1}$). Yet, literature reports that the most efficient wavelength to trigger the dimerization reaction is 435 nm,¹³⁷ despite a vastly different absorption coefficient ($\epsilon_{435 \text{ nm}} = 100 \text{ L mol}^{-1} \text{ cm}^{-1}$). For the modified action plot experiment, absorption at 450 nm was picked as a reference point, and the number of photons was adjusted accordingly (see **Table S 5**). Subsequently, laser experiments were conducted using a 100 Hz *ns*-pulsed tuneable laser system, irradiating 10 mM solutions of styrylpyrene in deuterated MeCN at wavelengths between 310 nm and 470 nm. More data points were recorded in the wavelength regime between 410 nm and 470 nm, since in this region the reactivity displays the greatest variations. To account for different laser output energies at different wavelengths, the irradiation time was adjusted accordingly. For a full description of the tuneable laser setup, as well as the experimental parameters, refer to **sections 8.3.3** and **8.6.1**.

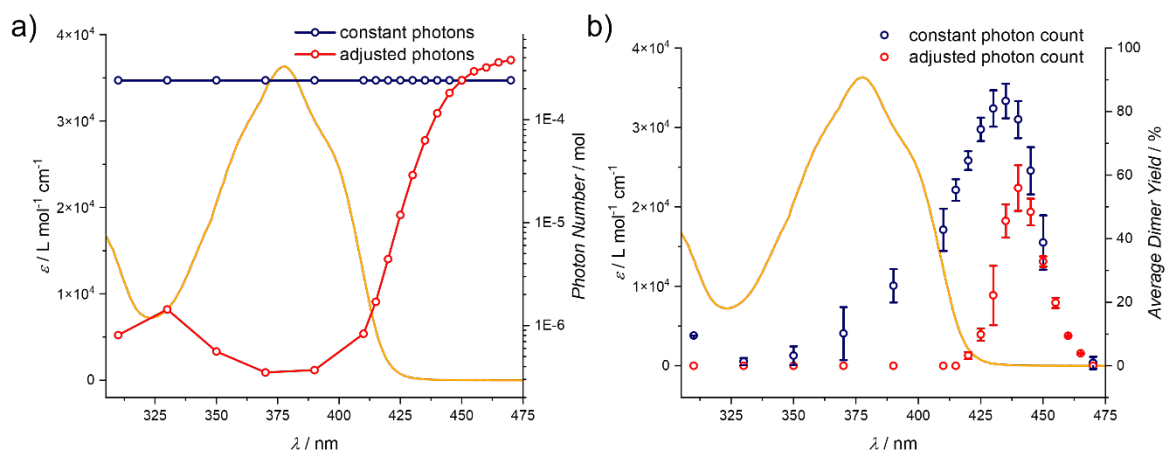


Figure 51: a) Overlay of the absorption spectrum of styrylpyrene and the applied photon counts. A logarithmic scale was chosen for the latter, to better visualise the shape of the profile. b) Action plots of the dimerization of styrylpyrene upon **constant** photon irradiation (adapted from *Marschner et al., Macromolecules* 2018, 51, 3802-3807) and upon irradiation with the photon number **adjusted** to the absorption spectrum. Error bars were obtained through 3x repetition of each experiment. For comparison, the absorption spectrum of styrylpyrene is overlaid.

In **Figure 51a**, the incident photons at different wavelengths are displayed for the constant-photon-count and the adjusted-photon-count experiment. The least photons are applied in the wavelength region between 370 nm and 390 nm, where the absorbance of styrylpyrene is maximal. Substantially more photons are applied in the visible light region, where the styrylpyrene absorption is lower. **Figure 51b** shows the obtained action plots after irradiation and $^1\text{H-NMR}$ spectroscopy analysis. It can clearly be seen that the wavelength-dependent reactivity profile is significantly narrower when the number of photons is adjusted to the absorption profile. While the conventionally obtained action plot exhibits significant dimer yield in the UV region, whereas in the modified action plot, no dimerization is observed at wavelengths shorter than 420 nm. Interestingly, the most efficient wavelength is slightly red-shifted, with the dimer yield peaking at 440 nm, compared to 435 nm in the conventional action plot. On the other hand, the absolute value of the maximum dimer yield is lowered by a third. These results emphasise that it is crucial to thoroughly monitor a chromophore with regard to its wavelength-dependent reactivity, before utilising it. The narrower, more red-shifted action plot underpins the suitability of styrylpyrene in λ -orthogonal systems, where precise reactivity windows are critical to selectively activate different photo-active species.

5.3 Concentration-Dependence

When the dimerization reaction is evaluated with regard to the chromophore concentration, several competing effects can be expected: It was shown that the dimerization occurs between an excited state molecule and a ground state molecule. Hence, the photodimerization is competing with several radiative and non-radiative relaxation pathways, depopulating the excited state. At lower concentrations, the reaction rate of a bimolecular dimerization reaction is lowered and will be affected even more due to the decreased probability of an encounter between an excited state molecule and a ground state molecule.¹⁸ However, this effect can be compensated by the greater penetration depth and the larger excess of photons available for excitation. To investigate which of these effects prevail, the [2+2] dimerization of styrylpyrene was carried out at two different concentrations (5 mM and 10 mM), screening a wavelength range between 415 nm and 465 nm (the wavelength range that was determined to lead to cycloaddition in the previous section). The resulting action plots are depicted in **Figure 52**.

While at 10 mM styrylpyrene concentration, the most efficient wavelength (440 nm) yield 56 % dimer, in the 5 mM experiment the yield is lowered by 25 % (relatively), 42 % dimer. This

is even though more photons are available per photo-active unit, and increased penetration depth. In a previous study it was reported that the dimerization reaction of styrylpyrene as a building block in polymer side chains has a higher reaction quantum yield than in free solution.¹³⁸ This was attributed to the confined environment in the polymer, resulting in a considerably higher local concentration of styrylpyrene. On the other hand, in the present experiment, the possibility of an excited state molecule encountering a ground state species for dimerization reaction is unfavored compared to other decay pathways which are concentration-independent (i.e., internal conversion, or fluorescence). Still, a 25 % drop in reaction yield is less than it would be expected from halving the concentration in a 2nd order bimolecular reaction (the reaction rate drops by 75 % when the concentration of the dimerization reactant is halved). It is therefore plausible that increased penetration depth and higher excess of photons still play a role, and the overall change in reactivity stems from the superposition of interplay of the aforementioned effects.

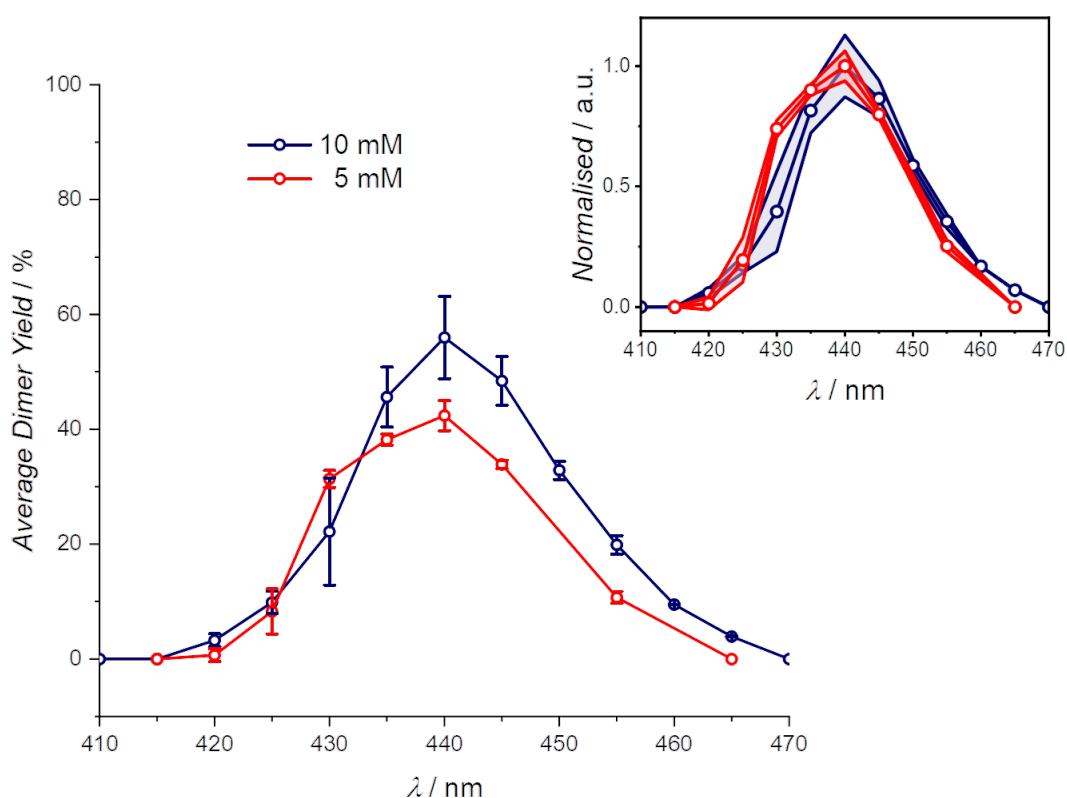


Figure 52: Overlay of the action plots of the dimerization of styrylpyrene at concentrations 5 mM and 10 mM in MeCN, with a constant number of absorbed photons. Inset: Normalised action plots. To make the slight blue-shift more visible, the error bars are enveloped.

Notably, at first glance, the shape and position of the action plot do not significantly change when switching to lower concentrations. At shorter wavelengths – in the wavelength-range

of the absorption band – most photons will be absorbed within the first millimetres of entering the solution, rendering a large fraction of the irradiation inaccessible to the majority of chromophores. At longer wavelengths, attenuation is lowered, and a larger portion of photons is able to penetrate through the entire pathlength of the sample, leading to higher conversion. With even longer wavelengths, the fraction of photons that is transmitted through the sample without leading to an excitation event will increase, eventually resulting in lower overall reaction yield. A trade-off between these two effects will partly determine the most efficient wavelength for the photoreaction, but excited state dynamics and competing absorbance of photo-adducts also play a role (refer to **section 3.4**). At lower chromophore concentrations, the influence of attenuation is expected to be less pronounced, therefore affecting the shape or position of the action plot. In the inset in **Figure 52**, the normalised action plots at 10 mM and 5 mM are depicted, revealing a slight blue-shift of the lower-concentration action plot. However, the most efficient wavelength is 440 nm in both action plots.

It must be noted that the range of concentrations in this experiment was limited. To reveal a more pronounced effect on the wavelength-dependent reactivity, a concentration range spanning over several orders of magnitude would likely be necessary. Due to practical reasons (i.e., analysis of the samples with $^1\text{H-NMR}$ spectroscopy) this was not possible. Still, the findings show that investigation of concentration-dependence is a valuable contribution to the characterization of a photo-induced reaction system.

5.4 Solvent-Dependence

Additionally, the [2+2] cycloaddition of styrylpyrene was carried out in a different solvent. DMSO was chosen because the absorption profile of styrylpyrene in DMSO displays a clear red-shift, and because of enhanced solubility of the chromophore. Moreover, DMSO- d_6 is a common deuterated solvent for $^1\text{H-NMR}$ analysis, allowing for a large number of conducted experiments. The absorption spectra of styrylpyrene in MeCN and DMSO are shown in **Figure 53** (left y -axis). It becomes apparent that the absorption profile in DMSO is slightly broadened and red-shifted by 11 nm, peaking at 389 nm. The juxtaposition of action plots in MeCN and DMSO in **Figure 53** (right y -axis) clearly shows a red-shift of the relative wavelength-dependent reactivity. The most efficient activation wavelength is shifted by 10 nm (from 440 nm to 450 nm). In addition, the dimer yield is noticeably lowered in DMSO, peaking at 15 % after 450 nm irradiation (compared to 56 % at 440 nm in MeCN). This discrepancy in reaction

efficiency is particularly interesting, because it is not accompanied by a decrease in absorbance. On the contrary, the maximum absorption in DMSO is slightly higher than in MeCN ($\epsilon_{\max}^{\text{DMSO}} = 37\,000 \text{ L mol}^{-1} \text{ cm}^{-1}$; $\epsilon_{\max}^{\text{MeCN}} = 36\,300 \text{ L mol}^{-1} \text{ cm}^{-1}$).

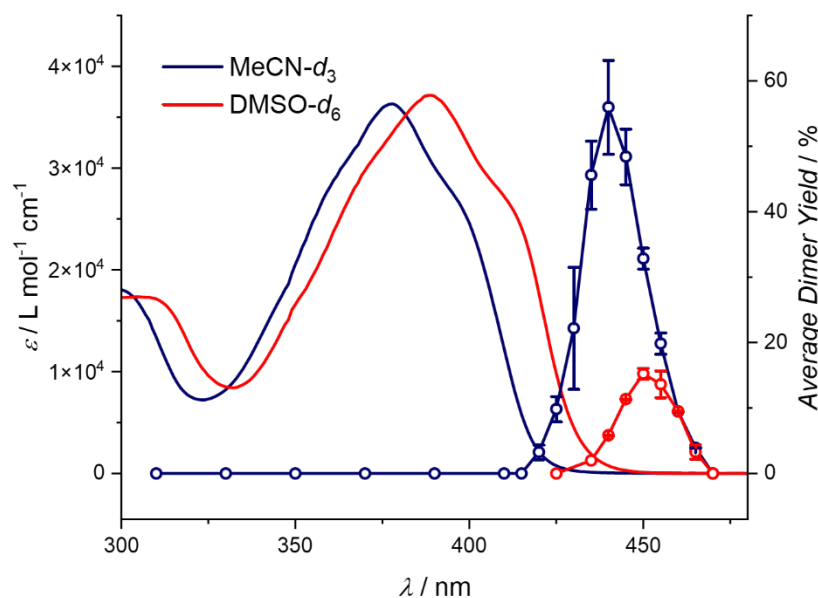


Figure 53: Overlay of absorption spectra of styrylpyrene in MeCN and DMSO, as well as solvent-dependent action plots (at 10 mM concentration in the respective solvent).

Intriguingly, the decrease in reactivity cannot be readily attributed to differences in excited state channel branching, either. Although radiative decay is an important competing relaxation pathway for this kind of reaction, the fluorescence quantum yield in MeCN is 1.6 times higher than in DMSO (**Figure S 38**). With regard to solvent-dependent fluorescence and reactivity, literature reports both increased and decreased fluorescence intensity (accompanied by an increase in reactivity), i.e., in the case of [2+2] cycloadditions of coumarin²⁵⁴ and stilbene.²⁵⁵ In the case of styrylpyrene, another important factor is its ability to form aggregates (stacking).²⁵⁶ The degree of stacking generally depends on the solvent, which was exemplified extensively in the case of DNA bases.²⁵⁷ Stacking can have a strong effect on the efficiency of photoreactions, because it can lead to favourable prearrangement of the photoactive moieties, facilitating the dimerization.²⁵⁸ The propensity for prearranged molecules enhancing the reactivity is generally correlated to the solvent polarity. In the case of polar solvents, solvophobic aggregation of nonpolar reactants is favoured.²⁵⁹ In the case of styrylpyrene, however, this does not seem to be applicable: DMSO is slightly more polar than MeCN, yet does not lead to higher reaction yield ($\epsilon_r^{\text{DMSO}} = 47.24$, $\mu_r^{\text{DMSO}} = 3.96 \text{ D}$; $\epsilon_r^{\text{MeCN}} = 36.64$,

$\mu^{\text{MeCN}} = 3.93 \text{ D}$).²⁶⁰ Another factor is therefore likely more dominant: DMSO is considerably more viscous than MeCN, surpassing its viscosity by a factor of close to 6 ($\eta^{\text{DMSO}} = 1.99 \text{ cP}$; $\eta^{\text{MeCN}} = 0.37 \text{ cP}$).²⁶⁰ In a more viscous environment, molecule motion is hindered, resulting in a lower probability of an excited-state molecule encountering a ground-state molecule before relaxing back into ground-state (refer to the previous chapters).¹⁷ It is also noteworthy that viscosity heavily depends on temperature, which is why it is of critical importance to conduct the photoreactions under constant temperature. This is further described in the following section.

5.5 Temperature-Dependence

While giving access to higher excited states without the need for elevated temperatures is one of the defining features of photochemistry, understanding the temperature-dependent behaviour of photoreactions can still be critical in the context of solvent viscosity (as outlined in the previous section), or biological applications. A small number of experiments was therefore carried out at elevated temperatures (37 °C), monitoring the efficiency of the [2+2] dimerization of styrylpyrene in MeCN at three different wavelengths (425 nm, 440 nm, and 460 nm). While only minor changes occur in the temperature dependent absorption profiles at 37 °C compared to 20 °C (**Figure 54**, left *y*-axis), interestingly, reactivity is lowered by a significant margin. Within the investigated range of wavelengths, the average dimer yield is decreased by 60-70 %, whereas the shape of the action plot remains unchanged (peak reactivity at 440 nm, **Figure 54**, right *y*-axis). These findings seemingly contradict the previous statement that higher temperatures will lead to lower viscosity, and hence accelerate the dimerization reaction (refer to previous section). However, in previous studies, elevated temperatures have been reported to shorten the triplet lifetime of styrylpyrene,²⁶¹ while also affecting the *cis/trans* isomerisation.²⁶² It is therefore possible that the affected *cis/trans* equilibrium disfavours the [2+2] cycloaddition, given that the *cis*-isomer of other enes has been reported to be less reactive in photodimerization reactions compared to the *trans*-isomer (i.e., in the case of 3-cyanovinylcarbazole²⁶³). It can also be reasoned that unfavourable relaxation pathways prevent the necessary excited state from being populated. Thermal scission of the cycloadduct (cycloreversion) is unlikely, since [2+2] cycloaddition and cycloreversion are thermally forbidden.

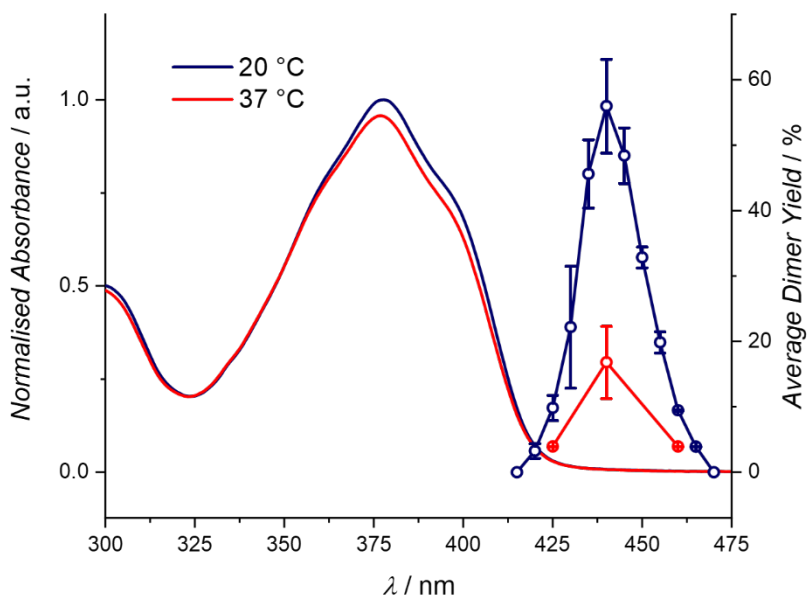


Figure 54: Overlay of absorption spectra of styrylpyrene at 20 °C and 37 °C, as well as temperature-dependent action plots (at 10 mM concentration).

5.6 Conclusion

In summary, in the present chapter, a new type of wavelength-dependent reactivity map was introduced and utilized to investigate the [2+2] cyclodimerization of styrylpyrene with regard to three critical parameters: Concentration, solvent, and temperature. The newly developed action plot method accounts for the absorption of a chromophore and supplies the sample with a constant number of *absorbed* photons, rather than a constant number of incident photons. The resulting action plot displays a slightly red-shifted conversion maximum, while simultaneously being considerably narrower than its conventional counterpart.

In the concentration dependent study, a somewhat lower reaction yield was found (25 % less yield at 5 mM than at 10 mM), which was attributed to a combination of attenuation effects, as well as a preference for radiative and non-radiative decay pathways that do not lead to photoreaction. When normalised, the data plot obtained at the lower concentration is slightly blue-shifted, which is associated with the lessened absorbance of the sample solution. However, to obtain a clearer picture, it will be necessary to conduct experiments covering a wider range of concentrations.

In contrast, changing the solvent from MeCN to DMSO led to a significant red-shift of the wavelength-dependent reactivity plot, while simultaneously reducing the overall dimer yield.

While it has been demonstrated numerous times that reactivity does not necessarily follow absorbance, this is the first time demonstrating that a solvent-induced bathochromic absorption shift can translate this non-congruence, leading to activation at longer wavelengths.

When carrying out the photoreaction at elevated temperatures (37 °C), counterintuitively, it does not proceed faster, but yields lower amounts of cycloadduct, while not causing any shift of the action plot. Although higher temperatures should lead to a lower viscosity and, hence, facilitate the encounter of two styrylpyrene moieties, a combination of unfavourable excited state dynamics as well as shifting of the *cis/trans* equilibrium towards the less reactive isomer likely result in a decrease of reactivity.

Table 5: Summarised findings after investigating the dimerization of styrylpyrene, varying different parameters.

Parameter changed	Relative change of maximum yield / %	Shift of reactivity maximum / nm
Photon count adjusted	-33	+5
10 mM → 5 mM	-25	0
MeCN → DMSO	-73	+10
20 °C → 37 °C	-70	0

In conclusion, the results of this chapter demonstrate that seemingly minor changes of certain critical parameters can have a vast influence on the reaction dynamics at different wavelengths. To fully characterise a photo-active chromophore and expose its true potential for λ -orthogonal photoreactions, revealing the influence of these parameters – at least qualitatively – is of critical importance.

6 CONCLUDING REMARKS

A summary of the results is given at the end of each chapter, which is why no extensive summary is given here. Nonetheless, the following chapter will try to encapsulate the findings of the thesis and put them into context with the introductory chapter.

In the present thesis, a new photoactive molecule, APAT, was designed through synthetic rationale, combining the bathochromic properties of an extended aromatic system and an electron-donating auxochrome. The compound was thoroughly characterised by means of spectroscopic properties and subjected to a detailed wavelength-dependent small-molecule ligation reaction, plotting the reaction yield as a function of wavelength. The experiments revealed that the reactivity is strongly shifted compared to the absorption spectrum, and that APAT can be activated at wavelengths up to 510 nm. Following this, a simple LED setup was used to employ APAT as a polymer end-group modification agent, revealing that full end-group conversion is possible up to 515 nm. To date, this is the most red-shifted tetrazole activated in a single-photon process. By shifting the frontier of visible light activated tetrazoles by almost 100 nm, it constitutes a valuable contribution to visible light-driven chemistry, moving towards exploitation of the full visible spectrum.

By combining APAT with a UV-activated chromophore, a binary photo-activated system was established that allowed for activation of different photoreactions at disparate wavelengths through a combination of distinct reaction quantum yields, as well as separated absorption spectra and action plots. After carefully selecting four different wavelengths based on the action plots of both chromophores, kinetic measurements of the photoreactions were conducted, exposing the two most suitable wavelengths for λ -orthogonality. The orthogonal nature of both reactions was demonstrated in a sequential LED-setup, switching between two colours of light in any order. The reaction system displays full sequence-independence, allowing for fully λ -orthogonal activation of both chromophores. This is the first time such a back-and-forth switching of light has been enabled in a batch reaction of two bond-forming reactions.

After demonstrating how certain features of chromophores can predetermine the wavelength-dependent reactivity profile and proving that detailed knowledge thereof can help with implementing λ -orthogonality, the final chapter addressed the modulation of wavelength-dependent reactivity through external stimuli. A new type of action plot was introduced,

taking into account the absorbance of a sample, and then applied to monitor the influence of parameters such as chromophore concentration, solvent, and temperature. These studies revealed vast differences in reactivity even through seemingly small changes in the environment. Especially, changes in solvent and temperature led to substantially lowered reaction yields, but lowering the concentration by half also resulted in a lower reaction yield. On the other hand, a red-shift of the absorption spectrum in DMSO translated into a red-shift of reactivity. This is the first demonstration that the non-congruence of absorbance and reactivity follows a bathochromic solvent effect. These unprecedented findings underline the importance of thoroughly mapping a chromophore's reactivity with regard to these parameters.

In conclusion, action plots are a powerful tool for characterising a single chromophore. However, comparing different action plots is problematic since the conditions they were recorded under vary from study to study. The present thesis elucidated the profound consequences such disparate conditions can have on the reactivity. The advanced methodology proposed herein allows comparison of the wavelength-dependent reactivity of multiple species alongside each other, thus eliminating the impact that different environments can have on different action plots. Furthermore, by measuring wavelength-dependent kinetics, traditional action plots are extended by another dimension, allowing for quantification of the λ -orthogonality of a given system. Hopefully, this contribution will prove valuable in the development of more λ -orthogonal systems and their application in polymer and material science.

7 OUTLOOK

APAT displays a range of interesting features, deeper investigation of which may prove worthwhile in the future. While APAT was utilized successfully as a polymer end-group modification agent, implementation of APAT into polymers – as side chain or end-group – and subsequent light-induced polymer-polymer ligation or network formation, are possible endeavours in the future. The unprecedented property of fluorescence-loss upon cycloaddition may also be exploited, i.e., if an APAT polymer chain is immobilised on a surface. Loss of fluorescence can then easily indicate successful surface modification. Fundamental work for modification of APAT with a polymer chain has already been done in this thesis, in form of the functional APAT derivatives APAT-OH and APAT-COOH, bearing a hydroxy group and a carboxylic acid group, respectively. These may either be used to further extend the molecule into a suitable initiator, such as a RAFT agent or an ATRP (atom transfer radical polymerisation) initiator. Likewise, APAT-OH can serve as an initiator in anionic polymerisation. Alternatively, the hydroxy group or the carboxylic acid group can be employed to attach the respective APAT derivative to a pre-existing polymer, i.e., a poly(ethyleneglycol) (PEG) chain. These polymers could then be tested with focus on their suitability as λ -orthogonal 3D-photoresists. An interesting element to characterise in this context is the two-photon-absorption (2PA) cross section of APAT, which quantifies its ability for non-linear absorption,¹⁶² which is readily achieved in a z-scan setup, where the sample is moved along the axis of a focussed laser beam.²⁶⁴ Large higher-order absorption cross sections are prerequisite for spatially resolved multiphoton lithography.²⁵¹ The red-shifted nature of the APAT absorption profile and wavelength-dependent reactivity may prove to be very beneficial in this respect.

The palette of applications for APAT may be extended by exploiting the pH-responsivity. The ability to switch the absorbance (and, possibly, the reactivity) back and forth between UV and visible light through addition of acid or base constitutes a smart-feature, enabling to further modulate the reactivity through an external trigger. Unfortunately, initial experiments in this direction were unsuccessful; although addition of acid disabled reactivity at 450 nm, neither was it shifted to the UV, nor could it be restored through neutralisation (despite full recovery of the absorption spectrum). It was speculated that water was the reason for the quenching effect. It may therefore be worthwhile to screen a number of acids and bases. Obviously, being able to switch the reactivity on and off offers a highly desirable additional level of control. It

was observed that in the presence of acid the protonated species APAT-H⁺ – upon irradiation with UV light – reacted with residual water highly efficiently, forming exclusively the water adduct (SP2, the structure of which is shown in **Figure 46** in **section 4.4**) as a main product. This is attributed to a strongly changed excited state manifold in the protonated molecule. SP2 was not isolated, but the product mixture displayed a purple colour, which – upon neutralisation – turned red, and could be switched back and forth as well through changes in pH-value. While SP2 was not the desired product, the smoothness of the reaction and the interesting halochromic properties may be worth investigating. It might be possible to transfer this excellent reactivity towards other nucleophiles such as alcohols, which could serve as a highly efficient, switchable ligation reaction.

A key obstacle in the present thesis was the difficulty of synthesising APAT in sufficient quantity, due to the inherent formation of isomers during the nitration step (section 3.2.1), which decreases the overall yield significantly – combined with the notoriously low reaction yields in the final synthetic step. It is therefore proposed that for future applications, the separation of isomers is omitted and instead the isomeric mixture is used for the following reaction steps, as well as the final photoreactions. This can greatly increase the availability of APAT, facilitating the design of future experiments. Naturally, the difference in reactivity of the isomeric mixture compared to the pure 1,8-isomer must be evaluated, but for many applications it may be dispensable.

Additionally, it can be interesting to modify the chromophore even further, i.e., by decorating it with additional dimethylamino groups. As a starting point, the *N,N*-dimethylamino pyrene diamine can be subjected to another methylation step, forming the *N,N,N',N'*-tetramethyl pyrene diamine, which could then undergo nitration as before. Of course, thorough reaction optimisation is required to avoid formation of a double-nitrated pyrene core, since the additional amino group may strongly activate the core for electrophilic substitution. If successful, the resulting *N,N,N',N'*-tetramethyldiamino pyrene aryl tetrazole may show even stronger red-shifted absorption and reactivity than APAT, thanks to the electron-rich nature of the pyrene chromophore. It would also be interesting to quantify the reaction quantum yield of this compound. Although the low efficiency of the APAT NITEC reaction is one of the basic conditions of the λ -orthogonal *o*MBA/APAT system, it might be beneficial to identify chromophores that react not quite so inefficiently, while still sufficing the quantum yield-based approach for λ -orthogonality.

It will also be necessary to extend the study of the influence of the chemical environment on light-driven cycloadditions - using styrylpyrene, tetrazoles or entirely different chromophores. Especially the temperature-dependence of systems other than styrylpyrene will be interesting to investigate. The strongly lowered reactivity of styrylpyrene at elevated temperatures was attributed mostly to an unfavourable *cis/trans* equilibrium, but also to disadvantageous excited state dynamics. Both these factors may not play a role in other photoactive systems, as the excited state manifold will be situated differently, and *cis/trans* isomerisation does not play a role. Consequently, elevated temperatures might indeed be suited to overcome problems posed, i.e., by highly viscous solvents. This way, instead of lowering the reactivity, DMSO (or other solvents that cause a red-shift) can be exploited to advance the bathochromic shift even more.

Similarly, extending the concentration dependence of photoreactions can give valuable insight into the role that light attenuation plays in the discrepancy between absorptivity and reactivity. While for styrylpyrene, a slight blue-shift of the action plot was observed at halved concentration, this finding might be fortified (or disproved) if the range of concentrations is greater, i.e., spanning over two or three orders of magnitude. Of course, this can cause problems on other fronts, such as sample preparation or analysis of the product mixture.

8 EXPERIMENTAL PART

8.1 Materials

All chemicals were reagent or analytical grade and used as received, unless stated otherwise. 11-bromo-undecan-1-ol (98 %, Combi-Blocks), 1-aminopyrene (97 %, Sigma-Aldrich), 1-bromopyrene (95 %, Alfa Aesar), 1-ethyl-3-(3-dimethylaminopropyl)carbodiimide hydrochloride (EDC, 98 %, Sigma-Aldrich), 4-(dimethylamino) pyridine (DMAP, >99 %, Sigma-Aldrich), 4-acetoxystyrene (96 %, Acros Organics), 4-carboxybenzaldehyde (98 %, Thermo Fisher Scientific), 4-cyano-4-(phenylcarbonothioylthio)pentanoic acid (97 %, Sigma-Aldrich), acetic acid (glacial, AJAX FineChem), acetic anhydride (analytical grade, Chem Supply), acetonitrile (HPLC grade, Chem Supply), acetonitrile- d_3 (>99 %, Sigma-Aldrich), aluminium oxide activated basic (for chromatography, Thermo Fisher Scientific), azoazobisisobutyronitrile (AIBN, 12 w% in acetone, recrystallized from ethanol, Sigma-Aldrich), benzaldehyde (99 %, Sigma-Aldrich), chloroform (99.8 %, Thermo Fisher Scientific), chloroform-D ($CDCl_3$, 99.8 % D, + silver foil, Nova Chem), cyclohexane (ACS grade, Merck), dichloromethane (analytical grade, Thermo Fisher Scientific), dimethyl sulfoxide-D ($DMSO-d_6$, 99.9 % D, Nova Chem), dimethylformamide (99.8 %, Sigma-Aldrich), ethanol (analytical grade, AJAX FineChem), hydrochloric acid (32 w%, Thermo Fisher Scientific), iodomethane (laboratory grade, Chem Supply), magnesium sulfate anhydrous (>98 %, Merck), methanol (analytical grade, Thermo Fisher Scientific), methyl methacrylate (99 %, deinhibited by passing through a basic aluminium oxide column prior to use, Sigma-Aldrich), N,N-dimethylacetamide (99+ %, Thermo Fisher Scientific), nitric acid (65 w%, Thermo Fisher Scientific), palladium(II) acetate (47 % Pd, Merck), palladium on carbon (10 w%, Sigma-Aldrich), potassium carbonate anhydrous (analytical grade, Chem Supply), p-toluenesulfonyl hydrazide (97 %, Sigma-Aldrich), pyridine (99 %, Sigma-Aldrich), sodium chloride (analytical grade, Thermo Fisher Scientific), sodium hydrogen carbonate (analytical grade, Thermo Fisher Scientific), sodium nitrite (97 %, Thermo Fisher Scientific), sodium sulfate anhydrous (analytical grade, Thermo Fisher Scientific), tetrahydrofuran (HPLC grade, Thermo Fisher Scientific), toluene (analytical grade, Thermo Fisher Scientific), triethanolamine (98 %, Alfa Aesar), triethylamine (>99 %, Sigma Aldrich), triphenylphosphine (99 %, Sigma-Aldrich).

Thin-layer chromatography (TLC) was performed on silica gel 60 F254 alumina sheets (Merck) and visualized by UV light. Column chromatography was run on an Interchim XS420 + SofTA Model 400 ELSD, or manually on silica gel 60 (0.04-0.06 mm, 230-400 mesh ASTM, Merck).

8.2 Analysis and Instrumentation

8.2.1 Nuclear Magnetic Resonance (NMR) Spectroscopy

QUT: ^1H -NMR, ^{13}C -NMR as well as DEPT 135, COSY, HSQC and HMBC-spectra were recorded on a Bruker System 600 Ascend LH, equipped with a BBO-Probe (5 mm) with z-gradient (^1H : 600.13 MHz, ^{13}C 150.90 MHz). Resonances are reported in parts per million (ppm) relative to tetramethylsilane (TMS). The δ -scale was calibrated to the respective solvent signal of CHCl_3 or DMSO for ^1H spectra and for ^{13}C spectra on the middle signal of the CDCl_3 triplet or the DMSO quintet. The annotation of the signals is based on HSQC-, COSY- and DEPT-experiments.

KIT: ^1H -NMR experiments were conducted on a Bruker Ascend 400 instrument, performing at 400 MHz. The δ -scale is referred to the respective deuterated solvents acetonitrile- d_3 or DMSO- d_6 , respectively. Abbreviations for the multiplicity of the respective signals are: singlet (s), doublet (d), doublet of the doublet (dd), triplet (t), quartet (q), quintet (qu), multiplet (m).

8.2.2 Diffusion Ordered Spectroscopy (DOSY)

DOSY experiments based on ^1H NMR were performed in CDCl_3 at 296 K on a Bruker 400 UltraShield spectrometer equipped with a Quattro Nucleus Probe (QNP) with an operating frequency of 400 MHz (^1H). A sequence with longitudinal eddy current delay (LED) using bipolar gradients was employed in order to compensate eddy currents. Bipolar gradient δ and a diffusion delay Δ were determined separately for each sample. Gradient strength was linearly incremented from 2% at 0.96 G to 95% at 45.7 G in 24 steps. The obtained data was processed with TopSpin 4.0.6 and Dynamics Center 2.5.3.

After Fourier transform of the 1D spectra, the signal decay along the gradients G was fitted to

$$(G) = I_0 * e^{-D * G^2 * \gamma^2 * \delta^2 * \left(\Delta - \frac{\delta}{3}\right)} * 10^4 \quad (8 - 1)$$

with the gyromagnetic ratio γ and the full signal intensity I_0 .

8.2.3 Liquid Chromatography Coupled Mass Spectrometry (LC-MS)

Liquid-chromatography coupled mass spectrometry (LC-MS) measurements were performed on an UltiMate 3000 UHPLC System (Dionex, Sunnyvale, CA, USA) consisting of a pump (LPG 3400SZ), autosampler (WPS 3000TSL) and a temperature-controlled column compartment (TCC 3000). Separation was performed on a C18 HPLC column (Phenomenex Luna 5 μ m, 100 Å, 250 \times 2.0 mm) operating at 40 °C. Gradient-free acetonitrile was used as eluent at a flow rate of 0.40 mL min⁻¹. The flow was split in a 9:1 ratio, where 90 % of the eluent was directed through a DAD UV-detector (VWD 3400, Dionex) and 10 % was infused into the electrospray source. Spectra were recorded on an LTQ Orbitrap Elite mass spectrometer (Thermo Fisher Scientific, San Jose, CA, USA) equipped with a HESI II probe. The instrument was calibrated in the m/z range 74-1822 using premixed calibration solutions (Thermo Scientific). A constant spray voltage of 3.5 kV, a dimensionless sheath gas and a dimensionless auxiliary gas flow rate of 5 and 2 were applied, respectively. The capillary temperature and was set to 300 °C, the S-lens RF level was set to 68, and the aux gas heater temperature was set to 100 °C. Samples were prepared at concentration of 0.5 mg mL⁻¹ in MeCN and filtered through 0.22 μ m PTFE membrane filters prior to injection.

8.2.4 DMAc-Size Exclusion Chromatography (SEC)

The SEC measurements were conducted on a PSS SECurity² system consisting of a PSS SECurity Degasser, PSS SECurity TCC6000 Column Oven (60 °C), PSS GRAM Column Set (8x150 mm 10 μ m Precolumn, 8x300 mm 10 μ m Analytical Columns, 1000 Å, 1000 Å and 30 Å) and an Agilent 1260 Infinity Isocratic Pump, Agilent 1260 Infinity Standard Autosampler, Agilent 1260 Infinity Diode Array and Multiple Wavelength Detector (A: 254 nm, B: 360 nm), Agilent 1260 Infinity Refractive Index Detector (35 °C). HPLC grade DMAc, 0.01 M LiBr, is used as eluent at a flow rate of 1 mL min⁻¹. Narrow disperse linear poly(styrene) (M_n :

266 g mol⁻¹ to 2.52x10⁶ g mol⁻¹) and poly(methyl methacrylate) (M_n: 202 g mol⁻¹ to 2.2x10⁶ g mol⁻¹) standards (*PSS ReadyCal*) were used as calibrants. All samples were passed over 0.22 μm PTFE membrane filters. Molecular weight and dispersity analysis was performed in *PSS WinGPC UniChrom* software (version 8.2).

8.2.5 Chromatography

Flash chromatography was performed on a *Interchim XS420+* flash chromatography system consisting of a SP-in-line filter 20-μm, an UV-VIS detector (200-800 nm) and a *SofTA Model 400* ELSD (55 °C drift tube temperature, 25 °C spray chamber temperature, filter 5, EDR gain mode) connected via a flow splitter (*Interchim Split ELSD F04590*). The separations were performed using a *Interchim* dry load column (liquid injection) and a *Interchim Puriflash Silica HP 30 μm* column or *Interchim Puriflash Silica HP 15 μm* column (were indicated).

8.2.6 UV/Vis Spectroscopy

QUT: UV-Vis spectra were recorded on a Shimadzu UV-2700 spectrophotometer equipped with a CPS-100 electronic temperature control cell positioner. Samples were prepared in solvent MeCN and measured in 10 mm Hellma Analytics quartz high precision cells at 25 °C. Molar absorption coefficients were obtained by measuring spectra at various concentrations and applying Beer-Lambert's law to calculate a linear fit:

$$OD = \varepsilon * d * c \quad (8 - 2)$$

KIT: The UV/Vis spectra were recorded on a Cary 100 UV-Visible Spectrophotometer (Agilent Technologies, USA) equipped with a tungsten halogen light source (190 to 900 nm, accuracy +/-2 nm) and a R928 PMT detector. The samples were baseline corrected with respect to pure solvent and spectra were recorded between 200 and 800 nm at ambient temperature.

8.2.7 Fluorescence Spectroscopy

Fluorescence spectra were measured using a Cary Eclipse Fluorescence Spectrophotometer from Agilent Technologies. Voltage was set to medium, and the excitation wavelength was set to 430 nm with an excitation and emission slit of 5 nm (scan rate 600 nm min⁻¹). Scan-range was 440-800 nm. Samples were measured at ambient temperature in Hellma Analytics quartz high precision cells with a path length of 10 mm.

Fluorescence Quantum yields were measured using Coumarin 307 in EtOH as a fluorescence standard ($\Phi_F = 0.56$), with excitation wavelength 395 nm, using the following formula:²⁶⁵

$$\Phi = \Phi_R * \frac{I}{I_R} * \frac{1 - 10^{-A_R}}{1 - 10^{-A}} * \frac{n^2}{n_R^2} \quad (8 - 3)$$

where Φ is the fluorescence quantum yield of compound, I is the integral of the fluorescence spectrum, A is the absorbance of the sample and n is the refractive index of the solvent. Index R indicates the same entries for the reference sample (C307 in EtOH).

8.3 Irradiation Setups

8.3.1 20 Hz Tuneable Laser System (QUT)

Laser experiments for the action plot measurements of APAT and DEF, as well as the kinetic measurements for *o*MBA, APAT and NHEM, were conducted using a *Coherent Opolette 355* tuneable OPO, operated at wavelengths between 210 nm and 2400 nm with a full width half maximum of 7 ns and a repetition rate of 20 Hz. The emitted pulse, which has a flat-top spatial profile, was expanded to 6 mm diameter using focussing lenses and directed upwards using a prism. The energy of the laser pulses was downregulated by an attenuator (polarizer). The beam was redirected into the vertical cylindrical hole of a custom-made sample holder, which contains the samples during the experiments. These glass vials were crimped 0.7 mL vials by LLG Labware, Lab Logistic Group GmbH (Art. Nr. 4-008202). The energy of the incident laser pulses was measured by an Energy Max PC power meter (Coherent) directly above the sample holder. Prism and sample holder were positioned in a way that the complete diameter of the hole of the sample holder was covered by the incident laser beam.

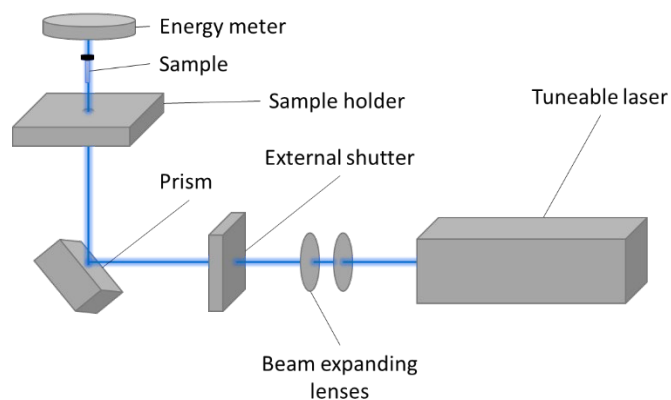


Figure S 1: Experimental setup for the tuneable laser experiments at QUT. Energy output is adjusted using an attenuator and read out with an energy meter before the sample is inserted into the sample holder.

Control over incident photon number

The number of photons n_p ($[n_p] = \text{mol}$) that a monochromatic laser pulse contains can be calculated by application of the Planck-Einstein relation from the energy of the pulse E_{pulse} , the incident wavelength λ , Planck's constant h and the speed of light c .²⁶⁶

$$n_p = \frac{E_{\text{pulse}} \lambda}{h c N_A} \quad (8 - 4)$$

If the absorption of the glass vial and the extent of reflection and scattering at the vial at the respectively relevant wavelength is known, a target energy value can be calculated that must be reached during the above-described measurement to guarantee that the desired number of photons penetrates the sample solution during the subsequent irradiation. The wavelength dependent transmittance of the glass vials was determined experimentally using the above setup. Three glass vials were randomly selected as calibration vials. For varying wavelengths and in each case at a constant power output of the laser the energy was measured both with and without the calibration vials fitted into the sample holder. The top parts of these vials were cut off to minimize errors in the procedure, since only the bottom and sides of the glass vials would contribute significantly to the reduction of the photon flux that enters the solution.

The measured energy per pulse without a calibration vial in the sample holder is denoted as E_0 and the measured energy per pulse with a calibration vial in the sample holder as E_n . The transmittance was calculated as the ratio of E_n to E_0 . The average transmittance over the measurements of the three vials (T_λ) was plotted together with the respective error (compare **Figure S 2**).

$$T_{\lambda} = \frac{E_n}{E_0} \quad (8 - 5)$$

The target energy per pulse E_0 can be calculated directly from the wavelength λ , the number of pulses k , the transmittance of the glass vial at the respective wavelength T_{λ} and the desired total photon count n_p .

$$E_0 = \frac{n_p N_A h c}{k T_{\lambda} \lambda} \quad (8 - 6)$$

By controlling the target E_0 at the respective wavelength, the number of photons that penetrate each sample solution of one set of experiments as described in the following subsections was guaranteed to be identical despite irradiation at different wavelengths.

Transmittance of glass vials

The transmittance of the glass vials that were used for photoreactions with the tuneable laser system was determined following a procedure described previously.¹¹³ Measurement of the energy of laser pulses at a constant energy output was carried out directly above the sample holder first without a glass vial in the sample holder and subsequently with an empty glass vial in the sample holder. The headspace section of the glass vials was removed for these measurements to detect only the absorbance of the bottom of the vial. The described procedure was performed for three individual glass vials to account for variabilities between the vials. The obtained averaged values are listed in **Table S 1**.

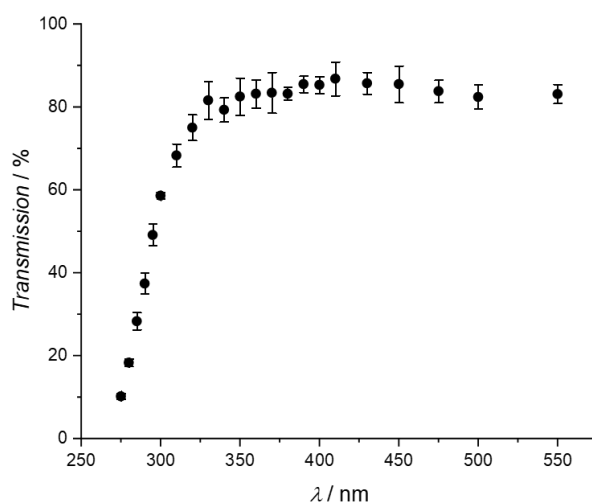


Figure S 2: Calibration of the glass vial transmittance.

Table S 1: Transmittance of the glass vials used for the laser experiments at QUT.

λ / nm	T_λ / %	Mean Deviation / %
275	10.2	0.7
280	18.3	0.9
285	28.3	2.1
290	37.4	2.5
295	49.1	2.6
300	58.6	0.8
310	68.3	2.8
320	75.0	3.1
330	81.6	4.5
340	79.3	2.9
350	82.5	4.5
360	83.2	3.4
370	83.4	4.9
380	83.2	1.6
390	85.5	2.0
400	85.3	2.0
410	86.8	4.1
430	85.7	2.6
450	85.5	4.4
475	83.8	2.7
500	82.4	2.9
550	83.1	2.3

8.3.2 LED Setup

LED irradiation experiments were conducted in a benchtop in-house built photoreactor, containing a magnetic stirrer and a 3D-printed sample holder, which could be placed on top of the LED. A tube was positioned so that the LED and sample holder were cooled by a constant stream of air. The sample holder guaranteed a distance of 10 mm between the LED and the bottom of the vial.

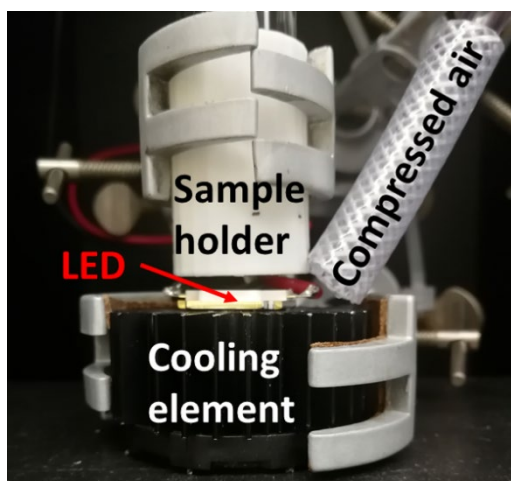


Figure S 3: Setup of the LED irradiation experiments.

LED emission spectra were recorded using an Ocean Insight Flame-T-UV-Vis spectrometer, with an active range of 200-850 nm and an integration time of 10 ms. LED output energies were recorded using a Thorlabs S401C thermopile sensor, with an active area of 100 mm² and a wavelength range of 190 nm – 20 μm, connected to a Thorlabs PM400 energy meter console. The emitted power from each LED was measured for 60 seconds at a fixed distance from the sensor, after which the mean and standard deviation of the emission could be determined. LEDs were cooled during measurement to minimise any thermal effects on the emission power or sensor performance.

8.3.3 100 Hz Tuneable Laser System (KIT)

An Innolas Tuneable Laser System SpitLight 600 OPO was applied as a light source. An optical parametric oscillator (OPO) was pumped with a diode pumped Nd:YAG laser (repetition rate 100 Hz). The energy of the laser pulses was downregulated by an attenuator (polarizer). The beam is redirected into the vertical cylindrical hole of a custom-made sample holder, which contains the samples during the experiments (**Figure S 4**). These glass vials are crimped 0.7 mL vials by LLG Labware, Lab Logistic Group GmbH (Art. Nr. 4-008202). The energy of the incident laser pulses was measured by an Energy Max PC power meter (Coherent) directly above the sample holder. Prism and sample holder are positioned in a way that the complete diameter of the hole of the sample holder is covered by the incident laser beam.

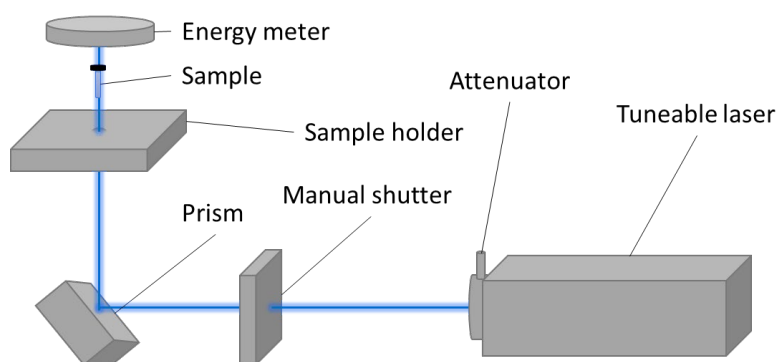


Figure S 4: Experimental setup for the tunable laser experiments at KIT. The energy output is regulated with the attenuator and controlled with the energy meter. Measurement of energy and irradiation of samples cannot be carried out simultaneously. An individual setting of the attenuator is necessary before each irradiation experiment. The shutter was opened and closed manually *via* the connected computer.

Control over incident photon number

Control over the incident photon number was performed similarly to the previously described setup (refer to **section 8.3.1**).

Transmittance of glass vials

The glass vials that were used for photoreactions at KIT were crimped 0.7 mL vials by LLG Labware, Lab Logistic Group GmbH (Art. Nr. 4-008202). Transmittance of the glass vials was determined similarly to the procedure described previously (refer to **section 8.3.1**)¹¹³. The obtained averaged values are listed in TABLE.

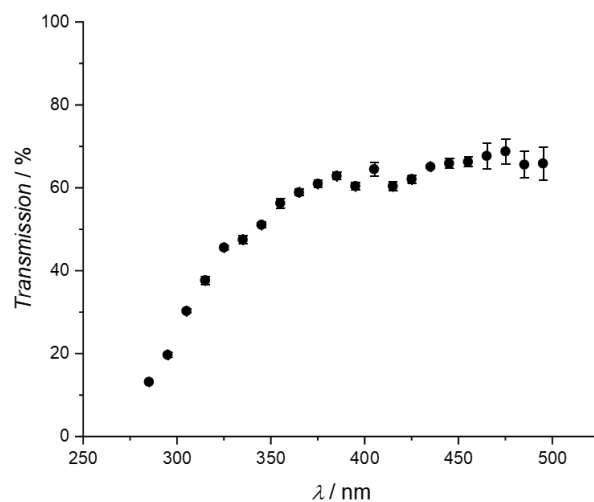


Figure S 5: Calibration of the glass vial transmittance.

Table S 2: Transmittance of the glass vials used for the laser experiments at KIT.

λ / nm	T_λ / %	Mean Deviation / %
285	13.2	0.2
295	19.7	0.6
305	30.3	0.5
315	37.7	1
325	45.6	0.5
335	47.5	1
345	51.1	0.6
355	56.3	1.2
365	58.9	0.8
375	61	0.9
385	62.9	0.9
395	60.4	0.9
405	64.5	1.6
415	60.4	1.1
425	62.1	0.9
435	65.1	0.3
445	65.9	1.2
455	66.3	1.2
465	67.7	3.1
475	68.8	3.0
485	65.6	3.2
495	65.9	4.0

8.4 APAT and Diethylfumarate Photoreaction

8.4.1 Sample Preparation for Action Plot Measurements

APAT and diethylfumarate were employed in a 1:4 ratio, with the total concentration being 0.5 mg mL^{-1} as per the LC-MS sample requirements. Sample solutions were freshly prepared every day and not kept overnight. Stock solutions (APAT: 0.46 mM ; diethylfumarate: 1.84 mM in MeCN) were prepared and degassed with N_2 for 15 min, then 0.3 mL were withdrawn and added to capped photo vials that had previously been degassed with N_2 for 5 min. The samples were irradiated using the Coherent *Opolette* tuneable laser system and subsequently were filtered and directly used for LC-MS.

8.4.2 Power Settings of the *ns*-Tuneable Laser for Action Plot Experiments

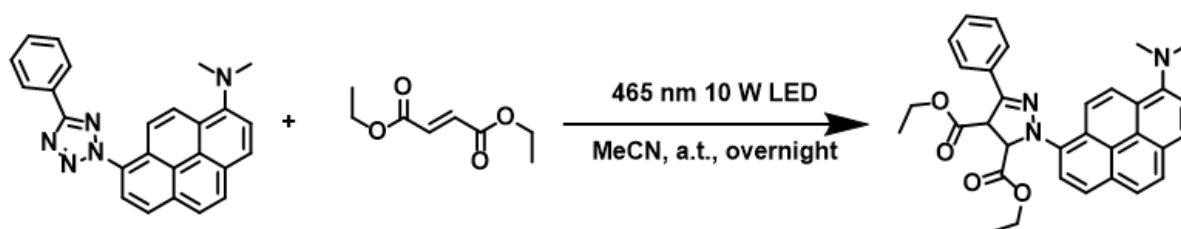
Table S 3: Required laser pulse energy for each wavelength, resulting in a constant number of photons after irradiation for 15 min at a pulse rate of 20 Hz. ^a Because wavelengths between 300-400 nm are generated by sum frequency generation (SFG), laser output energies in this range are significantly reduced, giving pulse energies between 165 and 690 μJ . The lower pulse energy was compensated by adjusting the irradiation time for the indicated experiments accordingly.

Wavelength / nm	Photon Energy / 10^{-19} J	Pulse Energy / mJ	Number of Photons / 10^{-4} mol
320	6.21	3.38 ^a	1.18
340	5.84	2.90 ^a	1.18
360	5.52	2.63 ^a	1.18
380	5.23	2.45 ^a	1.18
400	4.97	2.31 ^a	1.18
410	4.84	2.25	1.18
420	4.73	2.19	1.18
430	4.62	2.14	1.18
440	4.51	2.09	1.18

450	4.41	2.04	1.18
455	4.37	2.02	1.18
460	4.32	2.00	1.18
465	4.27	1.98	1.18
470	4.23	1.96	1.18
475	4.18	1.94	1.18
480	4.14	1.92	1.18
490	4.05	1.88	1.18
500	3.97	1.84	1.18
510	3.89	1.80	1.18
515	3.86	1.79	1.18
525	3.78	1.75	1.18

8.4.3 Isolation of Cycloadducts

8.4.3.1 CA_{DEF}

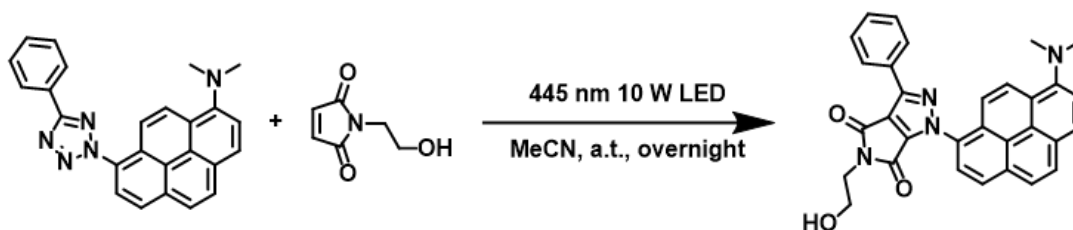


APAT (5 mg, 12.8 μmol , 1.00 eq.) and diethylfumarate (8.84 mg, 51.4 μmol , 4.00 eq.) were dissolved in 15 mL MeCN, the vial was equipped with a stirring bar, sealed, and degassed for 1 h by bubbling dry N_2 through the solution. The mixture was placed on top of a 10 W LED centred around 465 nm, cooled with a stream of compressed air, and irradiated for 16 h while stirring. Subsequently, the solvent was removed under vacuum, and the product was purified *via* silica gel column chromatography (n-hexane/ethyl acetate 4:1). The product was obtained as a yellow solid (5.13 mg, 75 %, R_f = 0.50 in n-hex/EA 4:1).

Due to formation of different diastereomers of the cycloadduct, the $^1\text{H-NMR}$ spectrum shows two sets of aliphatic signals. Moreover, an additional set of peaks is observed, which was attributed to the rearomatized pyrazole adduct (relative amount: 19 %).

$^1\text{H NMR}$ (600 MHz, Chloroform-*d*) δ [ppm] = δ 8.69 – 7.32 (m, 13H), 5.55 (s, 1H), 4.84 (s, 1H), 4.40 (q, 1H, *pyrazole adduct*), 4.36 – 4.24 (m, 2H), 4.01 (q, 1H, *pyrazole adduct*), 3.92 – 3.82 (m, 2H), 3.07 (s, 6H), 1.35 (t, 3H, *pyrazole adduct*), 1.30 (t, 3H), 0.91 – 0.81 (m, 3H, *pyrazole adduct*), 0.79 (t, 3H).

8.4.3.2 $\text{CA}_{\text{NHEM}}/\text{CA}_{\text{APAT}}$



APAT (6 mg, 15.4 μmol , 1.00 eq.) and NHEM (17.4 mg, 123 μmol , 8.00 eq.) were dissolved in 35 mL MeCN in a round bottom flask, equipped with a stir bar and sealed with a rubber septum. The mixture was degassed by bubbling a stream of dried nitrogen for 1 h. The flask was then placed on a magnetic stirrer and a 10 W 445 nm LED was placed at an angle underneath the flask, so that the stir bar did not block the light. While stirring and cooling with a stream of compressed air, the mixture was irradiated for 16 h. Subsequently, it was passed over neutral aluminum oxide and purified by Puriflash silica column (gradient CH/EA 9:1 \rightarrow 100 % EA). The solvent was evaporated, yielding 5.7 mg of a yellow solid (74 %).

$^1\text{H-NMR}$ (600 MHz, toluene-*d*₈) δ [ppm] = 8.68 (m, 2H), 8.56 (d, $J = 9.5$ Hz, 1H), 8.47 (d, $J = 9.5$ Hz, 1H), 8.00 (d, $J = 8.1$ Hz, 1H), 7.89 (d, $J = 8.2$ Hz, 1H), 7.81 (d, $J = 8.2$ Hz, 1H), 7.78 (d, $J = 8.8$ Hz, 1H), 7.65 (d, $J = 8.8$ Hz, 1H), 7.46 (d, $J = 8.2$ Hz, 1H), 7.34 – 7.29 (m, 2H), 7.20 – 7.16 (m, 1H), 3.48 (t, 2H), 3.43 (t, $J = 5.2$ Hz, 2H), 2.72 (s, 6H).

8.4.4 High-Conversion Cycloaddition of APAT and DEF

Sample preparation was done similarly to all other action plot measurements (see 8.4.1). The sample was irradiated with 465 nm laser light (2 mJ) for 180 min. Subsequently, the sample was subjected to LC-MS and analysed. The chromatogram is shown in section 10.3.2.

8.5 λ -Orthogonal Photoreactions of APAT and *o*MBA with

NHEM

8.5.1 Sample Preparation for Kinetic Measurements

APAT, *o*MBA and *N*-(2-hydroxy)ethyl maleimide were employed in a 1:1:8 ratio, with the total concentration being 0.5 mg mL⁻¹ as per the LC-MS sample requirements. Sample solutions were freshly prepared every day and not kept overnight. Stock solution (APAT: 0.23 mM; *o*MBA: 0.23 mM; NHEM: 1.82 mM in MeCN) was prepared and degassed with N₂ for 15 min, then 0.3 mL were withdrawn and added to capped photo vials that had previously been degassed with N₂ for 5 min. The samples were irradiated for the respective times indicated in **Table S 4**, using the Coherent *Opolette* tuneable laser system, and subsequently were filtered and directly subjected to LC-MS.

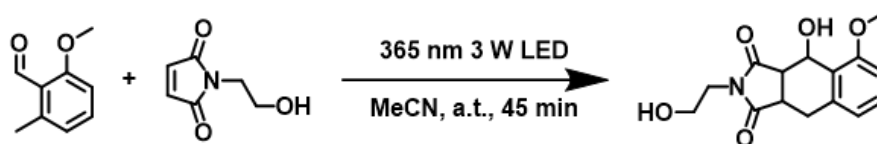
8.5.2 Power Settings of the *ns*-Tuneable Laser for Kinetic Measurements

Table S 4: Detailed specifications of the laser experiments for the kinetic study.

Wavelength / nm	Irradiation Time / min	Pulse Energy / μ J	Number of Photons / mol
320	0.1	500	1.17*10 ⁻⁷
320	0.2	500	2.33*10 ⁻⁷
320	0.4	500	4.86*10 ⁻⁷
320	0.8	500	9.72*10 ⁻⁷
360	1	500	1.50*10 ⁻⁶
360	2	500	3.00*10 ⁻⁶
360	4	500	5.99*10 ⁻⁶
360	8	500	1.20*10 ⁻⁵
360	19.3	500	2.89*10 ⁻⁵
390	3.6	364	4.32*10 ⁻⁶

390	7.2	364	$8.65 \cdot 10^{-6}$
390	14.3	364	$1.73 \cdot 10^{-5}$
390	28.6	364	$3.45 \cdot 10^{-5}$
390	120	364	$1.45 \cdot 10^{-4}$
450	5	2000	$3.85 \cdot 10^{-5}$
450	10	2000	$7.71 \cdot 10^{-5}$
450	15	2000	$1.16 \cdot 10^{-4}$
450	30	2000	$2.31 \cdot 10^{-4}$
450	156	2000	$1.20 \cdot 10^{-3}$

8.5.3 Isolation of CA_{oMBA}



*o*MBA (10 mg, 66.1 μ mol, 1.00 eq.) and NHEM (74.8 mg, 529 μ mol, 8.00 eq.) were dissolved in 16 mL MeCN in a crimp vial, equipped with a stirring bar, and sealed. The mixture was degassed by bubbling a stream of dried nitrogen for 30 min. The vial was then placed on top of a 3 W 365 nm LED on a magnetic stirrer. While stirring and cooling with a stream of compressed air, the mixture was irradiated for 45 min. Subsequently, it was purified by Puriflash silica column (gradient CH/EA 9:1 \rightarrow 100 % EA). The solvent was evaporated, yielding 11 mg of a white solid (57 %).

¹H NMR (600 MHz, MeCN-*d*₃) δ [ppm] = 7.08 – 6.94 (m, 1H), 6.72 – 6.58 (m, 2H), 5.48 – 5.34 (m, 1H), 3.61 (s, 3H), 3.47 – 3.26 (m, 4H), 3.11 (s, 1H), 3.02 – 2.75 (m, 3H), 2.75 – 2.56 (m, 2H).

8.5.4 Determination of Quantum Yields

The reaction quantum yield was determined by measuring kinetics of the conversion over time and performing least squares fits of the experimentally determined conversions to the library of theoretical conversions simulated in Matlab®, (Eq. (8 – 7)-(8 – 11)) at each time interval. For a range of different values of the quantum yield Φ , using the starting concentration $c(t_0)$, the molar decadic absorption coefficient ϵ , the pulse energy E_{pulse} and the

wavelength λ , the conversion after each laser pulse (n) was determined using the previous time step (n-1) by:

$$c_{oMBA}(t_n) = c_{oMBA}(t_{n-1}) - \frac{E_{pulse}\lambda}{hc} \phi_{oMBA} 10^{-\varepsilon_{oMBA}c_{oMBA}(t_{n-1})L} \quad (8-7)$$

$$c_{APAT}(t_n) = c_{APAT}(t_{n-1}) - \frac{E_{pulse}\lambda}{hc} \phi_{APAT} 10^{-\varepsilon_{APAT}c_{APAT}(t_{n-1})L} \quad (8-8)$$

$$c_{NHEM}(t_n) = c_{NHEM}(t_{n-1}) - \frac{E_{pulse}\lambda}{hc} \phi_{oMBA} 10^{-\varepsilon_{oMBA}c_{oMBA}(t_{n-1})L} - \psi \phi_{APAT} 10^{-\varepsilon_{APAT}c_{APAT}(t_{n-1})L} \quad (8-9)$$

$$c_{CA_{oMBA}}(t_n) = c_{CA_{oMBA}}(t_{n-1}) - \frac{E_{pulse}\lambda}{hc} \phi_{CA_{oMBA}} 10^{-\varepsilon_{CA_{oMBA}}c_{CA_{oMBA}}(t_{n-1})L} \quad (8-10)$$

$$c_{CA_{APAT}}(t_n) = c_{CA_{APAT}}(t_{n-1}) - \frac{E_{pulse}\lambda}{hc} \phi_{CA_{APAT}} 10^{-\varepsilon_{CA_{APAT}}c_{CA_{APAT}}(t_{n-1})L} \quad (8-11)$$

Given the long irradiation times, diffusion was not taken into account in this simulation. A library of simulations, with quantum yield values varying between 0 and 1, was generated for each sample, using the parameters outlined in **Table S 8** in **section 10.4.1**. Least squares fitting of the simulation library to the experimental data was then performed to determine the best fit simulation, and hence quantum yield.

8.5.5 Sample Preparation for Sequential LED Experiment

APAT, oMBA and *N*-(2-hydroxy)ethyl maleimide were employed in a 1:1:8 ratio, with the total concentration being 0.5 mg mL⁻¹ as per the LC-MS sample requirements. The solution (APAT: 0.23 mM; oMBA: 0.23 mM; NHEM: 1.82 mM in MeCN, 15 mL total) was filled in a crimp vial, equipped with a stir bar, sealed and degassed with N₂ for 30 min.

8.6 [2+2] Cycloaddition of Styrylpyrene in Disparate Environments

8.6.1 Sample Preparation of the Action Plot Experiments

For the photochemical experiments, stock solutions were prepared according to the specifications given below, and degassed by bubbling through dry nitrogen for 15 min. The stock solution was distributed into laser vials which had previously been flushed with dry nitrogen for 5 min. The vials were placed in the sample holder and irradiated using the Innolas Tuneable Laser system.

The stock solutions were prepared with two different concentrations (5 or 10 mM) and two different solvents (**Acetonitrile- d_3** and **DMSO- d_6**), in order to investigate the influence of concentration and solvent. The following samples were obtained:

5 mM: 0.80 mg (2.50 μmol) styrylpyrene in 0.5 mL of MeCN- d_3 or DMSO- d_6 .

10 mM: 1.60 mg (5.00 μmol) styrylpyrene in 0.5 mL of MeCN- d_3 or DMSO- d_6 .

The parameters set for the irradiation experiments are given in **Table S 5**:

Table S 5: Detailed specifications of the laser experiments for the attenuation-adjusted action plot, the concentration dependent action plot, and the solvent-dependent action plot.

Wavelength / nm	Number of pulses	Pulse Energy / μJ	Number of Photons / mol
310	1000	656	$8.09 \cdot 10^{-7}$
330	1000	854	$1.44 \cdot 10^{-6}$
350	1000	297	$5.61 \cdot 10^{-7}$
370	500	349	$3.51 \cdot 10^{-7}$
390	500	336	$3.69 \cdot 10^{-7}$
410	1000	339	$8.34 \cdot 10^{-7}$
415	1000	671	$1.70 \cdot 10^{-6}$
420	3000	571	$4.42 \cdot 10^{-6}$
425	8000	565	$1.19 \cdot 10^{-5}$

430	22500	476	2.90×10^{-5}
435	45000	514	6.29×10^{-5}
440	45000	928	1.16×10^{-4}
445	90000	718	1.82×10^{-4}
450	90000	931	2.42×10^{-4}
455	180000	573	2.95×10^{-4}
460	180000	616	3.22×10^{-4}
465	180000	679	3.60×10^{-4}
470	180000	692	3.80×10^{-4}

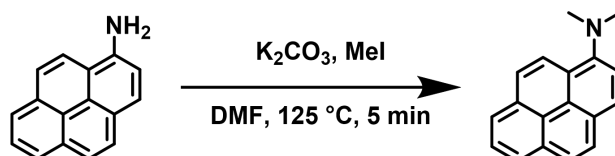
8.6.2 Temperature-Dependence Study

The temperature-dependent experiments were carried out in a similar setup, however, employing the QUT laser setup described in **section 8.3.1**, which operates at 20 Hz repetition rate. The irradiation times were adjusted accordingly (note that the different pulse energies have previously been shown to have no significant effect on the [2+2] cycloaddition of styrylpyrene¹³⁷). The sample vials were placed in a heated sample holder at constant $T = 37\text{ }^{\circ}\text{C}$ and allowed to warm up for 5 min, before irradiation was started.

8.7 Synthetic Procedures

8.7.1 *N,N*-(dimethyl)amino Pyrene Aryl Tetrazole

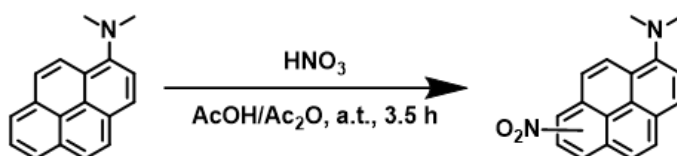
8.7.1.1 *N,N*-dimethyl pyrene-1-amine



Pyren-1-amine (4.96 g, 22.8 mmol, 1.00 eq.) and potassium carbonate (15.87 g, 114 mmol, 5.00 eq.) were combined in a round bottom flask and air was exchanged for argon. Dry DMF (30 mL) was added and, finally, iodomethane (7.11 mL, 16.2 g, 114 mmol, 5.00 eq.) was added dropwise over 10 min while stirring the brown solution. The flask was equipped with an argon filled balloon. Subsequently, the mixture was heated to 125 °C for 5 min and then allowed to cool down. Excessive iodomethane was quenched with 30 mL of MeOH, and the mixture was stirred for another 10 min. Ethyl acetate was added the mixture was extracted three times with water. The organic layer was dried over MgSO₄ and the solvent evaporated. The product was obtained as a brown oil and was used without further purification (5.27 g, 94 %).

¹H-NMR (600 MHz, CDCl₃) δ [ppm] = 8.48 (d, *J* = 9.2 Hz, 1H), 8.17-8.05 (m, 4H), 8.02-7.90 (m, 3H), 7.76 (d, *J* = 8.2 Hz, 1H), 3.07 (s, 6H).

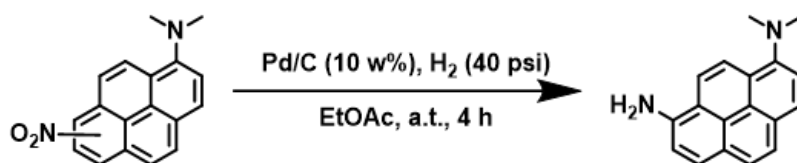
8.7.1.2 *N,N*-dimethyl nitropyrene-1-amine



N,N-dimethyl pyrene-1-amine (3.53 g, 14.4 mmol, 1.00 eq.) was dissolved in acetic acid (200 mL) and acetic anhydride (55 mL). Under vigorous stirring, HNO₃ (1.68 mL, 65 w%, 2.37 g, 36.5 mmol, 1.70 eq.) in 10 mL AcOH was added dropwise over 1 h to the brown solution. TLC indicated presence of starting material (*R*_f = 0.7 in CH/EA 4:1) and mono-nitrated product (*R*_f

= 0.5 in CH/EA 4:1). Another 0.3 eq. HNO₃ in 10 mL AcOH was added dropwise over an hour. This was repeated and each time the reaction was thoroughly monitored *via* TLC and ¹H-NMR spectroscopy to avoid formation of large amounts of double nitrated product. After a total amount of 2.5 eq. HNO₃ and 3.5 h reaction time, the mixture turned dark red and TLC indicated commencing formation of double nitrated product (R_f = 0.4 in CH/EA 4:1). The reaction was quenched with 150 mL H₂O. The mixture was extracted with chloroform four times and the organic layer washed with water twice, dried over MgSO₄ and filtered. The product was adsorbed onto Celite® filter agent and purified by column chromatography (silica, cyclohexane/ethyl acetate gradient (9:1 → 4:1 v/v)). Separation of regio-isomers was not achieved and the product contained *N,N*-dimethyl-8-nitropyren-1-amine, *N,N*-dimethyl-6-nitropyren-1-amine and *N,N*-dimethyl-3-nitropyren-1-amine in a ratio of 2:2:1, which was estimated from the relative peak integrals of the -NMe₂ signals in the ¹H-NMR spectrum. The product was obtained as a red powder (2.42 g, 58 %).

8.7.1.3 *N,N*-dimethyl pyrene-1,8-diamine



N,N-dimethyl nitropyrene-1-amine (2.36 g, 8.13 mmol) was dissolved in 130 mL ethyl acetate and Pd/C (692 mg, 10 w%, 650 μmol, 0.08 eq.) was added. After flushing with N₂ the vessel was filled with H₂ (40 psi) and shaken for 4 h. Over the course of the reaction, the mixture changed colour from dark red to blue with a yellow glint. The mixture was filtered over Celite® filter agent and the solvent was evaporated. The crude product was purified *via* Puriflash silica column (15 μm, cyclohexane/ethyl acetate gradient (99:1 → 4:1 v/v)). While the 1,3- and 1,6-substituted isomers were inseparable (R_f = 0.7 in CH/EA 1:1 v/v), a clean fraction of *N,N*-dimethylpyrene-1,8-diamine (R_f = 0.6 in CH/EA 1:1 v/v) was obtained. Position of the substituents was confirmed *via* NMR spectroscopy (¹H-NMR and ¹³C-NMR spectroscopy, correlation spectroscopy (COSY), heteronuclear multiple bond correlation (HMBC) and heteronuclear single-quantum correlation spectroscopy (HSQC)). The product was obtained as a brown oil (861 mg, 41 %, R_f = 0.6 in CH/EA 1:1 v/v).

¹H-NMR (400 MHz, CDCl₃) δ [ppm] = 8.40 (d, *J* = 9.5 Hz, 1H), 8.02 (d, *J* = 8.2 Hz, 1H), 7.99-7.89 (m, 2H), 7.85-7.73 (m, 2H), 7.71 (d, *J* = 8.2 Hz, 1H) 7.31 (d, *J* = 8.1, 1H), 4.29 (b, 2H), 3.05 (s, 6H).

¹³C-NMR (150 MHz, CDCl₃) δ [ppm] =147.61, 140.49, 128.16, 126.77, 126.50, 125.96, 125.53, 125.07, 124.39, 123.80, 119.37, 117.36, 116.56, 113.91, 45.65.

Determination of the regio-isomeric structure:

The 1D and 2D ¹H- and ¹³C-NMR spectra shown in **Figure S 6** help to confirm that the isolated *N,N*-dimethyl pyrene diamine is indeed the 1,8-isomer. The following observations led to deduction of the structure per method of elimination:

- 1) The aromatic region in the ¹H-NMR spectrum in **Figure S 6b** shows 8 doublets corresponding to 8 protons, each of which has an adjacent proton as per the COSY spectrum in **Figure S 6c**. The possibility of a 1,3-isomer is thus eliminated because a singlet for H² would be observed in this case.
- 2) In the ¹³C-NMR spectrum in **Figure S 6d**, the quaternary carbon atoms adjacent to the amino groups have the largest chemical shift (δ = 140 and δ = 148). They therefore can be assigned to C¹ and either C⁸ or C¹⁰, depending on which isomer is present. The DEPTQ-135 spectrum in **Figure S 6f** confirms that the C-atoms are quaternary.
- 3) In the HMBC spectrum in **Figure S 6e**, one of the identified C-atoms correlates to the -NMe₂ proton signal. This C-atom must be C¹.
- 4) In the same spectrum, C¹ correlates to three aromatic protons: H², H³ and H¹³.
- 5) The COSY spectrum in **Figure S 6c** reveals correlation of two of the protons, which are therefore H² and H³. Consequently, the remaining signal can be assigned to H¹³.
- 6) In the COSY spectrum, H¹² can easily be identified through the correlation with H¹³.
- 7) In the HMBC spectrum, H¹² correlates with what was identified as either C⁸ or C¹⁰ in step 2.
- 8) It is thus possible to identify C¹⁰ because the correlation in step 7 would not be possible between H¹² and C⁸. The isomer must be *N,N*-dimethyl pyrene-1,8-diamine (aminogroups attached to C¹ and C¹⁰).

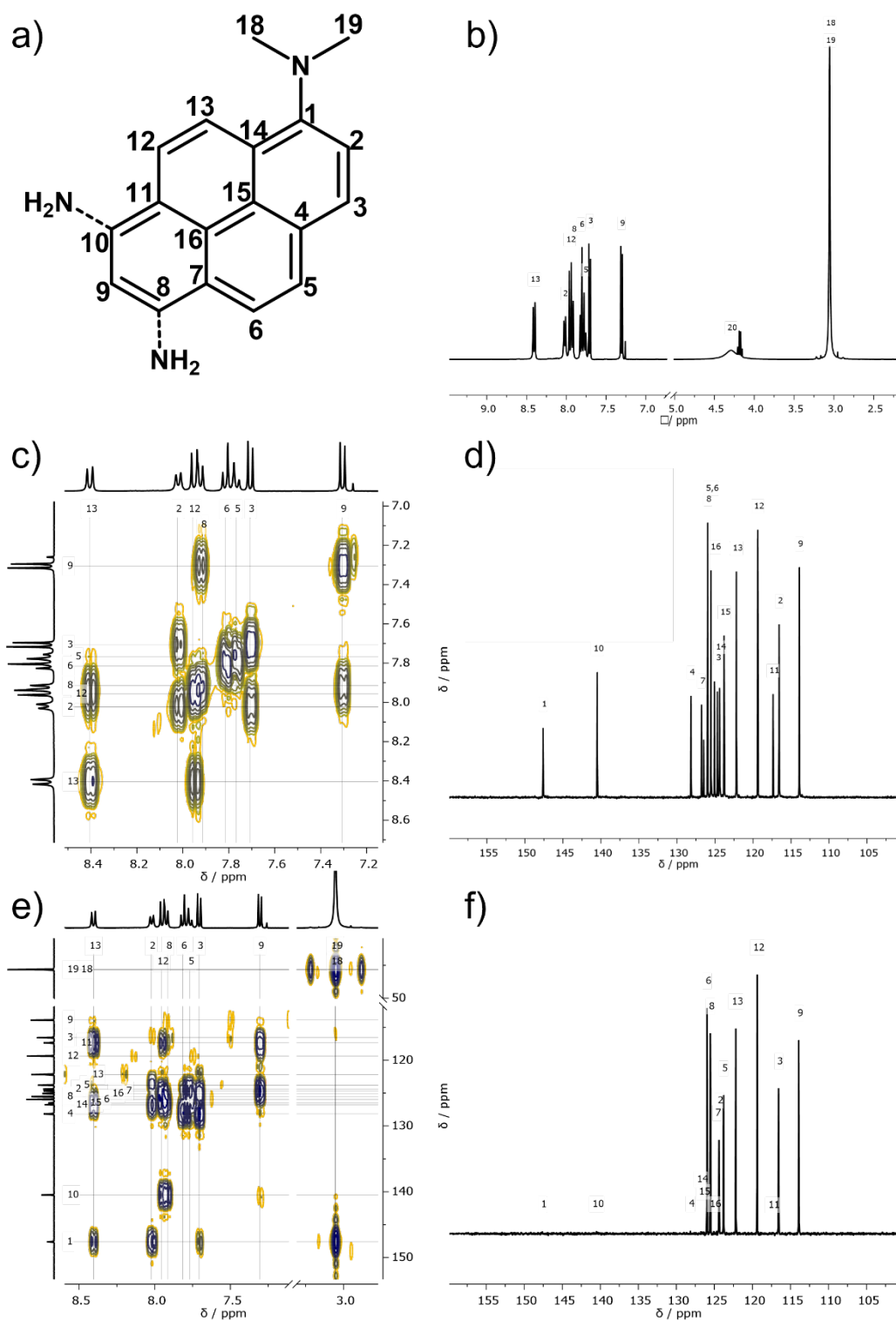
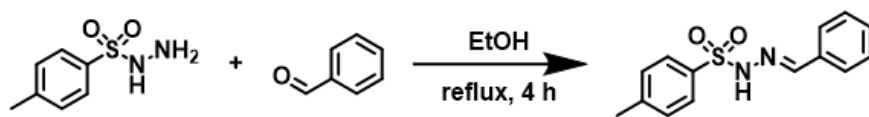


Figure S 6: Based on 1D and 2D NMR spectra the isomeric structure of *N,N*-dimethyl pyrene-1,8-diamine could be confirmed. All spectra were measured at ambient temperature in CDCl_3 . For clarity, only the relevant regions are shown and the rest of the spectra is omitted. a) Possible isomeric structures (1,6- and 1,8-isomer) of the product. b) ^1H -NMR spectrum. c) COSY, showing 3J couplings between protons. d) ^{13}C -NMR spectrum. e) HMBC, showing multiple-bond correlations between ^1H and ^{13}C nuclei. f) DEPTQ-135-NMR spectrum, showing only primary and tertiary carbons. (-CH and - CH_3).

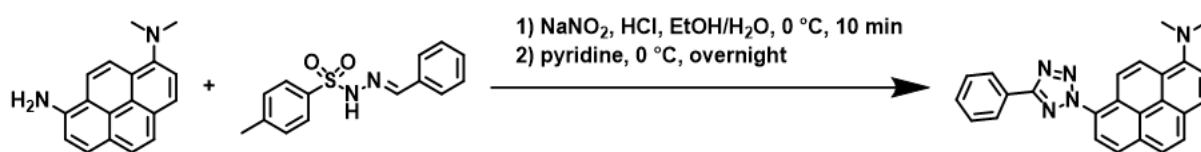
8.7.1.4 (E)-N'-benzylidene-4-methylbenzenesulfonohydrazide



A solution of benzaldehyde (1.00 g, 9.42 mmol, 1.00 eq.) and toluene sulfone hydrazide (1.75 g, 9.42 mmol, 1.00 eq.) in EtOH (20 mL) was refluxed for 4 h and subsequently poured into H₂O (100 mL). The precipitate was collected by filtration and dried in vacuum. The product was obtained as a white solid and used without further purification (2.55 g, 99 %).

¹H-NMR (600 MHz, DMSO-*d*₆) δ [ppm] = 11.43 (s, 1H), 7.90 (s, 1H), 7.80-7.71 (m, 2H), 7.59-7.49 (m, 2H), 7.46-7.32 (m, 5H), 2.35 (s, 3H).

8.7.1.5 *N,N*-dimethyl-8-(5-phenyl-2*H*-tetrazol-2-yl)pyren-1-amine (APAT)

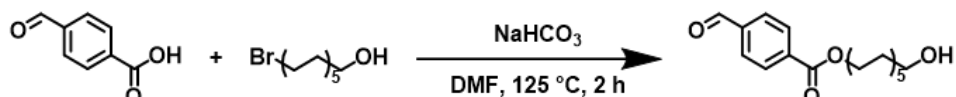


In a round bottom flask *N,N*-dimethyl pyrene-1,8-diamine (250 mg, 960 μmol, 1.00 eq.) was dissolved in a mixture of EtOH, H₂O (3 mL each) and HCl (294 μL, 37 w%, 3.46 mmol, 3.60 eq.) and cooled to -10 °C in an ice/salt mixture. In parallel, a solution of (E)-*N'*-benzylidene-4-methylbenzenesulfonohydrazide (610 mg, 1.25 mmol, 1.30 eq.) in pyridine (6 mL) was prepared and likewise cooled to -10 °C. To the aqueous mixture was added NaNO₂ (66.3 mg, 960 μmol, 1.00 eq.) in a minimum amount of ice-cold water dropwise while vigorously stirring. The yellow mixture immediately turned dark blue and was continuously cooled and stirred for 10 min. Subsequently, the blue diazonium salt solution was quickly transferred to the cooled pyridine solution and the flask rinsed with 6 mL of cooled pyridine (-10 °C). The reaction flask was covered and allowed to warm up to ambient temperature overnight. Subsequently, the now red mixture was poured into 100 mL of 1M HCl and stirred for one hour. Ethyl acetate was added, and the product extracted and washed with H₂O until the aqueous layer was neutral. The organic layer was dried over Mg₂SO₄, filtered, and evaporated. The crude product was purified *via* Puriflash silica column (30 μm, cyclohexane/ethyl acetate gradient (99:1 → 95:1 v/v)). Finally, the product was recrystallized from MeCN to obtain a yellow powder (110 mg, 29 %, R_f = 0.7 in CH/EA 4:1 v/v).

$^1\text{H-NMR}$ (600 MHz, CDCl_3) δ [ppm] = 8.58 (d, J = 9.6 Hz, 1H), 8.40-8.35 (m, 2H), 8.35-8.29 (m, 2H), 8.25-8.19 (d, J = 8.2 Hz, 2H), 8.12 (d, J = 8.9 Hz, 1 H), 8.00 (d, J = 8.8 Hz, 1H), 7.81 (d, J = 8.3 Hz, 1H), 7.62-7.51 (m, 3H), 3.09 (s, 6H).

$^{13}\text{C-NMR}$ (150 MHz, CDCl_3) δ [ppm] = 165.45, 150.44, 133.54, 130.72, 129.39, 127.31, 12645, 125.03, 124.12, 122.96, 120.27, 117.36, 45.81.

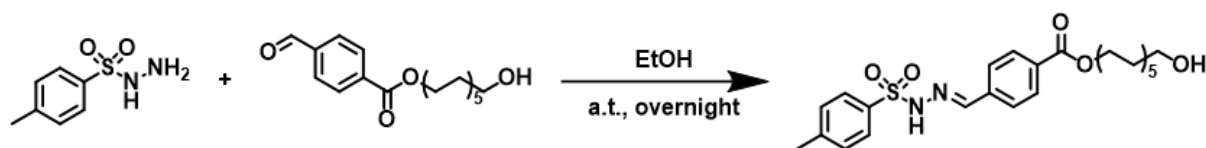
8.7.1.6 11-Hydroxyundecyl-4-formylbenzoate



In a round bottom flask 4-formyl benzoic acid (1.00 g, 6.66 mmol, 1.00 eq.), 11-bromo undecane-1-ol (2.18 g, 8.66 mmol, 1.30 eq.) and NaHCO_3 (1.12 g, 13.3 mmol, 2.00 eq.) were dissolved in 10 mL DMF and heated to $125\text{ }^\circ\text{C}$ for 2 h while stirring. After cooling down, the mixture was filtered, ethyl acetate (100 mL) was added, and the organic layer was washed with brine (3x 50 mL) and H_2O (50 mL). The organic layer was dried over Na_2SO_4 and the solvent evaporated. The product was obtained as a pale-yellow oil and used without further purification (2.13 g, 99 %)

$^1\text{H-NMR}$ (600 MHz, CDCl_3) δ [ppm] = 10.10 (s, 1H), 8.19 (d, J = 8.1 Hz, 2H), 7.95 (d, J = 8.1 Hz, 2H), 4.35 (t, J = 6.7 Hz, 2H), 3.63 (t, J = 6.6 Hz, 2H), 1.78 (p, J = 6.9 Hz, 2H), 1.58-1.52 (m, 2H), 1.47-1.41 (m, 2H), 1.33-1.25 (m, 12H).

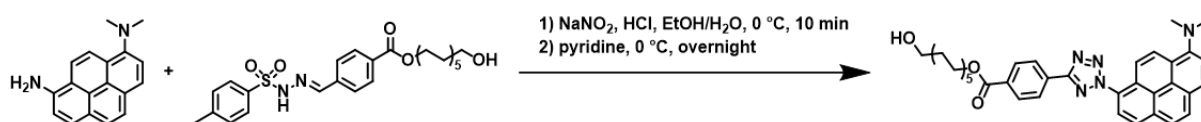
8.7.1.7 11-hydroxyundecyl (E)-4-((2-tosylhydrazineylidene) methyl) benzoate



11-Hydroxyundecyl-4-formylbenzoate (2.13 g, 6.65 mmol, 1.00 eq.) was dissolved in EtOH (20 mL) and toluene sulfone hydrazide (1.36 g, 7.31 mmol, 1.10 eq.) was added. The mixture was stirred at ambient temperature overnight. The solvent was evaporated, and the product was purified *via* silica column chromatography (2 % MeOH in DCM). After drying, the product was obtained as a white solid (2.01 g, 62 %, R_f = 0.1 in MeOH/DCM 2:98 v/v).

¹H-NMR (600 MHz, DMSO-*d*₆) δ [ppm] = 11.71 (b, 1H), 7.94 (d, *J* = 8.3 Hz, 2H), 7.76 (d, *J* = 8.1 Hz, 2H), 7.68 (d, *J* = 8.3 Hz, 2H), 7.41 (d, *J* = 8.1 Hz, 2H), 4.31 (s, 1H), 4.25 (t, *J* = 6.5 Hz, 2H), 2.36 (s, 3H), 1.69 (p, *J* = 6.8 Hz, 2H), 1.44-1.34 (m, 2H), 1.34-1.16 (m, 14 H).

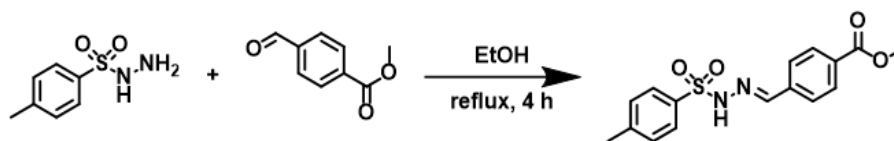
8.7.1.8 11-hydroxyundecyl 4-(2-(8-(dimethylamino)pyren-1-yl)-2H-tetrazol-5-yl)benzoate



In a round bottom flask 11-hydroxyundecyl (E)-4-((2-tosylhydrazineylidene) methyl) benzoate (250 mg, 960 μmol, 1.00 eq.) was dissolved in a mixture of EtOH, H₂O (3 mL each) and HCl (294 μL, 37 w%, 3.46 mmol, 3.60 eq.) and cooled to -10 °C in an ice/salt mixture. In parallel, a solution of **5b** (610 mg, 1.25 mmol, 1.30 eq.) in pyridine (6 mL) was prepared and likewise cooled to -10 °C. To the aqueous mixture was added NaNO₂ (66.3 mg, 960 μmol, 1.00 eq.) in a minimum amount of ice-cold water dropwise while vigorously stirring. The yellow mixture immediately turned dark blue and was continuously cooled and stirred for 10 min. Subsequently, the blue diazonium salt solution was quickly transferred to the cooled pyridine solution and the flask rinsed with 6 mL of cooled pyridine (-10 °C). The reaction flask was covered and allowed to warm up to ambient temperature overnight. Subsequently, the now red mixture was poured into 100 mL of 1M HCl and stirred for one hour. Ethyl acetate was added, and the product extracted and washed with H₂O until the aqueous layer was neutral. The organic layer was dried over Mg₂SO₄, filtered, and evaporated. The crude product was purified *via* silica column chromatography (cyclohexane/ethyl acetate gradient (4:1 → 2:1 v/v)). Finally, the product was recrystallized from MeCN to obtain a yellow powder (140 mg, 24 %, R_f = 0.53 in CH/EA 3:2 v/v).

¹H-NMR (600 MHz, CDCl₃) δ [ppm] = 8.61 (d, *J* = 9.6 Hz, 1H), 8.49-8.40 (m, 2H), 8.36-8.29 (m, 2H), 8.27-8.19 (m, 4H), 8.12 (d, *J* = 8.8 Hz, 1 H), 8.00 (d, *J* = 8.9 Hz, 1H), 7.82 (d, *J* = 8.3 Hz, 1H), 4.38 (t, *J* = 6.7 Hz, 2H), 3.64 (t, *J* = 6.6 Hz, 2H), 3.10 (s, 6H), 1.82 (dt, *J* = 6.8 Hz, 2H), 1.57 (dt, *J* = 8.2, 6.6 Hz, 2H), 1.51-1.45 (m, 2H), 1.43 - 1.25 (m, 12 H).

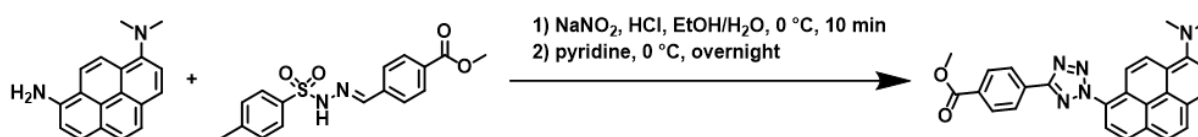
8.7.1.9 Methyl (*E*)-4-((2-tosylhydrazineylidene)methyl)benzoate



Methyl-4-formyl benzoate (250 mg, 1.52 mmol, 1.00 eq.) and toluenesulfonyl hydrazide (284 mg, 1.52 mmol, 1.00 eq.) were dissolved in EtOH and refluxed for 4 h. Subsequently, it was poured into 100 mL of water and the precipitate was collected by filtration. The result was dried *in vacuo*. The product was obtained as a white solid and used without further purification (437 mg, 87 %).

¹H-NMR (600 MHz, DMSO-*d*₆) δ [ppm] = 11.70 (s, 1H), 8.03 - 7.90 (m, 3H), 7.77 (d, 2H), 7.69 (d, 2H), 7.41 (d, *J* = 8.2 Hz, 2H), 3.85 (s, 3H), 2.35 (s, 3H).

8.7.1.10 methyl 4-(2-(8-(dimethylamino)pyren-1-yl)-2H-tetrazol-5-yl)benzoate

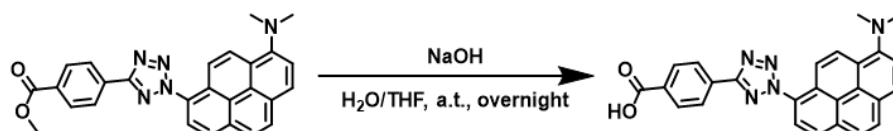


In a round bottom flask *N,N*-dimethyl pyrene-1,8-diamine (203 mg, 780 μ mol, 1.00 eq.) was dissolved in a mixture of EtOH, H₂O (2.5 mL each) and HCl (376 μ L, 37 w%, 2.81 mmol, 3.60 eq.) and cooled to -10 °C in an ice/salt mixture. In parallel, a solution of methyl (*E*)-4-((2-tosylhydrazineylidene)methyl) benzoate (436 mg, 1.31 mmol, 1.68eq.) in pyridine (5 mL) was prepared and likewise cooled to -10 °C. To the aqueous mixture was added NaNO₂ (53.8 mg, 780 μ mol, 1.00 eq.) in a minimum amount of ice-cold water dropwise while vigorously stirring. The yellow mixture immediately turned dark blue and was continuously cooled and stirred for 10 min. Subsequently, the blue diazonium salt solution was quickly transferred to the cooled pyridine solution and the flask rinsed with 5 mL of cooled pyridine (-10 °C). The reaction flask was covered and allowed to warm up to ambient temperature overnight. Subsequently, the now red mixture was poured into 100 mL of 1 M HCl and stirred for one hour. DCM was added, and the product extracted three times and washed with HCl, then water and finally saturated bicarb solution until the aqueous layer was neutral. The organic layer was dried over Mg₂SO₄, filtered, and evaporated. The crude product was purified *via*

silica column chromatography (cyclohexane/ethyl acetate gradient (4:1 → 2:1 v/v)). Finally, the product was obtained as a yellow powder (89 mg, 26 %, $R_f = 0.51$ in CH/EA 9:1 v/v).

$^1\text{H-NMR}$ (600 MHz, Chloroform-*d*) δ [ppm] = 8.58 (d, $J = 9.6$ Hz, 1H), 8.45 (d, $J = 9.6$ Hz, 2H), 8.34 – 8.29 (m, 2H), 8.26 – 8.20 (m, 4H), 8.10 (d, $J = 8.8$ Hz, 1H), 7.98 (d, $J = 8.9$ Hz, 1H), 7.80 (d, $J = 8.3$ Hz, 1H), 3.99 (s, 3H), 3.09 (s, 6H).

8.7.1.11 4-(2-(8-(Dimethylamino)pyren-1-yl)-2H-tetrazol-5-yl) benzoic acid

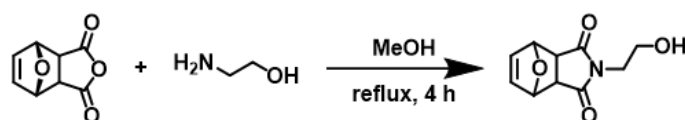


Methyl 4-(2-(8-(dimethylamino)pyren-1-yl)-2H-tetrazol-5-yl) benzoate (30 mg, 67.0 μmol , 1.00 eq.) was dissolved in 0.9 mL THF and 0.9 mL of aqueous 0.75 M NaOH solution was added. The mixture was stirred at ambient temperature overnight. The mixture was subsequently passed through a syringe filled with acidic aluminium oxide, and the solvent was evaporated under vacuum. The product was obtained as an orange solid (20.3 mg, 70 %).

$^1\text{H-NMR}$ (600 MHz, THF-*d*₈) δ [ppm] = 8.61 (d, $J = 9.6$ Hz, 1H), 8.45 – 8.42 (m, 2H), 8.39 (d, $J = 8.2$ Hz, 1H), 8.34 (d, $J = 9.6$ Hz, 1H), 8.31 (d, $J = 8.2$ Hz, 1H), 8.28 (d, $J = 8.3$ Hz, 1H), 8.26 – 8.22 (m, 2H), 8.17 (d, $J = 8.8$ Hz, 1H), 8.06 (d, $J = 8.9$ Hz, 1H), 7.88 (d, $J = 8.3$ Hz, 1H), 3.08 (s, 6H).

8.7.2 Maleimide End-Capped PMMA Chain

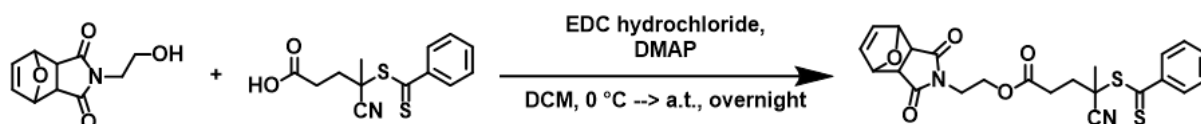
8.7.2.1 2-(2-hydroxyethyl)-3a,4,7,7a-tetrahydro-1H-4,7-epoxyisoindole-1,3(2H)-dione (furan-protected *N*-(2-hydroxy)ethyl maleimide



Furan-protected maleic anhydride (1.50 g, 9.03 mmol, 1.00 eq.) was suspended in 45 mL MeOH and cooled to 0 °C. A solution of 2-aminoethanol in 15 mL MeOH was added dropwise over 15 min, and the mixture was allowed to warm up to room temperature and finally refluxed for 4 h. The solvent was evaporated, and the product was recrystallized from MeOH to yield a white solid (673 mg, 35 %).

$^1\text{H-NMR}$ (600 MHz, CDCl_3) δ [ppm] = 6.52 (d, J = 0.9 Hz, 2H), 5.28 (dd, J = 1.0 Hz, 2H), 3.80-3.74 (m, 2H), 3.74-3.68 (m, 2H), 2.89 (d, J = 0.8 Hz, 2H).

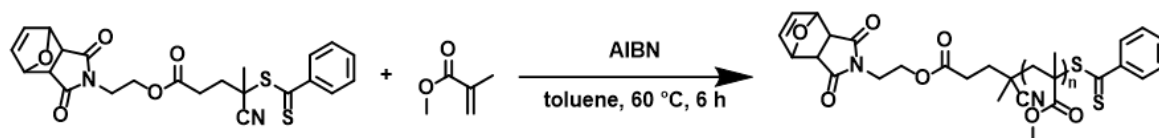
8.7.2.2 2-(1,3-dioxo-1,3,3a,4,7,7a-hexahydro-2H-4,7-epoxyisoindol-2-yl)ethyl 4-cyano-4-((phenylcarbonothioyl)thio)pentanoate (chain transfer agent)



4-cyano-4-((phenylcarbonothioyl)thio)pentanoic acid (572 mg, 2.05 mmol, 1.20 eq.) was added to a Schlenk tube and air was exchanged for argon in three cycles. Dry DCM (20 mL) and furan-protected *N*-(2-hydroxy)ethyl maleimide (357 mg, 1.71 mmol, 1.00 eq.) were added and the solution was cooled to 0 °C. Finally, EDC·HCl (527 mg, 2.56 mmol, 1.50 eq.) and DMAP (31.3 mg, 256 μmol , 0.15 eq.) were added and the mixture was stirred at 0 °C for two hours, then overnight at ambient temperature. Subsequently, DCM was added, and the solution was extracted with water and brine. The organic layer was dried over MgSO_4 and the solvent evaporated under vacuum at 25 °C, due to the heat sensitivity of the product. The product was purified *via* Puriflash silica column (cyclohexane / ethyl acetate gradient, 7:3 \rightarrow 1:1 v/v). The product was obtained as a red oil (570 mg, 71 %).

$^1\text{H-NMR}$ (600 MHz, CDCl_3) δ [ppm] = 8.00-7.84 (m, 2H), 7.57 (t, J = 7.4 Hz, 1H), 7.46-7.34 (m, 2H), 6.50 (d, J = 5.6 Hz, 2H), 5.26 (dd, J = 7.1 Hz, 1.5 Hz, 2H), 4.36-4.19 (m, 2H), 3.85-3.64 (m, 2H), 2.91-2.83 (m, 2H), 2.72-2.33 (m, 4H), 1.93 (s, 3H).

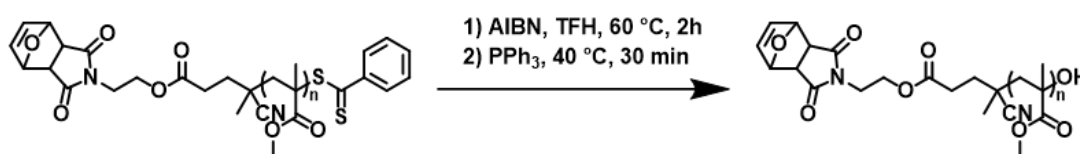
8.7.2.3 Furane-protected maleimide end-capped poly(methyl methacrylate)



CTA (188 mg, 398 μmol , 1.00 eq.) and azobisisobutyronitrile (AIBN, 13.1 mg, 79.7 μmol , 0.20 eq.) were added to a crimp vial equipped with a stirring bar. Using syringe needles, argon was flushed through for 15 min. Dry toluene (4.24 mL), that had previously been degassed with N_2 for 1 h, and methylmethacrylate (3.99 g, 39.9 mmol, 100 eq.) (deinhibited by passing

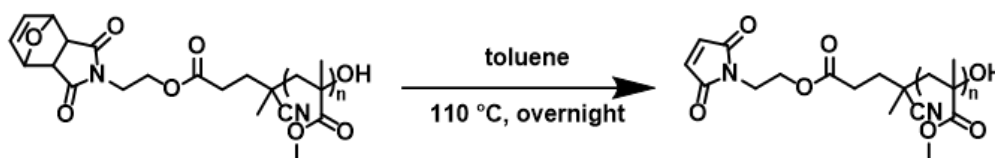
through a basic aluminium oxide column, then degassed with N₂ for 5 min), were added. A large excess of monomer was used to ensure high end-group fidelity. The mixture was again flushed with N₂ in an ice bath, and subsequently emerged into a heating block at 60 °C while stirring. After 6 h the reaction was stopped by exposing the reaction mixture to air and freezing in liquid N₂. Solvent and remaining monomer were evaporated *in vacuo*. The resulting oil was dissolved in a small amount of THF and precipitated twice into cold MeOH (600 mL), then dried *in vacuo*. The product was obtained as a light pink solid (1.18 g). ¹H-NMR spectroscopy was used to determine degree of polymerization and molecular weight (DP = 46, M_n = 5.1 kDa by ¹H-NMR, M_n = 4.7 kDa by SEC).

8.7.2.4 (ω-hydroxy) furane-protected maleimide end-capped poly (methyl) methacrylate



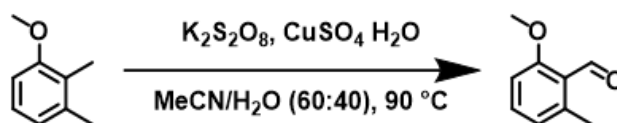
AIBN (55 mg, 355 μmol, 1.50 eq.) was dissolved in 30 mL THF and heated to 60 °C for 1 h. ω-(benzodithioate)-capped poly(methyl)methacrylate (1.18 g, 224 μmol, 1.00 eq.) was added and stirred for 1 h. 44 mg more AIBN was added and the solution was continuously stirred for one more hour, at which point the temperature was lowered to 1 h and PPh₃ (176 mg, 671 μmol, 3.00 eq.) was added. After stirring for 30 min, the solvent was evaporated, and the residue was dissolved in a minimum amount of THF and precipitated into cold MeOH. ¹H-NMR spectroscopy revealed loss of the RAFT end-group.

8.7.2.5 (ω-hydroxy) maleimide end-capped poly (methyl)methacrylate



(ω-hydroxy) furane-protected maleimide end-capped poly (methyl) methacrylate was dissolved in 60 mL toluene and heated to 110 °C overnight. The solvent was evaporated, and the residue was precipitated into cold MeOH (500 mL). The product was obtained as a white solid (596 mg, M_n(NMR) = 5.2 kDa, M_n(SEC) = 4.7 kDa, Đ = 1.16). The ¹H-NMR spectrum confirmed cleavage of the furan protection group.

8.7.3 2-methoxy-6-methylbenzaldehyde

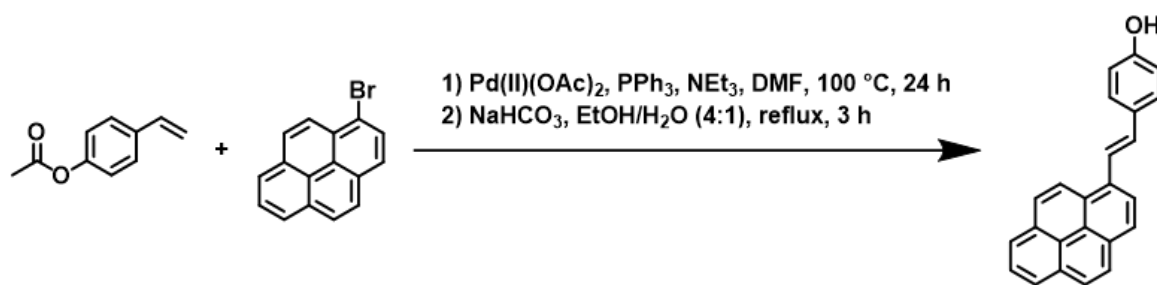


2,3-Dimethyl anisole (14.29 mL, 14.06 g, 103.24 mmol, 1.00 eq), copper sulfate pentahydrate (26.29 g, 105.30 mmol, 1.02 eq) and potassium peroxodisulfate (83.72 g, 309.71 mmol, 3.00 eq) were added to a mixture of acetonitrile/water (60:40, 800 mL) in a round bottom flask. The suspension was vigorously stirred and heated at $90\text{ }^\circ\text{C}$ in an oil bath using a reflux condenser, until thin layer chromatography (TLC) revealed that all the starting material had been consumed (45 to 60 min after the start of the reaction). The mixture was then cooled without stirring using an ice-bath. The mixture separated into a solid phase and two liquid phases. The liquid phases were decanted into a separating funnel and the heavier aqueous phase separated. The aqueous phase was extracted three times with 100 mL DCM, the organic phases were combined, washed twice with brine, dried over Na_2SO_4 and finally the volatiles were removed under reduced pressure. The crude product was submitted to sublimation under ambient pressure nitrogen atmosphere at $85\text{ }^\circ\text{C}$ oil bath temperature to yield 11.75 g (76 %) of colorless crystals.

$^1\text{H NMR}$ (600 MHz, $CDCl_3$) δ [ppm] = 10.52 (s, 1H), 7.49 (dd, $J = 8.4, 7.6$ Hz, 1H), 7.06 (d, $J = 8.4$ Hz, 1H), 6.86 (d, $J = 7.6$, 1H), 3.88 (s, 3H), 2.46 (s, 3H).

$^{13}\text{C NMR}$ (151 MHz, $CDCl_3$) δ [ppm] = 192.44, 163.30, 142.18, 134.56, 124.23, 123.49, 109.18, 55.91, 21.61.

8.7.4 Hydroxy-Styrylpyrene



Hydroxy-styrylpyrene was synthesized following a similar reaction procedure published previously in the literature.^{135, 199}

4-Acetoxy-styrene (0.54 mL, 0.58 g, 3.56 mmol, 1.00 eq.), 1-bromopyrene (1.00 g, 3.56 mmol, 1.00 eq.) and palladium(II) acetate (8.00 mg, 35.6 μ mol, 0.01 eq.), triphenylphosphine (18.7 mg, 71.1 μ mol, 0.02 eq.) and triethylamine (0.73 mL, 1.00 g, 9.88 mmol, 2.78 eq.) were dissolved in DMF (19.8 mL), degassed with nitrogen for 20 minutes and heated to 100 °C. After stirring for 1 day, the solvents were removed under reduced pressure. The obtained solid dissolved in ethyl acetate (ca. 100 mL), subsequently washed with water (3 x 50 mL) and brine (50 mL), dried over MgSO₄, filtered, and evaporated under reduced pressure.

To obtain the final hydroxy-structure the crude product was deprotected via suspension with NaHCO₃ (0.79 g, 9.44 mmol, 3.00 eq.) in a mixture of ethanol (100 mL) and water (25 mL) under reflux for 3 hours. The mixture was precipitated into a mixture of 1M HCl (100 mL) and ice water (300 mL), filtered, washed with water, and purified using a flash chromatography system (cyclohexane/ethyl acetate from 9:1 to 8:2) to obtain 0.50 g product (yield 41 %) as a yellow powder.

¹H-NMR (400 MHz, Acetonitrile-*d*₃) δ [ppm] = 8.60 (d, *J* = 9.3 Hz, 1H), 8.38 (d, *J* = 8.1 Hz, 1H), 8.25 - 8.20 (m, 3H), 8.17 (d, *J* = 9.3 Hz, 1H), 8.11 (d, *J* = 16.1 Hz, 1H), 8.10 (s, 2H), 8.03 (t, *J* = 7.7 Hz, 1H), 7.66 - 7.62 (m, 2H), 7.39 (d, *J* = 16.1 Hz, 1H), 7.1 - 7.2 (bs, 1H), 6.93 - 6.88 (m, 2H).

9 REFERENCES

1. de Grotthuss, T., Sur la décomposition de l'eau et des corps qu'elle tient en dissolution à l'aide de l'électricité galvanique. *Annales de chimie et de physique* **1806**, 58, 54-73.
2. Atkins, P. W.; De Paula, J., *Physikalische chemie*. John Wiley & Sons: 2013.
3. Atkins, P. W.; Friedman, R. S., *Molecular quantum mechanics*. Oxford university press: 2011.
4. Fantz, U.; Wunderlich, D., Franck–Condon factors, transition probabilities, and radiative lifetimes for hydrogen molecules and their isotopomers. *Atomic Data and Nuclear Data Tables* **2006**, 92 (6), 853-973.
5. Hesse, M.; Meier, H.; Zeeh, B., *Spektroskopische Methoden in der organischen Chemie*. Georg Thieme Verlag: 2005.
6. Lambert, J. B.; Biele, C.; Marsmann, H., *Spektroskopie: Strukturaufklärung in der Organischen Chemie*. Pearson: 2012.
7. Turro, N. J., *Modern molecular photochemistry*. University science books: 1991.
8. Jablonski, A., Efficiency of Anti-Stokes Fluorescence in Dyes. *Nature* **1933**, 131, 839.
9. Lakowicz, J. R., *Principles of Fluorescence Spectroscopy*. Springer US: 2013.
10. Berezin, M. Y.; Achilefu, S., Fluorescence Lifetime Measurements and Biological Imaging. *Chemical Reviews* **2010**, 110 (5), 2641-2684.
11. Kasha, M., Characterization of electronic transitions in complex molecules. *Discussions of the Faraday Society* **1950**, 9 (0), 14-19.
12. Koppelaar, D. W.; Lindon, J. C.; Tranter, G. E., *Encyclopedia of spectroscopy and spectrometry*. Academic Press: Place of publication not identified, 2010.
13. Spichty, M.; Turro, N. J.; Rist, G.; Birbaum, J.-L.; Dietliker, K.; Wolf, J.-P.; Gescheidt, G., Bond cleavage in the excited state of acyl phosphene oxides: Insight on the role of conformation by model calculations: a concept. *Journal of Photochemistry and Photobiology A: Chemistry* **2001**, 142 (2), 209-213.
14. Jöckle, P.; Kamm, P. W.; Lamparth, I.; Moszner, N.; Unterreiner, A.-N.; Barner-Kowollik, C., More than Expected: Overall Initiation Efficiencies of Mono-, Bis-, and Tetraacylgermane Radical Initiators. *Macromolecules* **2019**, 52 (1), 281-291.
15. Das, P. K.; Scaiano, J. C., The formation of two photoenols via a common pathway in the photochemistry of 2-methylbenzophenone. *Journal of Photochemistry* **1980**, 12 (1), 85-90.
16. Ikoma, T.; Akiyama, K.; Tero-Kubota, S.; Ikegami, Y., Time-resolved ESR studies on the excited triplet states and photoenolization of 2-methylacetophenone and related molecules. *The Journal of Physical Chemistry* **1989**, 93 (20), 7087-7091.
17. Behrendt, P. J.; Kim, H.-C.; Hampp, N., Laser-based depletion zone photoreaction: Selective synthesis of [2+2]-crossdimers of coumarin and 5-fluorouracil. *Journal of Photochemistry and Photobiology A: Chemistry* **2013**, 264, 67-72.
18. Wolff, T.; Görner, H., Photodimerization of coumarin revisited: Effects of solvent polarity on the triplet reactivity and product pattern. *Physical Chemistry Chemical Physics* **2004**, 6 (2), 368-376.
19. Blasco, E.; Sugawara, Y.; Lederhose, P.; Blinco, J. P.; Kelterer, A.-M.; Barner-Kowollik, C., Understanding Reactivity Patterns in Light-Induced Nitrile Imine Mediated Tetrazole–Ene Cycloadditions. *ChemPhotoChem* **2017**, 1 (5), 159-163.

20. Carey, F. A.; Sundberg, R. J., *Advanced organic chemistry : part B : reaction and synthesis*. Fifth edition. ed.; Springer: New York, 2007.
21. Brady, W. T.; Roe, R., Halogenated ketenes. XVI. Steric control in unsymmetrical ketone-olefin cycloadditions. *Journal of the American Chemical Society* **1971**, *93* (7), 1662-1664.
22. Büchi, G.; Inman, C. G.; Lipinsky, E. S., Light-catalyzed Organic Reactions. I. The Reaction of Carbonyl Compounds with 2-Methyl-2-butene in the Presence of Ultraviolet Light. *Journal of the American Chemical Society* **1954**, *76* (17), 4327-4331.
23. Krauch, C. H.; Farid, S.; Schenck, G. O., Photo-C4-Cyclodimerisation von Cumarin. *Chemische Berichte* **1966**, *99* (2), 625-633.
24. Diels, O.; Alder, K., Synthesen in der hydroaromatischen Reihe. *Justus Liebigs Annalen der Chemie* **1928**, *460* (1), 98-122.
25. Woodward, R. B.; Hoffmann, R., Stereochemistry of electrocyclic reactions. *Journal of the American Chemical Society* **1965**, *87* (2), 395-397.
26. Fukui, K.; Yonezawa, T.; Shingu, H., A Molecular Orbital Theory of Reactivity in Aromatic Hydrocarbons. *The Journal of Chemical Physics* **1952**, *20* (4), 722-725.
27. Woodward, R. B.; Hoffmann, R., *The Conservation of Orbital Symmetry*. Elsevier Science: 2013.
28. Lim, R. K. V.; Lin, Q., Photoinducible Bioorthogonal Chemistry: A Spatiotemporally Controllable Tool to Visualize and Perturb Proteins in Live Cells. *Accounts of Chemical Research* **2011**, *44* (9), 828-839.
29. Wu, H.; Devaraj, N. K., Inverse Electron-Demand Diels–Alder Bioorthogonal Reactions. *Topics in Current Chemistry* **2015**, *374* (1), 3.
30. Sammes, P. G., Photoenolisation. *Tetrahedron* **1976**, *32* (4), 405-422.
31. Herr, R. J., 5-Substituted-1H-tetrazoles as carboxylic acid isosteres: medicinal chemistry and synthetic methods. *Bioorganic & Medicinal Chemistry* **2002**, *10* (11), 3379-3393.
32. Benson, F. R., The Chemistry of the Tetrazoles. *Chemical Reviews* **1947**, *41* (1), 1-61.
33. Bladin, J. A., Ueber von Dicyanphenylhydrazin abgeleitete Verbindungen. *Berichte der deutschen chemischen Gesellschaft* **1885**, *18* (1), 1544-1551.
34. Scriven, E. F. V.; Ramsden, C. A., *Advances in Heterocyclic Chemistry*. Elsevier Science & Technology: San Diego, UNITED STATES, 2017.
35. Wong, M. W.; Leung-Toung, R.; Wentrup, C., Tautomeric equilibrium and hydrogen shifts of tetrazole in the gas phase and in solution. *Journal of The American Chemical Society* **1993**, *115* (6), 2465-2472.
36. Novak, I.; Kovač, B.; Klasinc, L.; Ostrovskii, V. A., Nitrogen lone pair interactions in organic molecules: a photoelectron spectroscopic study. *Spectrochimica Acta Part A: Molecular and Biomolecular Spectroscopy* **2003**, *59* (8), 1725-1731.
37. Ostrovskii, V. A.; Popova, E. A.; Trifonov, R. E., Chapter One - Developments in Tetrazole Chemistry (2009–16). In *Advances in Heterocyclic Chemistry*, Scriven, E. F. V.; Ramsden, C. A., Eds. Academic Press: 2017; Vol. 123, pp 1-62.
38. Ramsden, C. A., The influence of aza-substitution on azole aromaticity. *Tetrahedron* **2010**, *66* (14), 2695-2699.
39. Kiselev, V. G.; Cheblakov, P. B.; Gritsan, N. P., Tautomerism and Thermal Decomposition of Tetrazole: High-Level ab Initio Study. *The Journal of Physical Chemistry A* **2011**, *115* (9), 1743-1753.
40. Hantzsch, A.; Vagt, A., Ueber das sogenannte Diazoguanidin. *Justus Liebigs Annalen der Chemie* **1901**, *314* (3), 339-369.

41. Sivaguru, P.; Bhuvaneswari, K.; Ramkumar, R.; Lalitha, A., Synthesis of 5-substituted 1H-tetrazoles catalyzed by ceric ammonium nitrate supported HY-zeolite. *Tetrahedron Letters* **2014**, *55* (41), 5683-5686.
42. Zarghani, M.; Akhlaghinia, B., Magnetically separable Fe₃O₄@chitin as an eco-friendly nanocatalyst with high efficiency for green synthesis of 5-substituted-1H-tetrazoles under solvent-free conditions. *RSC Advances* **2016**, *6* (38), 31850-31860.
43. Abdollahi-Alibeik, M.; Moaddeli, A. L. I., Cu-MCM-41 nanoparticles: An efficient catalyst for the synthesis of 5-substituted 1H-tetrazoles via [3+2] cycloaddition reaction of nitriles and sodium azide. *Journal of Chemical Sciences* **2016**, *128* (1), 93-99.
44. Razavi, N.; Akhlaghinia, B., Cu(ii) immobilized on aminated epichlorohydrin activated silica (CAES): as a new, green and efficient nanocatalyst for preparation of 5-substituted-1H-tetrazoles. *RSC Advances* **2015**, *5* (16), 12372-12381.
45. Ghodsinia, S. S. E.; Akhlaghinia, B., A rapid metal free synthesis of 5-substituted-1H-tetrazoles using cuttlebone as a natural high effective and low cost heterogeneous catalyst. *RSC Advances* **2015**, *5* (62), 49849-49860.
46. Li, Y.; Gao, L.-X.; Han, F.-S., Efficient synthesis of 2,5-disubstituted tetrazoles via the Cu₂O-catalyzed aerobic oxidative direct cross-coupling of N-H free tetrazoles with boronic acids. *Chemical Communications* **2012**, *48* (21), 2719-2721.
47. Onaka, T.; Umamoto, H.; Miki, Y.; Nakamura, A.; Maegawa, T., [Cu(OH)(TMEDA)]₂Cl₂-Catalyzed Regioselective 2-Arylation of 5-Substituted Tetrazoles with Boronic Acids under Mild Conditions. *The Journal of Organic Chemistry* **2014**, *79* (14), 6703-6707.
48. Lam, P. Y. S.; Clark, C. G.; Saubern, S.; Adams, J.; Winters, M. P.; Chan, D. M. T.; Combs, A., New aryl/heteroaryl C-N bond cross-coupling reactions via arylboronic acid/cupric acetate arylation. *Tetrahedron Letters* **1998**, *39* (19), 2941-2944.
49. Livingstone, K.; Bertrand, S.; Jamieson, C., One-Pot Suzuki-Hydrogenolysis Protocol for the Modular Synthesis of 2,5-Diaryltetrazoles. *The Journal of Organic Chemistry* **2020**, *85* (11), 7413-7423.
50. Aridoss, G.; Laali, K. K., Highly Efficient Synthesis of 5-Substituted 1H-Tetrazoles Catalyzed by Cu-Zn Alloy Nanopowder, Conversion into 1,5- and 2,5-Disubstituted Tetrazoles, and Synthesis and NMR Studies of New Tetrazolium Ionic Liquids. *European Journal of Organic Chemistry* **2011**, *2011* (31), 6343-6355.
51. Liu, C.-Y.; Li, Y.; Ding, J.-Y.; Dong, D.-W.; Han, F.-S., The Development of Copper-Catalyzed Aerobic Oxidative Coupling of H-Tetrazoles with Boronic Acids and an Insight into the Reaction Mechanism. *Chemistry – A European Journal* **2014**, *20* (8), 2373-2381.
52. Lippmann, E.; Könnecke, A.; Beyer, G., Synthesis of 5-substituted 2-phenyl-tetrazoles. 1H-NMR- and mass spectra. *Monatshefte für Chemie* **1975**, *106* (2), 437-442.
53. Dimroth, O.; Merzenbacher, S., *Berichte der deutschen chemischen Gesellschaft* **1910**, *43*.
54. Ito, S.; Tanaka, Y.; Kakehi, A.; Kondo, K.-i., A Facile Synthesis of 2,5-Disubstituted Tetrazoles by the Reaction of Phenylsulfonylhydrazones with Arenediazonium Salts. *Bulletin of the Chemical Society of Japan* **1976**, *49* (7), 1920-1923.
55. Ramanathan, M.; Wang, Y.-H.; Liu, S.-T., One-Pot Reactions for Synthesis of 2,5-Substituted Tetrazoles from Aryldiazonium Salts and Amidines. *Organic Letters* **2015**, *17* (23), 5886-5889.
56. Imai, T.; Harigae, R.; Moriyama, K.; Togo, H., Preparation of 5-Aryl-2-Alkyltetrazoles with Aromatic Aldehydes, Alkylhydrazine, Di-tert-butyl Azodicarboxylate, and [Bis(trifluoroacetoxy)iodo]benzene. *The Journal of Organic Chemistry* **2016**, *81* (9), 3975-3980.

57. Chuprun, S.; Dar'in, D.; Kantin, G.; Krasavin, M., [3+ 2]-Cycloaddition of α -Diazocarbonyl Compounds with Arenediazonium Salts Catalyzed by Silver Nitrate Delivers 2, 5-Disubstituted Tetrazoles. *Synthesis* **2019**, 51 (21), 3998-4005.
58. Clovis, J. S.; Eckell, A.; Huisgen, R.; Sustmann, R., 1,3-Dipolare Cycloadditionen, XXV. Der Nachweis des freien Diphenylnitrilimins als Zwischenstufe bei Cycloadditionen. *Chemische Berichte* **1967**, 100 (1), 60-70.
59. Meier, H.; Heinzelmann, W.; Heimgartner, H., Direkter Nachweis von Diphenylnitrilimin bei der Photolyse von 2, 5-Diphenyltetrazol. *CHIMIA International Journal for Chemistry* **1980**, 34 (12), 504-506.
60. Csongár, C.; Leihkauf, P.; Lohse, V.; Tomaschewski, G., Photochemistry of arylsubstituted 2H-tetrazoles - direct spectroscopic determination of diarylnitrilimines. Deutscher Verlag für Grundstoffindustrie Karl Heine Str 27b, 04229 Leipzig: 1984; Vol. 24, pp 96-97.
61. Wang, Y.; Rivera Vera, C. I.; Lin, Q., Convenient Synthesis of Highly Functionalized Pyrazolines via Mild, Photoactivated 1,3-Dipolar Cycloaddition. *Organic Letters* **2007**, 9 (21), 4155-4158.
62. Huisgen, R.; Sauer, J.; Seidel, M., Ringöffnungen der Azole, VI. Die Thermolyse 2,5-disubstituierter Tetrazole zu Nitrilimininen. *Chemische Berichte* **1961**, 94 (9), 2503-2509.
63. Singh, S. P.; Kumar, D.; Prakash, O.; Kapoor, R. P., Hypervalent Iodine Oxidation of 1, 3, 5-Trisubstituted Pyrazolines: A Facile Synthesis of 1,3,5-Trisubstituted Pyrazoles. *Synthetic Communications* **1997**, 27 (15), 2683-2689.
64. Gamapwar, S. V.; Tale, N. P.; Karade, N. N., Dess–Martin Periodinane–Mediated Oxidative Aromatization of 1,3,5-Trisubstituted Pyrazolines. *Synthetic Communications* **2012**, 42 (17), 2617-2623.
65. Wang, Y.; Hu, W. J.; Song, W.; Lim, R. K. V.; Lin, Q., Discovery of Long-Wavelength Photoactivatable Diaryltetrazoles for Bioorthogonal 1,3-Dipolar Cycloaddition Reactions. *Organic Letters* **2008**, 10 (17), 3725-3728.
66. An, P.; Yu, Z.; Lin, Q., Design of oligothiophene-based tetrazoles for laser-triggered photoclick chemistry in living cells. *Chemical Communications* **2013**, 49 (85), 9920-9922.
67. Huisgen, R.; Sustmann, R.; Wallbillich, G., 1,3-Dipolare Cycloadditionen, XXIX. Orientierungsphänomene bei der Anlagerung von Nitrilimininen an α,β -ungesättigte Carbonester, Vinyläther und Enamine. *Chemische Berichte* **1967**, 100 (6), 1786-1801.
68. Huisgen, R.; Seidel, M.; Wallbillich, G.; Knupfer, H., Diphenyl-nitrilimin und seine 1,3-dipolaren additionen an alkene und alkine. *Tetrahedron* **1962**, 17 (1), 3-29.
69. Sustmann, R., A simple model for substituent effects in cycloaddition reactions. I. 1,3-dipolar cycloadditions. *Tetrahedron Letters* **1971**, 12 (29), 2717-2720.
70. Green, B.; Sheu, K., Synthesis of steroidal D-ring fused pyrazolines: Study of regiochemistry of addition. *Steroids* **1994**, 59 (8), 479-484.
71. Chandanshive, J. Z.; González, P. B.; Tiznado, W.; Bonini, B. F.; Caballero, J.; Femoni, C.; Comes Franchini, M., 1,3-Dipolar cycloaddition of nitrile imines with α,β -unsaturated lactones, thiolactones and lactams: synthesis of ring-fused pyrazoles. *Tetrahedron* **2012**, 68 (16), 3319-3328.
72. Wang, Y.; Song, W.; Hu, W. J.; Lin, Q., Fast Alkene Functionalization In Vivo by Photoclick Chemistry: HOMO Lifting of Nitrile Imine Dipoles. *Angewandte Chemie International Edition* **2009**, 48 (29), 5330-5333.
73. Blasco, E.; Sugawara, Y.; Lederhose, P.; Blinco, J. P.; Kelterer, A. M.; Barner-Kowollik, C., Understanding Reactivity Patterns in Light-Induced Nitrile Imine Mediated Tetrazole–Ene Cycloadditions. *ChemPhotoChem* **2017**, 1 (5), 159-163.

74. Kolb, H. C.; Finn, M.; Sharpless, K. B., Click chemistry: diverse chemical function from a few good reactions. *Angewandte Chemie International Edition* **2001**, *40* (11), 2004-2021.
75. Song, W.; Wang, Y.; Qu, J.; Lin, Q., Selective Functionalization of a Genetically Encoded Alkene-Containing Protein via "Photoclick Chemistry" in Bacterial Cells. *Journal of the American Chemical Society* **2008**, *130* (30), 9654-9655.
76. Jamieson, C.; Livingstone, K., *The Nitrile Imine 1,3-dipole: Properties, Reactivity and Applications*. Springer: 2020.
77. Wang, Y.; Lin, Q., Synthesis and Evaluation of Photoreactive Tetrazole Amino Acids. *Organic Letters* **2009**, *11* (16), 3570-3573.
78. Pla, D.; Tan, D. S.; Gin, D. Y., 5-(Methylthio) tetrazoles as versatile synthons in the stereoselective synthesis of polycyclic pyrazolines via photoinduced intramolecular nitrile imine-alkene 1, 3-dipolar cycloaddition. *Chemical science* **2014**, *5* (6), 2407-2415.
79. Oh, L. M., Synthesis of celecoxib via 1, 3-dipolar cycloaddition. *Tetrahedron letters* **2006**, *47* (45), 7943-7946.
80. Ostrovskii, V.; Trifonov, R.; Popova, E., Medicinal chemistry of tetrazoles. *Russian Chemical Bulletin* **2012**, *61* (4), 768-780.
81. Song, W.; Wang, Y.; Qu, J.; Madden, M. M.; Lin, Q., A Photoinducible 1,3-Dipolar Cycloaddition Reaction for Rapid, Selective Modification of Tetrazole-Containing Proteins. *Angewandte Chemie International Edition* **2008**, *47* (15), 2832-2835.
82. Li, Z.; Qian, L.; Li, L.; Bernhammer, J. C.; Huynh, H. V.; Lee, J.-S.; Yao, S. Q., Tetrazole Photoclick Chemistry: Reinvestigating Its Suitability as a Bioorthogonal Reaction and Potential Applications. *Angewandte Chemie International Edition* **2016**, *55* (6), 2002-2006.
83. Zhao, S.; Dai, J.; Hu, M.; Liu, C.; Meng, R.; Liu, X.; Wang, C.; Luo, T., Photo-induced coupling reactions of tetrazoles with carboxylic acids in aqueous solution: application in protein labelling. *Chemical Communications* **2016**, *52* (25), 4702-4705.
84. Tian, Y.; Jacinto, M. P.; Zeng, Y.; Yu, Z.; Qu, J.; Liu, W. R.; Lin, Q., Genetically encoded 2-aryl-5-carboxytetrazoles for site-selective protein photo-cross-linking. *Journal of the American Chemical Society* **2017**, *139* (17), 6078-6081.
85. Tian, Y.; Lin, Q., Genetic encoding of 2-aryl-5-carboxytetrazole-based protein photo-cross-linkers. *Chemical Communications* **2018**, *54* (35), 4449-4452.
86. Cheng, K.; Lee, J. S.; Hao, P.; Yao, S. Q.; Ding, K.; Li, Z., Tetrazole-Based Probes for Integrated Phenotypic Screening, Affinity-Based Proteome Profiling, and Sensitive Detection of a Cancer Biomarker. *Angewandte Chemie* **2017**, *129* (47), 15240-15244.
87. Yu, Z.; Ho, L. Y.; Lin, Q., Rapid, photoactivatable turn-on fluorescent probes based on an intramolecular photoclick reaction. *Journal of the American Chemical Society* **2011**, *133* (31), 11912-11915.
88. Yu, Z.; Ohulchanskyy, T. Y.; An, P.; Prasad, P. N.; Lin, Q., Fluorogenic, Two-Photon-Triggered Photoclick Chemistry in Live Mammalian Cells. *Journal of the American Chemical Society* **2013**, *135* (45), 16766-16769.
89. Stille, J.; Gotter, L., Polymers from 1, 3-dipole addition reactions: A bisnitrilimine dipole from a bistetrazole precursor. *Journal of Polymer Science Part B: Polymer Letters* **1968**, *6* (1), 11-14.
90. Estupinan, D.; Gegenhuber, T.; Blinco, J. P.; Barner-Kowollik, C.; Barner, L., Self-reporting fluorescent step-growth raft polymers based on nitrile imine-mediated tetrazole-ene cycloaddition chemistry. *ACS Macro Letters* **2017**, *6* (3), 229-234.
91. Mueller, J. O.; Voll, D.; Schmidt, F. G.; Delaittre, G.; Barner-Kowollik, C., Fluorescent polymers from non-fluorescent photoreactive monomers. *Chemical Communications* **2014**, *50* (99), 15681-15684.

92. Dietrich, M.; Delaittre, G.; Blinco, J. P.; Inglis, A. J.; Bruns, M.; Barner-Kowollik, C., Photoclickable Surfaces for Profluorescent Covalent Polymer Coatings. *Advanced Functional Materials* **2012**, 22 (2), 304-312.
93. Delaittre, G.; Goldmann, A. S.; Mueller, J. O.; Barner-Kowollik, C., Efficient Photochemical Approaches for Spatially Resolved Surface Functionalization. *Angewandte Chemie International Edition* **2015**, 54 (39), 11388-11403.
94. Rodriguez-Emmenegger, C.; Preuss, C. M.; Yameen, B.; Pop-Georgievski, O.; Bachmann, M.; Mueller, J. O.; Bruns, M.; Goldmann, A. S.; Bastmeyer, M.; Barner-Kowollik, C., Controlled Cell Adhesion on Poly(dopamine) Interfaces Photopatterned with Non-Fouling Brushes. *Advanced Materials* **2013**, 25 (42), 6123-6127.
95. Blasco, E.; Piñol, M.; Oriol, L.; Schmidt, B. V. K. J.; Welle, A.; Trouillet, V.; Bruns, M.; Barner-Kowollik, C., Photochemical Generation of Light Responsive Surfaces. *Advanced Functional Materials* **2013**, 23 (32), 4011-4019.
96. Stolzer, L.; Vigovskaya, A.; Barner-Kowollik, C.; Fruk, L., A self-reporting tetrazole-based linker for the biofunctionalization of gold nanorods. *Chemistry – A European Journal* **2015**, 21, 14309-14313.
97. Zoppe, J. O.; Ataman, N. C.; Mocny, P.; Wang, J.; Moraes, J.; Klok, H.-A., Surface-Initiated Controlled Radical Polymerization: State-of-the-Art, Opportunities, and Challenges in Surface and Interface Engineering with Polymer Brushes. *Chemical Reviews* **2017**, 117 (3), 1105-1318.
98. Wilke, P.; Abt, D.; Große, S.; Barner-Kowollik, C.; Börner, H. G., Selective functionalization of laser printout patterns on cellulose paper sheets coated with surface-specific peptides. *Journal of Materials Chemistry A* **2017**, 5 (31), 16144-16149.
99. Gegenhuber, T.; Abt, D.; Welle, A.; Özbek, S.; Goldmann, A. S.; Barner-Kowollik, C., Spatially resolved photochemical coding of reversibly anchored cysteine-rich domains. *Journal of Materials Chemistry B* **2017**, 5 (25), 4993-5000.
100. Buten, C.; Lamping, S.; Körsgen, M.; Arlinghaus, H. F.; Jamieson, C.; Ravoo, B. J., Surface functionalization with carboxylic acids by photochemical microcontact printing and tetrazole chemistry. *Langmuir* **2018**, 34 (5), 2132-2138.
101. Vonhören, B.; Roling, O.; Buten, C.; Körsgen, M.; Arlinghaus, H. F.; Ravoo, B. J., Photochemical Microcontact Printing by Tetrazole Chemistry. *Langmuir* **2016**, 32 (9), 2277-2282.
102. Darkow, R.; Yoshikawa, M.; Kitao, T.; Tomaschewski, G.; Schellenberg, J., Photomodification of a poly(acrylonitrile-co-butadiene-co-styrene) containing diaryltetrazolyl groups. *Journal of Polymer Science Part A: Polymer Chemistry* **1994**, 32 (9), 1657-1664.
103. Darkow, R.; Hartmann, U.; Tomaschewski, G., Synthesis, photomodification and characterization of homo- and copolymers with 2,5-bisaryltetrazolyl pendant groups. *Reactive and Functional Polymers* **1997**, 32 (2), 195-207.
104. Fan, Y.; Deng, C.; Cheng, R.; Meng, F.; Zhong, Z., In situ forming hydrogels via catalyst-free and bioorthogonal “tetrazole–alkene” photo-click chemistry. *Biomacromolecules* **2013**, 14 (8), 2814-2821.
105. Mueller, J. O.; Guimard, N. K.; Oehlenschlaeger, K. K.; Schmidt, F. G.; Barner-Kowollik, C., Sunlight-induced crosslinking of 1,2-polybutadienes: access to fluorescent polymer networks. *Polymer Chemistry* **2014**, 5 (4), 1447-1456.
106. Hufendiek, A.; Carlmark, A.; Meier, M. A. R.; Barner-Kowollik, C., Fluorescent Covalently Cross-Linked Cellulose Networks via Light-Induced Ligation. *ACS Macro Letters* **2016**, 5 (1), 139-143.

107. Willenbacher, J.; Wuest, K. N. R.; Mueller, J. O.; Kaupp, M.; Wagenknecht, H.-A.; Barner-Kowollik, C., Photochemical Design of Functional Fluorescent Single-Chain Nanoparticles. *ACS Macro Letters* **2014**, *3* (6), 574-579.
108. Yang, N. C.; Rivas, C., A new photochemical primary process, the photochemical enolization of *o*-substituted benzophenones. *Journal of the American Chemical Society* **1961**, *83* (9), 2213-2213.
109. Porter, G.; Tchir, M. F., Photoenolization of ortho-substituted benzophenones by flash photolysis. *Journal of the Chemical Society A: Inorganic, Physical, Theoretical* **1971**, (0), 3772-3777.
110. Findlay, D. M.; Tchir, M. F., Photoenolization of ortho-alkyl-substituted acetophenones: evidence for the enol triplet state. *Journal of the Chemical Society, Faraday Transactions 1: Physical Chemistry in Condensed Phases* **1976**, *72* (0), 1096-1100.
111. Gruending, T.; Oehlenschlaeger, K. K.; Frick, E.; Glassner, M.; Schmid, C.; Barner-Kowollik, C., Rapid UV Light-Triggered Macromolecular Click Conjugations via the Use of *o*-Quinodimethanes. *Macromolecular Rapid Communications* **2011**, *32* (11), 807-812.
112. Pauloehrl, T.; Delaittre, G.; Winkler, V.; Welle, A.; Bruns, M.; Börner, H. G.; Greiner, A. M.; Bastmeyer, M.; Barner-Kowollik, C., Adding Spatial Control to Click Chemistry: Phototriggered Diels–Alder Surface (Bio)functionalization at Ambient Temperature. *Angewandte Chemie International Edition* **2012**, *51* (4), 1071-1074.
113. Menzel, J. P.; Noble, B. B.; Lauer, A.; Coote, M. L.; Blinco, J. P.; Barner-Kowollik, C., Wavelength Dependence of Light-Induced Cycloadditions. *Journal of the American Chemical Society* **2017**, *139* (44), 15812-15820.
114. Mellows, S. M.; Sammes, P. G., Stereoselective trapping of a photo-enol. *Journal of the Chemical Society D: Chemical Communications* **1971**, (1), 21-22.
115. Segura, J. L.; Martín, N., *o*-Quinodimethanes: Efficient Intermediates in Organic Synthesis. *Chemical Reviews* **1999**, *99* (11), 3199-3246.
116. Charlton, J. L.; Alauddin, M. M., Orthoquinodimethanes. *Tetrahedron* **1987**, *43* (13), 2873-2889.
117. Krappitz, T.; Feist, F.; Lamparth, I.; Moszner, N.; John, H.; Blinco, J. P.; Dargaville, T. R.; Barner-Kowollik, C., Polymer networks based on photo-caged diene dimerization. *Materials Horizons* **2019**, *6* (1), 81-89.
118. Quick, A. S.; Rothfuss, H.; Welle, A.; Richter, B.; Fischer, J.; Wegener, M.; Barner-Kowollik, C., Fabrication and Spatially Resolved Functionalization of 3D Microstructures via Multiphoton-Induced Diels–Alder Chemistry. *Advanced Functional Materials* **2014**, *24* (23), 3571-3580.
119. Bauer, D. M.; Rogge, A.; Stolzer, L.; Barner-Kowollik, C.; Fruk, L., Light induced DNA–protein conjugation. *Chemical Communications* **2013**, *49* (77), 8626-8628.
120. Tischer, T.; Claus, T. K.; Bruns, M.; Trouillet, V.; Linkert, K.; Rodriguez-Emmenegger, C.; Goldmann, A. S.; Perrier, S.; Börner, H. G.; Barner-Kowollik, C., Spatially Controlled Photochemical Peptide and Polymer Conjugation on Biosurfaces. *Biomacromolecules* **2013**, *14* (12), 4340-4350.
121. Altintas, O.; Willenbacher, J.; Wuest, K. N.; Oehlenschlaeger, K. K.; Krolla-Sidenstein, P.; Gliemann, H.; Barner-Kowollik, C., A mild and efficient approach to functional single-chain polymeric nanoparticles via photoinduced Diels–Alder ligation. *Macromolecules* **2013**, *46* (20), 8092-8101.
122. Hildebrandt, K.; Kaupp, M.; Molle, E.; Menzel, J. P.; Blinco, J. P.; Barner-Kowollik, C., Star polymer synthesis via λ -orthogonal photochemistry. *Chemical Communications* **2016**, *52* (60), 9426-9429.
123. Anet, R., The photodimers of coumarin and related compounds. *Canadian Journal of Chemistry* **1962**, *40* (7), 1249-1257.

124. Trenor, S. R.; Long, T. E.; Love, B. J., Photoreversible Chain Extension of Poly(ethylene glycol). *Macromolecular Chemistry and Physics* **2004**, *205* (6), 715-723.
125. Nagata, M.; Yamamoto, Y., Synthesis and characterization of photocrosslinked poly(ϵ -caprolactone)s showing shape-memory properties. *Journal of Polymer Science Part A: Polymer Chemistry* **2009**, *47* (9), 2422-2433.
126. Kim, W. G., Photocure properties of high-heat-resistant photoreactive polymers with cinnamate groups. *Journal of Applied Polymer Science* **2008**, *107* (6), 3615-3624.
127. Moghaddam, M. J.; Hozumi, S.; Inaki, Y.; Takemoto, K., Functional monomers and polymers 159 synthesis and photochemical reactions of polymers containing thymine photodimer units in the main chain. *Journal of Polymer Science Part A: Polymer Chemistry* **1988**, *26* (12), 3297-3308.
128. Somlai, A. P.; Cozad, R. A.; Page, K. A.; Williams, H. R.; Creed, D.; Hoyle, C. E., The photochemistry of some main chain liquid crystalline 4, 4'-stilbene dicarboxylate polyesters. *Photochemical & Photobiological Sciences* **2008**, *7* (5), 578-587.
129. Trenor, S. R.; Shultz, A. R.; Love, B. J.; Long, T. E., Coumarins in Polymers: From Light Harvesting to Photo-Cross-Linkable Tissue Scaffolds. *Chemical Reviews* **2004**, *104* (6), 3059-3078.
130. Lewis, F. D.; Barancyk, S. V., Lewis acid catalysis of photochemical reactions. 8. Photodimerization and cross-cycloaddition of coumarin. *Journal of the American Chemical Society* **1989**, *111* (23), 8653-8661.
131. Shim, S. C.; Choi, K. Y.; Song, P. S., Studies on the phototoxicity of coumarin derivatives. *Photochemistry and Photobiology* **1978**, *27* (1), 25-31.
132. Lewis, F. D.; Howard, D. K.; Oxman, J. D., Lewis acid catalysis of coumarin photodimerization. *Journal of the American Chemical Society* **1983**, *105* (10), 3344-3345.
133. Ramamurthy, V.; Sivaguru, J., Supramolecular photochemistry as a potential synthetic tool: photocycloaddition. *Chemical reviews* **2016**, *116* (17), 9914-9993.
134. Kaur, G.; Johnston, P.; Saito, K., Photo-reversible dimerisation reactions and their applications in polymeric systems. *Polymer Chemistry* **2014**, *5* (7), 2171-2186.
135. Doi, T.; Kawai, H.; Murayama, K.; Kashida, H.; Asanuma, H., Visible-Light-Triggered Cross-Linking of DNA Duplexes by Reversible [2+ 2] Photocycloaddition of Styrylpyrene. *Chemistry–A European Journal* **2016**, *22* (30), 10533-10538.
136. Kehroesser, D.; Baumann, R.-P.; Kim, H.-C.; Hampp, N., Photochemistry of Coumarin-Functionalized SiO₂ Nanoparticles. *Langmuir* **2011**, *27* (7), 4149-4155.
137. Marschner, D. E.; Frisch, H.; Offenloch, J. T.; Tuten, B. T.; Becer, C. R.; Walther, A.; Goldmann, A. S.; Tzvetkova, P.; Barner-Kowollik, C., Visible Light [2 + 2] Cycloadditions for Reversible Polymer Ligation. *Macromolecules* **2018**, *51* (10), 3802-3807.
138. Frisch, H.; Menzel, J. P.; Bloesser, F. R.; Marschner, D. E.; Mundsinger, K.; Barner-Kowollik, C., Photochemistry in Confined Environments for Single-Chain Nanoparticle Design. *Journal of the American Chemical Society* **2018**, *140* (30), 9551-9557.
139. Frisch, H.; Mundsinger, K.; Poad, B. L. J.; Blanksby, S. J.; Barner-Kowollik, C., Wavelength-gated photoreversible polymerization and topology control. *Chemical Science* **2020**, *11* (10), 2834-2842.
140. D'Orazio, J.; Jarrett, S.; Amaro-Ortiz, A.; Scott, T., UV radiation and the skin. *International Journal of Molecular Sciences* **2013**, *14* (6), 12222-12248.
141. Stolik, S.; Delgado, J. A.; Pérez, A.; Anasagasti, L., Measurement of the penetration depths of red and near infrared light in human "ex vivo" tissues. *Journal of Photochemistry and Photobiology B: Biology* **2000**, *57* (2), 90-93.

142. Kovalenko, N.; Abdulkadirov, A.; Gerko, V.; Alfimov, M., Some peculiarities of diarylethylenes with 3-pyrenyl fragments. *Journal of Applied Spectroscopy* **1980**, *32* (6), 607-612.
143. Kovalenko, N.; Abdulkadyrov, A.; Gerko, V.; Alfimov, M., Luminescent and photochemical behaviour of diarylethylenes with 3-pyrenyl substituents. *Journal of Photochemistry* **1980**, *12* (1), 59-65.
144. Truong, V. X.; Li, F.; Ercole, F.; Forsythe, J. S., Wavelength-Selective Coupling and Decoupling of Polymer Chains via Reversible [2 + 2] Photocycloaddition of Styrylpyrene for Construction of Cytocompatible Photodynamic Hydrogels. *ACS Macro Letters* **2018**, *7* (4), 464-469.
145. Kalayci, K.; Frisch, H.; Barner-Kowollik, C.; Truong, V. X., Wavelength-Dependent Stiffening of Hydrogel Matrices via Redshifted [2+2] Photocycloadditions. *Advanced Functional Materials* **2020**, *30* (15), 1908171.
146. Frisch, H.; Kodura, D.; Bloesser, F. R.; Michalek, L.; Barner-Kowollik, C., Wavelength-Selective Folding of Single Polymer Chains with Different Colors of Visible Light. *Macromolecular Rapid Communications* **2020**, *41* (1), 1900414.
147. Ludwanowski, S.; Hoenders, D.; Kalayci, K.; Frisch, H.; Barner-Kowollik, C.; Walther, A., Modular functionalization and hydrogel formation via red-shifted and self-reporting [2+2] cycloadditions. *Chemical Communications* **2021**, *57* (6), 805-808.
148. Michalek, L.; Bialas, S.; Walden, S. L.; Bloesser, F. R.; Frisch, H.; Barner-Kowollik, C., 2D Fabrication of Tunable Responsive Interpenetrating Polymer Networks from a Single Photoresist. *Advanced Functional Materials* **2020**, *30* (48), 2005328.
149. Bialas, S.; Krappitz, T.; Walden, S. L.; Kalayci, K.; Kodura, D.; Frisch, H.; MacLeod, J. M.; Nelson, A.; Michalek, L.; Barner-Kowollik, C., Light-Gated Control of Conformational Changes in Polymer Brushes. *Advanced Materials Technologies* **2021**, 2100347.
150. Frisch, H.; Bloesser, F. R.; Barner-Kowollik, C., Controlling Chain Coupling and Single-Chain Ligation by Two Colours of Visible Light. *Angewandte Chemie International Edition* **2019**, *58* (11), 3604-3609.
151. Fritzsche, J., Ueber die festen Kohlenwasserstoffe des Steinkohlentheers. *Journal für praktische Chemie* **1866**, *97* (1), 290-303.
152. Ciamician, G.; Silber, P., Chemische Lichtwirkungen. *Berichte der deutschen chemischen Gesellschaft* **1902**, *35* (4), 4128-4131.
153. Beukers, R.; Berends, W., Isolation and identification of the irradiation product of thymine. *Biochimica et Biophysica Acta* **1960**, *41* (3), 550-551.
154. Sage, E.; Girard, P.-M.; Francesconi, S., Unravelling UVA-induced mutagenesis. *Photochemical & Photobiological Sciences* **2012**, *11* (1), 74-80.
155. Fairbanks, B. D.; Macdougall, L. J.; Mavila, S.; Sinha, J.; Kirkpatrick, B. E.; Anseth, K. S.; Bowman, C. N., Photoclick Chemistry: A Bright Idea. *Chemical Reviews* **2021**, *121* (12), 6915-6990.
156. Wagenknecht, H.-A., Unraveling the Pathways to UVA-Induced DNA Photodamage: (6-4) Photoproduct as a Potential "Trojan Horse". *ChemPhysChem* **2013**, *14* (14), 3197-3198.
157. Tsivgoulis, G. M.; Lehn, J. M., Multiplexing optical systems: Multicolor-bifluorescent-biredox photochromic mixtures. *Advanced Materials* **1997**, *9* (8), 627-630.
158. Menzel, J. P.; Noble, B. B.; Blinco, J. P.; Barner-Kowollik, C., Predicting wavelength-dependent photochemical reactivity and selectivity. *Nature Communications* **2021**, *12* (1), 1691.
159. Offenloch, J. T.; Gernhardt, M.; Blinco, J. P.; Frisch, H.; Mutlu, H.; Barner-Kowollik, C., Contemporary Photoligation Chemistry: The Visible Light Challenge. *Chemistry – A European Journal* **2019**, *25* (15), 3700-3709.

160. Ritter, S. C.; König, B., Signal amplification and transduction by photo-activated catalysis. *Chemical Communications* **2006**, (45), 4694-4696.
161. Rickgauer, J. P.; Tank, D. W., Two-photon excitation of channelrhodopsin-2 at saturation. *Proceedings of the National Academy of Sciences* **2009**, *106* (35), 15025-15030.
162. Göppert-Mayer, M., Über Elementarakte mit zwei Quantensprüngen. *Annalen der Physik* **1931**, *401* (3), 273-294.
163. Kaiser, W.; Garrett, C. G. B., Two-Photon Excitation in CaF₂: Eu²⁺. *Physical Review Letters* **1961**, *7* (6), 229-231.
164. LaFratta, C. N.; Fourkas, J. T.; Baldacchini, T.; Farrer, R. A., Multiphoton Fabrication. *Angewandte Chemie International Edition* **2007**, *46* (33), 6238-6258.
165. Zipfel, W. R.; Williams, R. M.; Webb, W. W., Nonlinear magic: multiphoton microscopy in the biosciences. *Nature Biotechnology* **2003**, *21*, 1369.
166. Barner-Kowollik, C.; Bastmeyer, M.; Blasco, E.; Delaittre, G.; Müller, P.; Richter, B.; Wegener, M., 3D Laser Micro- and Nanoprinting: Challenges for Chemistry. *Angewandte Chemie International Edition* **2017**, *56* (50), 15828-15845.
167. Fisher, W. G.; Partridge, W. P.; Dees, C.; Wachter, E. A., Simultaneous Two-Photon Activation of Type-I Photodynamic Therapy Agents. *Photochemistry and Photobiology* **1997**, *66* (2), 141-155.
168. Zou, Y. Q.; Lu, L. Q.; Fu, L.; Chang, N. J.; Rong, J.; Chen, J. R.; Xiao, W. J., Visible-light-induced oxidation/[3+ 2] cycloaddition/oxidative aromatization sequence: a photocatalytic strategy to construct pyrrolo [2, 1-a] isoquinolines. *Angewandte Chemie International Edition* **2011**, *50* (31), 7171-7175.
169. Truong, V. X.; Barner-Kowollik, C., Red-Light Driven Photocatalytic Oxime Ligation for Bioorthogonal Hydrogel Design. *ACS Macro Letters* **2021**, *10* (1), 78-83.
170. Allison-Logan, S.; Fu, Q.; Sun, Y.; Liu, M.; Xie, J.; Tang, J.; Qiao, G. G., From UV to NIR: A Full-Spectrum Metal-Free Photocatalyst for Efficient Polymer Synthesis in Aqueous Conditions. *Angewandte Chemie International Edition* **2020**, *59* (48), 21392-21396.
171. Ribelli, T. G.; Konkolewicz, D.; Pan, X.; Matyjaszewski, K., Contribution of Photochemistry to Activator Regeneration in ATRP. *Macromolecules* **2014**, *47* (18), 6316-6321.
172. Siewertsen, R.; Neumann, H.; Buchheim-Stehn, B.; Herges, R.; Näther, C.; Renth, F.; Temps, F., Highly Efficient Reversible Z-E Photoisomerization of a Bridged Azobenzene with Visible Light through Resolved S1($n\pi^*$) Absorption Bands. *Journal of the American Chemical Society* **2009**, *131* (43), 15594-15595.
173. Roke, D.; Stuckhardt, C.; Danowski, W.; Wezenberg, S. J.; Feringa, B. L., Light-Gated Rotation in a Molecular Motor Functionalized with a Dithienylethene Switch. *Angewandte Chemie International Edition* **2018**, *57*, 1-6.
174. Yu, Z.; Ho, L. Y.; Wang, Z.; Lin, Q., Discovery of new photoactivatable diaryltetrazoles for photoclick chemistry via 'scaffold hopping'. *Bioorganic & Medicinal Chemistry Letters* **2011**, *21* (17), 5033-5036.
175. Truong, V. X.; Li, F.; Forsythe, J. S., Versatile Bioorthogonal Hydrogel Platform by Catalyst-Free Visible Light Initiated Photodimerization of Anthracene. *ACS Macro Letters* **2017**, *6* (7), 657-662.
176. Lederhose, P.; Wüst, K. N. R.; Barner-Kowollik, C.; Blinco, J. P., Catalyst free visible light induced cycloaddition as an avenue for polymer ligation. *Chemical Communications* **2016**, *52* (35), 5928-5931.
177. Tuten, B. T.; Menzel, J. P.; Pahnke, K.; Blinco, J. P.; Barner-Kowollik, C., Pyreneacyl sulfides as a visible light-induced versatile ligation platform. *Chemical Communications* **2017**, *53* (32), 4501-4504.

178. Mueller, J. O.; Schmidt, F. G.; Blinco, J. P.; Barner-Kowollik, C., Visible-Light-Induced Click Chemistry. *Angewandte Chemie International Edition* **2015**, *54* (35), 10284-10288.
179. Laali, K. K.; Arrica, M. A.; Okazaki, T.; Bunge, S. D., Synthesis and Stable-Ion Studies of Regioisomeric Acetylnitropyrenes and Nitropyrenyl Carbinols and GIAO-DFT Study of Nitro Substituent Effects on α -Pyrenyl Carbocations. *European Journal of Organic Chemistry* **2008**, *2008* (36), 6093-6105.
180. Chen, K.-Y.; Chow, T. J., 1,7-Dinitroperylene bisimides: facile synthesis and characterization as n-type organic semiconductors. *Tetrahedron Letters* **2010**, *51* (45), 5959-5963.
181. Zollinger, H., *Color chemistry: syntheses, properties, and applications of organic dyes and pigments*. John Wiley & Sons: 2003.
182. Hammett, L. P., The effect of structure upon the reactions of organic compounds. Benzene derivatives. *Journal of the American Chemical Society* **1937**, *59* (1), 96-103.
183. Micikas, R. J.; Ahmed, I. A.; Acharyya, A.; Smith, A. B.; Gai, F., Tuning the electronic transition energy of indole via substitution: application to identify tryptophan-based chromophores that absorb and emit visible light. *Physical Chemistry Chemical Physics* **2021**, *23* (11), 6433-6437.
184. Hemmer, J. R.; Poelma, S. O.; Treat, N.; Page, Z. A.; Dolinski, N. D.; Diaz, Y. J.; Tomlinson, W.; Clark, K. D.; Hooper, J. P.; Hawker, C.; Read de Alaniz, J., Tunable Visible and Near Infrared Photoswitches. *Journal of the American Chemical Society* **2016**, *138* (42), 13960-13966.
185. Pascal, S.; Haefele, A.; Monnereau, C.; Charaf-Eddin, A.; Jacquemin, D.; Le Guennic, B.; Andraud, C.; Maury, O., Expanding the Polymethine Paradigm: Evidence for the Contribution of a Bis-Dipolar Electronic Structure. *The Journal of Physical Chemistry A* **2014**, *118* (23), 4038-4047.
186. Heo, J.; Ahn, H.; Won, J.; Son, J. G.; Shon, H. K.; Lee, T. G.; Han, S. W.; Baik, M.-H., Electro-inductive effect: Electrodes as functional groups with tunable electronic properties. *Science* **2020**, *370* (6513), 214-219.
187. Fast, D. E.; Lauer, A.; Menzel, J. P.; Kelterer, A.-M.; Gescheidt, G.; Barner-Kowollik, C., Wavelength-Dependent Photochemistry of Oxime Ester Photoinitiators. *Macromolecules* **2017**, *50* (5), 1815-1823.
188. Kalayci, K.; Frisch, H.; Truong, V. X.; Barner-Kowollik, C., Green light triggered [2+2] cycloaddition of halochromic styrylquinoxaline—controlling photoreactivity by pH. *Nature Communications* **2020**, *11* (1), 4193.
189. Price, R. B., Light curing in dentistry. *Dental Clinics* **2017**, *61* (4), 751-778.
190. Bechthold, M.; Weaver, J. C., Materials science and architecture. *Nature Reviews Materials* **2017**, *2* (12), 17082.
191. Jung, K.; Corrigan, N.; Ciftci, M.; Xu, J.; Seo, S. E.; Hawker, C. J.; Boyer, C., Designing with Light: Advanced 2D, 3D, and 4D Materials. *Advanced Materials* **2020**, *32* (18), 1903850.
192. Russew, M.-M.; Hecht, S., Photoswitches: From Molecules to Materials. *Advanced Materials* **2010**, *22* (31), 3348-3360.
193. Corrigan, N.; Ciftci, M.; Jung, K.; Boyer, C., Mediating Reaction Orthogonality in Polymer and Materials Science. *Angewandte Chemie International Edition* **2021**, *60* (4), 1748-1781.
194. Hildebrandt, K.; Pauloehrl, T.; Blinco, J. P.; Linkert, K.; Börner, H. G.; Barner-Kowollik, C., λ -Orthogonal Pericyclic Macromolecular Photoligation. *Angewandte Chemie International Edition* **2015**, *54* (9), 2838-2843.
195. Fichte, M. A. H.; Weyel, X. M. M.; Junek, S.; Schäfer, F.; Herbivo, C.; Goeldner, M.; Specht, A.; Wachtveitl, J.; Heckel, A., Three-Dimensional Control of DNA Hybridization by Orthogonal Two-Color Two-Photon Uncaging. *Angewandte Chemie International Edition* **2016**, *55* (31), 8948-8952.

196. Bléger, D.; Hecht, S., Visible-Light-Activated Molecular Switches. *Angewandte Chemie International Edition* **2015**, *54* (39), 11338-11349.
197. Pelloth, J. L.; Tran, P. A.; Walther, A.; Goldmann, A. S.; Frisch, H.; Truong, V. X.; Barner-Kowollik, C., Wavelength-Selective Softening of Hydrogel Networks. *Advanced Materials* **33** (39), 2102184.
198. Xu, S.; Yeow, J.; Boyer, C., Exploiting Wavelength Orthogonality for Successive Photoinduced Polymerization-Induced Self-Assembly and Photo-Crosslinking. *ACS Macro Letters* **2018**, *7* (11), 1376-1382.
199. Bialas, S.; Michalek, L.; Marschner, D. E.; Krappitz, T.; Wegener, M.; Blinco, J.; Blasco, E.; Frisch, H.; Barner-Kowollik, C., Access to Disparate Soft Matter Materials by Curing with Two Colors of Light. *Advanced Materials* **2019**, *31* (8), 1807288.
200. Zhang, X.; Xi, W.; Huang, S.; Long, K.; Bowman, C. N., Wavelength-Selective Sequential Polymer Network Formation Controlled with a Two-Color Responsive Initiation System. *Macromolecules* **2017**, *50* (15), 5652-5660.
201. Batchelor, R. R.; Blasco, E.; Wuest, K. N. R.; Lu, H.; Wegener, M.; Barner-Kowollik, C.; Stenzel, M. H., Spatially resolved coding of λ -orthogonal hydrogels by laser lithography. *Chemical Communications* **2018**, *54* (19), 2436-2439.
202. Elamri, I.; Abdellaoui, C.; Bains, J. K.; Hohmann, K. F.; Gande, S. L.; Stinal, E.; Wachtveitl, J.; Schwalbe, H., Wavelength-Selective Uncaging of Two Different Photoresponsive Groups on One Effector Molecule for Light-Controlled Activation and Deactivation. *Journal of the American Chemical Society* **2021**, *143* (28), 10596-10603.
203. DeForest, C. A.; Anseth, K. S., Cytocompatible click-based hydrogels with dynamically tunable properties through orthogonal photoconjugation and photocleavage reactions. *Nature Chemistry* **2011**, *3* (12), 925-931.
204. Wu, M.; Lin, X.; Tan, X.; Li, J.; Wei, Z.; Zhang, D.; Zheng, Y.; Zheng, A.-x.; Zhao, B.; Zeng, Y.; Liu, X.; Liu, J., Photoresponsive Nanovehicle for Two Independent Wavelength Light-Triggered Sequential Release of P-gp shRNA and Doxorubicin To Optimize and Enhance Synergistic Therapy of Multidrug-Resistant Cancer. *ACS Applied Materials & Interfaces* **2018**, *10* (23), 19416-19427.
205. Bochet, C. G., Wavelength-selective cleavage of photolabile protecting groups. *Tetrahedron Letters* **2000**, *41* (33), 6341-6346.
206. Bochet, C. G., Orthogonal Photolysis of Protecting Groups. *Angewandte Chemie International Edition* **2001**, *40* (11), 2071-2073.
207. Bochet, C. G., Two Decades of Chromatic Orthogonality. *Israel Journal of Chemistry* **2021**, *61* (7-8), 486-495.
208. Hansen, M. J.; Velema, W. A.; Lerch, M. M.; Szymanski, W.; Feringa, B. L., Wavelength-selective cleavage of photoprotecting groups: strategies and applications in dynamic systems. *Chemical Society Reviews* **2015**, *44* (11), 3358-3377.
209. Lerch, M. M.; Hansen, M. J.; Velema, W. A.; Szymanski, W.; Feringa, B. L., Orthogonal photoswitching in a multifunctional molecular system. *Nature Communications* **2016**, *7*, 12054.
210. Ishida, S.; Fukaminato, T.; Kitagawa, D.; Kobatake, S.; Kim, S.; Ogata, T.; Kurihara, S., Wavelength-selective and high-contrast multicolour fluorescence photoswitching in a mixture of photochromic nanoparticles. *Chemical Communications* **2017**, *53* (59), 8268-8271.
211. Menzel, J. P.; Feist, F.; Tuten, B.; Weil, T.; Blinco, J. P.; Barner-Kowollik, C., Light-Controlled Orthogonal Covalent Bond Formation at Two Different Wavelengths. *Angewandte Chemie International Edition* **2019**, *58* (22), 7470-7474.

212. Frisch, H.; Marschner, D. E.; Goldmann, A. S.; Barner-Kowollik, C., Wavelength-Gated Dynamic Covalent Chemistry. *Angewandte Chemie International Edition* **2018**, *57* (8), 2036-2045.
213. Einstein, A., Strahlungs-Emission und -Absorption nach der Quantentheorie. *Deutsche Physikalische Gesellschaft* **1916**, *18*, 318.
214. Einstein, A., Zur Quantentheorie der Strahlung. *Physikalische Zeitschrift* **1917**, *18*, 121.
215. Gordon, J. P.; Zeiger, H. J.; Townes, C. H., The Maser---New Type of Microwave Amplifier, Frequency Standard, and Spectrometer. *Physical Review* **1955**, *99* (4), 1264-1274.
216. Maiman, T. H., Stimulated Optical Radiation in Ruby. *Nature* **1960**, *187* (4736), 493-494.
217. Zewail, A. H., Femtochemistry. *The Journal of Physical Chemistry* **1993**, *97* (48), 12427-12446.
218. Bucksbaum, P. H., Ultrafast control. *Nature* **2003**, *421* (6923), 593-594.
219. Eichler, H. J., *Laser: Bauformen, Strahlführung, Anwendungen*. 7 ed.; Springer-Verlag: Berlin, Heidelberg, 2010.
220. Lauterborn, W.; Kurz, T., *Coherent optics: fundamentals and applications*. Springer Science & Business Media: 2003.
221. Eichler, H. J.; Eichler, J.; Lux, O., *Lasers: Basics, Advances and Applications*. Springer International Publishing: 2018.
222. Demtröder, W., *Laserspektroskopie 2: Experimentelle Techniken*. Springer-Verlag: 2013.
223. Boyd, R. W., *Nonlinear optics*. Academic press: 2020.
224. Sutherland, R. L., *Handbook of nonlinear optics*. CRC press: 2003.
225. Pavone, F. S.; Campagnola, P. J., *Second harmonic generation imaging*. CRC Press Boca Raton: 2014.
226. Brieke, C.; Rohrbach, F.; Gottschalk, A.; Mayer, G.; Heckel, A., Light-Controlled Tools. *Angewandte Chemie International Edition* **2012**, *51* (34), 8446-8476.
227. Phillips, D., Light relief: photochemistry and medicine. *Photochemical & Photobiological Sciences* **2010**, *9* (12), 1589-1596.
228. Wu, L.; Baghdachi, J., *Functional polymer coatings: principles, methods, and applications*. John Wiley & Sons: 2015.
229. Krell, K.; Harijan, D.; Ganz, D.; Doll, L.; Wagenknecht, H.-A., Postsynthetic Modifications of DNA and RNA by Means of Copper-Free Cycloadditions as Bioorthogonal Reactions. *Bioconjugate Chemistry* **2020**, *31* (4), 990-1011.
230. Kumar, G. S.; Lin, Q., Light-Triggered Click Chemistry. *Chemical Reviews* **2020**, *121* (12), 6991-7031.
231. Olson, J. P.; Banghart, M. R.; Sabatini, B. L.; Ellis-Davies, G. C. R., Spectral Evolution of a Photochemical Protecting Group for Orthogonal Two-Color Uncaging with Visible Light. *Journal of the American Chemical Society* **2013**, *135* (42), 15948-15954.
232. Guaresti, O.; Crocker, L.; Palomares, T.; Alonso-Varona, A.; Eceiza, A.; Fruk, L.; Gabilondo, N., Light-driven assembly of biocompatible fluorescent chitosan hydrogels with self-healing ability. *Journal of Materials Chemistry B* **2020**.
233. Delafresnaye, L.; Hooker, J. P.; Schmitt, C. W.; Barner, L.; Barner-Kowollik, C., Chemiluminescent Read-Out of Degradable Fluorescent Polymer Particles. *Macromolecules* **2020**, *53* (14), 5826-5832.

234. Delafresnaye, L.; Zaquen, N.; Kuchel, R. P.; Blinco, J. P.; Zetterlund, P. B.; Barner-Kowollik, C., A Simple and Versatile Pathway for the Synthesis of Visible Light Photoreactive Nanoparticles. *Advanced Functional Materials* **2018**, *28* (23), 1800342.
235. Roethlisberger, P.; Kalignedian, V.; Leumann, C., Modulation of Excess Electron Transfer through LUMO Gradients in DNA Containing Phenanthrenyl Base Surrogates. *Chemistry: a European journal* **2017**, *23* (9), 2022-2025.
236. Fifer, E. K.; Heflich, R. H.; Djurić, Z.; Howard, P. C.; Beland, F. A., Synthesis and mutagenicity of 1-nitro-6-nitrosopyrene and 1-nitro-8-nitrosopyrene, potential intermediates in the metabolic activation of 1,6- and 1,8-dinitropyrene. *Carcinogenesis* **1986**, *7* (1), 65-70.
237. Hashimoto, Y.; Shudo, K., Preparation of pure isomers of dinitropyrenes. *Chemical and pharmaceutical bulletin* **1984**, *32* (5), 1992-1994.
238. Friedman, B.; O'Shaughnessy, B., Kinetics of intermolecular reactions in dilute polymer solutions and unentangled melts. *Macromolecules* **1993**, *26* (21), 5726-5739.
239. Dietrich, M.; Glassner, M.; Gruending, T.; Schmid, C.; Falkenhagen, J.; Barner-Kowollik, C., Facile conversion of RAFT polymers into hydroxyl functional polymers: a detailed investigation of variable monomer and RAFT agent combinations. *Polymer Chemistry* **2010**, *1* (5), 634-644.
240. Techert, S.; Schmatz, S.; Wiessner, A.; Staerk, H., Photophysical Characteristics of Directly Linked Pyrene-Dimethylaniline Derivatives. *The Journal of Physical Chemistry A* **2000**, *104* (24), 5700-5710.
241. Reichardt, C., Solvatochromic Dyes as Solvent Polarity Indicators. *Chemical Reviews* **1994**, *94* (8), 2319-2358.
242. Medinger, T.; Wilkinson, F., Concentration dependence of quantum yield of triplet-state production of pyrene in ethanol. *Transactions of the Faraday Society* **1966**, *62* (0), 1785-1792.
243. Foggi, P.; Pettini, L.; Santa, I.; Righini, R.; Califano, S., Transient absorption and vibrational relaxation dynamics of the lowest excited singlet state of pyrene in solution. *The Journal of Physical Chemistry* **1995**, *99* (19), 7439-7445.
244. Duhamel, J., New Insights in the Study of Pyrene Excimer Fluorescence to Characterize Macromolecules and their Supramolecular Assemblies in Solution. *Langmuir* **2012**, *28* (16), 6527-6538.
245. Druzhinin, S. I.; Ernsting, N. P.; Kovalenko, S. A.; Lustres, L. P.; Senyushkina, T. A.; Zachariasse, K. A., Dynamics of Ultrafast Intramolecular Charge Transfer with 4-(Dimethylamino)benzotrile in Acetonitrile. *The Journal of Physical Chemistry A* **2006**, *110* (9), 2955-2969.
246. Lee, Z. Y.; Raghavan, S. S.; Ghadessy, F. J.; Teo, Y. N., Rapid and sensitive detection of acrylic acid using a novel fluorescence assay. *RSC Advances* **2014**, *4* (104), 60216-60220.
247. Heiler, C.; Bastian, S.; Lederhose, P.; Blinco, J. P.; Blasco, E.; Barner-Kowollik, C., Folding polymer chains with visible light. *Chemical Communications* **2018**, *54* (28), 3476-3479.
248. Ram, V. J.; Sethi, A.; Nath, M.; Pratap, R., *The Chemistry of Heterocycles: Nomenclature and Chemistry of Three to Five Membered Heterocycles*. Elsevier: 2019.
249. Irshadeen, I. M.; De Bruycker, K.; Micallef, A. S.; Walden, S. L.; Frisch, H.; Barner-Kowollik, C., Green light LED activated ligation of a scalable, versatile chalcone chromophore. *Polymer Chemistry* **2021**, *12* (34), 4903-4909.
250. Hatano, J.; Okuro, K.; Aida, T., Photoinduced Bioorthogonal 1,3-Dipolar Poly-cycloaddition Promoted by Oxyanionic Substrates for Spatiotemporal Operation of Molecular Glues. *Angewandte Chemie International Edition* **2016**, *55* (1), 193-198.
251. Yang, L.; Mayer, F.; Bunz, U. H.; Blasco, E.; Wegener, M., Multi-material multi-photon 3D laser micro- and nanoprinting. *Light: Advanced Manufacturing* **2021**, *2*, 1-17.

252. Peterson, J. A.; Yuan, D.; Winter, A. H., Multiwavelength Control of Mixtures Using Visible Light-Absorbing Photocages. *The Journal of Organic Chemistry* **2021**, *86* (14), 9781-9787.
253. Velema, W. A.; van der Berg, J. P.; Szymanski, W.; Driessen, A. J. M.; Feringa, B. L., Orthogonal Control of Antibacterial Activity with Light. *ACS Chemical Biology* **2014**, *9* (9), 1969-1974.
254. Muthuramu, K.; Murthy, V. R., Photodimerization of coumarin in aqueous and micellar media. *The Journal of Organic Chemistry* **1982**, *47* (20), 3976-3979.
255. Syamala, M.; Ramamurthy, V., Consequences of hydrophobic association in photoreactions: photodimerization of stilbenes in water. *The Journal of Organic Chemistry* **1986**, *51* (19), 3712-3715.
256. Sharif, M.; Reimann, S.; Wittler, K.; Knöpke, L. R.; Surkus, A. E.; Roth, C.; Villinger, A.; Ludwig, R.; Langer, P., 1-(Arylalkenyl) pyrenes—Synthetic, Structural, Photophysical, Theoretical, and Electrochemical Investigations. Wiley Online Library: 2011.
257. Norberg, J.; Nilsson, L., Solvent influence on base stacking. *Biophysical Journal* **1998**, *74* (1), 394-402.
258. Ihara, T.; Fujii, T.; Mukae, M.; Kitamura, Y.; Jyo, A., Photochemical ligation of DNA conjugates through anthracene cyclodimer formation and its fidelity to the template sequences. *Journal of the American Chemical Society* **2004**, *126* (29), 8880-8881.
259. Ito, Y.; Kajita, T.; Kunimoto, K.; Matsuura, T., Accelerated photodimerization of stilbenes in methanol and water. *The Journal of Organic Chemistry* **1989**, *54* (3), 587-591.
260. Haynes, W. M., *CRC Handbook of Chemistry and Physics, 93rd Edition*. Taylor & Francis: 2012.
261. Arai, T.; Okamoto, H.; Sakuragi, H.; Tokumaru, K., Mechanism for photoisomerization of 1-styrylpyrene. Finding of a novel type of triplet energy surface with two decay funnels. *Chemical Physics Letters* **1989**, *157* (1-2), 46-50.
262. Kikuchi, Y.; Okamoto, H.; Aral, T.; Tokumaru, K., Effects of solvents and substituents controlling the adiabatic or diabatic modes of the cis→ trans isomerization of styrylpyrenes in the excited singlet state. *Chemical Physics Letters* **1994**, *229* (4-5), 564-570.
263. Fujimoto, K.; Yamada, A.; Yoshimura, Y.; Tsukaguchi, T.; Sakamoto, T., Details of the ultrafast DNA photo-cross-linking reaction of 3-cyanovinylcarbazole nucleoside: cis–trans isomeric effect and the application for SNP-based genotyping. *Journal of the American Chemical Society* **2013**, *135* (43), 16161-16167.
264. Sheik-Bahae, M.; Said, A. A.; Wei, T.-H.; Wu, Y.-Y.; Hagan, D. J.; Soileau, M.; Van Stryland, E. W. In *Z-scan: a simple and sensitive technique for nonlinear refraction measurements*, Nonlinear Optical Properties Of Materials, International Society for Optics and Photonics: 1990; pp 41-51.
265. Williams, A. T. R.; Winfield, S. A.; Miller, J. N., Relative fluorescence quantum yields using a computer-controlled luminescence spectrometer. *Analyst* **1983**, *108* (1290), 1067-1071.
266. French, A. P.; Taylor, E. F., *An Introduction to Quantum Physics*. Taylor & Francis: 1979.

10 APPENDIX

10.1 NMR-Spectra

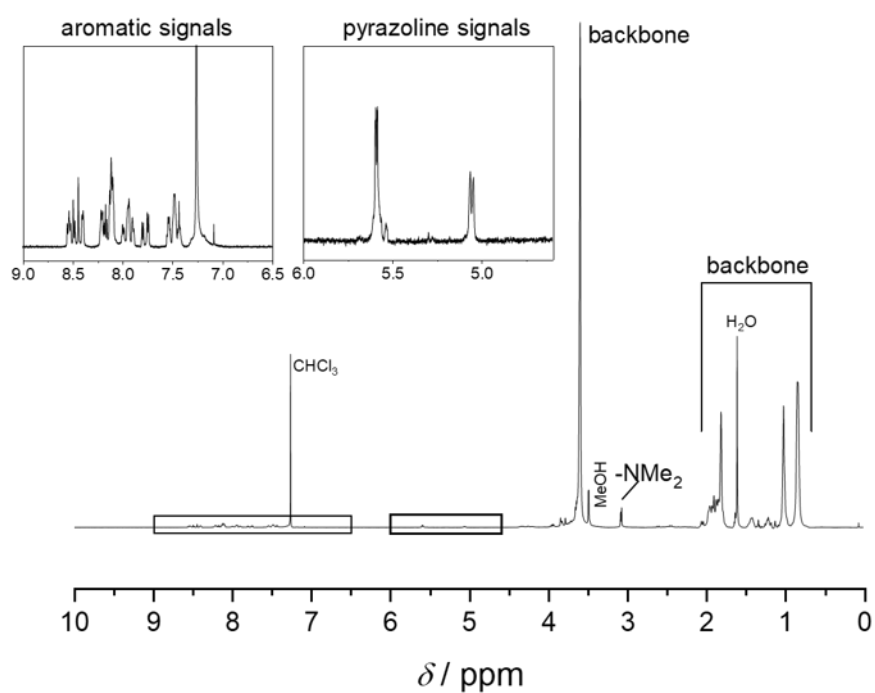


Figure S 7: $^1\text{H-NMR}$ spectrum in CDCl_3 of the isolated polymeric fraction after polymer end-group ligation of APAT and maleimide end-capped PMMA at 452 nm for 2.5 h.

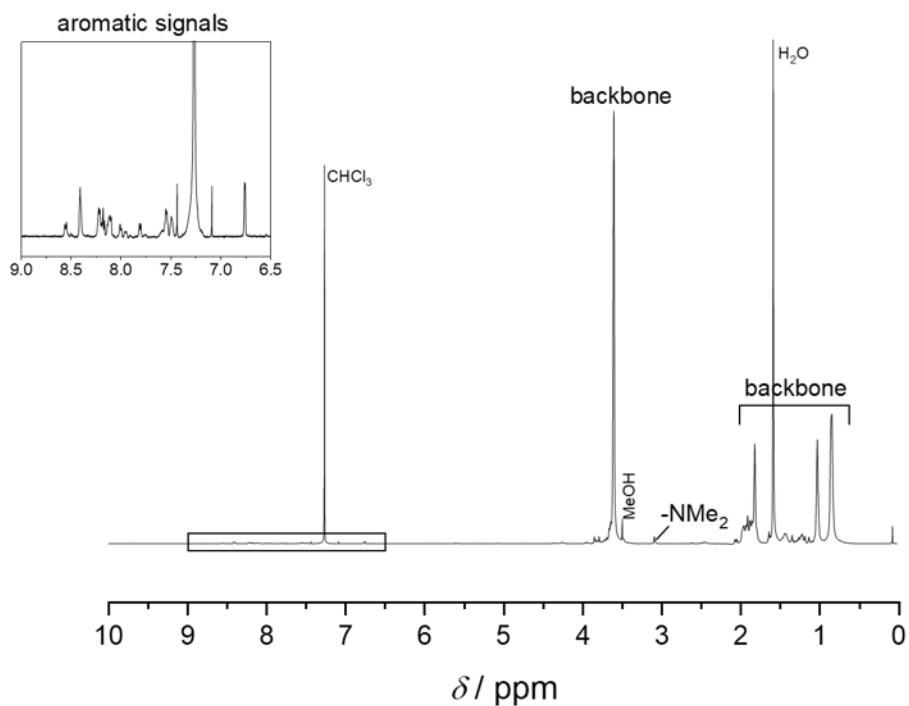


Figure S 8: $^1\text{H-NMR}$ spectrum in CDCl_3 of the isolated polymeric fraction after polymer end-group ligation of APAT and maleimide end-capped PMMA at 500 nm for 3.7 h.

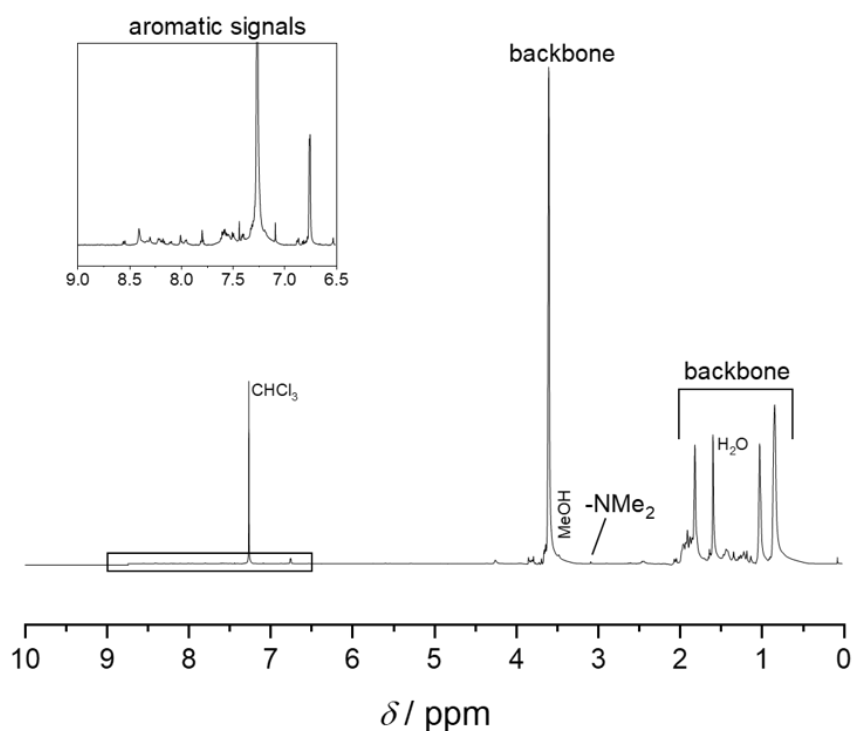


Figure S 9: $^1\text{H-NMR}$ spectrum in CDCl_3 of the isolated polymeric fraction after polymer end-group ligation of APAT and maleimide end-capped PMMA at 515 nm for 4.7 h.

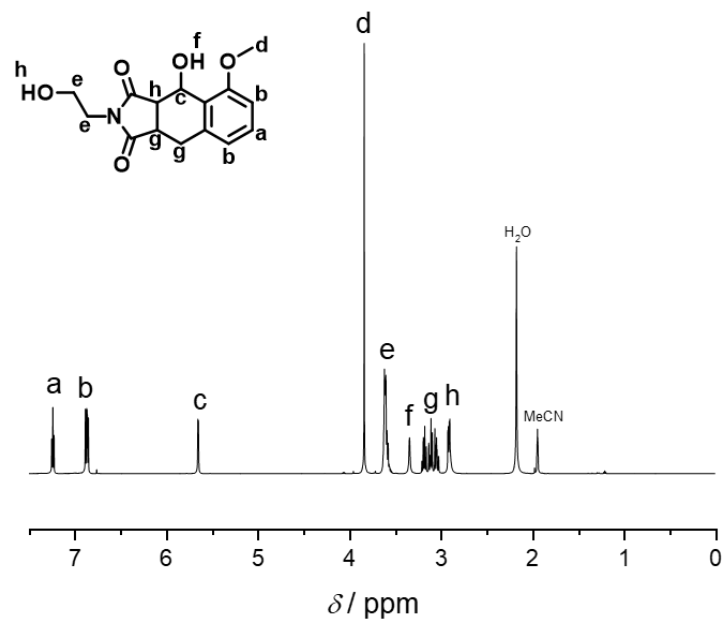


Figure S 10: ¹H-NMR spectrum of CA₀MBA in MeCN-d₃.

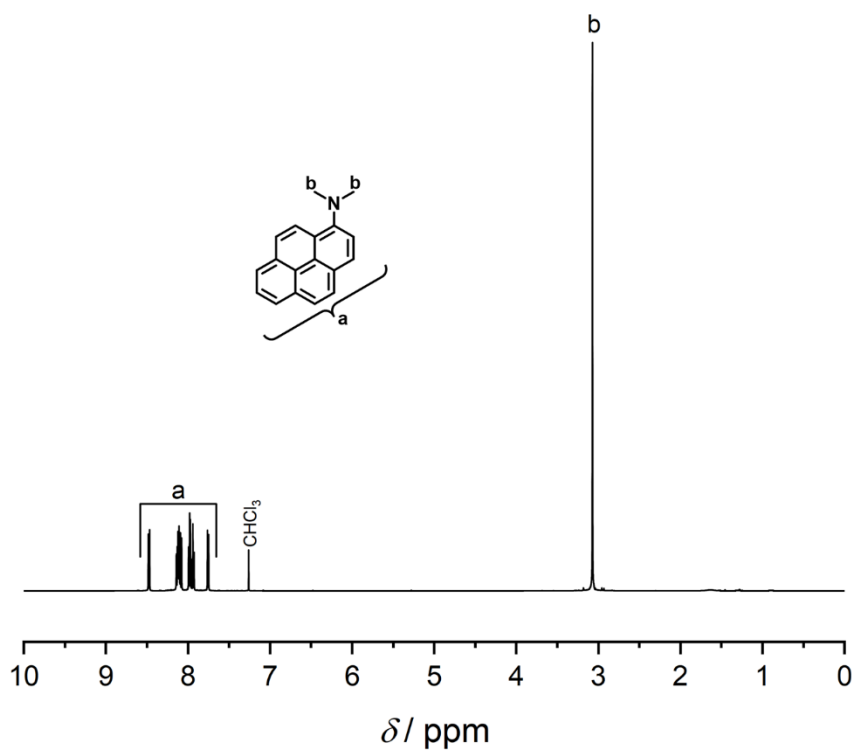


Figure S 11: ¹H-NMR spectrum of N,N-dimethyl pyrene-1-amine in CDCl₃.

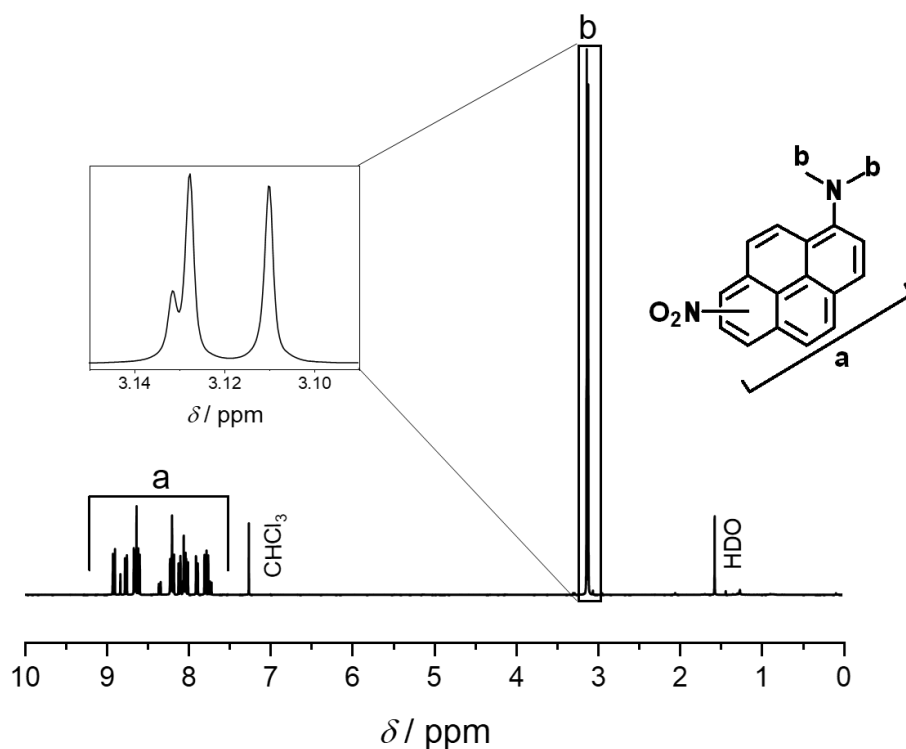


Figure S 12: $^1\text{H-NMR}$ spectrum of *N,N*-dimethyl nitropyrene-1-amine. Relative amounts of the three isomers can be estimated by integrating the $-\text{NMe}_2$ signals at $\delta = 3.10\text{-}3.14$. *N,N*-dimethyl-3-nitropyrene-1-amine is the only isomer displaying a singlet, stemming from the H-atom in the C^2 -position of the pyrene.

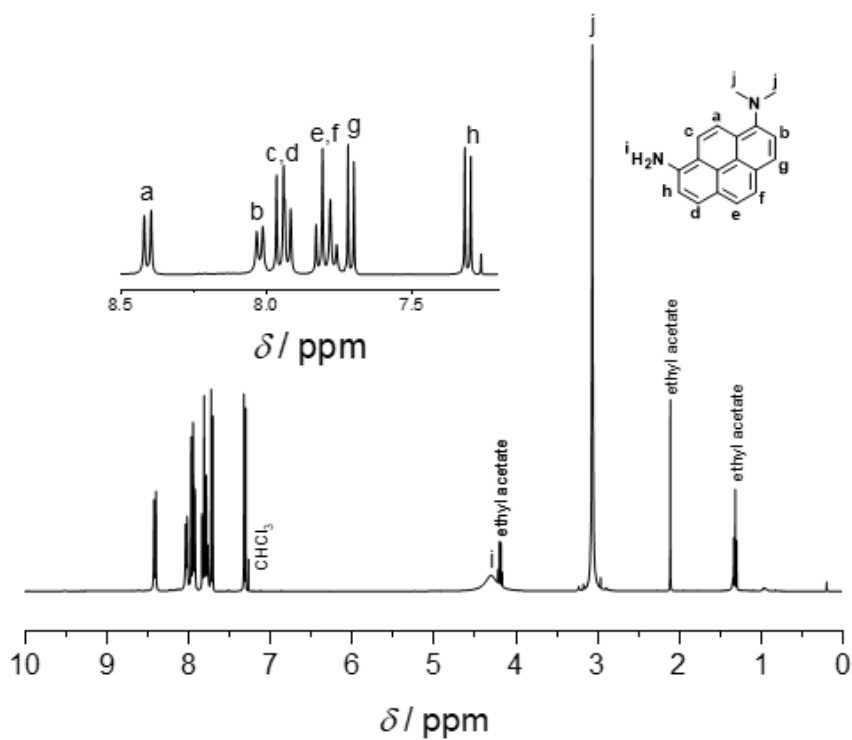


Figure S 13: $^1\text{H-NMR}$ spectrum of *N,N*-dimethyl pyrene-1,8-diamine in CDCl_3 .

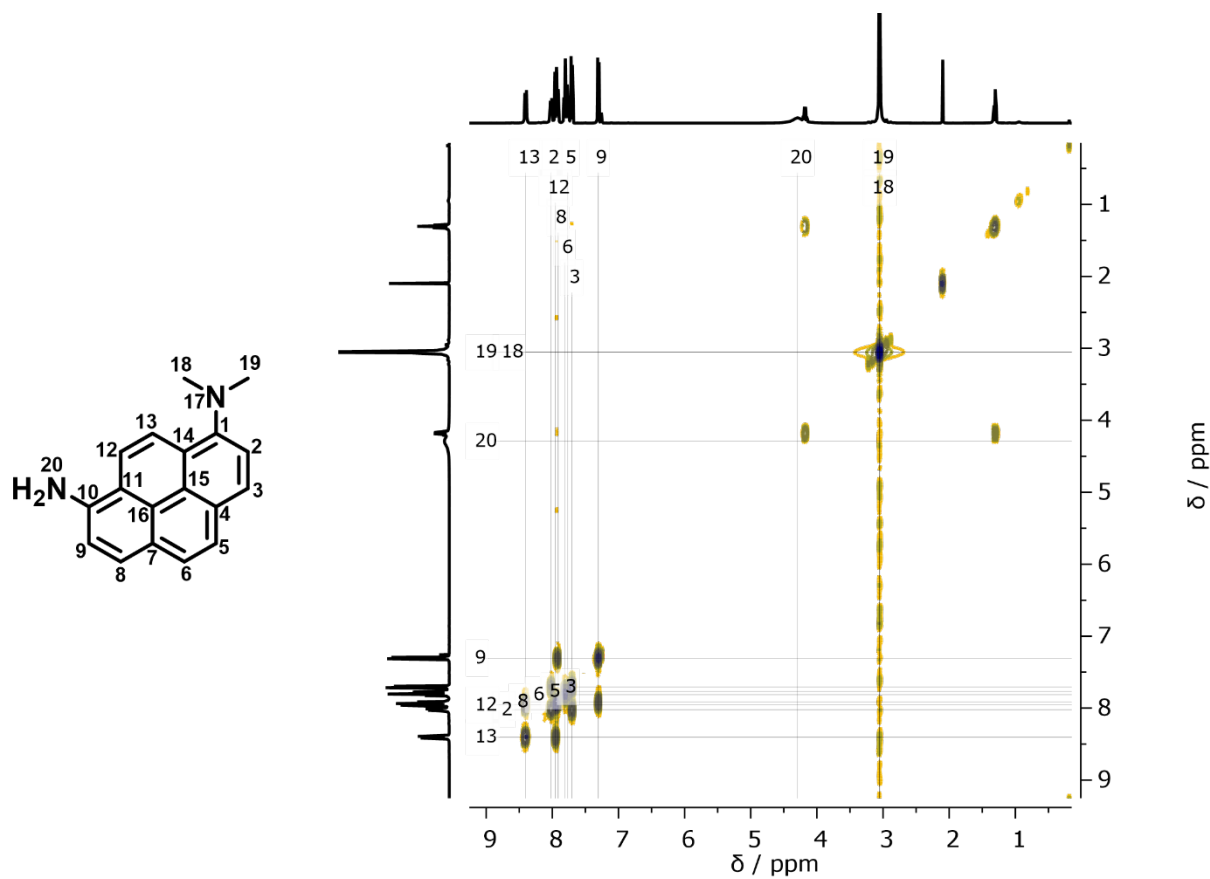


Figure S 14: COSY measurement of *N,N*-dimethyl pyrene-1,8-diamine in CDCl₃.

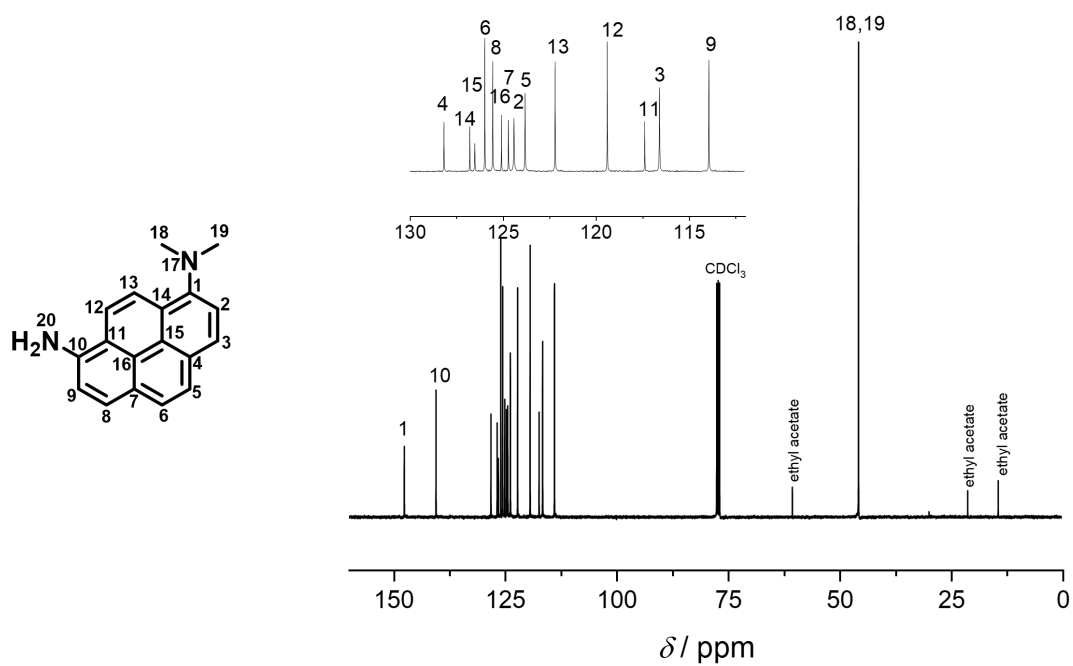


Figure S 15: ¹³C-NMR spectrum of *N,N*-dimethyl pyrene-1,8-diamine in CDCl₃.

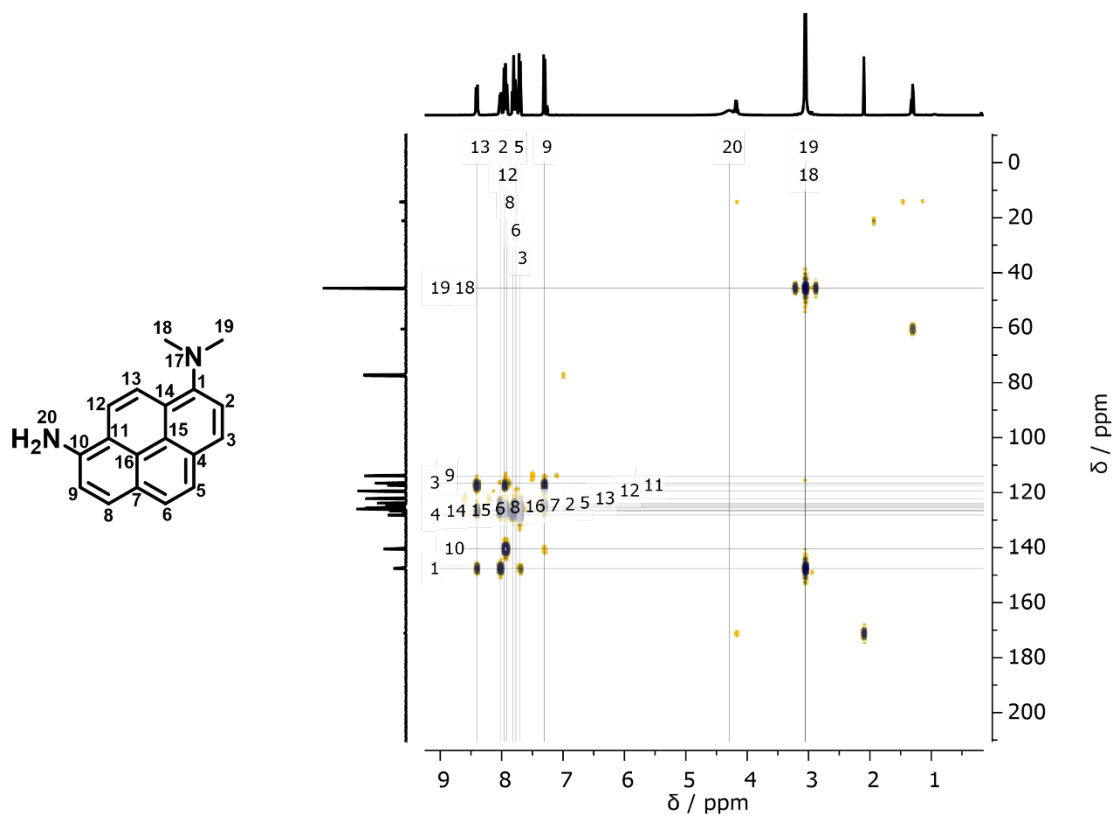


Figure S 16: HMBC measurement of *N,N*-dimethyl pyrene-1,8-diamine in CDCl_3 .

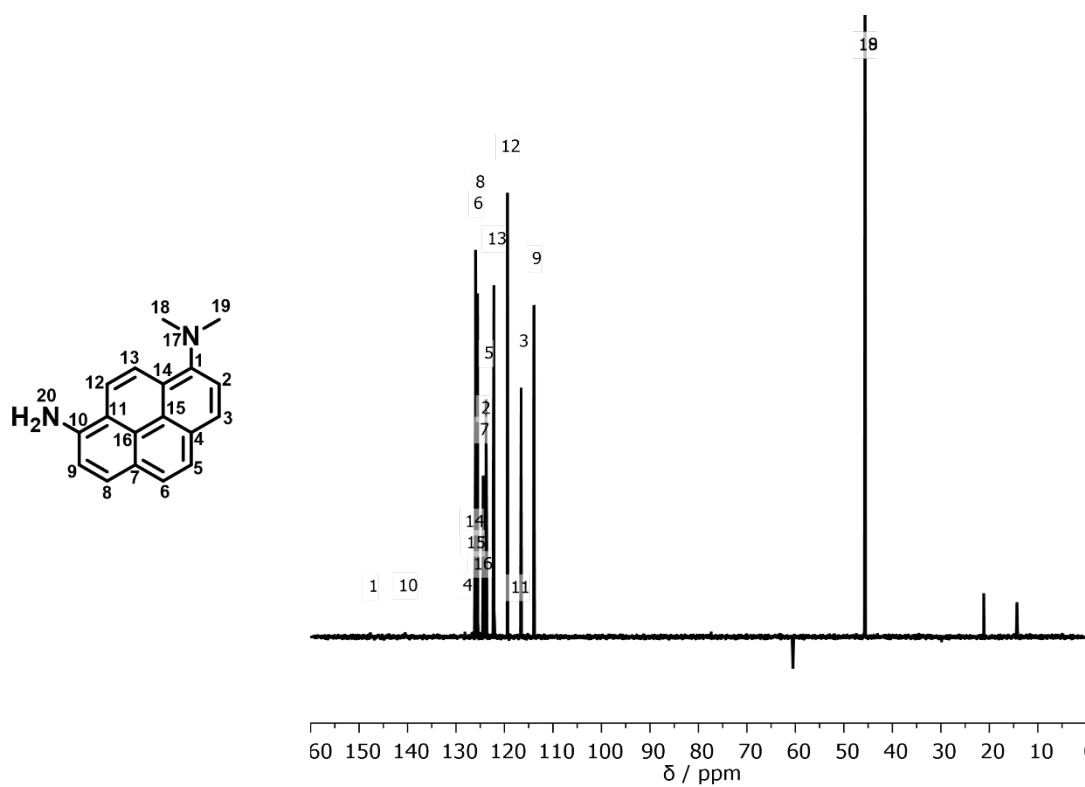


Figure S 17: DEPTQ-135 measurement of *N,N*-dimethyl pyrene-1,8-diamine in CDCl_3 .

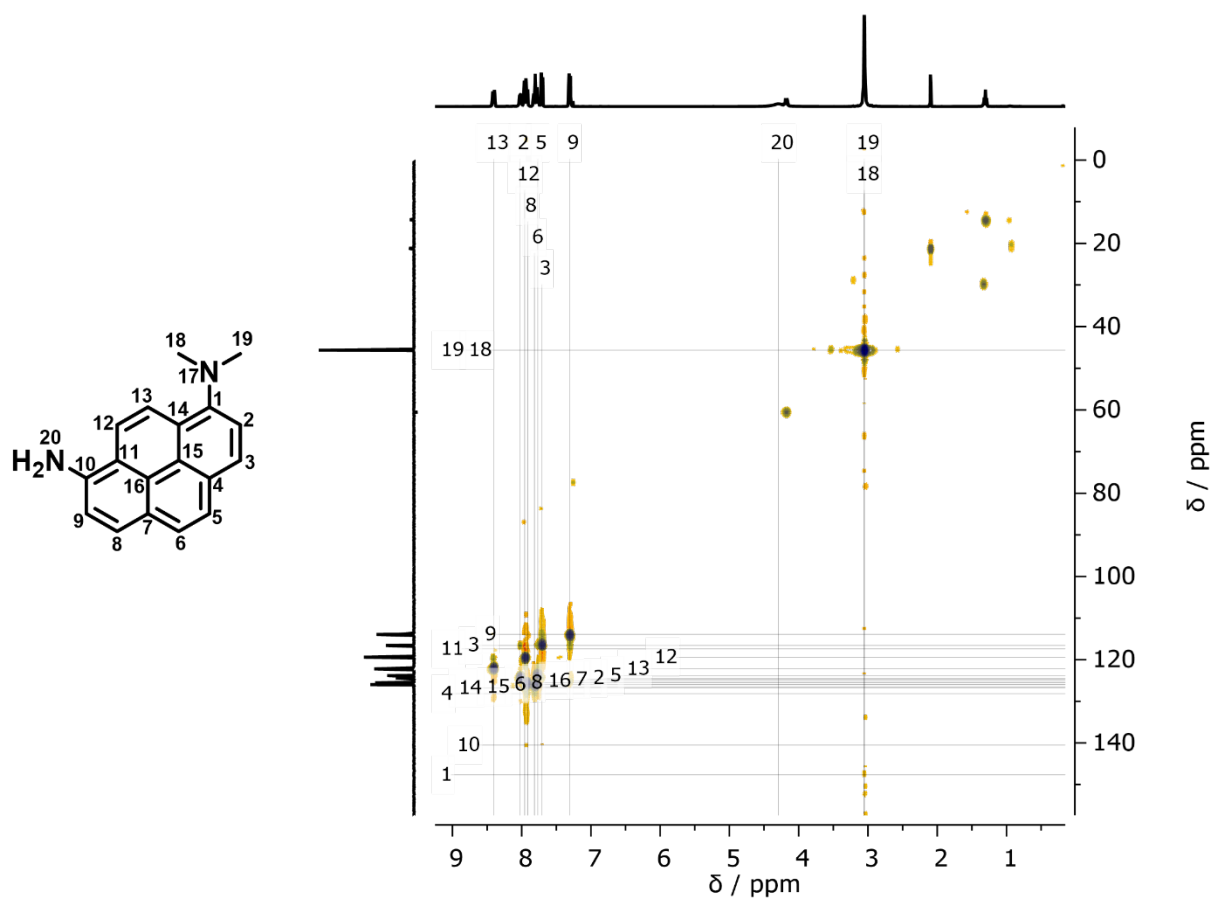


Figure S 18: HSQC measurement of *N,N*-dimethyl pyrene-1,8-diamine in CDCl₃.

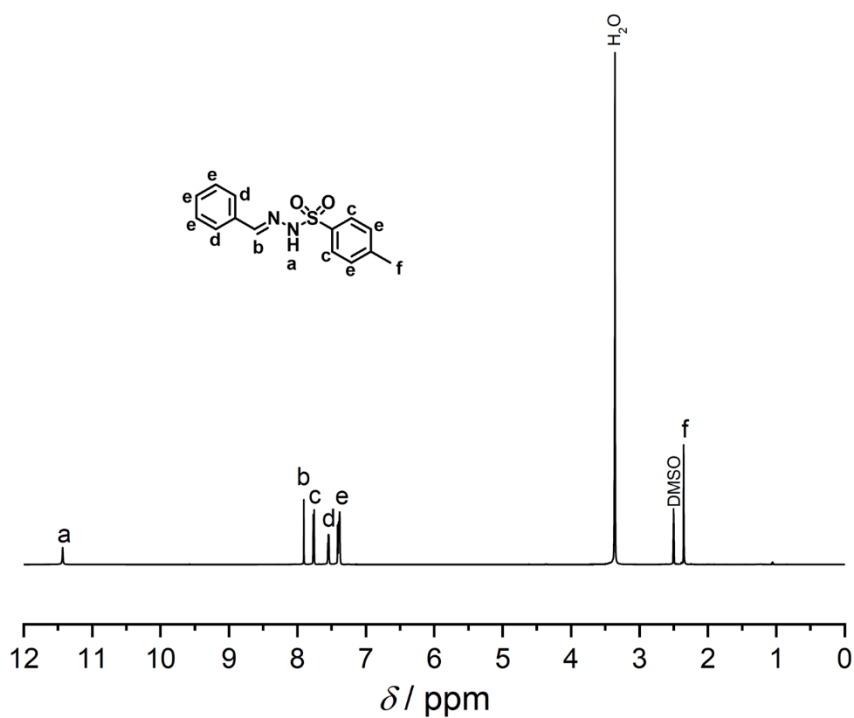


Figure S 19: ¹H-NMR spectrum of (*E*)-*N'*-benzylidene-4-methylbenzenesulfonylhydrazide in DMSO-d₆

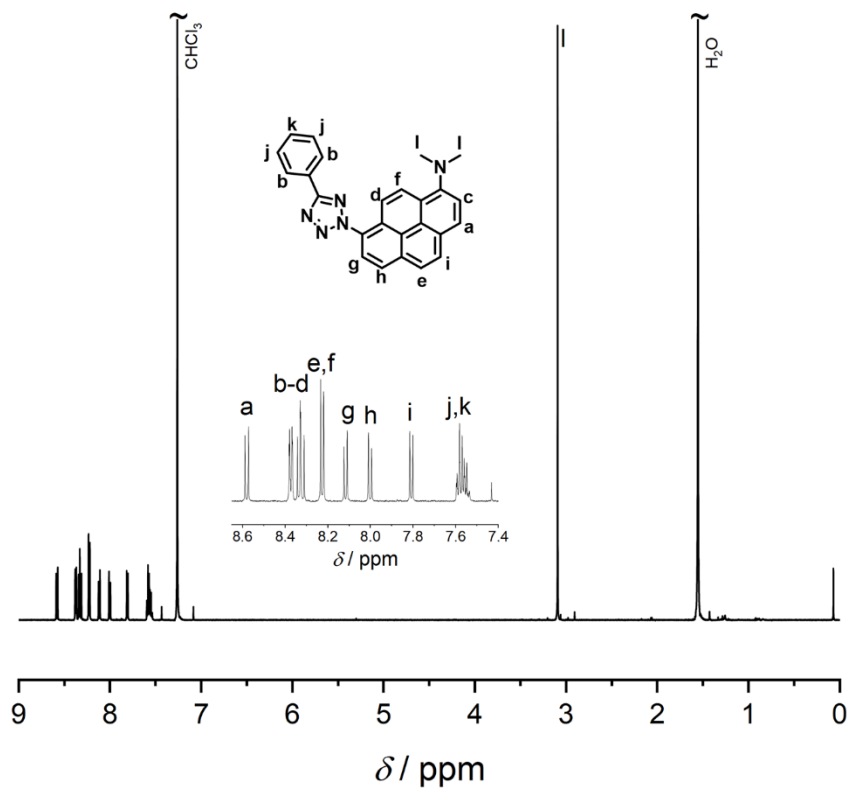


Figure S 20: $^1\text{H-NMR}$ spectrum of APAT in CDCl_3 .

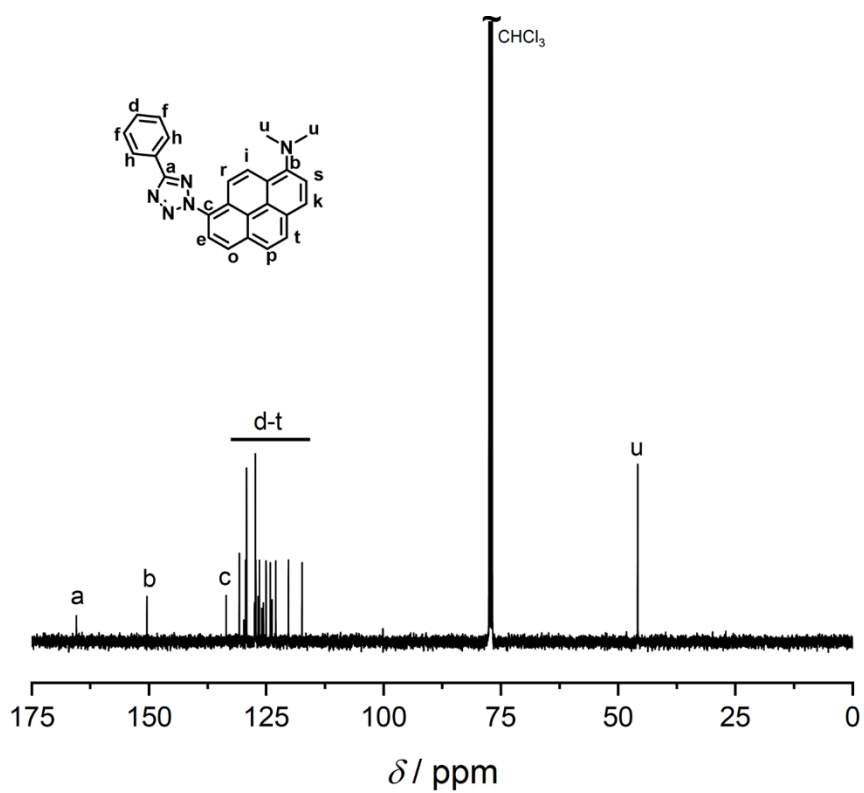


Figure S 21: $^{13}\text{C-NMR}$ spectrum of APAT in CDCl_3 .

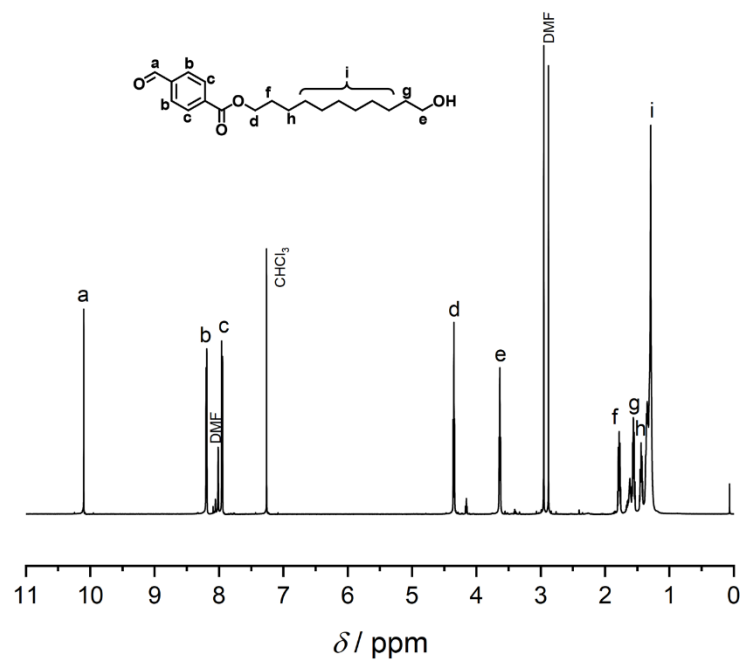


Figure S 22: $^1\text{H-NMR}$ spectrum of 11-hydroxyundecyl-4-formylbenzoate in CDCl_3 .

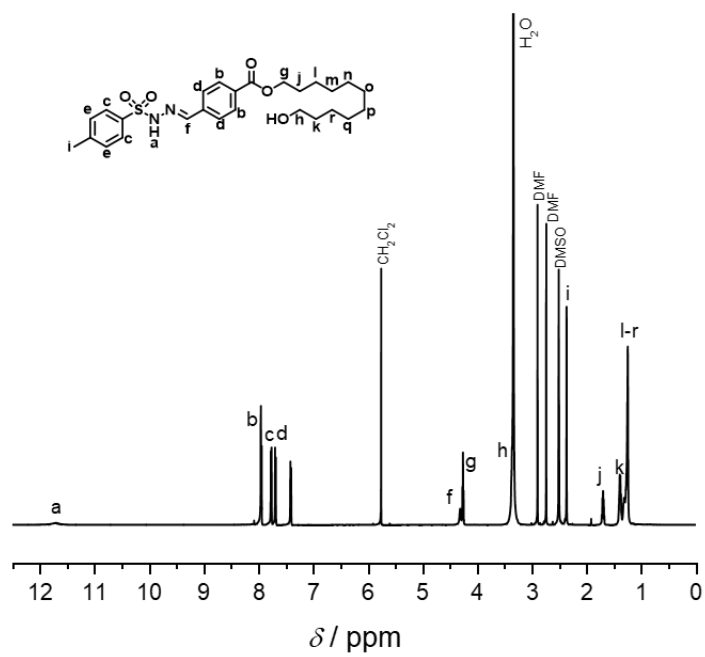


Figure S 23: $^1\text{H-NMR}$ spectrum of 11-hydroxyundecyl (*E*)-4-((2-tosylhydrazineylidene)methyl)benzoate in $\text{DMSO-}d_6$

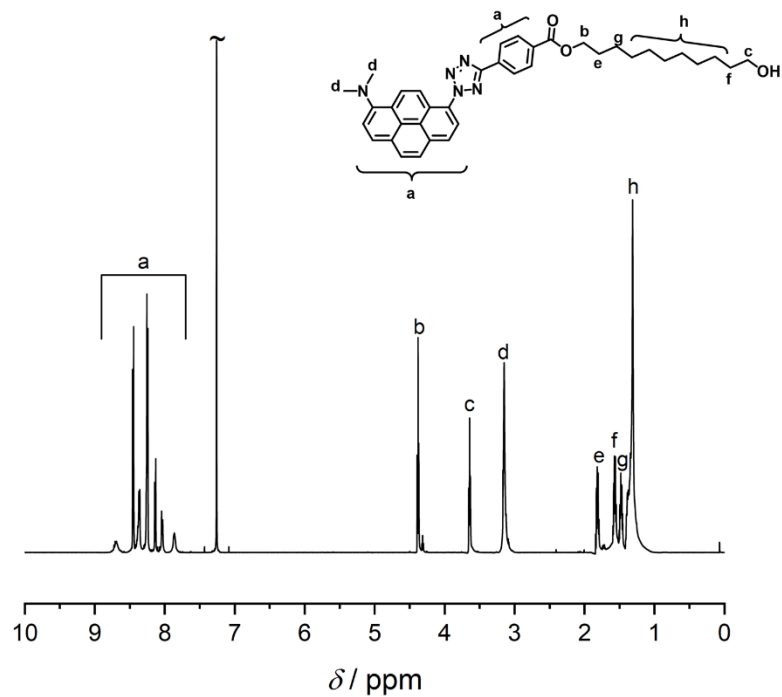


Figure S 24: ¹H-NMR spectrum of 11-hydroxyundecyl 4-(2-(8-(dimethylamino)pyren-1-yl)-2H-tetrazol-5-yl)benzoate in CDCl₃.

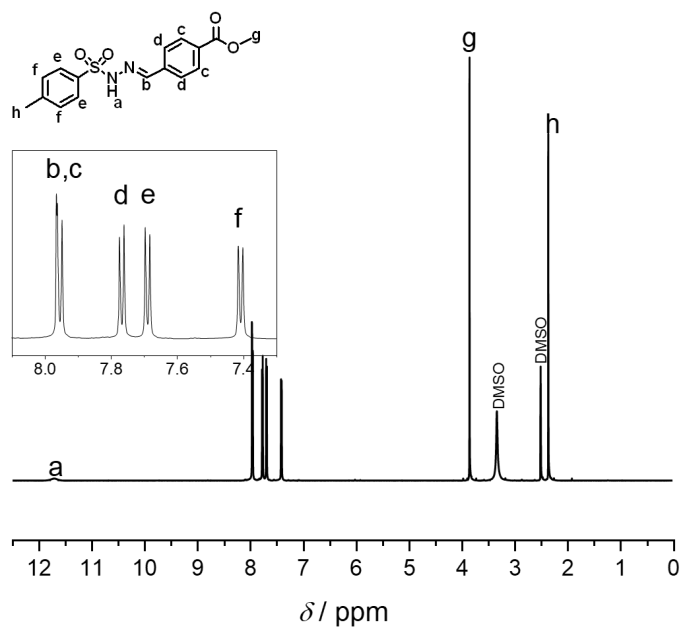


Figure S 25: ¹H-NMR spectrum of methyl (E)-4-((2-tosylhydrazineylidene)methyl)benzoate in DMSO-*d*₆.

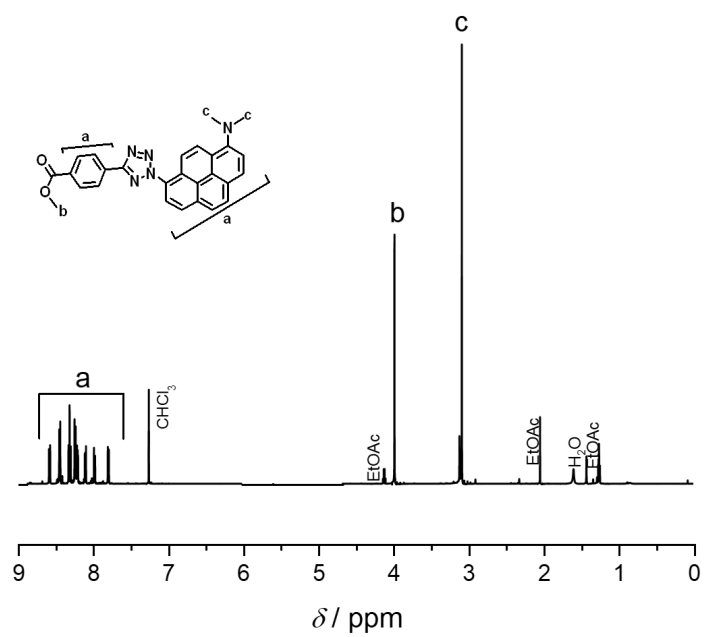


Figure S 26: $^1\text{H-NMR}$ spectrum of methyl 4-(2-(8-(dimethylamino)pyren-1-yl)-2H-tetrazol-5-yl)benzoate in CDCl_3 .

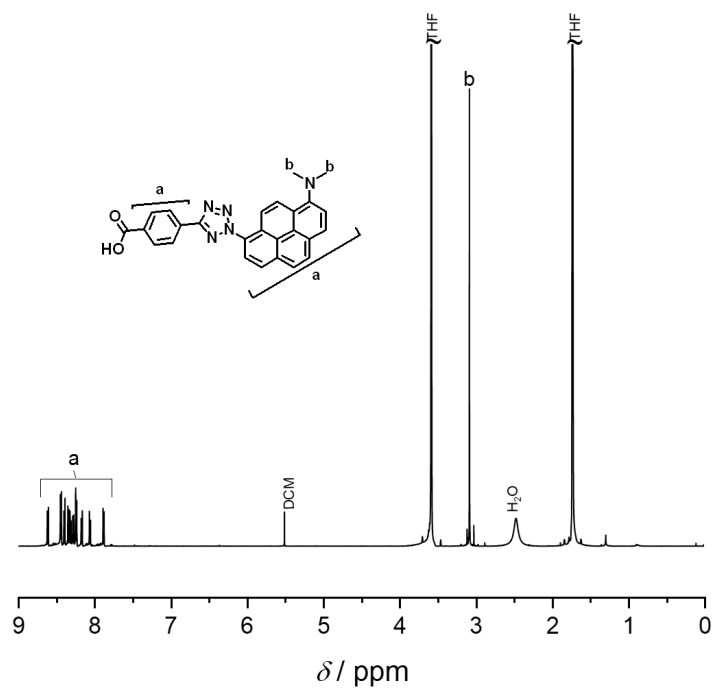


Figure S 27: $^1\text{H-NMR}$ spectrum of 4-(2-(8-(dimethylamino)pyren-1-yl)-2H-tetrazol-5-yl)benzoic acid in $\text{THF-}d_8$.

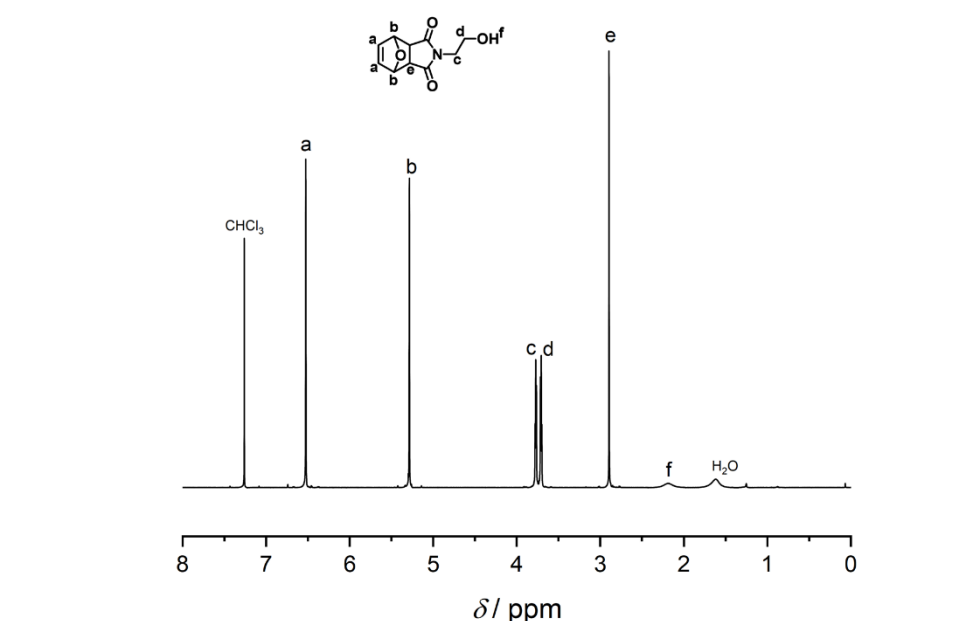


Figure S 28: ¹H-NMR spectrum of 2-(2-hydroxyethyl)-3a,4,7,7a-tetrahydro-1H-4,7-methanoisindole-1,3(2H)-dione (furan-protected *N*-(2-hydroxy)ethyl maleimide) in CDCl₃.

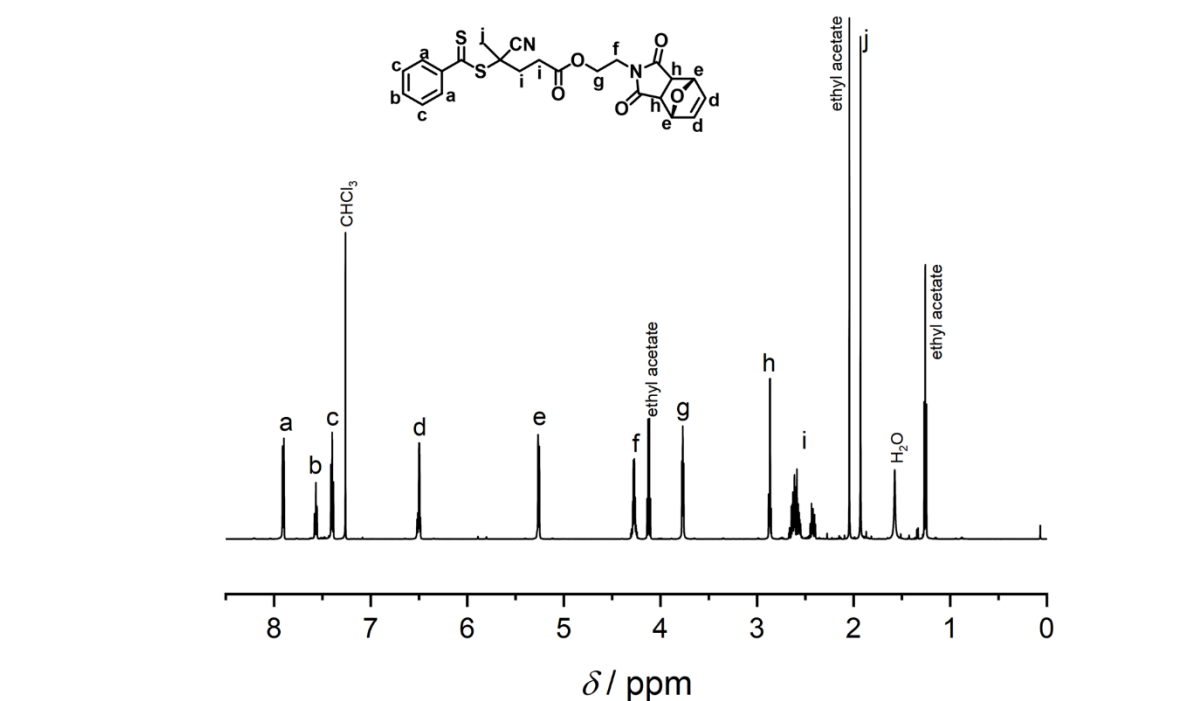


Figure S 29: ¹H-NMR spectrum of 2-((4*R*,7*S*)-1,3-dioxo-1,3,3*a*,4,7,7*a*-hexahydro-2*H*-4,7-epoxyisindol-2-yl)ethyl-4-cyano-4-((phenylcarbonothioyl)thio)pentanoate (chain-transfer agent, CTA) in CDCl₃.

10.2 Steady State Spectroscopy

10.2.1 Absorption Spectra

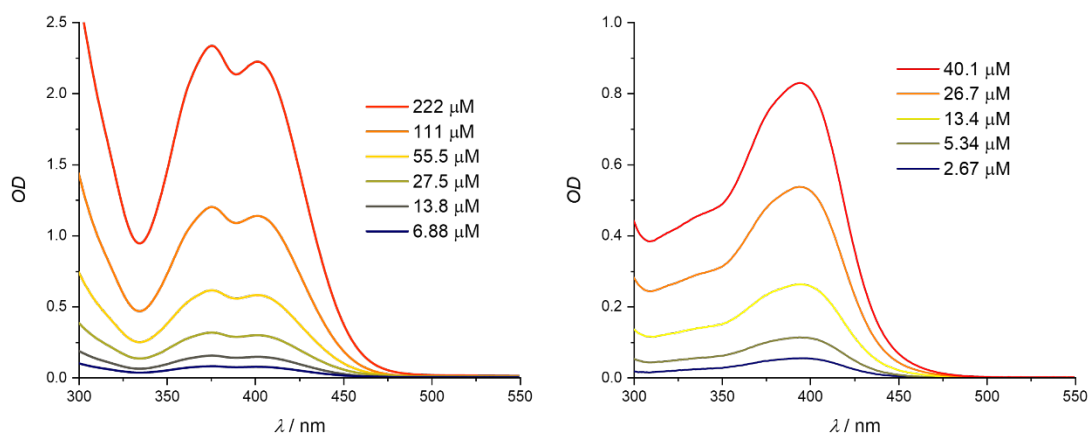


Figure S 32: Concentration series of the absorption spectra of APAT (left) and CA_{DEF} (right) in MeCN. All spectra were measured in 1 cm quartz cuvettes at ambient temperature.

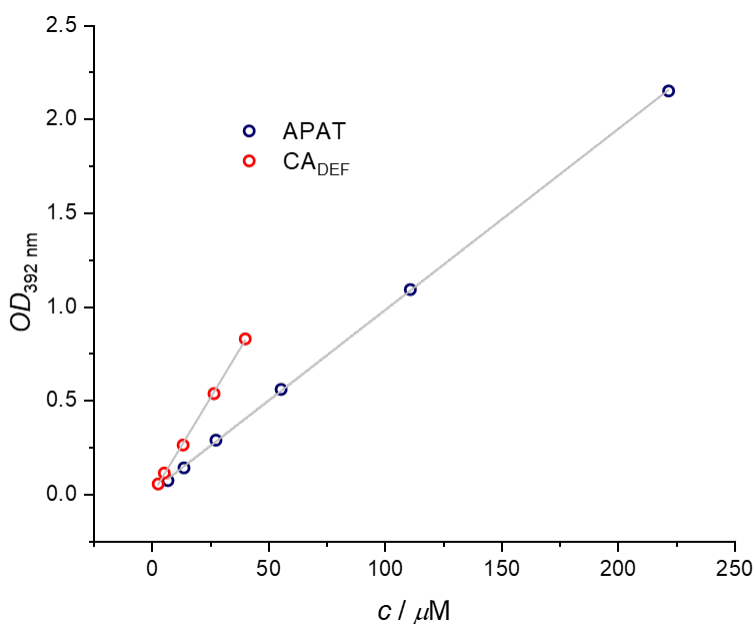


Figure S 33: Linear fits of the absorbance (OD) at 392 nm (scan wavelength of the LC-MS UV detector) after recording UV/Vis spectra of APAT (concentrations 6.94 μM, 13.9 μM, 27.8 μM, 55.6 μM, 111 μM and 222 μM) and CA_{DEF} (2.67 μM, 5.34 μM, 13.4 μM, 26.7 μM, 40.1 μM) in MeCN. The linear regression lines gave the absorption coefficients $\epsilon_{392 \text{ nm}}^{\text{APAT}} = 9600 \text{ L mol}^{-1} \text{ cm}^{-1}$ and $\epsilon_{392 \text{ nm}}^{\text{CA}_{\text{DEF}}} = 20500 \text{ L mol}^{-1} \text{ cm}^{-1}$.

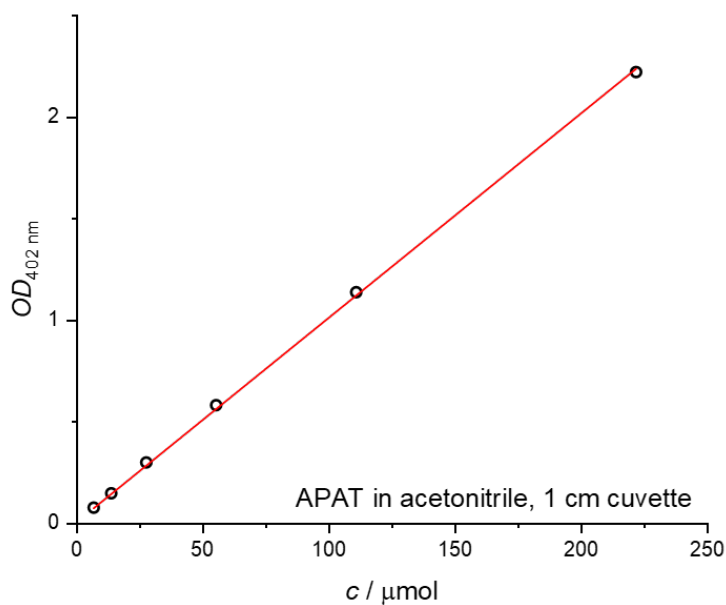


Figure S 34: Linear fit of the absorbance (OD) at 402 nm after recording UV/Vis spectra of APAT in MeCN at concentrations $6.94 \mu\text{M}$, $13.9 \mu\text{M}$, $27.8 \mu\text{M}$, $55.6 \mu\text{M}$, $111 \mu\text{M}$ and $222 \mu\text{M}$. Slope of the linear regression line gave the absorption coefficient $\epsilon_{402 \text{ nm}} = 10080 \text{ L mol}^{-1} \text{ cm}^{-1}$.

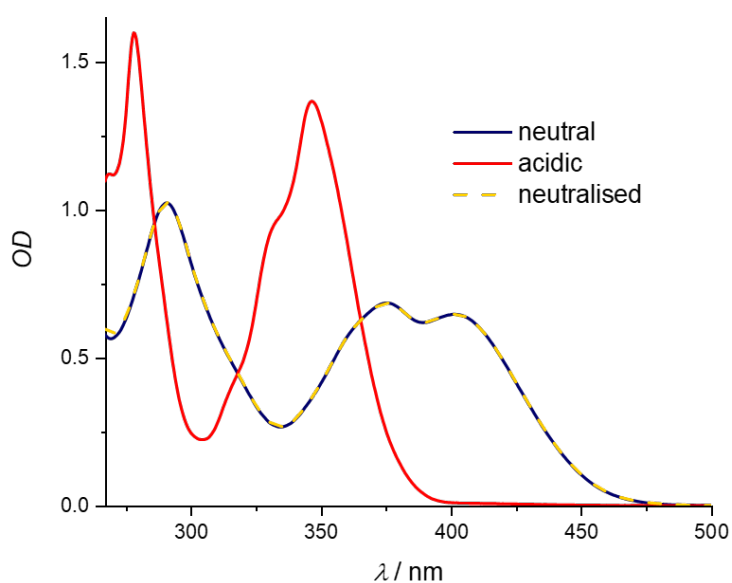


Figure S 35: Switching APAT absorption through pH changes. Adding tosylsulfonic acid induces a hypsochromic shift into the UV region. Adding an equal amount of triethylamine restores the original absorption spectrum. Spectra were recorded at $c = 0.32 \text{ mM}$ in a 2 mm cuvette, at ambient temperature.

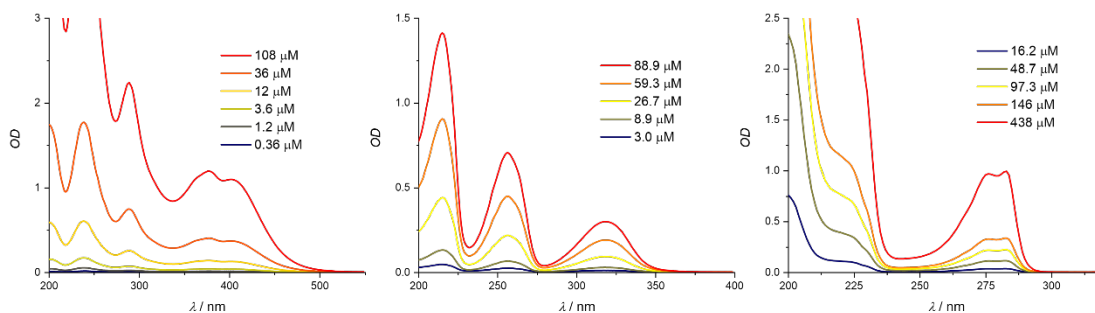


Figure S 36: Concentration series of the absorption spectra of CA_{APAT} (left), $oMBA$ (centre) and CA_{oMBA} (right). CA_{APAT} and $oMBA$ were measured in MeCN. CA_{oMBA} was measured in MeCN/ H_2O (92:8), as per the LC-MS gradient. All spectra were measured in 1 cm quartz cuvettes at ambient temperature.

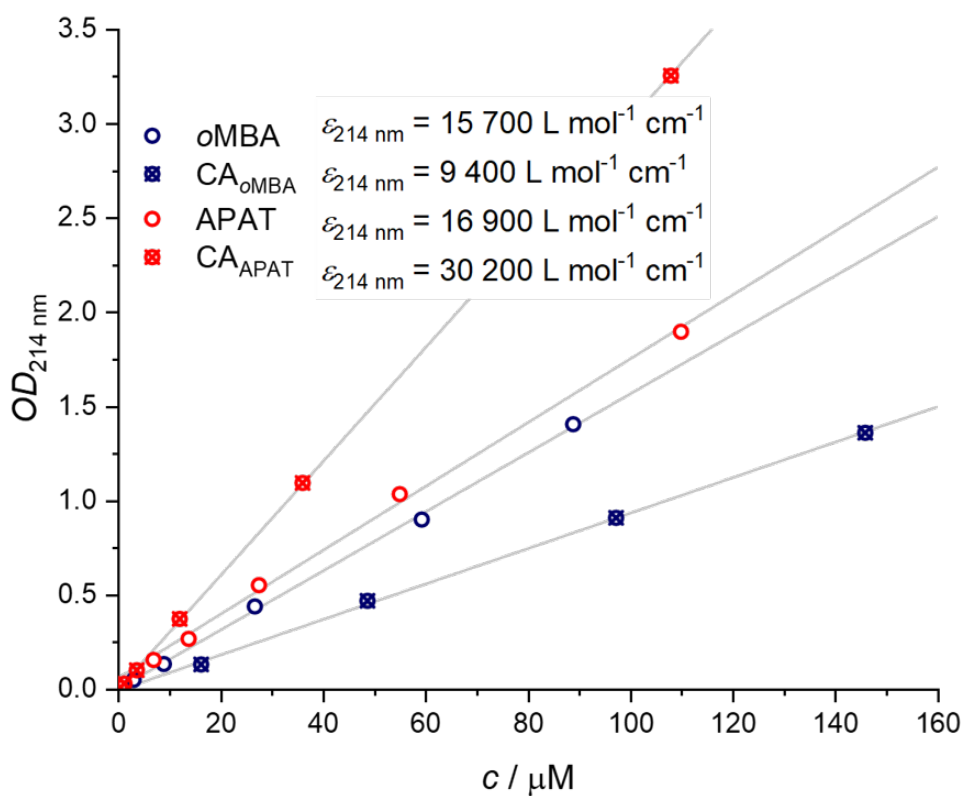


Figure S 37: Linear fits of the absorbance (OD) at 214 nm (scan wavelength of the LC-MS UV detector) after recording UV/Vis spectra of $oMBA$ (concentrations 3.0 μ M, 8.9 μ M, 26.7 μ M, 59.3 μ M and 88.9 μ M), CA_{oMBA} (concentrations 16.2 μ M, 48.7 μ M, 97.3 μ M and 146 μ M) APAT (concentrations 6.94 μ M, 13.9 μ M, 27.8 μ M, 55.6 μ M, and 111 μ M), and CA_{APAT} (0.37 μ M, 1.2 μ M, 3.6 μ M, 12.0 μ M, 36 μ M and 108 μ M) in MeCN.

10.2.2 Fluorescence Spectra

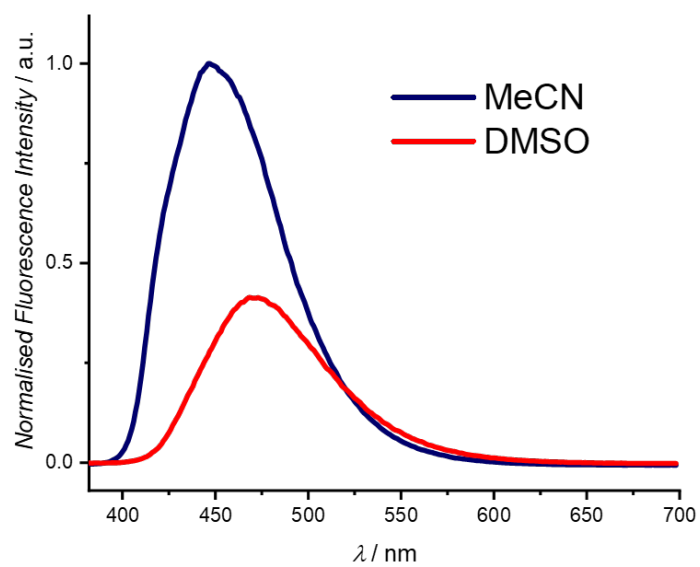


Figure S 38: Fluorescence spectra of styrylpyrene in MeCN and DMSO after 370 nm excitation.

10.3 Results of APAT and Diethylfumarate Photoreaction

10.3.1 LC-MS Results of the Action Plot Experiments

Table S 6: Results of the laser experiments. Reaction conversion was determined via LC-MS. Error bars were obtained through 3x repetition of every experiment. Due to very long irradiation time the experiments between 320 nm and 400 nm were repeated 2x.

Wavelength / nm	CA _{DEF} Yield / %	Average CA _{DEF} Yield / %	Error / %
320	11.1		
320	14.0	12.5	1.4
340	3.3		
340	5.5	4.4	1.1
360	2.3		
360	1.7	2.0	0.3
380	2.3		
380	3.3	2.8	0.5
400	6.1		
400	2.4	4.2	1.8
410	10.1		
410	11.9	10.9	0.9
410	10.8		
420	12.0		
420	13.3	13.1	0.9
420	14.1		
430	13.8		
430	14.0	13.8	0.2
430	13.7		
440	12.9		
440	14.6	14.4	1.2
440	15.8		
450	13.2		
450	14.9	14.2	0.7
450	14.4		
455	12.9		
455	10.7	11.8	1.1
460	11.6		
460	9.7	10.3	0.9

460	9.7		
465	8.0	8.2	0.2
465	8.4		
470	8.5		
470	8.4	7.9	0.7
470	7.0		
475	3.3		
475	3.2	3.1	0.2
475	2.9		
480	2.8		
480	2.7	2.7	0.0
480	2.7		
490	1.6		
490	1.5	1.6	0.1
490	1.6		
500	0.6		
500	0.6	0.6	0.0
500	0.6		
510	0.3		
510	0.2	0.2	0.0
510	0.2		
515	0.0		
515	0.0	0.0	0.0
515	0.0		
525	0.0		
525	0.0	0.0	0.0
525	0.0		

10.3.2 Prolonged Irradiation Time Experiments

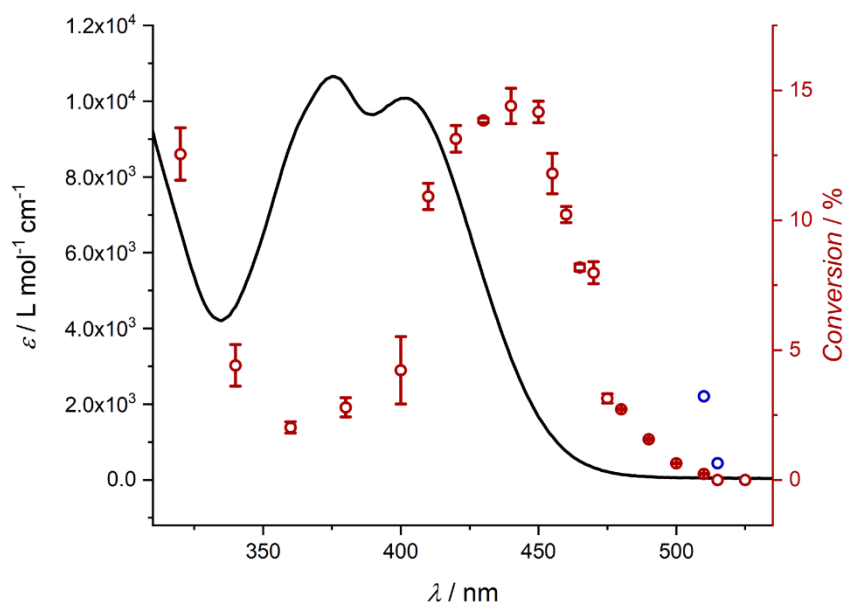


Figure S 39: Action plot of NITEC between APAT and DEF, including two additional data points after 25-fold increase of incident photons at wavelengths 510 nm and 515 nm, yielding 3 % and 0.6 % of CA_{DEF} , respectively.

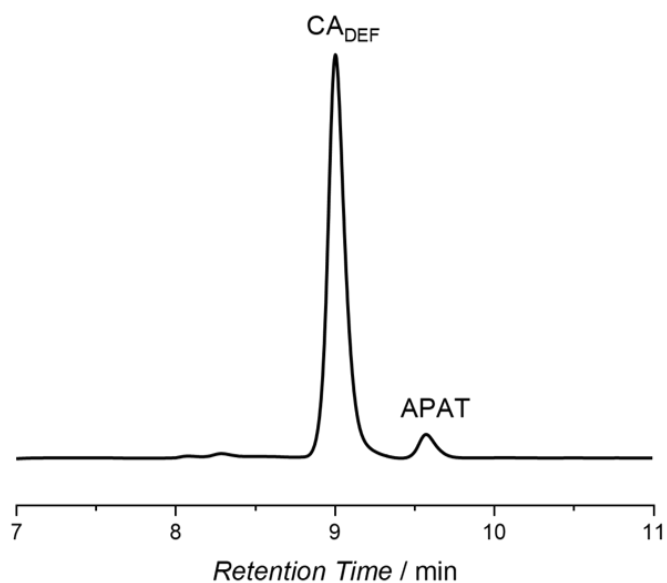


Figure S 40: LC-MS chromatogram after 465 nm irradiation of APAT and diethylfumarate for 180 min. After determining the peak integral ratio and taking into account the molar absorptivity at the scan wavelength for both species, the conversion is calculated to be 89 %.

10.4 λ -Orthogonal Photoreactions of APAT and *o*MBA with

NHEM

10.4.1 Results of Kinetic Measurements

Table S 7: Results of the laser experiments. Reaction conversion was determined via LC-MS. Error bars were obtained through 3x repetition of every experiment.

Wavelength / nm	Irradiation Time / min	Average Yield CA _{APAT} / %	Standard Error CA _{APAT} / %	Average Yield CA _{<i>o</i>MBA} / %	Standard Error CA _{<i>o</i>MBA} / %	Average degree of rearomati- zation / %
320	0.1	0.0	0.0	23.0	0.4	-
320	0.2	0.0	0.0	38.0	0.7	-
320	0.4	0.0	0.0	66.4	0.9	-
320	0.8	0.0	0.0	89.0	1.5	-
360	1	0.4	0.0	9.0	0.4	0
360	2	0.6	0.3	16.4	2.9	0
360	4	0.7	0.4	32.2	3.8	0
360	8	2.3	0.4	59.7	0.8	59
360	19	4.3	0.2	91.2	0.3	97
390	3.6	0.7	0.0	1.0	0.2	100
390	7.2	1.4	0.0	2.1	0.2	100
390	14.3	2.8	0.5	4.5	0.6	100
390	28.6	4.5	0.1	9.1	0.1	100
390	120	21.1	2.8	45.4	1.1	100
450	5	5.7	0.1	0.0	0.0	85
450	10	10.8	0.4	0.0	0.0	97
450	15	14.7	0.5	0.0	0.0	100
450	30	32.0	0.8	0.0	0.0	77
450	156	86.2	3.4	0.0	0.0	100

Table S 8: Quantum yield simulation parameters.

Excitation wavelength / nm	320	360	390	450
$E_{\text{pulse}} / \mu\text{J}$	500	500	364	2000
L / cm		1.0		
$c_{\text{OMBA}}(t_0) / \text{mol L}^{-1}$		$0.23 \cdot 10^{-3}$		
$c_{\text{APAT}}(t_0) / \text{mol L}^{-1}$		$0.23 \cdot 10^{-3}$		
$c_{\text{NHEM}}(t_0) / \text{mol L}^{-1}$		$1.82 \cdot 10^{-3}$		
$\epsilon_{\text{OMBA}} / \text{L mol}^{-1} \text{cm}^{-1}$	3300	100	3	0
$\epsilon_{\text{APAT}} / \text{L mol}^{-1} \text{cm}^{-1}$	6800	9200	10000	1700
$\epsilon_{\text{NHEM}} / \text{L mol}^{-1} \text{cm}^{-1}$	420	40	0.6	0
$\epsilon_{\text{CA-OMBA}} / \text{L mol}^{-1} \text{cm}^{-1}$	0	0	0	0
$\epsilon_{\text{CA-APAT}} / \text{L mol}^{-1} \text{cm}^{-1}$	9400	1000	10100	3200
$\Phi^{\text{OMBA}} / \%$	18 ± 2	10 ± 2	20 ± 8	-
$\Phi^{\text{APAT}} / \%$	-	$(2.5 \pm 0.5) \cdot 10^{-3}$	$(2.5 \pm 0.5) \cdot 10^{-3}$	$(1.5 \pm 0.5) \cdot 10^{-2}$

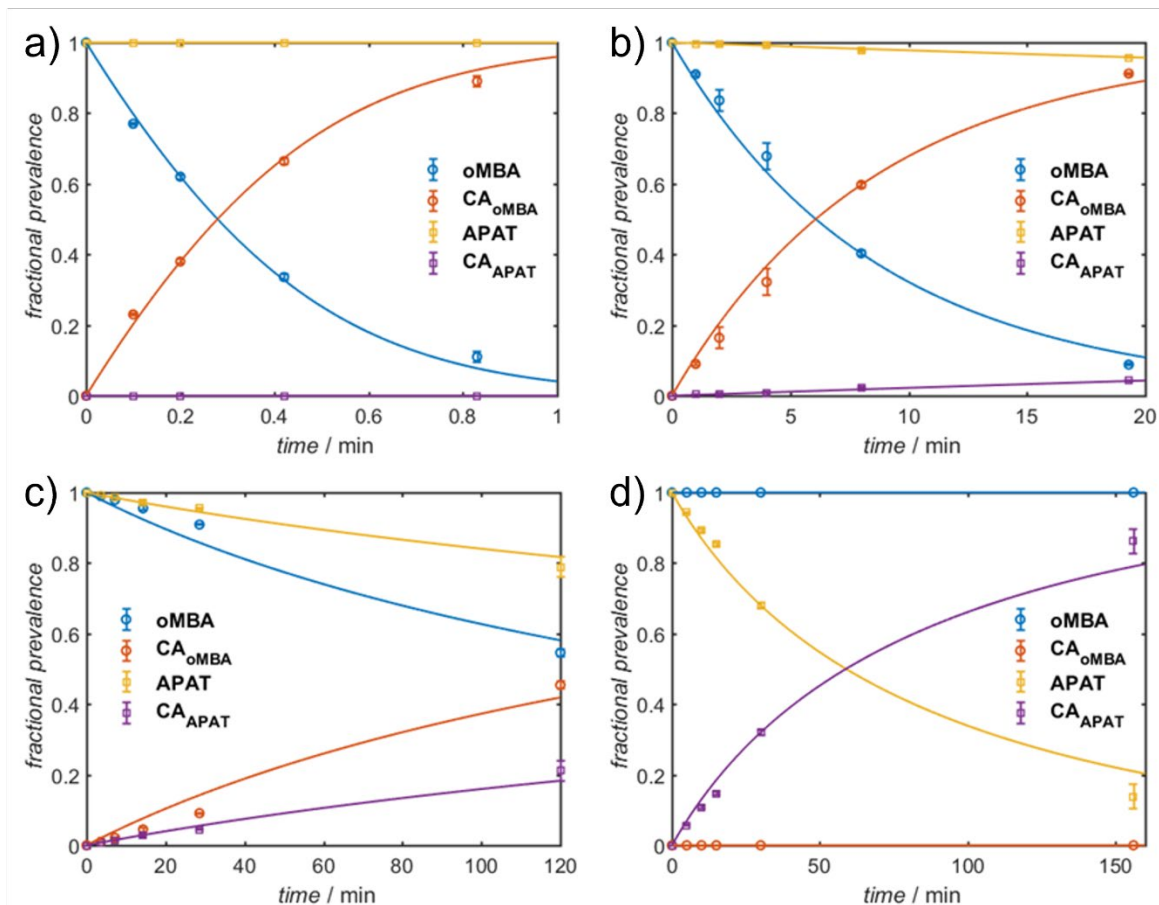


Figure S 41: Experimental time-dependent conversions (dots) of oMBA cycloaddition and APAT cycloaddition with NHEM in MeCN during irradiation with a) 500 μJ pulses of 320 nm, b) 500 μJ pulses of 360 nm, c) 364 μJ pulses of 390 nm and d) 2000 μJ pulses of 450 nm. All experiments were conducted at ambient temperature, using 20 Hz laser irradiation. Best-fit theoretical simulations used to determine reaction quantum yield are shown as solid lines.

10.4.2 Results of Sequential LED-Experiment

Table S 9: Results of the sequential LED experiment. Reaction conversion was determined via LC-MS. Uncertainties of absorption coefficients were used to calculate errors.

Wavelength / nm	Total Irradiation Time / min	Average Yield CA _{APAT} / %	Standard Error CA _{APAT} / %	Average Yield CA _{OMBA} / %	Standard Error CA _{OMBA} / %	Degree of Rearomati- zation / %
325	15	0.0	0.0	25.6	0.8	-
325	30	0.0	0.0	45.4	1.0	-
325	45	0.0	0.0	60.7	1.0	-
445	85	10.6	0.3	59.7	1.0	46
445	125	23.6	0.6	59.9	1.0	33
445	165	35.3	0.8	59.8	1.0	36
Dark	205	35.4	0.8	59.9	1.0	36
Dark	245	35.8	0.8	59.8	1.0	36
Dark	285	36.2	0.8	60.1	1.0	35
445	325	43.1	0.8	59.9	1.0	44
445	365	51.1	0.8	60.3	1.0	50
445	405	59.2	0.8	59.9	1.0	57
325	420	60.1	0.8	69.6	0.9	56
325	435	58.7	0.8	77.0	0.7	57
325	450	60.1	0.8	83.6	0.6	58

10.4.3 Temperature-Stability of APAT

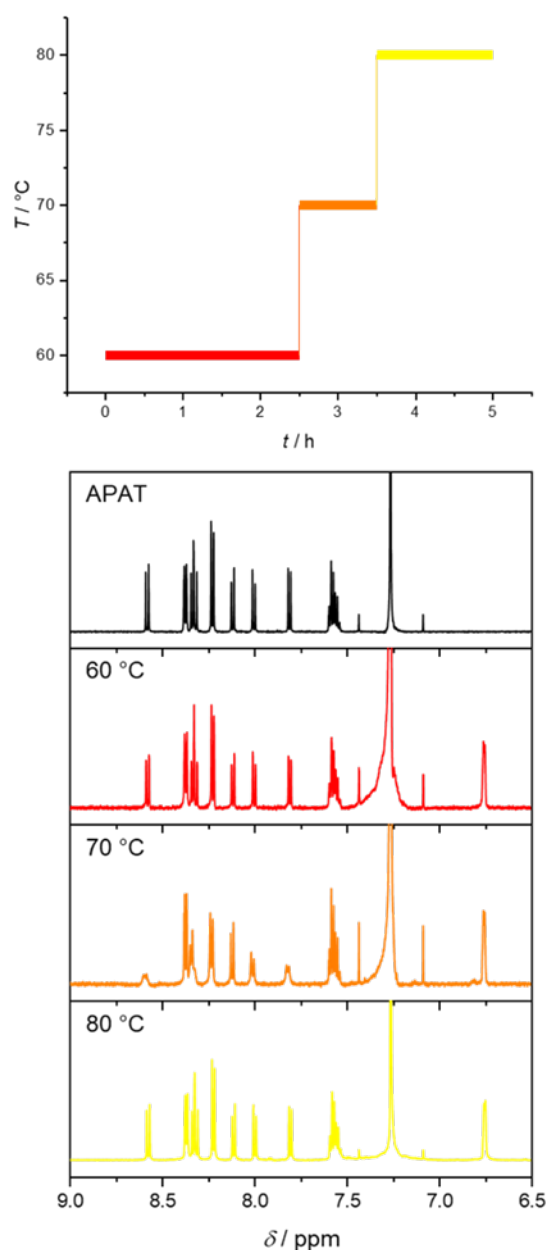


Figure S 42: Testing of the temperature-stability of APAT. A mixture of APAT and maleimide end-capped PMMA in MeCN was heated to 60 °C for 2.5 h, then 70 °C for 1 h, and then 80 °C for another 1.5 h. Samples were withdrawn and measured in CDCl₃ at ambient temperature. For clarity, only the characteristic aromatic region of the ¹H-NMR spectra is shown. The signal at 6.55 ppm corresponds to the vinylic protons of the maleimide. No change of signals was detected in the ¹H-NMR spectra, indicating that APAT is stable at T ≤ 80 °C, which is close to the solvent boiling point. Therefore, we rule out thermal formation of the nitrile imine. This is consistent with literature, which states that tetrazoles are temperature-stable up to ~160-220 °C.

10.5 Results of the [2+2] Cyclodimerization of Styrylpyrene

10.5.1 Results of Action Plot Experiments with Adjusted Photon Number

Table S 10: Results of the action plot experiments with adjusted photon number. Reaction conversion was determined via ¹H-NMR spectroscopy. Error bars were obtained through 3x repetition of every experiment.

Wavelength / nm	Average Dimer Yield / %	Standard Deviation / %
310	0.0	0.0
330	0.0	0.0
350	0.0	0.0
370	0.0	0.0
390	0.0	0.0
410	0.0	0.0
415	0.0	0.0
420	3.3	1.1
425	9.9	1.9
430	22.2	9.3
435	45.6	5.2
440	56.0	7.2
445	48.4	4.3
450	32.9	1.6
455	19.9	1.6
460	9.5	0.1
465	3.9	0.0
470	0.0	0.0

10.5.2 Results of Action Plot Experiment at 5 mM Concentration

Table S 11: Results of the action plot experiments at 5 mM concentration. Reaction conversion was determined via $^1\text{H-NMR}$ spectroscopy. Error bars were obtained through 3x repetition of every experiment.

Wavelength / nm	Average Dimer Yield / %	Standard Deviation / %
415	0.0	0.0
420	0.7	1.1
425	8.3	3.9
430	31.4	1.5
435	38.2	0.9
440	42.4	2.6
445	33.9	0.7
455	10.7	1.0
465	0.0	0.0

10.5.3 Results of Action Plot Experiments in $\text{DMSO-}d_6$

Table S 12: Results of the action plot experiments in $\text{DMSO-}d_6$. Reaction conversion was determined via $^1\text{H-NMR}$ spectroscopy. Error bars were obtained through 3x repetition of every experiment.

Wavelength / nm	Average Dimer Yield / %	Standard Deviation / %
425	0.0	0.0
435	2.0	0.0
440	5.8	0.1
445	11.4	0.1
450	15.2	0.8
455	13.6	2.0
460	9.5	0.1
465	3.3	1.1
470	0.0	0.0

10.5.4 Results of Action Plot Experiments at 37 °C

Wavelength / nm	Average Dimer Yield / %	Standard Deviation / %
425	3.9	0.0
440	16.8	5.5
460	3.9	0.0

11 ACKNOWLEDGEMENTS

I want to thank my principal supervisor, Christopher Barner-Kowollik, my cotutelle supervisor Andreas-Neil Unterreiner, and my co-supervisor, James Blinco, for the opportunity to do research under their guidance, their continuous support and positive feedback, and the incredible time I had in Brisbane and Karlsruhe over the past years.

I want to thank my collaborators who helped me conduct and improve my research, and without whom some of this work would not have been possible: David Marschner and Hendrik Frisch for developing the stypy project and helping with the analysis. Leona Rodrigues for synthesising oMBA and spending endless time patiently helping me with everything LC-MS related. Sarah Walden for calculating the quantum yields and for her ability to explain physics to chemists. Philipp Jöckle for being a great mentor and helping me bring my master's project to maturity, and for one of the best and most exciting holidays I've ever had. I also want to thank Sandra Wiedbrauk for helping me in the beginning of my time as a PhD, for her support and advice. Thanks to Philipp Menzel for many insightful discussions on photochemistry, and to Jessica Pelloth for many a coffee break and lots of fun talks in the gardens.

I want to express my gratitude to the entire macroarc group, who were incredibly supportive in every way and every situation, be it in the lab, the office, in the pub or at the beach. I cannot even begin to list the great days and nights we had together. Trivia nights, scooter trips on Straddie, gin tastings, paint'n'sips, or crocodile hunting in NT will never be forgotten, and greatly contributed to my mental health during these tumultuous times.

In addition, I would like to thank the Olzmann group and the femto group at KIT, for many interesting and funny conversations in the seminar room and plentiful contributions to our black piggybank. Special thanks go to Julia Leier for her helpful advice.

A group of people for whom I want to express my greatest thankfulness are my friends and roommates in the infamous Turbot St: Christian, David, Susanna, Kristina (you count as one) and Julian for the great time, holidays, discussions, fruit salads and excessive cooking sessions. You guys made life so, so much easier when I was overwhelmed by my PhD-life and helped me keep my sanity. At this point, thanks are also due to the Felon's Brewing Co. for being a haven on Wednesdays.

The people I want to thank most, though, are my family both in Germany and Australia. Thank you, Brian, Dani, Nina, and Mia, for giving me a wonderful family Christmas in times of shut borders. My biggest thanks go to my parents, who never stopped supporting me even for one second. You made all this possible in the first place. Without you I wouldn't be where I am now.

Last but certainly not least I want to thank my eternally supportive partner, Michaela. You stayed with me all this time, shared everything with me and let me be part of your life against an entire planet and nine hours of time difference between us. One day, we may come back together (at least for a long vacation).

12 ACADEMIC OUTPUT

Publications in peer-reviewed journals

- *More than Expected: Overall Initiation Efficiencies of Mono-, Bis- and Tetraacylgermane Radical Initiators*
Joeckle, P.*; **Kamm, P. W.***; Lamparth, I.; Moszner, N.; Unterreiner, A.-N.; Barner-Kowollik, C. *Macromolecules* **2019**, 52, 281-291.
- *Photocycloadditions in disparate chemical environments*
Marschner D. E*;**Kamm, P. W.***; Frisch, H.; Unterreiner, A.-N.; Barner-Kowollik, C. *Chem. Commun.* **2020**, 56, 14043-14046.
- *Green-light induced cycloadditions*
Kamm, P. W.; Blinco, J.P.; Unterreiner, A.-N.; Barner-Kowollik, C. *Chem. Commun.* **2021**, 57, 3991-3994.
- *Sequence-independent activation of photoreactions using two colours of light*
Kamm, P. W.; Rodrigues, L.L; Walden, S. L.; Blinco, J.P.; Unterreiner, A.-N.; Barner-Kowollik, C. *Chem. Sci.* **2021**, 13, 531-535.

* Contributed equally

Conference contributions

- *Photocycloadditions in Disparate Chemical Environments*
Marschner D. E; Kamm, P. W.; Frisch, H.; Unterreiner, A.-N.; Barner-Kowollik, C.
Queensland Annual Chemistry Symposium (QACS), **2020**
- *Green-Light Induced Cycloadditions*
Kamm, P. W.; Blinco, J.P.; Unterreiner, A.-N.; Barner-Kowollik, C.
Future Materials Symposium, **2021**